Investigating the combustion and emission characteristics of lignocellulosic derived future fuels with novel chemical reactivity in a heavy-duty compression ignition engine

Timothy Deehan

Submitted in partial fulfilment of the requirements
for the degree of Doctor of Philosophy at
University College London

February 2023

I, Timothy Deehan, confirm that the work presented in this thesis is my own. Where information has been derived from other sources, I confirm that this has been indicated in the thesis

Dated 04/02/2023

Abstract

It is indisputable that anthropogenic climate change has severely impacted the global environment. The continual growth in greenhouse gas emissions since the industrial revolution has increased the global average temperature, disrupted weather patterns and will soon turn habited parts of the world inhospitable to human life. A vital step in lowering net CO_2 emissions as the global economy transitions away from fossil fuels is increasing the role of biofuels as a CO_2 neutral source of hydrocarbon fuel.

This work presents experimental studies on the impact of molecular structure on combustive characteristics and emissions in a heavy-duty compression ignition engine, representative of engines in difficult to decarbonise sectors. Modifications to the engine allowed for direct measurements on the process of combustion, whilst exhaust gases and particulates were measured in real time. Four series of engine tests were carried out under constant injection duration and timing. Each focused on a specific subset of potential future fuels, such that direct comparisons between combustion performance would provide insight into; novel chemical reaction pathways, novel bio-derivable chemical structures, widening the pool of waste-based biofuel feedstocks or the considerations needed when designing future fuels.

In tests on methyl nonanoate esters, the inclusion of a Michael Acceptors (α, β-unsaturated carbonyls) was found to reduce the duration of ignition delay. Tests on lactone isomerism found ring-size to have greater influence on ignition delay than alkyl chain length. Date pit methyl esters were found to exhibit similar combustive characteristics and emissions to rapeseed methyl esters, improving the outlook for adoption of additional waste-based feedstocks. The etherification of an alcohol derived from lignocellulosic biomass significantly reduced the duration of ignition delay in test fuels blends even at a low 3.5 % conversion yield.

Impact statement

Currently, there is little research covering how changes in chemical structure affect fuel performance in engines similar in size, or larger than, the engine used as the testing facility in this work. The overwhelming majority of work which does cover different chemical structures in compression ignition (CI) engines focuses on biodiesels, which over the last 15 years have become a widely available product at fuel stations across Europe, North and South America, and some parts of South East Asia, and such FAME based fuels have been researched extensively. The work presented here is impactful as three of the four results chapters do not consider biodiesels, instead focusing on novel future fuels derived from lignocellulosic biomass – a largely over-looked feedstock for heavy-duty CI engines, and each results chapter is in the early stage of being published.

The first systematic study presented draws upon existing knowledge used in the field of organic synthetic chemistry and how certain chemical structures can improve combustion characteristics. Understanding how the unique chemical structures change biofuel performance allows for specific engine operation which improve fuel consumption and pollutant formation. The results from the study of Michael Acceptors was presented to Members of Parliament in the House of Commons, at the STEM for Britain event on the 7th of March, 2022.

The remaining chapters each contribute to the advancement of feedstock choice and work has commenced on publishing each results chapter as a research paper. The final chapter includes a chemical synthesis as a proof-of-concept for chemical reactions which can upgrade molecules that are typical of lignocellulosic biomass into molecules that are more appropriate for CI engines. The results from this work will lead to further academic investigations and importantly, highlight to private industry that biofuel alternatives to road diesel can be produced from biomass with simple conditions and non-toxic catalysts.

The remaining chapter focused on biodiesel produced from date pits, an abundant waste product across North Africa and the Middle East, and does not contribute to the fuel vs food debate. This project was undertaken in collaboration with Dr. Lamya AL-Haj, at Sultan Qaboos University in Oman. Following the experimental studies, the group at SQU launched a university

campus bus running on the date pit esters covering over 250 km to date, and proves that the feedstock will contribute to decarbonisation of road fuel across the Middle East and North Africa.

Finally, whilst not contributing to the work in this thesis, the author tested a series of bunker fuels blending with an unknown biofuel in a collaboration with BP to independently test these fuels ahead of a biofuel bunkering trial. The role of biofuels is extremely vital in decarbonising shipping as there is a significant lack of progress in the industry to replace fossil fuels, and this work shows vessel operators that there are viable routes to decarbonise their bunker fuel. In response to this work, BP and the EPSRC have supported a PhD project to continue this work.

Acknowledgments

I would not be writing these acknowledgments if it were not for the continuous support from my supervisors, Dr Paul Hellier and Professor Nicos Ladommatos. In the first three years of my time at UCL, the constant assistance from Prof. Ladommatos really pushed me in the direction I needed to adapt to the engineering principles needed to set up a 750 kg engine at a research facility with no prior experience – not even in using a wrench. I cannot fathom how he answered all my inexperienced questions with patience and a smile. Throughout the entire duration and especially in my final years at UCL, Dr. Hellier was a rock who guided not only myself, but several other students through the hardship of the COVID-19 pandemic. It is only thanks to his endless optimism and compassion that I have made it to finalising this work. Thank you for the understanding, guidance and patience.

Additional thanks to Professor Jim Anderson in UCL's chemistry department, who accepted my request to synthesise a fuel in his lab and for his input on the specifics of my project work there.

Thanks also to Dr. Midhat Talibi, for the advice he provided and for all the PGTA work he sent my way. I greatly enjoyed being involved in the undergraduate labs and the work helped me go to the pub a bit more often. Thank you to Dr. Victor Kärcher for all his help in setting up some crucial parts of the testing facility and for all the tips and tricks he taught me – they were invaluable later down the line. To all the fellow PhD students I shared the subbasement corridor with, which after five and half years are too numerous to list, thank you all for the companionship and shared struggles. Finally, to Sunita Sisodiya, thank you for coming in so often throughout the pandemic, I had got bored of talking to myself in the lab. Good luck with the engine I have left you with.

To all the technicians in the workshop who I constantly pestered for help with random nuts and bolts, or with a strange solidworks diagram that made little sense – thank you for putting up with me. And thank you especially to Kee Lam, for all the jokes and for the weeks where you spent more time in my lab than I did.

To all of my friends outside of my life at UCL, thank you all for the words of support you have offered through the years. Thank you for all the jokes and I look forward to drinking something fizzy with all the boys soon.

I cannot thank my mother, Katherine Kelleher, enough for the life she worked so hard to provide for my sister and me. Thank you for the help every step of the way. Thank you as well to my father and sister for your support. And thank you to Burrata, for making sure my hands are never free from scratches.

Finally, to my partner in crime, Chloë Ridyard. Thank you for everything you have helped me through. It is hard to know who is more nuts, myself for pursuing a PhD in a field I had no experience in, or you, for putting up with my complaints for so many years.

Contents

List of Figures

List of Tables

Nomenclature

ANHRR	Apparent net heat release rate
ASI	After start of injection
ATDC	After top dead centre
Bis-THFA	Bis-tetrahydrofurfuryl alcohol
BTDC	Before top dead centre
BX (X=any number)	Biodiesel blend X% biodiesel v/v% in diesel
CAD	Crank angle degree
CFR	Cooperative fuel research engine
CO	Carbon monoxide
CO_2	Carbon dioxide
CR	Common rail
C-SOC	Constant start of combustion
CX (X=any number)	The carbon at position 'X' according to IUPAC convention
D8k	Volvo D8k engine
DAQ	Data acquisition
DCM	Dichloromethane
DDdl	Delta dodecalactone
DDl	Delta decalactone
DNl	Delta nonalactone
DPME	Date pit methyl ester
DUl	Delta undecalactone
Dyno	Dynamometer
ECU	Engine control unit
EtD	Ethyl decanoate
EtD2	Ethyl dec-2-enoate
EtO	Ethyl octanoate
EtO2	Ethyl oct-2-enoate
ETU	Engine timing unit
FAE	Faty acid ester
FAME	Fatty acid methyl ester
GC	Gas chromatography
GC-MS	Gas chromatography-mass spectrometry

GDdl	Gamma dodecalactone
GDl	Gamma decalactone
GHG	Greenhouse gas
GHpl	Gamma heptalactone
GHxl	Gamma hexalactone
GNl	Gamma nonalactone
GOl	Gamma octalactone
GUl	Gamma undecalactone
GVl	Gamma valerolactone
HCl	Hydrochloric acid
HVO	Hydrogenated vegetable oil
ID	Ignition delay
IMEP	Indicated mean effective pressure
MA	Michael Acceptor
mmol	milli-mols
MN	Methyl nonanoate
MN2	Methyl non-2-enoate
MN3	Methyl non-3-enoate
MW	Molecular weight
N_2	Nitrogen
NI	National instruments
NMR	Nuclear magnetic resonance
NO	Nitrogen monoxide
NO_2	Nitrogen dioxide
NO_x	Nitrogen oxides
NPN	Negative positive negative sensor
O_2	Oxygen
OME	Oxymethylene dimethyl ethers
PAH	Polyaromatic hydrocarbons
PHRR	Peak heat release rate
PRV	Pressure relief valve
PS	Pressure sensor
PSU	Power supply unit
PWM	Pulse width modulated

RBF	Round bottom flask
Ref. D	Reference diesel
RME	Rapeseed methyl ester
RPM	Revolutions per minute
SOC	Start of combustion
THC / UHC	Unburnt hydrocarbons
THF	Tetrahydrofuran
THFA	Tetrahydrofurfuryl alcohol
TLC	Thin layer chromatography
wt	weight

1. Introduction

The concentration of CO_2 in Earth's atmosphere has increased drastically since the start of the industrial revolution and widespread consumption of fossil fuels commenced. As CO_2 absorbs light in the infrared spectrum, it is classed as a greenhouse gas and a high concentration in the atmosphere contributes to global temperature rise.[1] There is extensive evidence supporting this and the associated implications, such as rising sea levels, glacial melt and disruption of oceanic currents, which have driven forward research into the reduction of anthropogenic CO_2 production.[2,3]

A major contribution to CO_2 production in the EU is the transport sector, accounting for 22 % of all CO_2 emissions.[4] Electric powered vehicles are now rising as a market percentage in the EU. The European Environment Agency is aiming to halve the number of conventional fossil fuel powered cars present by 2030, and removing their presence entirely in cities by 2050 due to rising health concerns with regards to NO_x and particulate emissions from diesel engines .[5]

Provisional data for the UK indicates that the transport sector accounted for 31.5 % of the UK's CO_2 emissions in 2021, with the majority of this coming from on-road transport.[6] Additionally, data available for 2018 indicates that diesel goods transport vehicles currently account for almost 25 % of fuel consumption in the UK that year.[7] Heavy goods vehicles are affected by road weight limits for how much load they can transport per vehicle, and currently electric batteries on electrified cars reach up to 25 % of the total vehicle weight.[8] Conversion of goods transport vehicles to a fully electric fleet is currently impeded by this weight factor, as a battery powered vehicle will be not be permitted to transport the same cargo weight as a conventional fuel powered vehicle. This problem can be overcome by increasing power density of batteries or a thorough redesign of the UK road systems, neither of which are immediately feasible options. The travel range remains a serious barrier to full EV adoption, with the most advanced vehicles still limited to ranges close to 300 km between charges.[9,10] As such, heavier goods vehicles which rely on transporting as much cargo as possible are likely to remain powered by conventional fuels and combustion engines until new technologies not yet known are developed to replace them.

To reduce the emissions of CO_2 contributed from goods vehicles, the approach of using biofuels is of increasing interest as this would require little modification to existing vehicle fleets. Whilst not all biofuels emit the same amount of CO_2 during combustion, biofuels exist in a closed carbon cycle. The CO_2 emissions resultant from their use are ideally equal to or less then the carbon fixated from the atmosphere by the growth of the biological source of the fuel. As of 2017, the EU commission classes a biofuel as suitable for use if it offers a 50 % greenhouse gas emission saving when compared to conventional fuel over their full lifecycle.[11] For this to be an achievable goal, the fuel must be as unchanged from native biomass as possible. However, the production of fatty acid methyl esters (FAME), the most common biofuel alternative to diesel, uses methanol as a key component in production. In 2014, 75 % of global methanol production was sourced from natural gas or syngas, and stocks of methanol produced by fermentation are in early stages of full commercialisation.[12] FAME therefore cannot be considered a true biofuel in this sense as some of the energy produced during combustion is still derived from fossil fuels.

Alongside public awareness of rising CO_2 levels there is now a drive to reduce harmful NO_x and particulate emissions due to the health hazards that they are linked to. The air and fuel mixing in a diesel engine is often not as homogenous as a gasoline engine, and local hotspot zones in the chamber will appear.[13] As formation of NO_x is favoured at higher temperatures, its production is an invariability of efficient combustion in these hotspot zones. Particulate formation is initiated by the pyrolysis of fuel – burning of fuel in very low oxygen environments. It has been shown that using oxygenated fuels can improve the oxidation of aromatic soot particles, leading to a reduction in particulate emissions.

Biodiesel is the current leading biomass sourced fuel replacement of diesel as it requires little to no modification to existing compression ignition engines and has a straightforward production method. Biodiesel burns very readily, producing a high flame temperature, leading to a reduction in particulate formation but an increase in NO_x formation when compared to standard diesel.[14–16]

A pressing issue with biofuels is the food vs fuel debate. Biodiesel is produced from chemical conversion of vegetable oils and animal fats. The fuel is blended

29

with diesel to produce blends and are named after their blend ratio – B10 is 90 % fossil diesel, 10 % biodiesel. The use of biofuels in today's market is increasingly common and finding routes to fuels which are not competing with the traditional food crops is a crucial goal.[17]

There is often disagreement in biofuel debate on whether crops high in sugars/ starches should be grown for use as biofuels, as this crop mass competes with food production for society. This leads current biofuel efforts to focus on using plant biomass sources which do not compete with food availability. This investigation will focus primarily on biofuels which do not compete in the food vs fuel debate, by focusing on chemical structures found in lignocellulosic biomass, or biodiesel derived from waste-based feedstocks.

Heavy-duty engines operate at significantly slower speeds relative to light-duty engines, allowing greater time for novel fuel molecular structures and unique kinetic pathways to influence the duration of ignition delay, combustion phasing or emissions. This work presents investigations on four groups of similar molecules with slight differences in molecular structure, which are likely to influence fuel reactivity and therefore change overall fuel characteristics when tested in a low-speed engine.

This thesis will review the relevant literature on the process of combustion in compression ignition engines, the conversion of biomass to biofuels, pollutant formation in engines and the impact of molecular structure in heavy-duty engines. This will be followed by a discussion on the development of a heavy-duty engine testing facility, followed by a discussion on experimental set up and conditions. Four results chapters discussing investigations of potential future fuels will be a presented, followed by conclusions and recommendations for further work.

2. Literature review

This thesis is concerned with designing new biofuels and testing their performance in heavy duty compression ignition engines. The literature reviewed here will focus on combustion in compression ignition engines and the suitability of biofuels to replace fossil diesel in the context of heavy-duty engines.

The first section will review literature on the fundamental processes occurring when a fuel ignites an engine. The second section will briefly introduce the well-established process of producing biofuels from biomass and then discuss the literature on new potential biofuels and their production. The third section will discuss literature on the formation of gaseous pollutants and soot during the process of combustion. The final section will review relevant literature focusing on biofuels and the influence of molecular structure in heavy-duty compression ignition engines.

2.1. Combustion in compression ignition engines

Heavy goods vehicles, off-road machinery and boats use reciprocating compression ignition engines which run on diesel fuel. The reciprocating compression ignition engine was first prototyped in 1895 by Rudolf Diesel, for whom diesel engines are named. Fossil diesel fuel is a mixture of various hydrocarbons which are fractionated from crude oil based on compounds boiling between 150-380 ^{o}C.[18]

Spark ignition engines utilise a lower boiling point fraction of crude oil than diesel in addition to light fuels which are not derived from fossil fuel, such as ethanol. In homogenous charge engines, the fuel/air mixture enters the combustion chamber where it is compressed and ignited by an electrical discharge from a spark plug. The combustion flame then propagates from the spark plug as the origin point.[19]

Compression ignition (CI) engines do not utilise a spark plug for ignition, rather they rely on the decomposition and autoignition of the fuel under conditions of elevated temperature and pressure. Following fuel injection, the fuel atomises into small droplets. The high temperature air in the chamber initiates combustion of vapour emerging from droplets at the forefront of the fuel spray,

according to the manner of fuel injection. The vast majority of modern diesel engines inject the diesel fuel directly into the combustion chamber with air supplied unthrottled from the intake valve/valves. The injection pressure is typically very high (up to several hundred or thousand bar), and in heavy duty engines the chamber size is large, facilitating ample fuel air mixing to initiate combustion.[20]

Smaller diesel engines run at a higher speed than heavy-duty so there is less time for this fuel/air mixing to occur. Light duty engines previously used an auxiliary chamber to facilitate fuel-air mixing. This indirect injection method is now an outdated technology as injection pressures and fuel/air mixing has been improved significantly. As these improvements continued, the use of an auxiliary chamber was no longer necessary with piston bowl geometry now a the dominant influence on the progress of combustion.[21]

During the compression and power stroke of the CI engine, the combustion chamber is a highly turbulent environment. These turbulent conditions have caused difficulties in conducting accurate research into the exact mechanism of combustion. The process of combustion involves high pressures, temperatures, and complex chemical reactions. Early attempts at predicting this process relied on specialist computational models and experimental facilities which struggled to accurately replicate the true conditions of the combustion chamber.[22] It was considered very difficult to model the relationships between fuel spray behaviour, flame structure and fuel burning rates.

This changed when Dec (1997) proposed a conceptual model of compression ignition combustion using laser sheet imaging to make direct quantitative and accurate measurements in a direct injection compression diesel engine.[23] The conceptual model presented has aided the subsequent development of complex models. The following sections will describe the stages of combustion within a quiescent compression engine, drawing heavily on the work of Dec (1997).[23]

2.1.1. Ignition delay

Ignition delay is the period between the start of fuel injection and the start of combustion, typically measured in crank angle degrees (CAD). Optical laser imaging shows that as the fuel jet enters the combustion chamber, it initially remains a liquid and the fuel jet entrains air. Fuel injection pressure typically

ranges from 1000-2000 bar, whereas in-cylinder air pressure at time of injection is roughly 50-100 bar. This pressure difference and the residual heat within the chamber causes large fuel droplets to rapidly atomise to fine droplets. The fuel jet enters the chamber and begins atomizing at ~ 950 K. As the fuel droplets vaporise, their momentum entrains hot air into the fuel jet, expanding the spray as it penetrates into the chamber.
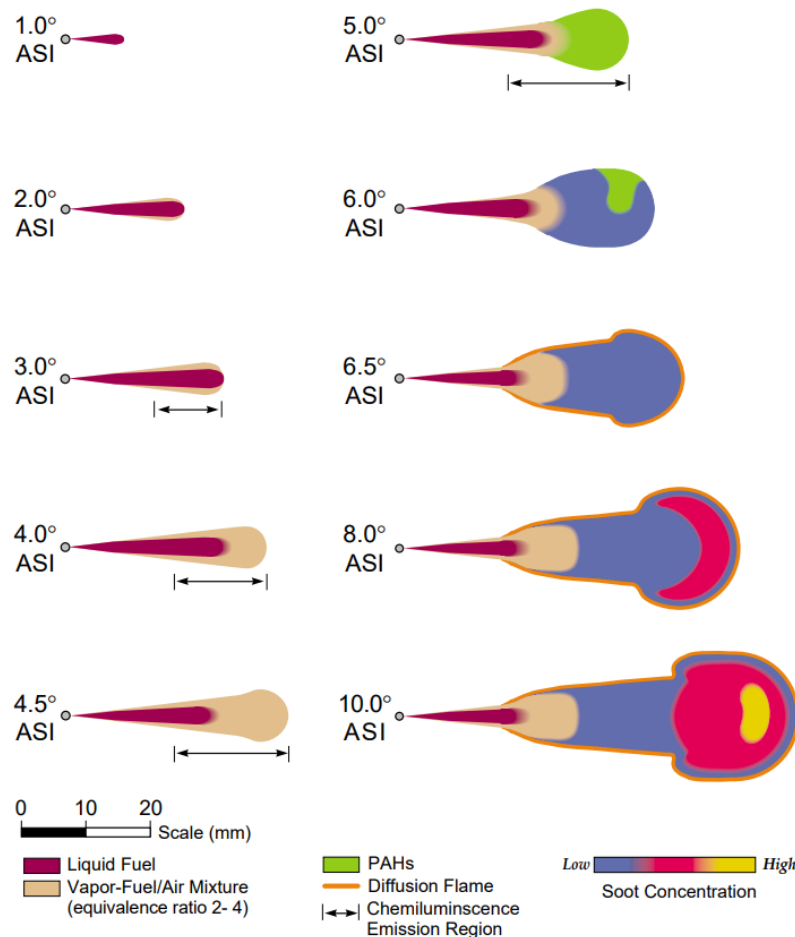
Figure 2.1: Outlining the changes in fuel jet structure following injection, outlining the separate regions of the jet and the formation of the diffuse flame.[24]

The entrainment of hot air into the fuel jet encourages fuel air mixing, resulting in no pure fuel region within the jet. The jet is now a fuel rich mixture, with a fuel air ratio of 2-4 and fuel vaporisation having lowered the temperature to ~ 650 K. The leading region of the spray has a narrow boundary with a stoichiometric fuel air mixture and ignition chemistry begins here (Figure 2.1).

Dec et al. continued their investigations and utilising chemiluminescence measurements found that the initial ignition in the downstream portion of the fuel stream jet was observed as early at 3.5 CAD following injection. At this

point the fuel/air vapour region was still small in size, but by 4.5 CAD had expanded rapidly with the majority of chemiluminescence indicating ignition in the extensive rich vapour region. An important observation was that autoignition did not occur from a single point, but from multiple points in the fuel simultaneously.[25]

2.1.2. Start of combustion

The key steps of diesel combustion were identified by using chemiluminescence imaging in an optically accessible engine. Diesel combustion starts with spontaneous autoignition, followed by a rapid premixed burning process. Autoignition happens at a critical temperature range of between 900-1000 K, at which accumulated hydrogen peroxide rapidly decomposes to OH radicals. As the forefront of the liquid fuel spray reaches this temperature, hydrogen atoms are abstracted from the fuel molecules and replaced by oxygen in a series of low-temperature branching reactions, described further in Section 2.1.5 . At the angle of peak heat release rate, roughly 6-6.5 CAD after injection, the molecules contained within diesel fuel have begun to break down in the leading region of the fuel spray, forming a fuel rich premixed combustion zone. This zone contains many products of rich combustion, such as large fuel fragments, polyaromatic hydrocarbons (PAHs) and soot, and continued oxidation reactions further raise the temperature to 1150 K. Along the fuel air boundary of the jet a 'mixing-controlled' diffuse flame forms, which rapidly surrounds the jet and begins consuming the locally available oxygen.
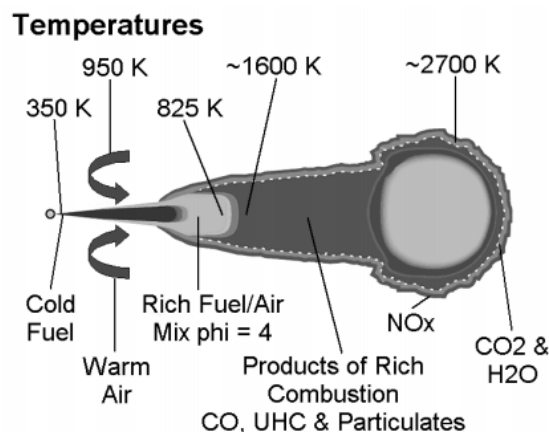
Figure 2.2: Summary of the fuel burning process, showing fuel jet and diffusion flame temperatures.[26]

2.1.3. Diffusion flame

At 8-10 CAD after start of injection (ASI) the diffusion flame has surrounded the jet with the premixed combustion zone providing soot and large hydrocarbon (HC) fragments as fuel. The leading region of the spray begins to spread outwards reaching its maximum penetration into the chamber. Here, the highest concentrations of soot are seen, and the flame reaches its highest temperature of ~2700 K. Oxygen diffuses in from the surrounding air allowing for complete combustion within this flame. Soot quickly moves outward from the leading region into the diffuse flame where it fully oxidises to final gaseous products such as CO_2, CO and H_2O. NOx production begins concurrently here via thermal oxidation of the nitrogen present in the air. These combustion products move outwards from the diffuse flame region and mix with the excess air, cooling and becoming leaner.

2.1.4. Air motion in high-speed CI engines

The above describes the process in a quiescent combustion chamber. 'Quiescent' in this case is a chamber without turbulence and reduced air motion. These chambers are only found in the largest engine designs, such as marine applications. A large chamber volume allows for adequate fuel air mixing at slow speed in these engines. Engines which run faster than 2000 RPM rely on modifications to the air intake and piston crown to encourage fuel air mixing by introducing air motion.

Air swirl is the rotation of air around the cylinder and is generated by bringing air into the cylinder with a high angular momentum. The air intake port can be designed in a way to introduce angular momentum, such as designing the port to be helical or by using a deflector wall. A helical port forces the air into a rotational movement prior to encountering the intake valve and a deflector wall partially blocks a segment of the intake valve, causing preferential air intake on one side of the valve. Air swirl will decay due to friction with the cylinder wall, with up to a third of the initial momentum being lost by top dead centre in the first compression stroke.

Piston crown modifications facilitate the generation of swirl by forcing the air into a compact bowl. During compression, the air is forced into this space and as its

angular momentum is conserved, the angular velocity increases. Additionally, when piston crowns are not flat, such as those with in-piston combustion chambers, squish is introduced.[21] As the piston crown is not flat there is a difference in distance from the crown to the cylinder roof along the piston profile. During the compression stroke, air is forced down into the combustion chamber as portions of the piston crown approach the cylinder roof and during the early stage of the expansion stroke there is opposite movement of air from the chamber to the cylinder wall.[27] In compression ignition engines this squish motion significantly amplifies the intake generated swirl. Air velocity within the chamber is therefore highest immediately prior to top dead centre (TDC) in the compression stroke which increases the entrainment of hot air into the fuel jet, leading to the efficient fuel air mixing necessary for high-speed compression ignition engines.[28]

2.1.5. Low temperature reaction kinetics

Low temperature reaction kinetics are radical propagations which lead towards branching reactions and an exponential increase in the radicals present in the combustion chamber. The propagating radical reactions dominate these low temperature reactions (T<900 K). Westbrook (2000) described a general reaction scheme for hydrocarbon fuels during the ignition delay period as follows:[29,30]

Equation 2-1
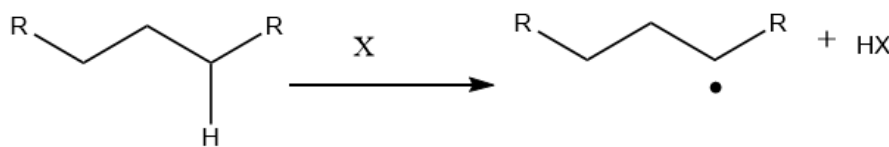
The initiating step for radical production is hydrogen abstraction from the alkyl chain in the hydrocarbon fuel. This can be abstracted by HO_2 or OH radicals and is the single external radical consumed for Equation 2-1 to Equation 2-7. Once the alkyl radical is formed, oxygen molecules can undergo addition reactions with the chain as shown in Equation 2-2.

Equation 2-2
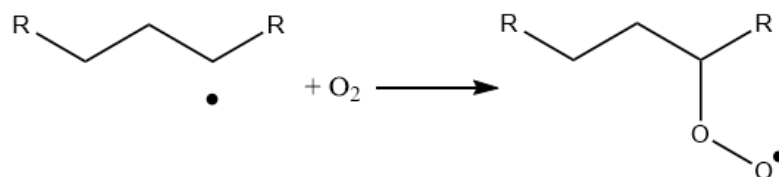
This radical species can now isomerise by abstracting a hydrogen from an adjacent carbon (Equation 2-3). This new carbon centred radical is unstable and will readily react with molecular oxygen (Equation 2-4)

Equation 2-3
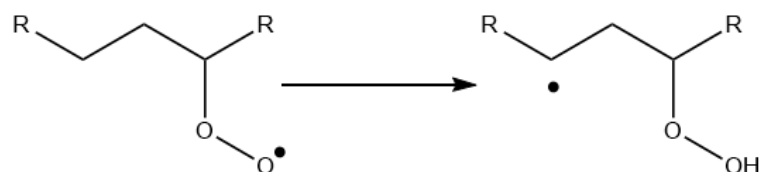
Equation 2-4
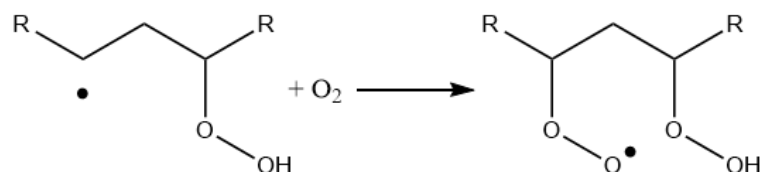
This new radical peroxy species readily break down to form a ketoperoxy species and a hydroxy radical (Equation 2-5).

Equation 2-5
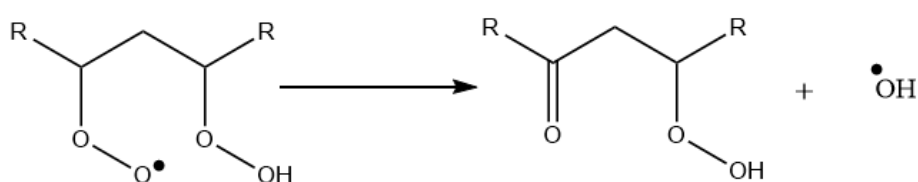
This ketoperoxy species will be unstable at higher temperatures, as it increases to 900-1000 K from the initial energy release, leading to further decomposition (Equation 2-6 & Equation 2-7). Overall, Equation 2-1 Equation 2-7 consume one radical species and generate three radicals, each of which can act as initiator 'X' in Equation 2-1, setting the ground for an exponential increase in fuel decomposition. Equations 2.5 – 2.7 each generate a free radical species, so can be thought of as the 'start' of combustion.

Equation 2-6
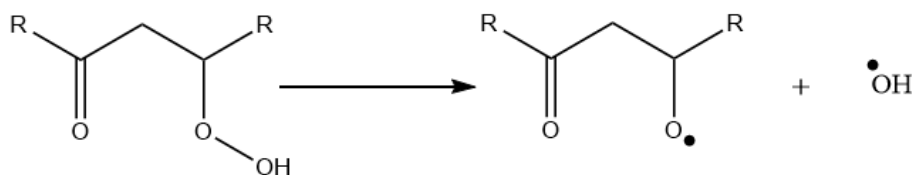
Equation 2-7
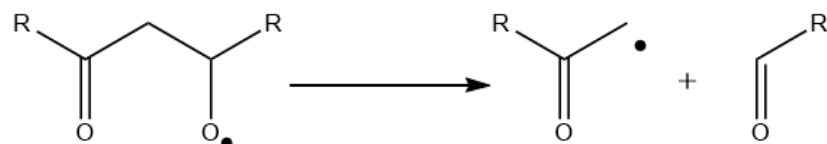
Equation 2-1 through to Equation 2-7 are a general representation of initiation in a linear alkane. Molecular structures such as ethers, alkenes, esters and aromatics will often influence how species 'X' in Equation 2-1 will initiate these kinetic pathways. In ethers as an example, the etheric oxygen has lowered the C-H bond strength on the two adjacent carbons, so the initial hydrogen abstraction is most likely to occur adjacent to the ether and with lower energy requirements to initiate – resulting in the better ignition qualities of ethers compared to alkanes.[31,32]

2.2. Biofuels

2.2.1. Overview of biofuels

Fossil fuels have traditionally been characterised based on common properties of boiling point, viscosity and density. These fuels are prepared by fractional distillation from crude oil which can have thousands of different molecules present as a mixture. When examining a biological source of chemicals, there is not the same wide range of chemicals available in bulk. For example, when considering plant biomass, the natural polymers, cellulose, hemicellulose and lignin constitute more than 90 % of the dried biomass weight. The extensive range of single molecular components found in crude oil is not seen in these basic polymers and therefore biofuels are much more discrete in structure. In addition to the plant's structural polymers, some plants such as sunflower or rapeseed have been cultivated for their oils, a fatty acid derived triglyceride.

2.2.2. Fatty acid derived fuels

Fatty acid derivatives were the first bio-based fuels more advanced than burning bulk plant material. Whale oil was used in the 19th century and Rudolf Diesels' first engine ran on peanut oil.[33]

Fatty acids have a core structure of a hydrophilic carboxylic acid group with a single hydrocarbon chain consisting of 4+ carbon atoms. This aliphatic chain may be saturated or unsaturated and the number of double bonds, if present, is determined by the structure of the fatty synthase enzymes present in an organism.

Carboxylic acid   Aliphatic hydrocarbon chain.
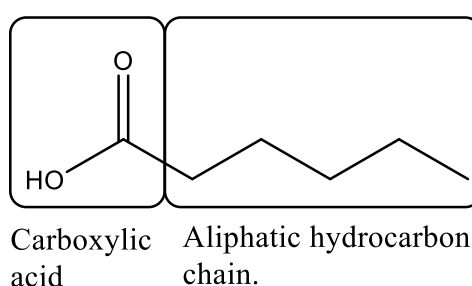
Figure 2.3 :Example of a simple fatty acid

Fats are a key macronutrient for life, alongside carbohydrates and proteins. A small percent of fatty acids can be found as cholesterols, the precursor to hormone production. A much larger and significant number of fatty acids is found in triglycerides such as animal fats/vegetable oils and as phospholipids, the major component of cell membranes as shown in Figure 2.3. Fatty acids are very rarely found naturally as a free acid in organisms, instead being found in one of these forms.
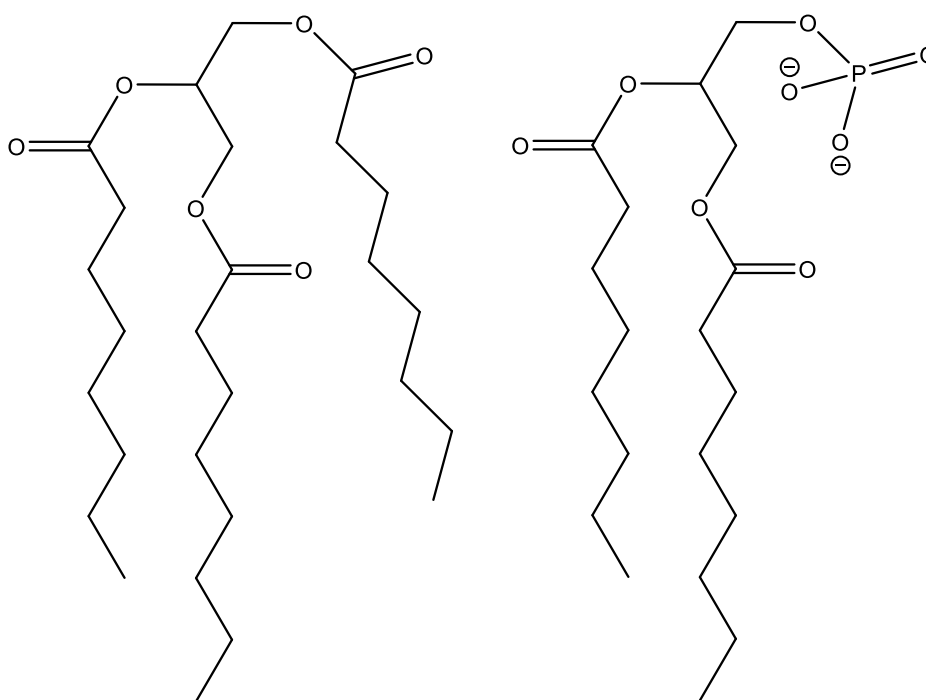
Figure 2.4: Triglyceride (Left) and Phospholipid (Right)

Triglycerides are a tri-ester of three fatty acid molecules and a single glycerol molecule, while phospholipids consist of two fatty acid molecules, a single glycerol molecule and a charged phosphate group (Figure 2.4).

Every microorganism produces fatty acids and while there are over 1000 naturally occurring fatty acids, just 25 of these occur widely in nature and are commercially significant.[34]

2.2.2.1. Biofuels from fatty acids

The main source of fat/oil feedstock for fatty acid methyl ester (FAME) production comes from vegetable oil crops, such as rapeseed, peanuts, sunflower seeds etc. with many different species producing similar fatty acids. Palmitic acid, a saturated 16 carbon long acid, is found in all animal lipids (20-30 %) and in almost all seed oils (5-50 %).[34]

Variation in the fatty acids produced by individuals of the same species is incredibly rare. Kunitsky et al. (2005) developed a technology for identifying unknown microbe cultures, by extracting the triglycerides from cultures and converting the extracts into FAME which are more volatile than triglycerides and detected by gas chromatography and mass spectrometry (GC-MS). Microbes will produce only a select range of fatty acids, so the FAME detected by GC-MS can be compared to known fingerprints of tested microbes. This technology

works as despite there being over 1000 fatty acids available in nature, single species make only a select few and therefore E. coli strains can be identified through determining the ratio of specific fatty acids present.

Flagella et al. (2002) studied how the percentage of oleic acid in sunflower seeds could change with environmental conditions.[35] Using the same plot of land over two years, the effects of change in rainfall and harvest time was compared with changes in fatty acid profile. It was found that both these variations did not significantly alter the percentage of oleic acid in the seeds, the total content of which varied from 79-84 %. The study further highlighted that when growing crops for FAME production, the biofuel product at the end will be highly homogenous in chemical composition, unlike the wide variety found in fossil fuel sources. This has led to research using different FAME molecules to test how singular chemical differences, such as the presence/absence of a double bond, two double bonds, cis/trans isomerization of any double bonds present, and of carbon chain length impact on combustion and emissions characteristics in diesel engines.[36]

2.2.2.2. Production and use of FAME

Fatty acid methyl esters are the fuel most commonly derived from fatty acids. These are produced by breaking triglycerides into individual chains via transesterification with methanol, shown in Figure 2.5.
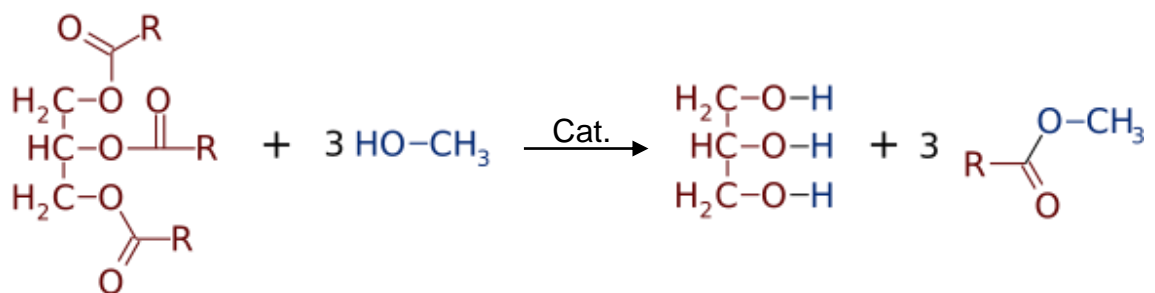
Figure 2.5: Transesterification of triglycerides to FAME and glycerol[37]

To start this process, vegetable oils are reacted with methanol and an acid or base catalyst in a reactor. Once complete, crude biodiesel is separated from crude glycerine. Both these products are purified and refined before being packaged. The most common catalyst used is a base, as these have lower costs than acidic catalysts, have shorter reaction times and have higher yields of FAME.[38] However, basic catalysis is more susceptible to water impurities and

free fatty acids in the vegetable oil feedstock. There is an increasing use of supercritical conditions to perform this process as supercritical transesterification does not require catalysts (lower waste production) and has very short reaction times. This process is not yet widespread as the high temperatures and pressures required do not offer an economic benefit over traditional catalysis reactors.[39,40]

FAME has several key differences to diesel fuel obtained from crude oil. The main advantage of biodiesel is its potential to be a fully renewable fuel – provided a sustainable source of methanol or ethanol is available. As a fuel, biodiesel has been reported to burn cleaner than fossil diesel, with a reduction in emissions of; carbon monoxide, unburnt hydrocarbons, polyaromatic hydrocarbons and particulates. However, several studies identified somewhat greater NO_x emissions than fossil diesel.[41] A more detailed consideration of biodiesel combustion in a heavy-duty engine is made later in the literature review (Section 2.4.1 Fatty acid methyl esters).

Biodiesel also has disadvantages relative to fossil diesel. The main disadvantage is its higher freezing point. Biodiesel has a variety of freezing points depending on the number of specific FAME molecules are present. Some biofuels can still be solid at 20 °C, a significant barrier for B100 blends of biodiesel colder climates.[42]

2.2.2.3. Hydrogenated vegetable oil

Hydrotreated vegetable oil (HVO) is a paraffinic liquid fuel and commercially available. HVO fuel is produced from soybean oil, rapeseed oil, used cooking oil and palm oil mill effluent. These are sources of triglycerides and HVO production competes with biodiesel production for the same feedstocks.[43] HVO, known as renewable diesel in the US and Canada, has grown in popularity as a biofuel in Europe as it is not subject to the 7% blend wall applied to FAME, and blending of HVO therefore allows for greater greenhouse gas (GHG) emission savings to be achieved.[44]

HVO is comprised of straight chain and branched hydrocarbons with little to no aromatic or sulphur compounds. As a result, its reported properties include a higher cetane number, improved emissions quality, high energy content, lower density, lower viscosity and higher combustion efficiency than fossil diesel.[45,46]
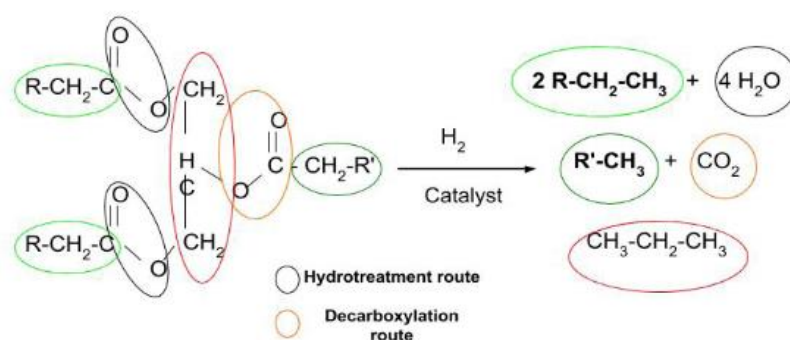
Figure 2.6: Hydrogenation of a triglyceride producing paraffinic HVO, water, CO2 and propane - Neste renewable diesel handbook.[44]

2.2.3. Plant sourced polymers

Plant material is mostly comprised of three polymers, namely cellulose, hemicellulose and lignin. By plant weight these polymers account for >90 % of the dry mass, with the ratio of each varying based on plant species. For instance, hardwoods often contain 40-50 % cellulose whilst cotton is almost 90 % cellulose. Lignin is an aromatic polymer and is responsible for plant rigidity. Hardwoods are 30-40 % lignin whilst herbaceous plants are often only up to 20 % lignin. Finally, hemicellulose constitutes 10-35 % of plant matter and with an amorphous nature, acts as a crosslinking tool connecting the various plant structures to each other.[47,48] There are other natural polymers such as pectin or polynucleotides, but as these represent a very small percent of plant mass or contain a high percent of molecular bound nitrogen, they are not considered as potential biofuel sources.

2.2.4. Cellulose

Cellulose is a polysaccharide chain made from d-glucose, a hexose sugar with a regular repeating unit, shown in Figure 2.7. This polymer can be many thousands of repeat units in length and it is the most abundant polymer on earth.[49] Cellulose production primarily from wood pulp and cotton is estimated to be 7.5 * 10^{10} tonnes annually.[50]
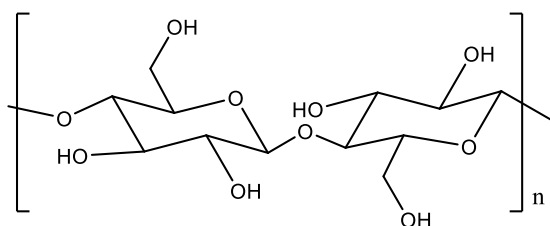
Figure 2.7: Regular repeat unit of cellulose; α, β 1-4 linked pair of d-glucose molecules

The free hydroxyl groups on cellulose allow for extensive hydrogen bonding between adjacent polymer chains. This leads to a very crystalline structure in cellulose and a high polymer strength which provides a natural resistance to hydrolysis.

2.2.4.1. Ethanol production from glucose and cellulose

Glucosic ethanol is a widely used biofuel across Europe, and North and South America. In 2017, US production of corn starch bioethanol alone was $5.025*10^7$ metric tonnes.[51] An increasing number of markets are including ethanol in place of gasoline, with a standardised classification system for these blends, i.e. E25 is 25 % ethanol and 75 % gasoline. Different blends are available in different markets, such as E85 which is distributed in Sweden, and E100 in Brazil where flexible vehicles which can run on pure ethanol are in production.[17] The bioethanol produced in Brazil comes from sugarcane, where a hectare of cane can produce 4,000 litres of bioethanol per year.[52] As glucose and starch are both consumed as food, there has been growing interest in cellulose as a potential source of ethanol but this has not yet been fully commercialised.

Cellulose as a polysaccharide chain is an excellent source of energy for organisms, which can degrade the chain. Animals which have a cellulose heavy diet (cows, horses etc) have symbiotic bacteria in their guts which have evolved the necessary enzymes to break down cellulose polymer chains.

The main route of cellulose to fuel utilises bacteria that contain cellulase enzymes to break down the chain to monosaccharides and subsequently ferment these sugars into ethanol.[53] As lignocellulosic biomass is very resistant to chemical or microbial attack, further research into cellulosic ethanol has focused on optimising this process. Cellulase enzymes are highly specific as they will break down cellulose chains, but will have limited ability to break down hemicellulose chains and will be completely ineffective at lignin degradation.[54]

Optimisation of this overall process follows two themes. The first is provision of a purer cellulose stream. Zhang et al. (2009) have outlined optimisation processes for the pre-treatment of lignocellulosic biomass to remove hemicelluloses and lignin from biomass so that a high percentage cellulose feedstock is available for fermentation.[55]

The second theme pursued genetic modification of the bacteria used. Yomano et al. have investigated limiting gene expression in E. coli, thereby allowing co-metabolism of xylan and cellulose chains which would remove the pre-treatment cost of removing hemicelluloses. However, the study noted that whilst co-metabolism in the E.coli was successfully increased, xylose (hemicellulose) metabolism lagged far behind that of glucose metabolism.[56] Potentially the modified E.coli still struggle to degrade significant levels of hemicellulose, a barrier which must be overcome for production of hemicellulosic ethanol.

2.2.5. Lignin

Lignin accounts for 30 % of organic carbon found in the biosphere and is comprised of phenolic monomer units as shown in Figure 2.8 which are crossed linked into its macrostructure by enzyme catalysed radical coupling reactions.[57,58]
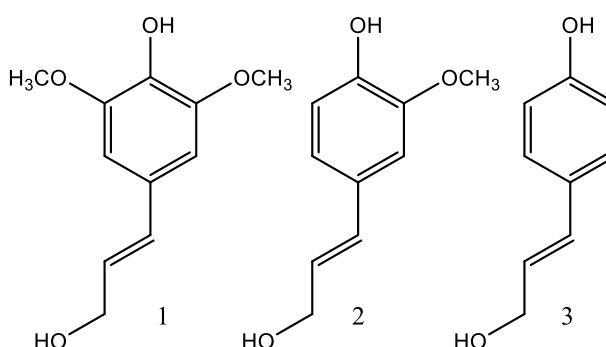
Figure 2.8: The three common lignin monomers; sinapyl alcohol (1), coniferyl alcohol (2) and paracoumaryl alcohol (3).

Lignin is incredibly resistant to chemical attack and the conversion of lignin to fine chemicals has been extensively researched owing to its abundance as a renewable source of aromatic compounds, which are traditionally synthesised from benzene extracted from crude oil.[59]

In 2017, 49 million tonnes of lignin was produced as waste from paper milling and burnt on site for electricity generation.[60] This abundance of lignin has led to significant interest in upgrading lignin to higher value fuel for automobile use.[61]

The macrostructure of lignin results in it being highly resistant to chemical modification and research into its biofuel potential has been extensive. There is yet to be a market implementation of any lignin derived fuel which provides a net energy gain over the processing of the lignin. The degradation of lignin

involves heavy metal catalysts, expensive ionic liquids or very intensive temperatures and pressures.[62] Ionic liquids and heavy metal catalysts are typically very expensive to produce, hence why industry has not yet moved beyond the research and pilot stages of fuel production from lignin.

2.2.6. Hemicellulose

Hemicellulose is a group of a few polysaccharide chains which are amorphous in structure and perform the function of connecting the plant cellulose microfibres to the lignin and pectin structures of plants. The term hemicellulose originated from E. Schulz in 1891, to *'designate polysaccharides extractable, in comparison to cellulose, from higher plants by aqueous alkaline solutions'.*[63]

The major polysaccharide under the hemicellulose branch are the xylan heteropolymers. Xylans are polymers with a xylose (5 carbon/pentose) sugar backbone, as shown in Figure 2.9. Unlike cellulose, xylans have branches coming off this backbone. The designation of the class of xylan depends on which sidechains are present.

These different xylans are outlined in Table 2.1, with the structure of side group chains X, Y and Z shown in Figure 2.9.
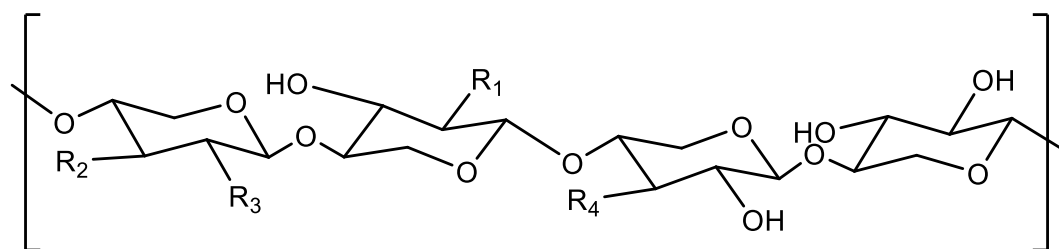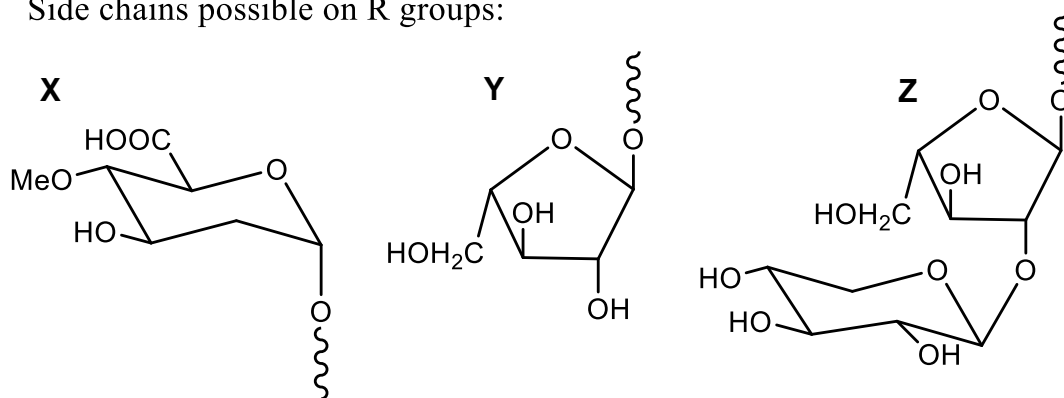
Figure 2.9: Xylan backbone chain with 'R' positions shown, which can be any of the three possible sidechain groups (x, y, z) shown below.

46

Xylan structure	R_1 Group	R_2 Group	R_3 Group	R_4 Group
Homoxylan	-OH	-OH	-OH	-OH
Glucuronoxylans	X	-OH	-OH	-OH
Arabinoglucuronoxylans	X	Y	-OH	-OH
Glucuronoarabinoxylans	X	Y	Y	Z
Arabinoxylans	-OH	Y	Y	Y

These 5 xylans are found in different sources at various levels. Homoxylans are found in small amounts throughout many plants and are also found in a few species of algae where it replaces cellulose as the cell wall support, accounting for up 50 % of cell weight.[64]

Glucuronoxylans accounts for 15-30 % of the weight of hardwood species. Arabinoglucuronoxylans account for 5-10 % by weight of grasses, cereals and softwoods. Arabinoxylans account for up to 30 % by weight in cereals. Finally, Glucuronoarabinoxylans account for 15-30 % by weight of grasses and cereals.

The branching nature of hemicelluloses lead to it having a much more amorphous nature relative to cellulose and lignin. Hemicellulose tends to be much shorter in total length, averaging at 500-3000 sugar units, compared to cellulose at 7000-15,000 sugar units. An amorphous nature and lower molecular weight lead hemicelluloses to be more susceptible to hydrolysis and chemical attack.[65] As hemicelluloses are much more readily extractable compared to cellulose or lignin, this component of biomass is an excellent starting point when considering the production of future biofuels.

2.2.7. Fuels from hemicellulose

2.2.7.1. Hemicellulosic ethanol

As hemicellulose polymers are made up of monosaccharide building blocks, these sugars can potentially be digested by microbes, just as cellulose can be. However, hemicellulose has a highly diverse macrostructure, with different monosaccharides side chains and more unique bond structures. This presents a greater challenge to industrially produce ethanol from hemicelluloses than in

the case of cellulose. Shallom et al. (2003) identified seven different families of enzymes which perform a function relevant to hemicellulose degradation.[66] These families are divided according to their core function, such as cleaving the xylose back bone, or cleaving the functional monosaccharide groups which can branch off the backbone. Out of the microbial species tested, there was found to be between 4–13 different enzymes present which contribute to the degradation of hemicellulose.[66] This presents a very different challenge for optimising ethanol production from hemicellulose when compared to cellulose (which as a much more ordered structure has only 3 broad classes of enzymes found for its degradation by microbes).[67]

Hahn-Hägerdal et al. (1994) investigated a new species of yeast which can metabolise pentose sugars, such as xylose, and noted that the ethanol productivity of the best xylose-fermenting yeast is still fivefold lower than yeast working on glucose.[68]

Improving ethanol productivity from xylose has been an area of increasing study. A cellulose/hemicellulose mixed stream for fermentation removes the inbuilt cellulose isolation step, which is necessary for cellulose fermentation and allows more native biomass material to be used from crops grown for the purpose of fermentation. Ethanol production from hemicellulose still faces many challenges. Despite promise being shown in gene modifications of several strains of yeast, there is yet to be an agreed-upon solution for hemicellulose fermentation that can be implemented industrially.[69]

2.2.7.2. Hemicelluloses to furfural

Furfural is a 5 carbon, aromatic molecule and is readily synthesised from xylose and other C-5 sugars by dehydration in sulfuric acid as shown in Figure 2.10.
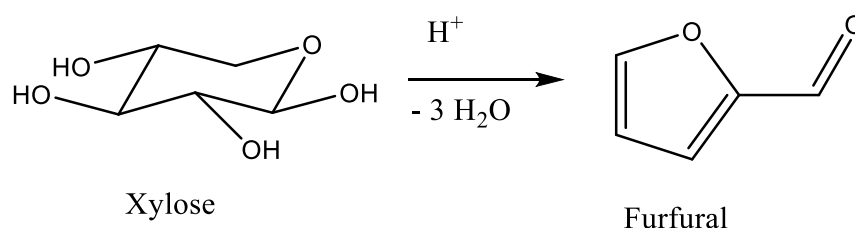
Figure 2.10: Acid catalysed dehydration of xylose to furfural

Furfural was first identified in 1845 by Dr George Fownes, who was investigating an oil produced from the reaction of bran with sulfuric acid.[70] The

Quaker Oats Company began mass manufacturing of furfural in 1922 from their waste oat husks, approximately 50-70,000 tonnes per year. From there the interest in furfural has only increased as a renewable, non-petroleum sourced chemical feedstock. Furfural is now used as a solvent, a starting material for polymer production, in resins for construction and as a precursor to bio-derived fuels.[71,72]

Furfural is currently produced by direct conversion of plant biomass, with yields of 3-10 % of the total biomass feedstock. China, South Africa and the Dominican Republic account for the bulk of global furfural production.[73] However, these industries still use the original batch process designed in 1922, running at low efficiencies, producing large amount of waste and at a cost of $1700/tonne of furfural.[74] Due to the need for low cost furfural if it is to be used as a fuel, there has been extensive research into optimising this process.

An important step to a high yield furfural process could be found from dividing the traditional Quaker Oats process in two. Currently, the biomass goes into a single reactor and furfural is extracted following some time. This process has a procedural inefficiency in that unconverted xylose may be produced, or much of the available xylose remains in the xylan hemicelluloses.

Hong et al. (2016) investigated the pre-treatment process for extraction of xylose from biomass depends on the biomass source.[75] Their investigation found the optimal conditions for xylose extraction from corn stover to be 120 $^\circ$C, a 2.5 weight percentage of sulfuric acid and 1.5-hour residence time. This gave an 82 % xylan to xylose conversion, much higher than current industrial methods.[75]

Xing et al. (2011) published an extensive study of both the technical and economical optimization of furfural production.[76] Through optimization of a batch process, they were able to convert a high percentage weight xylose stream with 90 % yield to furfural. Acetic acid and formic acid were also produced as side products, originating from acetal side groups in xylan chain branches. These chemicals are also sought after by many industries, and the authors' process isolated these to be sold. The authors estimated their whole process uses only 25 % of the energy needed for current furfural production, and is able to

produce furfural at $366 per tonne, as of 2011,[76] (with crude oil costing $412 per tonne at this time).[77]

2.2.7.3. Furfurals as fuels

As an easily producible platform chemical, there has been extensive research into potential products of furfural conversion. Mariscal et al. (2016) reviewed the published routes that converted furfural into platform chemicals, fuel-like molecules and fuels themselves.[78] Figure 2.11 outlines the variety of chemical products producible.
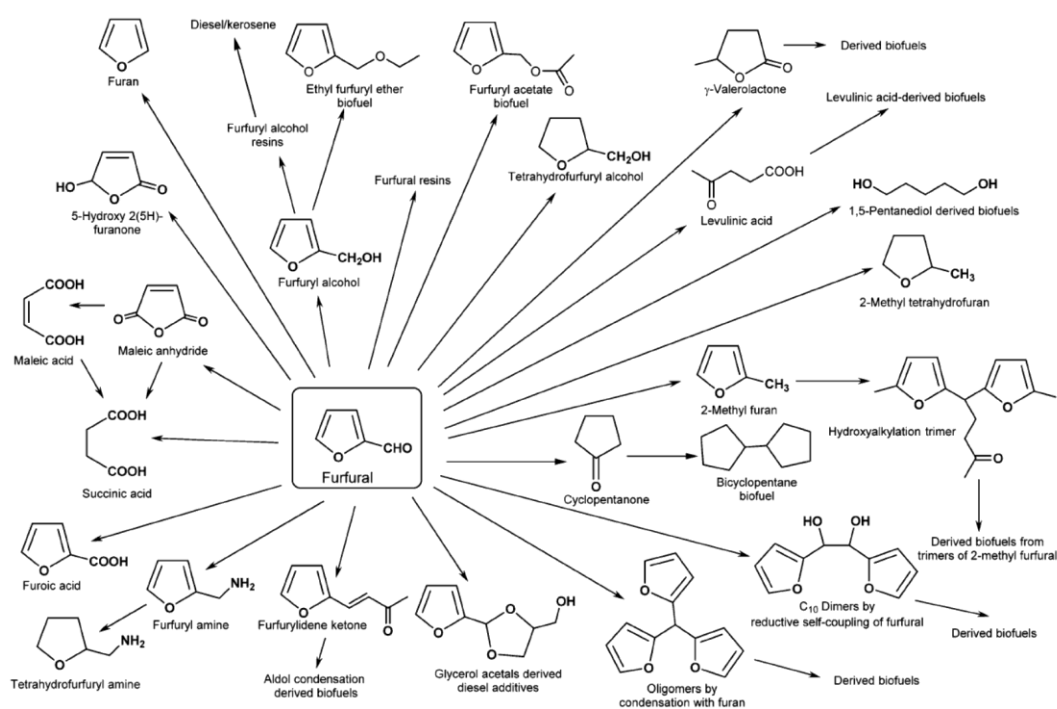
Figure 2.11: Summary of potential furfural derived chemicals and fuels. Published in and replicated from Mariscal et al, 2016.[78]

Many of the molecules shown in Figure 2.11 are too small and volatile for use in diesel engines. Their interest as fuels focused on blending with gasoline, such as ethyl furfuryl ether being investigated as a gasoline blend candidate for its anti-knock properties.[79] Ethyl furfuryl ether has also been investigated as a potential diesel blending candidate, but was found to be immiscible with fossil diesel.[80]

There are further molecules that have been synthesised from furfural with boiling points and a carbon number (C9-C22) that are more typical of diesel fuels. However, these larger oligomers which are closer in molecular weight to diesel fuel were not tested as fuels. Instead, these molecules were chemically converted via hydrodeoxygenation into straight chain alkanes.[81] These alkanes

produced are replicates of molecules found in diesel fuel. However, the process of hydrodeoxygenation uses highly forcing conditions, 400 $^{\circ}$C and 5 MPa.[82]

The energy intensive process of hydrodeoxygenation used to convert these oligomers is potentially a superfluous step if these oligomers can already combust under certain engine testing conditions. The conversion energy consumed may be higher than any improved energy output from combusting the final alkanes over these oligomers. The researchers in these cases were often not engineers with access to an engine for combustion experiments. It is therefore unlikely that they would have expanded their research to test the furfural derived oligomers and see how these perform in an engine – instead opting to continue conversion of their furfural starting point and get as close to diesel fuel alkanes as possible.

The current processes of transforming furfural into viable fuels for diesel engines has not yet been commercialised and oligomers produced via simple coupling reactions have not yet been tested for their full potential as fuel molecules.

2.3. Pollutant formation

Internal combustion engines running on fossil fuels are a major source of greenhouse gas (GHG) emissions and toxic pollutants such as nitrogen oxides (NO and NO_2), carbon monoxide (CO), unburnt hydrocarbons (UHC) and particulate matter. The contribution to pollution from the transport sector is significant, for example in the United States in 2020, the transportation sector accounted for 27% of total GHG emissions. Over 50% of this comes from passenger vehicles and light to heavy-duty trucks alone, the remaining comes from larger vehicles such as aircraft, trains and boats.[83]

Irrefutable is the requirement to reduce anthropogenic GHG emissions. Deriving energy from the biosphere which exists in a closed carbon cycle is the inspiration for biofuels, where the carbon emitted from manufacturing and burning the fuel is equal to or lesser than the carbon dioxide absorbed by the biomass during its life cycle.

Whilst increased use of biofuels reduces the net increase of atmospheric CO_2, it will not necessarily affect the short-term emission of the remaining pollutants. CO, NO_x UHC and soot have a more direct impact on human health, acting as carcinogens and contributing to environmental damage like acid rain or increased radiative forcing.[84]

It is important to understand the formation mechanisms which contribute to the emissions of these pollutants. Previously discussed is the increased homogeneity in fuel molecular structure offered by biofuels over fossil fuels, allowing a closer focus on how changes in molecular structure led to significant changes in pollutant formation.

2.3.1. Nitrogen oxides

NO_x is a mixture of nitrogen oxides, NO and NO_2 are the most prevalent and important in internal combustion engine emissions. Nitrogen oxides are harmful to human health, are a major contributing factor in smog formation and are crucial in acid rain formation. NO_x formation is well understood through 3 major pathways, noted as thermal, fuel and prompt NO_x.[85]

2.3.1.1. Thermal NO_x

The main source of NO_x during the combustion process is the oxidation of atmospheric nitrogen, requiring in-cylinder temperatures above 1800 K. The kinetics of this process have been well studied, known as the Zeldovich mechanism after it was first identified by Zeldovich in 1946.[86] The extended Zeldovich mechanism reactions governing thermal NO formation are shown in Equation 2-8 Equation 2-10.

$$N_2 + O \leftrightarrow NO + N \qquad \textit{Equation 2-8}$$

$$N + O_2 \leftrightarrow NO + O \qquad \textit{Equation 2-9}$$

$$N + OH \leftrightarrow NO + H \qquad \textit{Equation 2-10}$$

Equation 2-8 is the rate limiting step requiring the high temperatures and proceeds at a slower rate than hydrocarbon oxidation. The equations are all reversible in nature, requiring high oxygen concentrations and residence time at high temperatures for significant NO formation.[87]

2.3.1.2. Prompt NO$_x$

Described as 'Prompt NO$_x$' and identified by Fenimore et al, is the reaction between hydrocarbons and atmospheric nitrogen.[88] The reaction occurs in the laminar premixed flame zone (Section 2.1.2) and can be formed in significant quantities in some combustion environments, such as fuel rich low temperature flames.[85,87] After reacting to form nitrogen containing fragments, the nitrogen is able to form NO$_x$ through reactions with OH radicals which are frequently found within the cylinder. The formation occurs as shown in Equation 2-11 Equation 2-15 below:

$$CH + N_2 \leftrightarrow HCN + N$$

Equation 2-11

$$CH_2 + N_2 \leftrightarrow HCN + NH$$

Equation 2-12

$$N + O_2 \leftrightarrow NO + O$$

Equation 2-13

$$HCN + OH \leftrightarrow CN + H_2O$$

Equation 2-14

$$CN + O_2 \leftrightarrow NO + CO$$

Equation 2-15
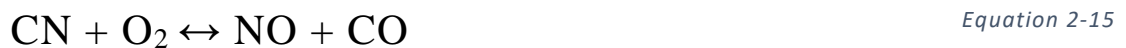
2.3.1.3. Fuel NO$_x$

The final significant source of NO$_x$ emissions is the oxidation of molecularly bound nitrogen within the supplied fuel. The amount of fuel NOx produced in this manner is correlated with the amount of molecular bound nitrogen and the kinetics of the fuel burning.[89] Fuel NOx is considered almost negligible in most cases, as nitrogen is found only in trace amounts in fossil fuel. Where additives such as ethyl hexyl nitrate are required to ensure consistent combustion, the consideration of fuel NOx increases.[87]

2.3.1.4. Formation in compression ignition engines

NO formation primarily occurs in the mixing of controlled diffuse flame in compression ignition engines as this is where the chemical reactions occurring are close to stoichiometric, favouring high NO formation. The burned gases forming in the diffusion flame then diffuse both outward away from the flame front and inward into the flame rich zone.[89] NOx formation will be greatest when

the burned gas temperatures are highest, typically close to the point of highest pressure. Following the top dead centre piston position, the cylinder volume increases, lowering the gas temperature as it expands. Decreasing temperatures due to this expansion will 'freeze' the NO chemistry at a faster rate in compression engines than spark ignition, so less decomposition of the NO occurs.[89]

2.3.1.5. Formation of NO$_2$

In compression ignition engines the NO$_2$ can be 10 to 30% of the total nitrogen oxides emitted.[89] Merryman et al. (1975) investigating nitrogen oxide formation noted pyrolysis and oxidative processes yielded small quantities of NO$_2$, and proposed the following NO$_2$ formation pathway:[90]

$$NO + HO_2 \leftrightarrow NO_2 + OH$$

<div align="right">*Equation 2-16*</div>

$$NO + OH \leftrightarrow NO_2 + H$$

<div align="right">*Equation 2-17*</div>

NO2 will subsequently be converted to NO:

$$NO_2 + O \leftrightarrow NO + O_2$$

<div align="right">*Equation 2-18*</div>

The NO$_2$ conversion shown in Equation 2-18 may be quenched by mixing with cooler gases in the combustion chamber. Zones of cooler air/ fuel mixture can occur readily in compression ignition engines operating at light lode.[91]

2.3.2. Carbon monoxide

Carbon monoxide (CO) is a product of incomplete combustion. CO emissions from internal combustion engines are controlled by the relative air/fuel ratio. Higher air to fuel ratios will lower the volume of CO and likewise richer air/fuel ratios will see higher volumes. CO formation is one of the principal reaction steps in the hydrocarbon combustion mechanism shown by Equation 2-19. CO can be further oxidised to CO$_2$ at a slower rate and is shown by Equation 2-20.[92]

$$RH \rightarrow R \rightarrow RO_2 \rightarrow RCHO \rightarrow RCO \rightarrow CO$$

$$CO + OH \rightarrow CO_2 + H$$
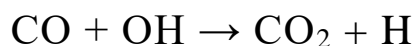
The amount of oxygen available during combustion ultimately dictates how complete the combustion process can be. In spark ignition engines where the air/fuel ratio is maintained to a near stoichiometric ratio, there are conditions which can lead to an excess of fuel being available, thus leading to incomplete combustion. Diesel engines operate under lean conditions and typically emit such low values of CO that they can be considered unimportant and as such, investigations into compression ignition CO formation is lacking.[92]

2.3.3. Unburnt hydrocarbons

As with CO, unburnt hydrocarbons are a product of incomplete combustion. There are several plausible reasons for unburnt hydrocarbon emissions which can be focused into either the fuel avoiding combustion entirely or only partial oxidation occurring.

Partial oxidation can be caused by both lean and rich fuel conditions. Under both of these conditions the flame may fail to propagate through the air/fuel mixture whilst the temperatures and pressures remain high, leading to unreacted or partially reacted hydrocarbons. Fuel near the flame edge could diffuse away from the main jet, entering a region of the cylinder which is too lean for stoichiometric combustion to occur. A long ignition delay will therefore increase the levels of unburnt hydrocarbons, as it allows more time for fuel at the leading edge of the spray to diffuse away from any flames and increase the likelihood of fuel impinging on the chamber wall. Rich mixtures which fail to ignite can arise from fuel entering at low velocity, or if the fuel has a high viscosity.[93]

2.3.4. Soot formation

Soot particles are a product of incomplete combustion arising from small precursor molecules, acting as building blocks for aromatic rings. These aromatic rings develop into polyaromatic hydrocarbons (PAHs) which finally aggregate into particle nuclei.[94] Soot particles are toxic to human health when

inhaled and soot directly contributes significantly to radiative forcing, second only to CO_2 in terms of how much energy it absorbs.[95]

Soot is a carbon-based solid substance with a rough C/H ratio of 8:1. As soot formation initiates with the formation of aromatic rings, the initial new soot is typically much lower, with C/H ratios of 1:1. The amount of hydrogen present decreases as the soot matures.[96]
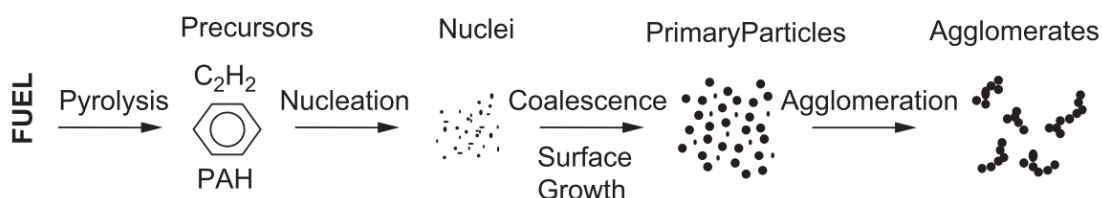
Figure 2.12 Schematic diagram depicting five contributory processes for soot formation from liquid fuel to solid agglomerates. (Tree and Svensson, 2007)

The process of soot formation is shown in Figure 2.12. Pyrolysis is a process of chemical change in organic molecules at high temperatures in the absence of oxygen. These initial reactions are endothermic in nature and so are highly temperature dependent. The main products from pyrolysis which are classed as soot precursors are unsaturated hydrocarbons, polyacetylenes, polyaromatic hydrocarbons (PAHs) and most importantly acetylene.[96] These precursors will undergo radical addition reactions with vinyl radicals to form 1, 3 butadiene, phenyl radicals and then aromatic species such as phenylacetylene. Further addition of vinyl radicals will increase the number of aromatic rings in the molecule to form PAHs.[94]

The PAHs eventually reach a size where they begin to nucleate, react and combine to form nascent soot particles, which typically have a C:H ratio of 1.4-2.5 and are more aromatic than aliphatic in nature.[97] Nucleation is the formation of particles from the PAHs and precursor radicals, the smallest of these identifiable particles are 1.5–2 nm in size. These initial particles do not contribute significantly to the overall soot mass but do provide important surface sites for particle growth later in the combustion process.[98] Soot growth on the surface of the particle continues to interact with gaseous hydrocarbons. This increases the total particle mass, even in parts of the flame which are cooler and less reactive. The majority of soot mass is accumulated during this growth period, so the residence time of these particles has the greatest influence on the total mass.[98]

The final two processes contributing to soot growth are coalescence and agglomeration. Young soot nuclei are able to coalesce when they collide, where the two roughly spherical particles combine to form a single roughly spherical particle with conservation of the total mass. Agglomeration occurs when these particles stick together without coalescing, instead forming chain like structures in which the individual particles retain their original shape.[96] Lee et al. (2001) found these primary soot particles to range in diameter from 20 to 50 nm, averaging 30 nm in size.[99] Following combustion these agglomerates will increase in size with diameters ranging from 100 nm to 2,000 nm.[100]

Dec (1997) developed a conceptual model of DI compression ignition combustion which included detailed observations on soot development during the combustion cycle.[23] Between 4.5 to 5.0 CAD after start of injection (ASI) fuel breakdown and PAH formation had begun uniformly throughout the leading portion of the jet in the premixed flame. By 6.0 CAD small soot particles were detected throughout large portions of the fuel jet cross section. At this point a diffusion flame forms on the jet periphery and soot particles begin to grow larger in a thin layer adjacent to this periphery. It is noted that the formation of the diffuse flame does not lead to an increase in soot concentration at the periphery.

Towards the end of the premixed burn phase of combustion (7.0 to 9.0 CAD ASI) the diffuse flame remains reactive, and soot formed within moves inwards into the jet. This movement formed a zone of high soot concentration in the leading edge of the jet where the soot remains and does not move further in. At this point in the chamber there is a low concentration of soot particles still forming in the flame region closest to the liquid fuel jet, larger soot particles forming on the diffuse flame periphery, and the largest particles growing in the high concentration soot zone in the fuel vapour jet head region.[23]

The premixed air is consumed by 9.0 CAD ASI and the mixing-controlled combustion phase begins. The head vortex is well formed with a high soot concentration within. The soot formation processes occurring are steady, with small soot particles developing upstream of the fuel vapour jet, large particles forming in the diffuse flame, and the largest particles forming in the head read region of the jet. Soot particles will continue to accumulate in the vortex head where they will continue to grow in size. As these soot particles move out of the

jet and into the diffusion flame they will begin to oxidise through reactions with OH radicals.[23]

The final process affecting the emitted soot particles during combustion is their oxidation. This oxidation can occur throughout the soot formation processes discussed so far and at any time during the combustion process. Soot is highly resistant to oxidation due to its stable aromatic structure, so temperatures in excess of 1300 K are necessary for soot oxidation. As the fuel and decomposition products react with oxygen, the formation of CO will prevent any further interaction of that carbon from forming any precursors or coalescing with existing soot particles.[94,96]

Tree and Svensson (2007) further describe how physical parameters in the combustion chamber can influence the soot formation process. In-cylinder temperature has the greatest effect on soot formation. As the reactions for soot formation are endothermic, the rate of formation will increase with temperature. Increasing temperature also facilitates soot oxidation reactions. Peak soot formation therefore occurs between 1500-1700 K and at higher temperatures the total soot levels decrease.[96,101]

It is stated that the effects of pressure change on soot formation are hard to quantify as changes in pressure directly influence in-cylinder temperature, thermal diffusivity and flame behaviour. Tree and Svensson conclude that it is intuitively accepted that higher pressures lead to higher soot formation as there are other studies which show direct correlation between increased pressure and factors which would directly increase soot formation; increased precursor formation and faster particle collisions.[96]

The final physical parameter which affects soot formation is the air/fuel stoichiometry. Oxygen is fundamental to the combustion process, providing the necessary temperature increase which allows soot formation, and it is fundamental to the oxidation of soot. Hora and Glassman (1989) investigating the soot levels in ethylene and propane flames found that increasing the levels of oxygen present in the flames initially increases the level of soot formed, and later decreases as the stoichiometry increases past 10:1.[102]

Fuel composition and structure are also significant in soot formation. Soot is mostly comprised of carbon, so fuels with more carbon are likely to emit more

soot, whilst oxygenated fuels are likely to produce less soot. Ladommatos et al. (1997) and Xiao et al. (1999) examined sooting heights in a flame burner and undertook emissions testing of fuel blends in a cooperative research engine (CFR). They highlighted the significance of fuel molecular structure on soot formation. They determined that increasing the ratio of aromatic content within the fuel lead to an increase in smoke emissions, whilst increasing the ratio of oxygenated content within the fuel lead to a reduction in smoke emissions. It was further shown that inclusion of C to C double and triple bonds, inclusion of cyclic rings, and the inclusions of side chain branching increases the sooting tendency of single component fuels.[103–105]

2.4. Impacts of molecular structure in heavy-duty engines

Heavy-duty engines have received some focus as research facilities to test fuel properties, but this has mostly been in the context of already commercially viable fuels. A dominating theme in fuel research with heavy-duty engines is fatty acid methyl esters, with research consisting of new crop oils, ethyl esters and different blending ratios with fossil diesel. In recent years, the European Commission has introduced new legislation tackling the sustainability criteria of biofuels with a goal to move past crop-based fuels and towards advanced feedstocks, such a production waste, e-fuels and crops grown on degraded land.[106] The more traditional feedstock, vegetable oils, is in limited supply and growing competition for higher value industries, such as green oleochemicals and sustainable aviation fuel are likely to outcompete road transport fuels for the limited feedstocks.[107]

The diesel engine was invented in 1897 and used peanut oil as a fuel, predating decades of progress in petroleum refining, and so vegetable oils have remained a topic of engine research for over a century.[108] Over this time period, engines have undergone serious modifications. The engines used 70 years ago differ from those used today, not so much in the underlying principles of compression ignition, but differ in fuel delivery systems, piston geometries and air intake. A major driver of these changes has been pollutant control, with the Euro I-IV legislation aiming to reduce engine emissions over time.[19] For this reason, the

following review on fuel molecular structure in heavy duty engines will be limited to the last two decades.

2.4.1. Fatty acid methyl esters

Wang et al. (2000) conducted an emissions study in real-world conditions to determine the on-road emissions of biodiesels.[109] The study took nine vehicles currently in operation and manufactured between 1987-1994, as a sample of the trucks which operated on American roads at the time. The controlled variations between the vehicles were vehicle weight, engine displacement and engine horsepower. Tests were performed using a transportable emissions testing lab, a dynamometer to simulate different load conditions and a mobile data logging system, all of which were attached to the vehicle chassis. The fuel tested was a B35 soybean methyl ester (SME) blend and a reference fossil diesel. Wang et al. found the B35 fuel blend emitted less CO than fossil diesel, regardless of the engine or driving cycle tested. They also found that cylinder volume had an effect, as the engines with a 14l displacement emitted less CO than the 11.1l engines. NOx emissions from B35 increased relative to fossil diesel in the 14l engines, but decreased relative to diesel in the 11.1l engines. Unburnt hydrocarbon emissions decreased moderately in both engines and particulate emissions decreased significant in both engines. These outcomes were concluded to result from the oxygenated portion of SME. This increased combustion efficiency, lowering CO, THC and particulates, whilst shortening the duration of ignition delay which could increase NOx as it allows greater time for thermal NOx production.[109]

McCormick et al. (2001)[110] investigated how the source of biodiesels impacted emissions in heavy-duty engines. They investigated FAME produced from oils of common feedstocks; linseed, soybean, rapeseed, tallows and lard. Additional single component esters were tested, which represented the common esters found in the previously mentioned feedstocks, so that changes in chemical structure between these esters could be investigated. Their study therefore allowed conclusions to be drawn from differences in ester length, alcohol used in transesterification, and increasing the number of unsaturated bonds in the esters. The engine used was an 11.1l displacement DCC 60 series, the same used by Wang et al, discussed in the previous paragraph.[109,110] Across the full

set of fuels, NOx emissions were found to be lower than the reference fossil diesel for the saturated methyl and ethyl esters, and all the unsaturated esters produced higher NOx than the reference fuel. All of the esters tested produced significantly lower particulate matter than the reference fossil diesel, with the exception of methyl linoleate (C18:2), which had the highest degree of unsaturation of all the tested esters. The authors did note that the engine performance with this fuel was poor, and this result will therefore be excluded from further discussion of this paper. McCormick also found that there was no difference in NOx/particulate emissions arising from transesterification with methanol or ethanol. Instead, a strong correlation was found between the physical properties of the esters which arise from chemical structure and the observed NOx. Strong linear correlations with increasing NOx emissions were observed from increasing fuel density and increasing the percentage of fuel saturation. However, it should be noted that the fuel density and degree of fuel unsaturation were already correlated, with the unsaturated esters exhibiting a higher density than saturated ones. The final observation from this study is that particulate emissions were higher from unsaturated fuels than saturated, but a linear correlation between density and particulates was not observed.[110]

Päivi et al. (2002)[111] investigated the effectiveness of aftertreatment catalysts on NOx emissions in heavy-duty engines also reached similar conclusions for popular biodiesels, rapeseed methyl ester (RME), used cooking oil methyl ester (Ucome) and SME. They found that increasing the amount of ester in the fuel blends lowered the CO, THC and particulates, but increased the NOx. RME and SME contain a high % of unsaturated esters, and as with previous studies these fuels exhibited a significant increase in NOx, whilst Ucome, which contains more saturated esters, emitted NOx comparable to the fossil diesel.[111]

A more recent study on chemical structure of esters was undertaken by Zhu et al. (2016)[112], where five single component esters were tested in a heavy-duty engine. The engine was a 3.9 l, 4-cylinder engine with a maximum speed of 2,800 RPM, making the engine very similar in geometry and speed to the D8k engine discussed in this work. The esters tested were methyl laurate (C12:0), palmitate (C16:0), stearate (C18:0), oleate (C18:1M) and ethyl oleate (C18:1E), which as a series allow changes in fatty acid length, alcohol moiety and unsaturation to be investigated.[112] Zhu et al. tested variable loads, ranging from

0.19 to 0.68 MPa BMEP. They found that increasing the length of the fatty acid moity in the esters reduced the duration of ignition delay at both injection pressures, increased the duration of combustion at the lower load and led to lower PHRRs. Inclusion of the double bond (unsaturation) lengthened the duration of ignition delay and shortened the duration of combustion. Conversely, changing the alcohol moiety from methyl to ethyl shortened the ignition delay and lengthened the duration of combustion.

Considering exhaust emissions results, a clear trend was shown by Zhu et al. in that the total unburnt hydrocarbon and CO emissions increased as the fatty acid chain length increased. This trend was apparent at both load conditions, but increasing the engine load led to a significant decrease in THC and CO, and the relative difference between the esters reduced. Increasing the chain length led to a reduction in NOx emissions. However, engine load was far more influential in the magnitude of NOx emissions. The level of NOx emitted by each ester more than doubled from the lowest to the highest load condition, whilst the absolute difference between the varying length esters was almost unchanged. Comparing the emissions of the unsaturated esters, inclusion of a double bond led to lower THC and CO emissions, and higher NOx emissions. This is attributable to both a slightly longer ignition delay allowing for greater mixing, and higher PHRRs.[89] Changing the alcohol moiety to ethanol on the ester led to higher THC and CO, but lower NOx at low loads, and no difference in NOx at high loads.

Finally, Zhu et al. found that chemical structure and load appeared to have no impact on smoke opacity, but every ester tested exhibited significantly less smoke than the reference diesel. Particulate size distribution favoured nucleation mode particulates under 50nm, with the esters emitting a higher concentration of these than the reference diesel.[112]

In a broader context, including high-speed light-duty diesel engines, fatty acid methyl esters have been the subject of countless research over the previous 20 years. Reviews by Xue et al. (2011)[113] and Altarazi et al. (2022)[114] discussing the work from over 100 publications each, both came to very similar broad conclusions, as follows, that can be applied to all FAMEs:

- Increasing the blend volume of FAME reduces CO and THC emissions. Particulate emissions also decrease at light load, but are comparable to fossil diesel at very high load.
- NOx emissions are more linked to combustion properties than inherent chemical structure. Adjusting the experimental conditions to account for varying viscosity and injection timings will influence the NOx emissions more than biodiesel type.

2.4.2. Alcohols

The use of readily available bio-alcohols which can be fermented or produced easily from biomass, generally limited to methanol, ethanol and butanol, have been tested in fuel blends with diesel to assess their impact on emissions.

McCormick et al. (1997)[115] fuelled two different heavy-duty engines with several representative oxygenated compounds; ethanol, octanol, decanoic acid and SME. The experiments blended a variable amount of each fuel into diesel so that the fuel blend contained either 1%wt fuel oxygen or 2%wt fuel oxygen. The work showed a strong correlation in that at either wt% of fuel oxygen, significantly lower particulates were emitted by all the oxygenated fuel blends compared to the reference fossil diesel. Higher THC was detected from the ethanol and octanol fuel tests, indicating that alcohols are likely to exhibit incomplete combustion. The THC levels observed from SME and decanoic acid 1%wt blend were very close to the reference diesel, and at the 2%wt blend the THC detected from SME was 10% lower than the reference diesel. No significant trend was observed in the NOx emissions across the oxygenates; octanol and decanoic acid exhibited lower NOx emissions, whilst ethanol and SME exhibited higher emissions. Instead, NOx emissions correlated with the cetane number – octanol and decanoic acid both have cetane numbers within the range of the reference fossil diesel tested, whilst ethanol has a significantly lower cetane number and SME a higher cetane number than the reference diesel.

Shamun et al. (2016)[116] investigated how partially premixed combustion of alcohols would influence particulate emissions in compression ignition engines. Partially premixed methanol, ethanol and naphtha gasoline fuel were tested in a 12.7l Scania D13 engine. The engine was modified to act as a single cylinder

research facility, the fuels were injected at pressures from 1200-2000 bar and injection timing was varied between 20-40 CAD BTDC. Shamun et al found that neither alcohol emitted any particulates larger in size than 30 nm. Methanol was found to exhibit a higher number of particulates than ethanol and both alcohols emitted significantly fewer particulates than the reference naphtha gasoline.[116]

2.4.3. Oxygenated aromatics

Han et al. (2020 & 2021)[117,118] have published studies investigating the combustion performance and emissions from blends of oxygenated aromatics which can be isolated from lignocellulosic biomass. The study investigated butanol, anisole (aromatic ether) and benzaldehyde (aromatic aldehyde), blended with n-heptane at ratios of 80%, 60% and 60% respectively. It was found that butanol exhibited the longest ignition delay, an expected result given the low cetane value of butanol. Anisole exhibited a duration of ignition delay close to butanol, whilst benzaldehyde exhibited an ignition delay similar to the reference diesel at the higher load test condition. Han et al. attribute the difference in duration of ignition delay between anisole and benzaldehyde to the different reactivity of the ether vs aldehyde structure, despite similar chemical formulas of C_7H_8O and C_7H_6O respectively. The ether linkage is assumed to dissociate quickly into a CH_3 and phenoxy radical, which is a highly stable radical and is relatively resistant to further oxidation. This lowers the number of highly reactive radicals to initiate hydrogen abstraction with the heptane molecules, increasing the duration of ignition delay.[119] However, benzaldehyde would dissociate and produce the formyl radical, CHO, a radical which is known to be an active and important species in low temperature reactions, and the phenyl radical which is likewise a highly reactive radical species.[119,120] Regarding soot emissions, Han et al. found that benzaldehyde produced similar levels of soot as the reference diesel, butanol produced almost zero soot mass and anisole produced soot close to half that of benzaldehyde. Aromatic molecules tend to produce high levels of soot as the phenyl radical is one of the important soot precursors, shown previously in Figure 2.12. Therefore, fuels which already contain the precursors are more likely to produce high soot.[121] Anisole and butanol produced levels of NOx similar to the reference diesel, whilst the benzaldehyde blend produced noticeably higher NOx than the other fuels. This result is unexpected, as no trend was found between the maximum

temperature and the timing of this temperature. Instead, the authors suggest the adiabatic flame temperatures of the fuels are important. Anisole and benzaldehyde emitted almost identical levels of THC, which were higher than the reference diesel, and the butanol blend emitted the lowest THC. Anisole emitted nearly twice the CO of benzaldehyde, an expected result given the longer duration of ignition delay which resulted in pockets of air fuel mixture to not reach sufficient temperatures to fully oxidise.[122]

2.4.4. Ethers

The ether moiety is defined as an oxygen atom bound to two carbon atoms. Two ethers have received significant attention as fuels for compression ignition engines. The first is dimethyl ether (DME) with the formula C_2H_6O, and the second is polyoxymethylene ethers (POME) with the formula $CH_3O(CH_2O)_nCH_3$, a repeating polymer of different sizes which can be manufactured in several ways from methanol, formic acid and CO_2.[123] Ethers are known ignition improvers, owing to their higher cetane number than most fuels. They typically exhibit lower CO and THC emissions owing to their similar chemical structure to alcohols.[32,124] Work on DME in heavy-duty engines by Tsuchiya et al. (2006)[125] found that the engine parameters could be modified easily, such that operating with DME can give similar engine performance as diesel fuel. DME under these conditions reduced the amount of soot, NOx, THC and CO emissions compared to the diesel fuel and were sufficiently lower than the low emissions standards which were introduced in Japan in 2009.[125]

Pélerin et al. (2020)[126] used different molecular weight (MW) oxymethylene ethers (OME) as test fuels in a heavy-duty compression ignition engine, to compare the combustion performance and the emissions. They found little difference between small and large MW OMEs for the majority of the tests, except for the in-cylinder pressure and particulates. The combustion performance, particulates, CO and THC were lower than the reference diesel, whilst the NOx emissions were unchanged between the fuels used. Low MW OMEs were reported to exhibit higher in-cylinder pressures than high MW OMEs, an expected trend as the lower heating value of the test fuel and carbon to oxygen ratio both decrease as the MW of the ether increases. Increasing the MW of the ether lead to lower particulates, which is also an expected result

given that the lower carbon to oxygen ratio and more molecularly bound oxygen will reduce particulate formation.[32,126]

2.5. Knowledge gaps:

Heavy-duty engines will remain in use for the foreseeable future, as they cannot be fully replaced by batteries and electrical motors. However, a viable alternative to fossil diesel fuel is needed to reduce the contribution of the transport industry to climate change. Currently, there is only one biofuel used in diesel markets, fatty acid methyl esters. FAME is produced from the oils from plant biomass, which competes with using the oils for food and the process does not utilise the majority of the total plant biomass. Research into producing diesel replacement fuels has not progressed as far as for gasoline replacements. E100 is used in Brazil extensively but biodiesel is limited with a 7 % blend wall in the EU. Biofuel sourced molecules often go through many chemical conversion steps using heavy metal catalysts, upgrading into larger molecules and finally hydro-deoxygenated into paraffinic structures very similar to those found in fossil diesel.[127] This final step is particularly intensive and the precursor large molecules have not been tested themselves as diesel replacement candidates. It is suggested here that it may be unnecessary to convert molecules to diesel like fuels if the precursor molecules which are easier to produce can still perform adequately as a fuel in a compression ignition engine.

From this literature review several conclusions and knowledge gaps can be drawn:

- There is limited scope in the testing of new biofuels in heavy duty diesel engines. The majority of research has been driven to production of molecules which replicate hydrocarbons found in diesel or FAME.
- Oxygenated fuels, especially ethers perform well in compression ignition engines and changing the operating parameters can result in close to equal performance between oxygenated fuels and fossil diesel.
- Oxygenated fuels with similar durations of ignition delay and combustion phasing to fossil diesel will generate lower particulate,

unburnt hydrocarbon and carbon monoxide emissions compared to fossil diesel as the molecularly bound oxygen facilitates complete oxidation of the fuel.

- In compression ignition engines, no overall trend between oxygen content in fuel and nitrogen oxide emissions can be made. Nitrogen oxide emissions result from trends in overall combustive characteristics, such as duration of ignition delay, size of the premixed vs diffusion-controlled burn phase, maximum in-cylinder temperatures and duration of combustion. The presence of molecular oxygen does not independently dictate trends for any of these parameters, instead the local chemical structure surrounding the oxygen is more important, with alcohols, ethers, esters and acids all having different expected fuel performance.

- Hemicellulose, compared to cellulose, has been shown to be much harder to utilise as a fermentation feedstock for ethanol, unlike cellulose, despite being a far easier polymer to work with chemically. Hemicellulose remains an under-utilised feedstock for biofuels compared to sugars and oils, despite the much higher abundance of hemicelluloses.

- The chemistry of furfural and its derivatives has been well studied with routes to biofuels identified. However, the final conversion steps to these biofuels involve energy intensive steps. Studies comparing the combustion properties of the reagents and fuel products of these reactions are lacking.

The literature reviewed so far is not exhaustive in covering all aspects of biofuels, the process of combustion, or engine operation, as each of these three fields of research remain wide in scope. Considering the knowledge gaps discussed, the main objectives of the experimental work undertaken are summarised here:

- Specific studies into novel chemical structures are lacking for compression ignition engine and instead the focus is on alcohols and acids which constitute fatty acid esters. Functional groups which have unique chemical reactivity based on their structure will be investigated to understand how certain chemical reactions can

influence the low temperature reaction kinetics at the start of combustion.

- There exists a wide variety of organic compounds in nature which can be isolated, such as lactones, which can be found in fruits, beer and perfumes. Two series of lactones will be tested in a systematic investigation on the impact of lactone molecular structure on combustive characteristics and emissions. Understanding the viability of these compounds could open further research into unlocking large scale isolation and production of these compounds.

- Furfural provides an excellent starting point to develop a novel fuel for compression ignition engines and remains a feedstock which has received little attention for compression ignition engines. A synthesis of a potential fuel from tetrahydrofurfuryl alcohol will be undertaken to produce a novel ether which will then be tested in a heavy-duty compression ignition engine.

- Whilst research into fatty acid esters is a saturated field, biodiesels remain a prevalent biofuel in many markets, owing to the ease of their manufacture. Researching the potential of novel feedstocks for fatty acid esters will remain a useful endeavour for as long as compression ignition engines remain in use, as they are key to reducing net CO2 emissions from transport. Date pits are an abundantly available waste-stream in the Middle East and the viability of date pit methyl esters as future fuels will be determined.

3. Development of a heavy-duty engine test facility

This chapter introduces the testing facility utilised in this work, focusing on the design choices made and difficulties encountered during development of the facility. The final configuration of the experimental facility will be referred to briefly at times when necessary for clarification of the development process, with a full and in-depth description of the facility available in the experimental set-up (Chapter 4).

For the purposes of understanding the experimental facility and applied methodologies set up without an overview of the development of the facility and the issues encountered, this chapter may be skipped. Both a development chapter and methodology chapter are included as the engine type itself lends significant weight to the novelty of the work undertaken so far, while the engine type also necessitated close to four years of time and work prior to the commencement of the experimental tests.

The development of the heavy-duty engine facility constituted a major part of this work, the undertaking of which was significantly hindered by the COVID-19 pandemic.

On commencing the project, it was decided that the research engine used should represent the current and future applications of CI engines. Part of this meant a 'road ready' heavy duty engine and not a specifically designed research engine. Many systems had to be replaced for the engine's integration into the research facility, unlike a specific research engine. This integration was made difficult by the engine size and limited access to information on the specifications of the engine, such as electrical systems and troubleshooting support.

The timeline of the project overlapped significantly with the COVID-19 pandemic which disrupted supply chains and prevented regular access to the facility. For example, as of February 2022, many suppliers of the swaged piping necessary for the high-pressure fuel system remained unavailable.

3.1. Volvo D8k engine

A Volvo D8k 320 engine was selected as the platform for development of the testing facility for biofuels research. The D8k was advertised by Volvo as being 'Biofuel ready', with a Euro 6 compliant B100 engine modification available. The engine was available in Volvo's FE and FL trucks, which were used for city deliveries, regional distribution, light construction work and inter-city coaches.[128–130] The D8k engine first came into manufacture in 2013 and is still being produced in 2022.[131]

The Volvo D8k was selected over a larger engine available from Scania, despite the larger engines more direct applicability to heavy-duty sectors. The Volvo D8k's smaller size would result in lower fuel consumption, favouring the investigation of a larger variety of test fuels of limited availability. To ensure experimental repeats and confidence in results, it was estimated that one litre of each test fuel was necessary prior to commencement of any tests.

Diesel engines for light and heavy goods vehicles vary from 80 mm to 150 mm in bore diameter and have a re-entrant shaped piston bowl. The specification of the D8k was therefore considered representative of the majority of medium to large compression ignition (CI) engines. As has been discussed in Chapter 1, light duty diesel engines are likely to be phased out across Europe in the coming decade, with only large goods vehicles remaining on road utilising CI engines, for which the D8K works well as a model engine.

3.1.1. Engine corrosion

Prior to acquisition of the D8k engine utilised, it was held in an unsuitable environment and exposed to the atmosphere, resulting in significant corrosion to exposed components. Internal investigations were necessary to validate the integrity of the combustion chambers and piston crowns. The engine head was removed and the combustion chamber was found to be in good order (Appendix, Figure 12.7), however several key components, including the valve rockers, valve washers and the camshaft had succumbed to severe rusting, as shown in Figure 3.1.

Figure 3.1: Overhead view of the D8k valve rockers and Jake brake control prior to reassembly, evident is the severe rust and corrosion.

With the internal combustion chamber free of any noticeable defects, the following parts were replaced prior to reassembly; valve springs, valve washers, rockers, rocker arms, overhead camshaft, head gasket and head bolts.

3.1.2. Auxiliary parts

Integration into the research facility necessitated the removal of several engine components which were now redundant.

Some of these parts were made redundant as their function would be performed with greater accuracy elsewhere in the facility. The parts replaced were; engine loom and electrical system (Section 4.8), engine radiator and fan (Section 4.2), fuel filter (Section 3.1.3), pressure sensors / thermocouples (Section 4.5) and the engine control unit (Section 4.7).

The remaining parts removed performed functions no longer necessary for the test facility and so were not replaced. These parts were; engine air compressor, turbocharger, steering manifold, exhaust after-treatment, alternator and air heater. Where applicable, blanking plates were designed to block off any connecting oil or coolant channels. These plate designs can be found in the appendix, Figure 12.8 and Figure 12.9.

3.1.3. Prototype parts

The D8k engine acquired for the testing facility was later found out to be a prototype model. After initial testing by Volvo as a prototype for an unknown length of time, it was sold to a secondary company and held in unsatisfactory conditions which led to corrosion on some parts. After a few years without operation, it was acquired for use in the project discussed in this thesis.

As a prototype engine, some component designs were not yet finalised and differed from the specifications which were later used in mass production.

The engine purchased was in some instances found to be incompatible with current Volvo parts, requiring changes to the fuel filter system. The fuel filter was replaced with a paper in-line filter between the header tank and high-pressure pump, with the original fuel filter housing is bypassed entirely (Section 4.3).

A second issue encountered was that of the manual crank turner. The D8k engine provides access to a gear to turn the flywheel manually by hand, however, the tool procured from Volvo for this job was incompatible with the specific engine acquired. The slot for the tool was far larger than the tool, which prevented secure engagement between the gear and flywheel (Figure 3.2). In order to turn the flywheel, two threaded spokes were inserted into the flywheel and a metal bar between these bolts provided leverage for turning. The spokes and bar were removed after the starter motor was successfully linked with the lab office controls.

Figure 3.2: Cranking adapter for Volvo FE coach flywheels not centred with the intended flywheel access location.

3.2. In-cylinder pressure transducer installation

To measure in-cylinder pressure during combustion experiments, a Kistler type 6052C High temperature pressure sensor was installed in the engine head in communication with cylinder 1. The specifications of the transducer can be found in the Appendix, Table 12.2.

The installation required drilling of a hole through the engine head while ensuring that no oil or coolant channels were breached. Rudimentary maps of the coolant channels were made with a flexible micro-camera. Ultrasonic signal tests (Appendix Figure 12.11) were then performed at several locations on the engine head (Figure 3.3), which confirmed solid metal for a continuous 16 mm at site M6, indicating that there was no risk of breaching an oil or coolant channel.
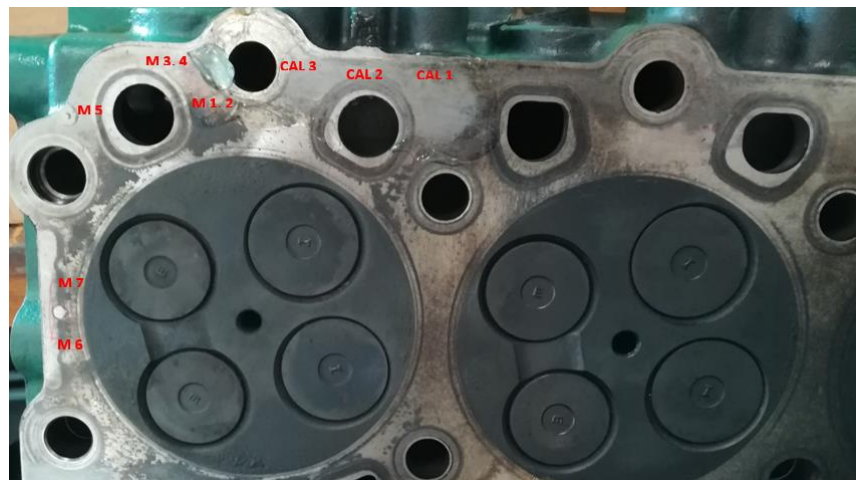
Figure 3.3: Calibration and measurements sites on the underside of the D8k engine head. Site M6 was selected for the pressure transducer thread to be drilled.

The transducer thread was drilled through at an angle of 19°, positioned 2 mm from the cylinder edge between the exhaust valves. Figure 12.12 and Figure 12.13 in the appendix highlight the angle of the drill in schematic form and a basic image showing the drill location.

3.3. Braking system and power control

3.3.1. Schenck Type W Eddy-Current Dynamometer

The testing facility already contained a Schenck Type W Eddy-Current Dynamometer and control unit, but these had been decommissioned 20 years prior to the current study. This dynamometer works by converting mechanical energy from the engine into heat through electrical energy. For integration into

the new testing facility there were three tasks; testing the integrity of the system, recommissioning the unit, coupling the brake to the D8k's flywheel and connecting the brake to the facility cooling water supply.

The dynamometer contains an override switch which checks if running water is detected. The brake was initially not connected to the labs cooling flow, so this switch was first bypassed and a hand drill connected to the brake simulated engine speed. The control unit reacted accordingly, supply electrical energy to resist the rotation of the hand drill, confirming that the brake was in working order. A schematic of the brake and control unit can be found in the appendix, Figure 12.14 and Figure 12.15.

3.3.2. Coupling unit

The D8k flywheel and Schenk dyno coupling points were of different sizes and specification, having been designed to differing industrial standards some 50 years apart. The size of both the engine and dyno prevented the use of a solid short coupling. A flexible shaft coupling was therefore a necessary addition to the testing facility to safely couple the engine to the dyno and provide flexibility on any small angular misalignment.
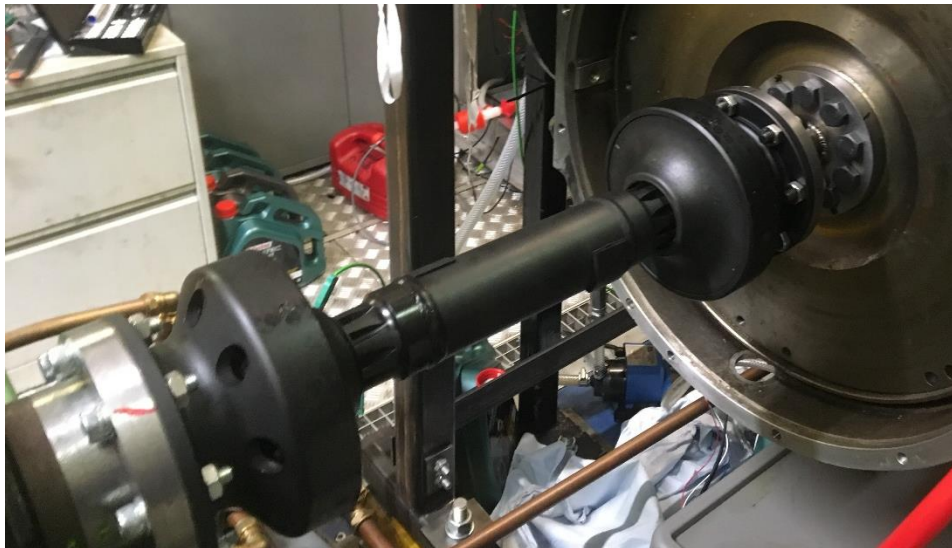
Figure 3.4: Flexible shaft coupling unit and adapter plates connecting the D8k flywheel to the Eddy-current dyno.

The coupling unit was designed to specification by GKN Powertrain and two short adapter plates were further required to finalise the coupling, shown in

Figure 3.4. The design specifications for the coupling unit and two adapter plates can be found in the appendix, Figure 12.16 and Figure 12.17.

3.3.3. Cooling connection

The eddy-current dyno requires a constant flow of cooling water to operate and avoid damage to the unit during engine operation. The water inlet and outlets on the dyno were converted to 22 mm copper pipe fittings, shown in Figure 3.5, and integrated into the laboratory chilled water supply along with the engine, forming part of the laboratory cooling circuit. An overview of cooling in the test facility is given in Section 4.2 and the development is discussed further in Section 3.9.
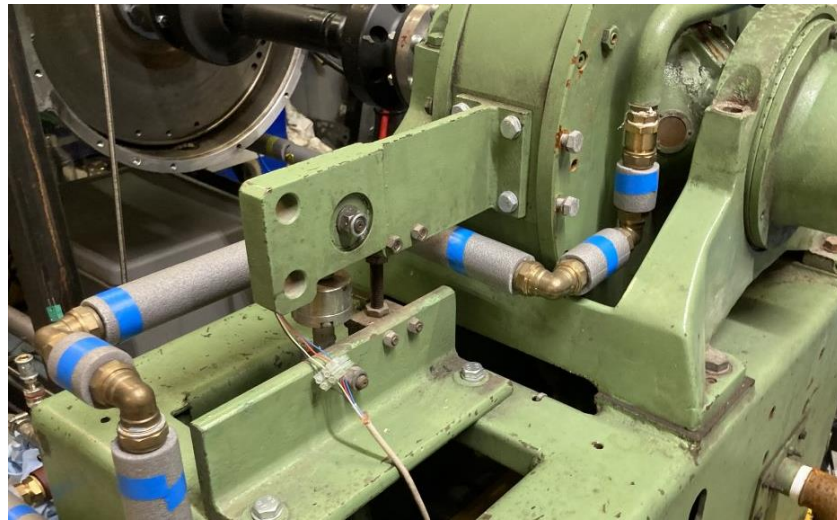
Figure 3.5: Schenk Eddy-Current dyno with new copper pipework fittings.

3.4. D8k start up

Marketing material available from Volvo on the B8r coach indicated that the truck cab start up would draw a minimum of 70 Ah. There was no indication of what percentage of this was required by the starter motor rather than the additional electrical equipment. To ensure that the minimum power requirements would be met on more than one starter cycle, two 12 V 135 Ah leisure batteries were obtained and connected to the starter motor in series to supply a 24 V current. These were secured within a plastic lidded box to prevent any metallic objects accidentally encountering the live terminals, shown in Figure 3.6.
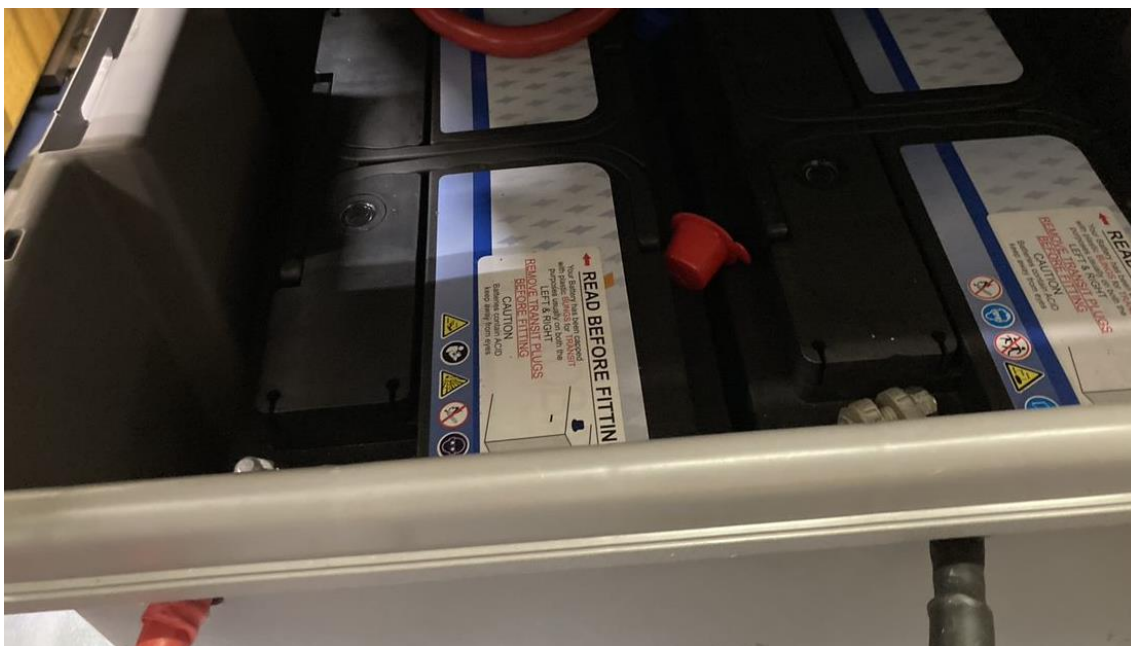
Figure 3.6: Two leisure batteries connected in series, contained in a strong plastic box.

3.5. Engine split injection system

With a total cylinder displacement of 7.7 l, the D8k would consume a higher quantity of fuel than previous engines installed in the lab. The scope of this work included the synthesis of new potential biofuels and testing single component fuels with limited availability, as unique molecules, not in blends with fossil diesel. Supplying a 7.7 l engine with sufficient synthesised fuel would have been a major challenge. Additionally, some of the test fuels might have had properties which could damage the fuel pump components. Determining how much fuel is required for continual optimum operation and how damaging some fuels will be to engine components was outside the scope of this work. Therefore, it was decided that a single cylinder on the engine would be supplied with the test fuel of interest and the remaining cylinders supplied with fossil diesel. There is precedent for running an engine in this way, particularly heavy-duty engines, as it reduces the volume of test fuels required and would also reduce the amount of time required to synthesise test fuels.[42,117]

It was assumed that for ~ 5 minutes of testing 1 litre of fuel would be required based on previous work on smaller engines within the research group. The high fuel consumption of the D8k necessitated a split fuel system approach, as some of the intended prototype testing fuels were limited in availability. A low volume fuel system, discussed further in Section 4.4, was utilised to supply one of the

six cylinders with a research fuel, designating it as the 'research cylinder' whilst the remaining five cylinders were supplied diesel from a header tank. This design choice further necessitated a split exhaust system so that exhaust gases produced from the test fuel could be isolated from exhaust gases produced by the back five cylinders.

3.5.1. Low volume fuel system connection

The operation of the fuel system is discussed in Section 4.4. During installation issues arose from the closure of private businesses which specialised in high pressure pipe swaging due to the Covid-19 pandemic. An injection pressure of 700 bar was selected for the experiments described in this work, which was far higher than pipework available from major suppliers could accommodate. The fuel system was designed with specialist fuel pipe fittings in mind, which were usually available from small specialist suppliers, but were unavailable from any major supplier. Working with what was available, all the essential connections for operation were possible. However, these connections relied on excessive connecting valves and old pipework, causing fuel leaks to be an occasional problem and the pipework often required the external threads for fittings to be repaired.

3.5.2. Split exhaust system

The supply of test fuel to injector one and diesel to the remaining five injectors required a split exhaust system to isolate combustion products from the test fuel for analysis. This was achieved by removing the exhaust manifold and separating the section for cylinder one and welding plates in-between it and the remaining five. A new pipe was then welded to the exhaust coming out of cylinder one, with bosses added for the necessary thermocouples and exhaust lines to analysers installed.

Figure 3.7: Exhaust manifold for the D8k engine.

Figure 3.7, shows the split exhaust, with the back five cylinders' exhaust still flowing through the turbocharger manifold before recombining with the exhaust from cylinder one at the muffler chamber. The negative pressure of the test cell extraction systems prevented the exhaust gas from the back five cylinders from diluting that from the number one cylinder ahead of the connection point.

3.6. Common rail fuel circuit

The D8k was purchased from a market reseller, not as a research engine direct from Volvo. During the development of the testing facility some limited information relating to the electrical controls, engine geometry, piston firing order, oil and coolant networks was obtained, however, the design specifications of the pressure sensor (PS) and pressure relief valve (PRV) could not be ascertained. Information from previous projects was available for a Bosch PS and PRV, which were readily available to procure alongside a Bosch common rail. This was integrated into the testing facility as part of the fuel circuit redirection for injector one and the low volume fuel system. The D8k injector pipe for injector one was removed and instead linked to the Bosch common rail. From the Bosch common rail, two valve-controlled pipes were installed for injector one and the low volume fuel system. A new control system for the injection pressure was designed, discussed in Section 4.5. The original PRV and PS locations on the D8k common rail were plugged. Figure 3.8 shows the

connection between the two common rails and Figure 3.9 shows a schematic view of the fuel supply.

Figure 3.8: D8k commons rails and fuel supply pipework for the injectors
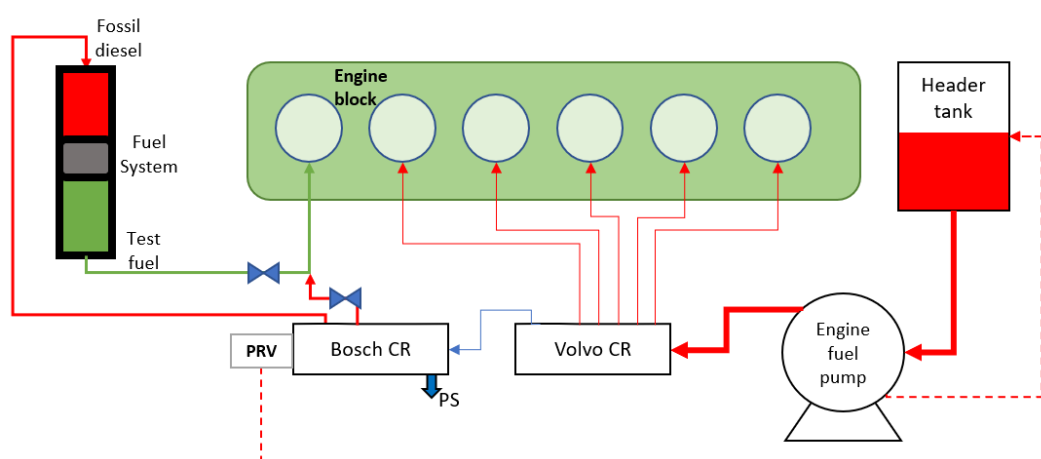
Figure 3.9: Schematic view of how the fossil diesel and test fuels are supplied to the D8k. Shown is the additional Bosch original Volvo common rails (CR) and the location of the pressure relief valve (PRV) and pressure sensor (PS) on the Bosch common rail. Also shown are a pair of two-way valves which allow the fuel supply to switch between low volume fuel system test fuel or common rail diesel.

3.7. Data acquisition and communications

Injection opening timings and duration were controlled via an AVL timing unit triggered by a single pulse every 720 CAD to provide a reference point for the combustion cycle. This was achieved by an AND gate reading a crankshaft and camshaft signal input to produce a unified signal for the AVL timing unit. It was important that a camshaft and crankshaft signal were available for proper timing of the engine and the combustion system. As the D8k is a four-stroke engine, each cylinder only experiences a fuel injection and combustion event every two rotations of the crankshaft, but one rotation of the camshaft. Combining these two signal sources allowed for accurate determination of the piston position, engine speed and maintained the correct firing order between stop/starts.

3.7.1. Crankshaft encoder

An incremental encoder was necessary to time the rotation of the engine. A plate with a shaft extension was designed and attached to the flywheel of the D8k. A Baumer incremental encoder (Appendix, Figure 12.18) was procured for signal generation from the crankshaft. This encoder has an internal bearing allowing it to produce 3,600 pulses per revolution of the crankshaft. This bearing was tightened onto the flywheel shaft. To secure the encoder in position a simple plate with a shaft was attached and held by two metal prongs (Appendix, Figure 12.19). From the encoder, two signals were taken, a one pulse per revolution (TDC) and 3,600 pulses per revolution (clock).

3.7.2. Camshaft sensor

The D8k featured an existing sensor measuring the camshaft speed as an injector backup system if the engine ECU failed. The magnetic induction sensor was positioned above a timing gear, which was one of the gears connecting the camshaft and crankshaft together. This wheel had seven teeth, two are paired together and the remaining five are equally spaced apart, generating six signals from the induction sensor, as shown by Figure 3.10.
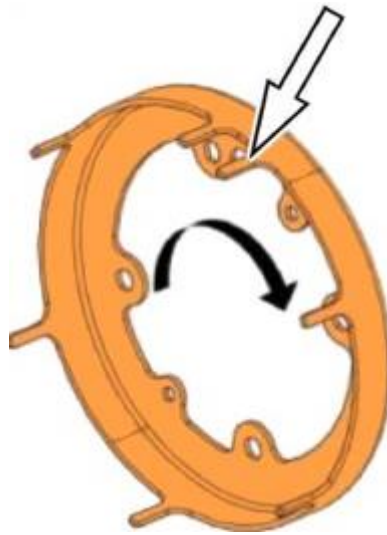
Figure 3.10: Toothed timing wheel which provides rotational timing information for the original injector fail-safe system. Highlighted is the pair of teeth which generate a unique signal.

The pulses generated by the sensor were the same for the five spaced out teeth with a unique pulse generated by the paired teeth. The signal generated from the sensor over one camshaft rotation is shown in Figure 3.11, pulses A to F represent one rotation and pulse G is the first of the second rotation. As shown, pulses B to F are similar with two peaks and two troughs. Pulses A and G are unique with a single trough and peak.
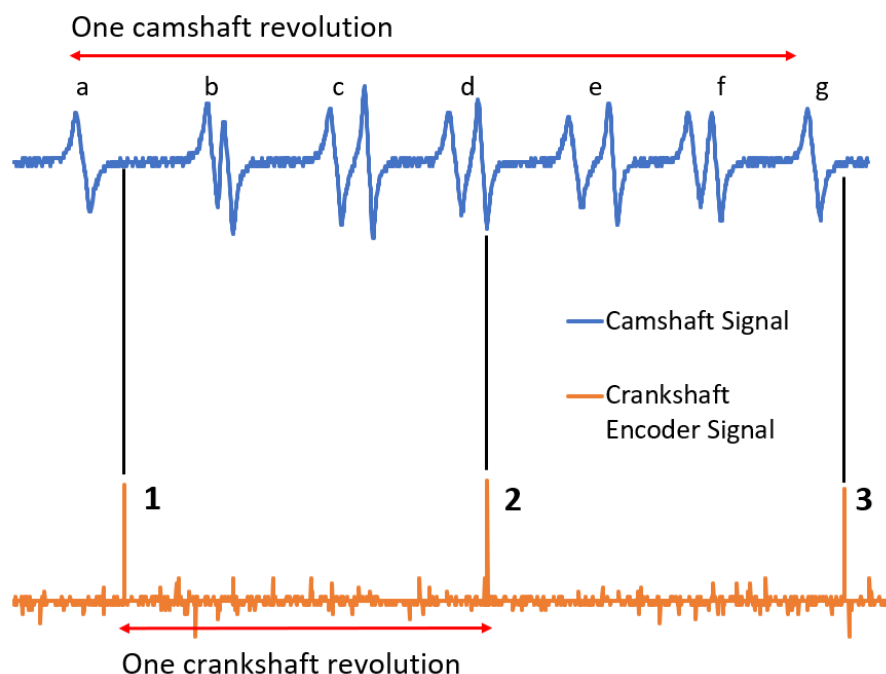
Figure 3.11: Signal generated from the magnetic induction sensor and the crankshaft TDC over one camshaft revolution.

Whilst an existing sensor already timed to the camshaft was useful, unfortunately the signal shapes presented a difficult manipulation challenge. An

81

initial attempt to combine the signals focused on the reduced width of the unique pulse. As highlighted in Figure 3.11, if the crankshaft sensor was positioning correctly the TDC pulse would overlap with the second trough in pulse d from the camshaft. Inclusion of an inverter between the camshaft signal and the AND gate would allow the trough of peak d to join with every second TDC from the crankshaft. However, issues arose with the equipment and chips available as the amplitude of the peaks and troughs generated from the sensor varied with engine speed, from 1.5 V to 2.5 V as speed increased from 100-200 RPM. The starter motor for the engine was limited to 200 RPM and as the combustion system was not yet finalised, the amplitude change could not be tested at higher speeds. The variable signal size and further problems with the inverter experiencing limited effectiveness at the low voltages generated at low speed presented too complicated an issue for the project.

Instead of working towards a more complicated circuit board for the current sensor, a Turck proximity induction sensor was procured and installed in the rocker cover. The sensor was aimed at one of the camshaft lobes which act on the valve rockers to open the intake and exhaust valves, shown in Figure 3.12. This produced a much wider signal than the previous sensor, that at its maximum width it would match the duration of the valve opening. The

crankshaft sensor was easily positioned such that one of the two TDC pulses overlapped with the output from the camshaft sensor.
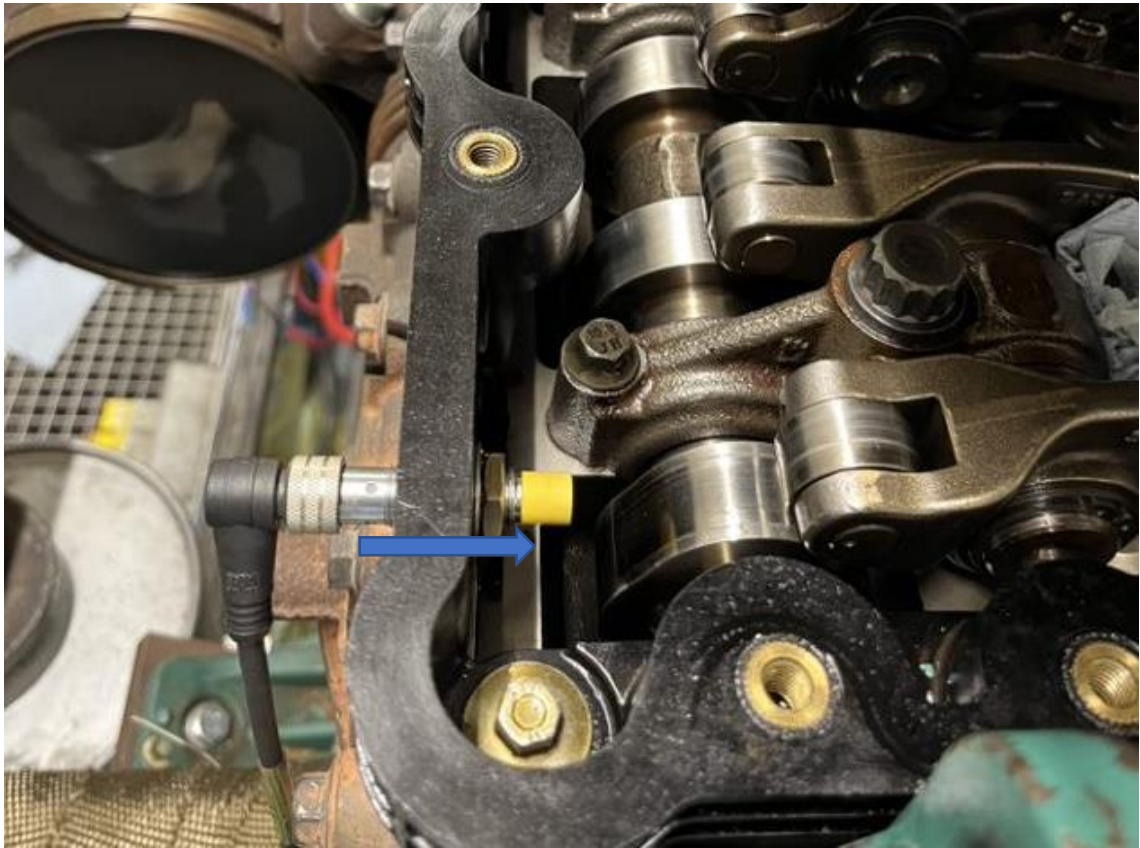
Figure 3.12: Camshaft sensor pointed at the camshaft lobes for controlling the rockers.

After appropriate signal processing, the signal from the camshaft sensor was combined with one of the two pulses from the crankshaft encoder to supply a single short pulse every 720, referred to as the 'AVL input signal' for further references.

3.8. AVL engine timing unit

The AVL engine timing unit (ETU) has eight independent channels with a modifiable TTL signal which can be set to CAD or time-based signals. The AVL input signal was used to time the start of combustion at 0 CAD. From here, the signals to the injectors were timed at 120 CAD intervals. Initially the combustion was mis-timed as shown in Figure 3.13, so the TDC offset had to be found and this was determined by manually inspecting these two signals and adjusting the timing of the control signals as appropriate.
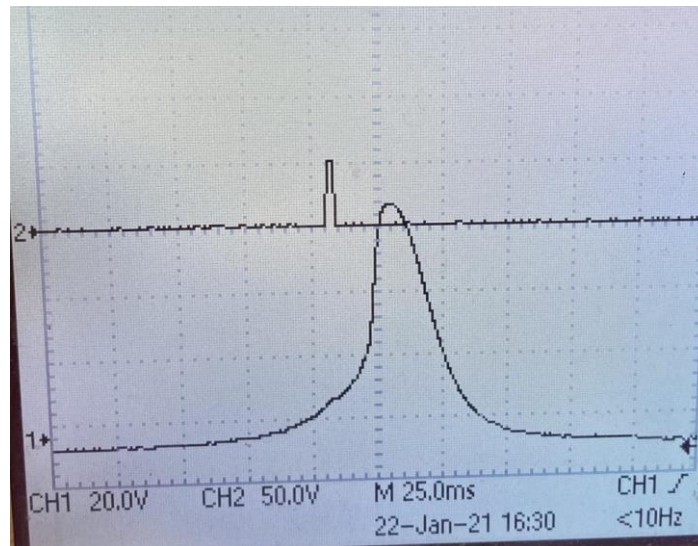
Figure 3.13: TDC signal (top) and in-cylinder pressure trace (bottom).

During adjustments of the timing, it was discovered that two channels of the AVL did not function as intended, one of these could only generate signals above a certain pulse width. The second was generating extra pulses randomly during the first 10 seconds of running the D8k. The channels were reorganised and regular combustion was achieved with these adjustments.

To supply the LabView code with the necessary TDC signal, the AVL input signal pulse was first spliced, but this led to grounding issues with the PCi card. The code was set to trigger on a rising edge, so the malfunctioning AVL channel which only generated large pulses was used to send a 'TDC' signal.

Finally, a more accurate TDC offset was established with analysis of the temperature-entropy diagram for the D8k, outlined by Tazerout et al. (1999).[132]

3.9. Engine cooling water

Engines require optimum temperature ranges for operation, affecting heat transfer from the combustion chamber, air / fuel mixing and viscosity of lubricating oil for moving parts. It was necessary to establish a cooling system which kept the engine temperature close to a steady state condition. An overview of the final state of the cooling system is outlined in Section 4.2.

3.9.1. Heat exchanger

The D8k engine's maximum brake power is 235 kW, but the maximum power dissipation of the brake is 80 kW. The engine operating conditions were

modified so that 80 kW would be the maximum braking power of the D8k. A hydraulic heat exchanger which could dissipate 72 kW of heat was procured, alongside a smaller 4 kW exchanger for the spill fuel, shown in Figure 3.14.

Figure 3.14: Small 4 kW heat exchanger for the fuel spill above the larger 72 kW exchanger for the engine coolant.

3.9.2. Water heater and pump

A water heater was readily available in the testing facility for integration into the coolant circuit. The 72-kW heat exchanger could easily overcool the water, so a heater was necessary for steady state conditions. The original heater drew a high current and after two months short circuited, melting the wire connections. A new heater was procured which could heat water to 80 °C with a thermostatic shut off switch. The thermostatic protection prevented this heater from maintaining a high enough temperature to keep the engine water hot, the previous heater could be set to 120 °C. This was solved by swapping the heating elements between the heaters and removing the thermostatic protection.

To prevent air bubbles forming inside the heater, it had to be bled over two hours whilst the engine heated up after each replacement of the cooling water. To keep the water flow through the engine constant a Viscomat pump with a maximum speed of 14 l/min was installed. The pump drew a high current and frequently tripped its electrical circuit in the testing facility. This issue was resolved with a power regulator which lowered the potential current draw and the pump operating speed.

3.9.3. Copper pipework

The coolant circuit was designed using 22 mm copper piping and many thermocouples were included for accurate readings of the coolant from multiple points in the circuit. Fittings were assembled from multiple parts which facilitated both the connections to the dyno and to the D8k. The heat exchangers used standard fittings and were simple to integrate. Figure 3.15 shows an example of how the copper piping was integrated with the D8k's existing coolant outlets.
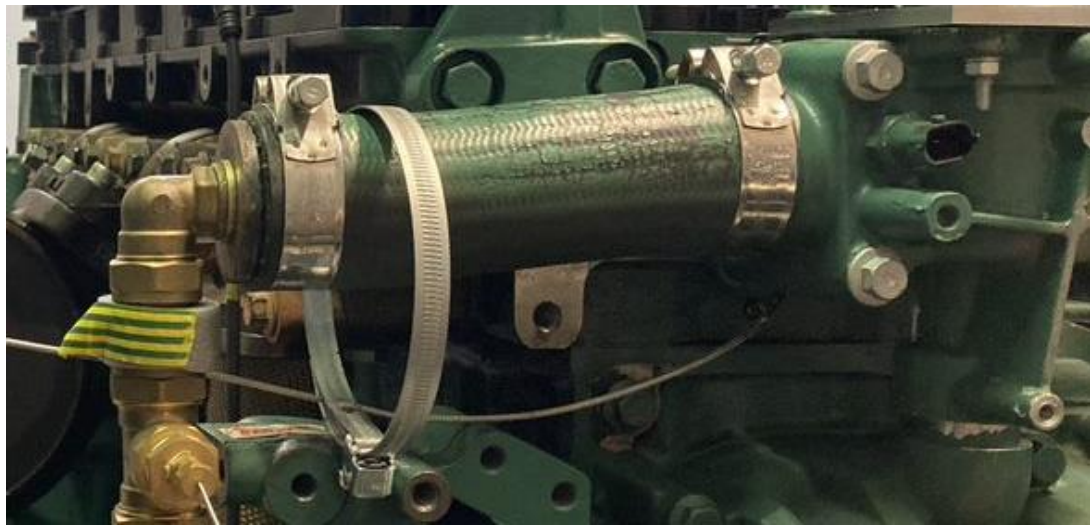
Figure 3.15: 22 mm copper pipework elbow, connected to the existing coolant outlet for the engine.

The exposed copper pipe for the engine coolant was found to transfer too much heat to the surrounding air, leading to the Burkert valve (discussed later in this section) to not accurately control the temperature. Additionally, the pipework which contained the testing facility cold water supply was frequently covered in condensation and was beginning to rust some of the fittings around the heat exchanger. Both of these problems were solved with a layer of standard insulation over the pipework.

3.9.4. Thermostat housing

The D8k utilises a water recirculation system which is controlled by a wax thermostat, visible at position 2 in Figure 3.16. Once cooling water enters the engine, it remains within the head and main body of the engine until the temperature of the coolant reaches 85 °C. It then melts the wax within the thermostat valve, which reroutes the water towards the engine radiator system for cooling.
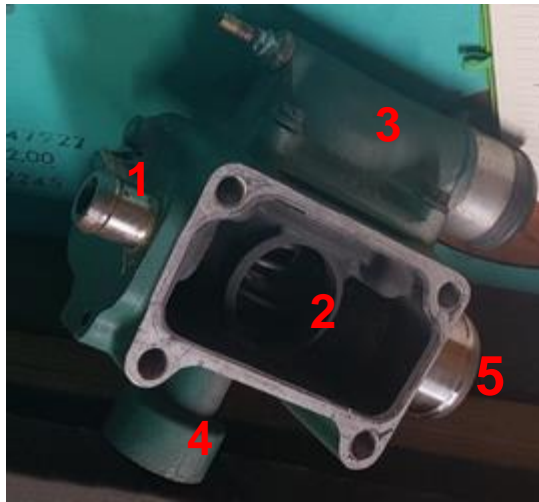
Figure 3.16: D8k thermostat housing. 1, cab heater return. 2, wax valve. 3, cab heater outlet. 4, thermostat housing return to engine body. 5, radiator outlet.

The housing had an inlet and outlet for the cab heater, an outlet for the radiator and return outlet to the engine body. As the heater and radiator were no longer within the testing facility, and the facility could not be heated to 85 $^{\circ}$C regularly for testing, the operation of the thermostat housing had to be redesigned. Each of the five points noted in Figure 3.16 were subject to modification.

The cab heater return was attached to a transparent expansion tank held above the engine, allowing the coolant level to be monitored from the lab office. The cab heater outlet was removed and replaced with a blanking plate (Appendix, Figure 12.20a).

The wax valve was removed and the space was filled with an acrylic plug (Appendix, Figure 12.20b) which blocked the housing return to the engine body, preventing recirculation of coolant from the engine head. The plug now directs water through the radiator outlet to the heat exchanger.

3.9.5. Burkert valve

The coolant heat exchanger's high rate of heat transfer outpaced the coolant heater and engine heat generation. To prevent overcooling of the coolant, two control valves were placed in series. The first was a manual ball valve, which is opened at the end of experiments to bring the engines temperature down quickly. The second was a solenoid valve with proportional response, which remains utilised throughout engine operation.

A thermocouple was positioned between the coolant heater and engine inlet, the shortest length of pipe throughout the network. This thermocouple reading was used as a control temperature for the solenoid valve, set to 72 °C. The LabView code utilises a feedback loop and learning algorithm to apply a voltage to the solenoid valve which proportionally opens or closes the valve to control the flow rate of lab cooling water to the exchanger. The development of this feedback loop, its integration into the LabView controls and the desired voltage values for the valve took several weeks of trial and error.

3.9.6. Coolant deterioration

Throughout the trial-and-error testing of the coolant circuit, the engine coolant was replaced twice. The coolant deterioration was attributed to the engine internal coolant channels containing rust and metallic particles from previous storage conditions. A full coolant replacement required manual restarts of the pump and bleeding of the circuit.

3.10. Air compressor

The air compressor was the only redundant part removed which had an external oil inlet, but internal oil outlet. Oil which exits the air compressor is directed over the timing gears adjacent to the flywheel. To continue this function and remove the compressor, a new oil line was designed with a blanking plate. A pressure gauge was also installed here to monitor oil pressure. Figure 3.17 shows the original pipework (1), pressure gauge (2) and blanking plate (3). A schematic for the blanking plate and spout directing oil flow to the gears can be seen in the appendix, Figure 12.21.
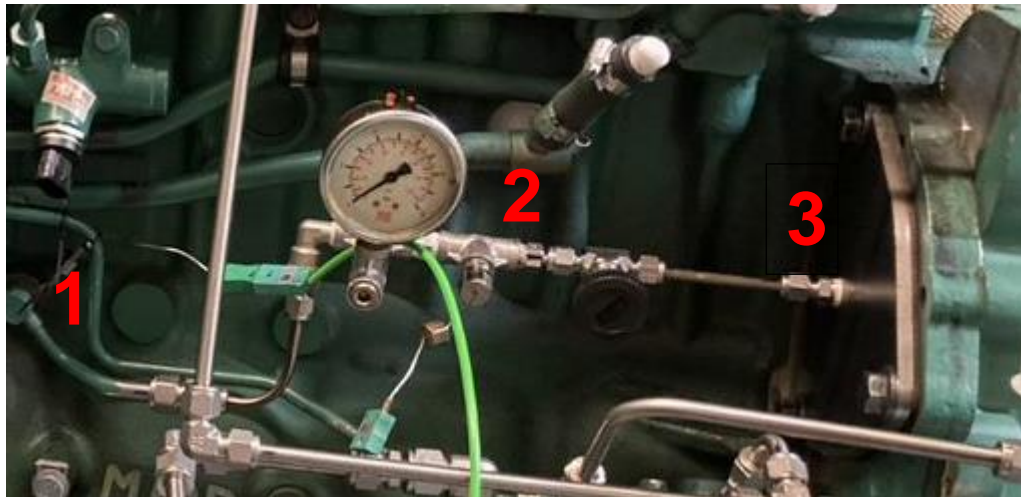
Figure 3.17: New oil line and blanking plate replacing the air compressor.

3.11. LabView and office controls

A brief discussion on LabView is presented here as working with this software does constituent part of the facility development. The role of LabView in the facility operation is described in greater details in Section 4.8.3.

An in-house developed engine data acquisition and control code was developed with LabView for previous projects in this facility. The incremental encoder for the crankshaft has a resolution of 0.1 CAD, whilst previous encoders had a 0.2 CAD resolution. This doubling of resolution therefore doubled the rate at which the code ran, which required more computational power than the available PC's.

The code communicates with the testing facility through two National Instruments PCI cards, one for time sensitive measurements, such as pressures, and the second for less sensitive readings, such as coolant thermocouple readings. Moving one of the two cards to a different PC reduced the computational requirements for both PCs. The code for these two cards was heavily interwoven in one environment, therefore moving the code across was a lengthy process, requiring several revisions and stress testing of the code.

Further updates necessary to the code for the new testing facility were; updating the geometry of the engine and subsequent equations for in-cylinder volume, introducing experimental logging on the PC which did not read the incremental encoder, integration of the coolant solenoid valve code and the

integration of code to communicate with the gas analysers. The final version of the code which ran during experiments was the 4th major revision of this code through the project, with the updates occurring over several months.

4. Experimental systems and methodology

This chapter focuses on the experimental facilities used for this work and is divided into two main sections. Firstly, the research engine, a Volvo D8k will be introduced and the modifications made to the engine discussed. Secondly, the D8k test bed will be discussed. The laboratory utilised previously housed a significantly smaller high-speed engine, so several adaptions were required to integrate the D8k with the control and measurement systems available.

Figure 4.1 briefly overviews the key features of the engine testing facility. The features of lesser importance are not included for legibility, instead these are shown and discussed in greater detail in the following sections.

Table 4.1 highlights the key components providing necessary functions for operating the D8k engine as a research tool.
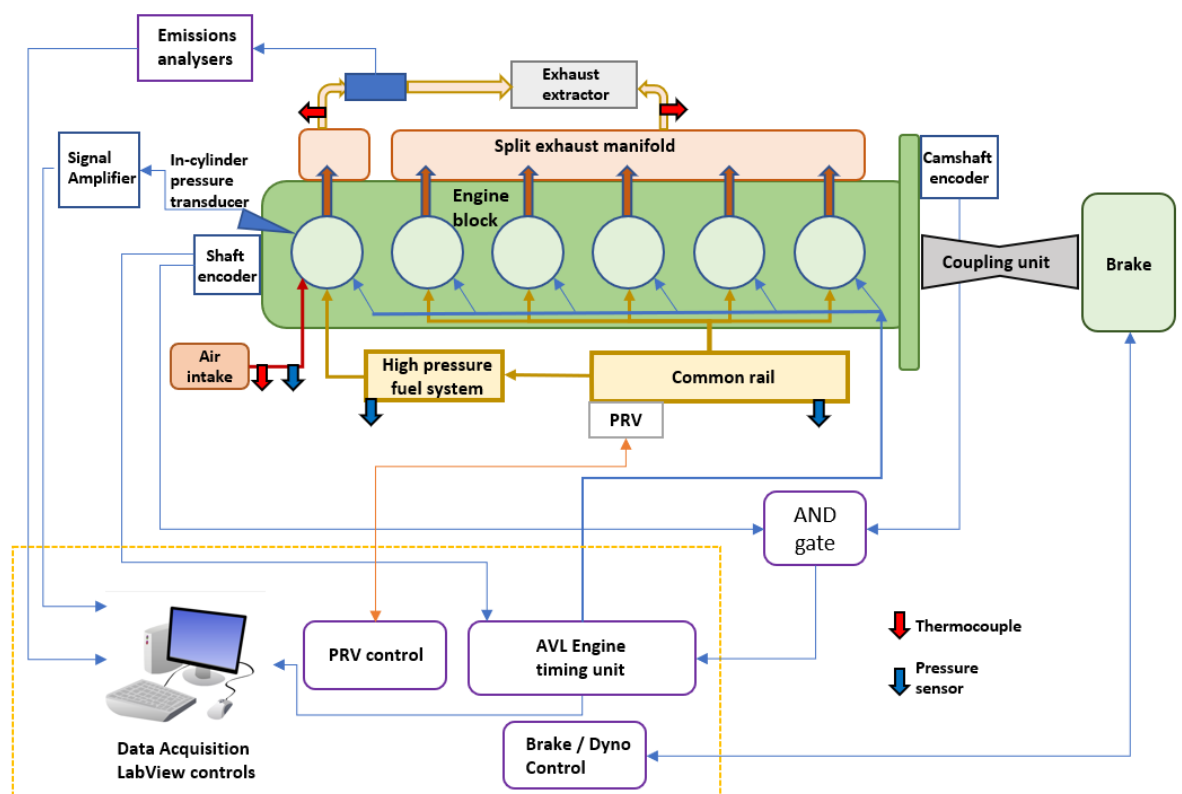
Figure 4.1: Overview of the testing facility, showing signal flow between the control components. All thermocouples and pressure sensors signal lines have been omitted for clarity, each of these sends a unidirectional signal to the LabView controls.

Key Function	Components
Test Facility	Volvo D8k Engine
Data Acquisition and Controls	National instruments (NI) LabVIEW V19 NI PCI-6251 Card NI PCI-6224 Card Ni USB-6001 Card

Timing control
     Crankshaft encoder
     Camshaft sensor
	
	 Baumer EIL580-T Optopulse
	 Turck Inductive Proximity Sensor NI10U-M12-AN6X-H1141

Thermocouples	K type
Engine Timing Unit	AVL ETU
Brake	Schenk Eddy Current Dynamometer W130
In-cylinder pressure sensor	Kistler type 6052c
Coolant circuit control valve	Burkert 2/2-way-solenoid control valve pilot op.6223-A20,0FFMSGM85-K-024/DC-1

4.1. Volvo D8k

The D8k engine first came into manufacture in 2013 and is still produced in 2022.[131] Table 4.2 shows the specification of the D8k engine.

Table 4.2: Volvo D8k engine specifications.[133,134]

Specification	
No. of cylinders	6
Displacement	7.7 dm^3
Stroke	135 mm
Bore	110 mm
Compression ratio	17.5: 1
Firing Order (Where cylinder 1 is that furthest from the flywheel)	1, 4, 2, 6, 3, 5
Engine Dimensions h*w*l (mm)	1004.06 * 830 * 1252.17
Combustion chamber geometry (mm)	
Piston diameter	108.195 ± 0.012
Con Rod length	213.5
Cylinder bore	110
Crank radius	67.5
Clearance volume mm^3	775.7
Piston bowl geometry	Re-entrant design

The D8k's bore of 110 mm, a compression ratio 17.5:1 and re-entrant piston bowl geometry are close in design to heavy-duty diesel engines for light and heavy goods vehicles. Fuel testing results from the D8k can therefore be representative of larger on-road engines, which is important to the applicability of these results. As previously discussed, passenger vehicle and small goods automotive diesel engines are likely to be phased out across Europe in the coming decade, with only large goods vehicles remaining on road utilising diesel engines, for which the D8K works well as a model engine.

4.2. Engine oil and coolant supply and control

The engine's oil system control valves and pumps were initially all internal. Figure 4.2 is a simplified schematic showing the flow of lubricating oil through the engine, adapted from information voluntarily provided by Volvo UK.
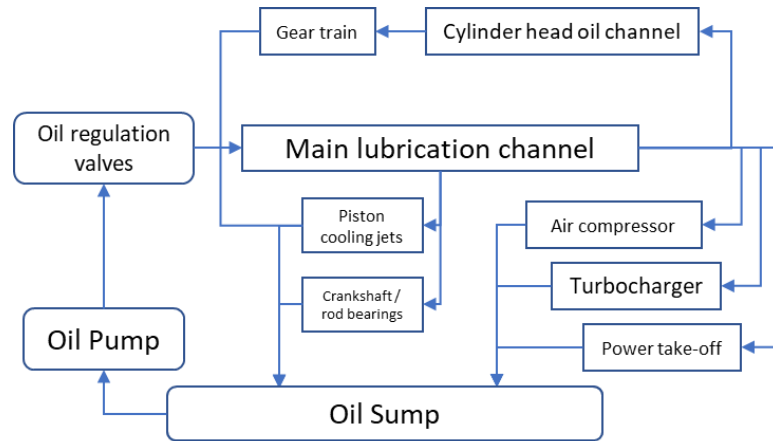
Figure 4.2 Simplified schematic showing movement of oil through the D8k

Following removal of the air compressor and turbocharger several blanking plates were designed to maintain integrity of the oil system. A pressure gauge and thermocouple for the oil temperature were installed alongside new pipework which replaced the air compressor, shown previously in Section 3.10 (Figure 3.17).
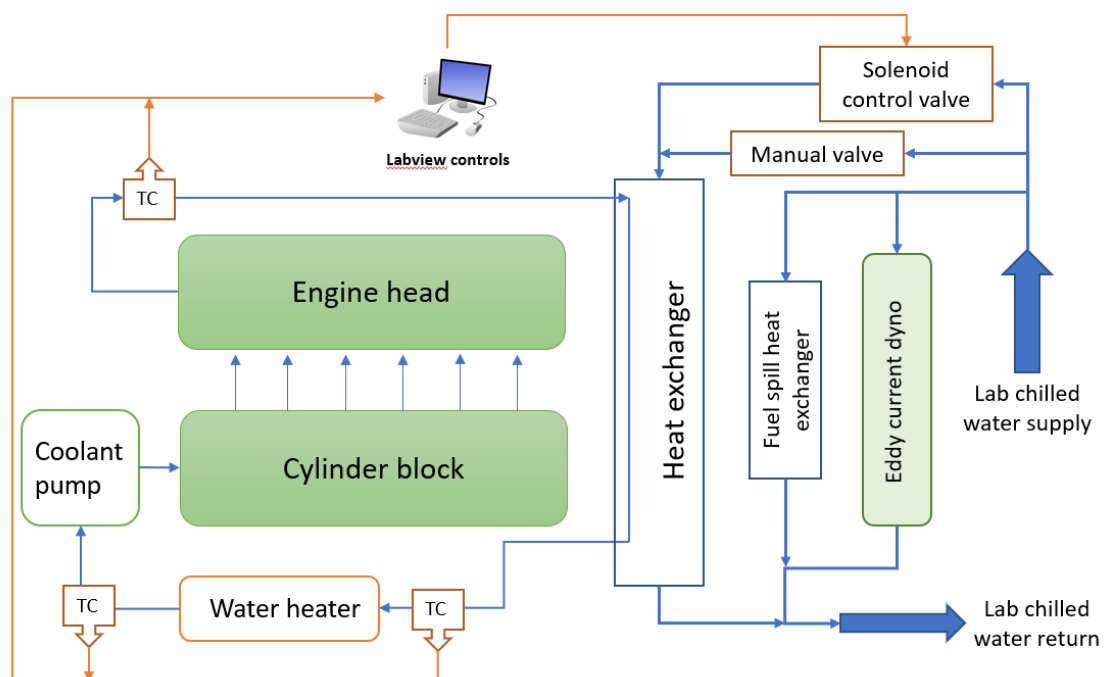
Figure 4.3: Schematic representation of engine coolant supply and conditioning.

A schematic depiction of the flow of cooling water through the lab is shown in Figure 4.3. Thermocouples provided temperature readings of the coolant from several points in the circuit to the LabVIEW DAQ. The volume of cold water flowing to the heat exchanger was controlled by a PWM signal generated in LabVIEW and a Burkert 2/2-way-solenoid control valve.

4.3. Diesel supply

The D8k high-pressure fuel pump relies on a hand pump to prime the engine fuel system and this hand pump was one of the external components not supplied with the engine. The existing fuel hosing was therefore replaced with stainless steel tubing and the engine feed pump was connected to a 5 L reserve tank with a 1.5 m head for supply pressure.

The high-pressure fuel spill from the header pump, common rail, filter and injectors undergoes expansion upon returning to atmospheric pressure, increasing the spill fuel temperature. In a standard vehicle the fuel reservoir effectively dissipates this heat from expansion, however the fuel tank used was small and top fed and so a heat exchanger was used in the fuel return line prior to tank so that any heat generated by the expansion did not cause a safety issue. Figure 4.4 shows the engine common rail fuel circuit in schematic form.
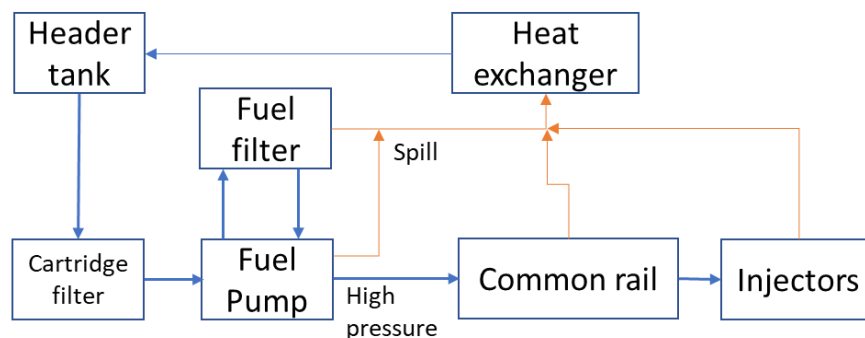
Figure 4.4: Schematic representation of fuel flow from tank to injector and spill return.

4.4. Test fuel supply

A low volume fuel system was utilised for supplying the test fuels, designed by Hellier in 2013. Figure 4.5 shows a schematic of this fuel supply to the test cylinder 1. The fuel system consisted of a pressure vessel with two free moving pistons, which transferred pressure from one chamber containing fossil diesel as a hydraulic fluid to another containing the test fuel. The pistons were sealed

against the vessel bore with Viton o-rings to prevent any fuel crossover or contamination. The fossil diesel was supplied from the common rail circuit, so that the number one injector was supplied fuel at the same pressure as the other five injectors supplied directly from the common rail. For further details of the low volume system design and operating procedure see 'The molecular structure of future fuels', Hellier, 2013.[135]
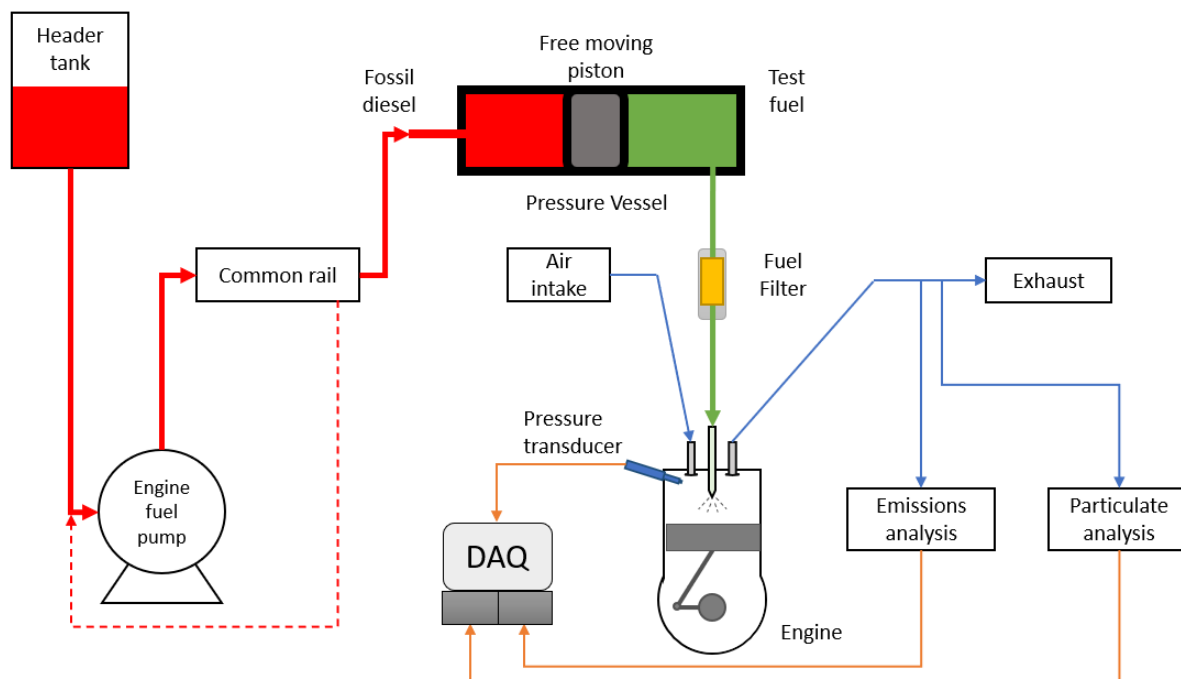
Figure 4.5: Low volume fuel system within the engine fuel circuit.

4.5. Common rail pressure relief valve

Without access to the D8k ECU, the common rail pressure control required the development of a custom-made control system. Figure 4.6 shows a basic schematic of this system.
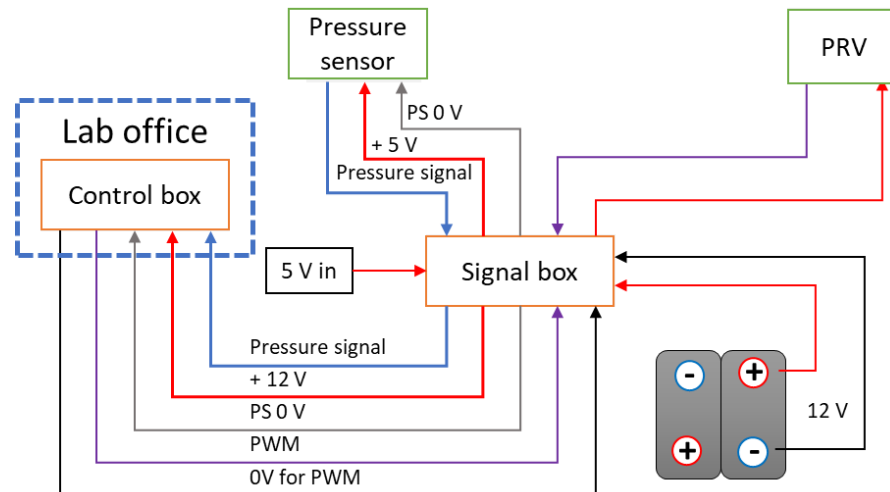
Figure 4.6 Communications and controls for the common rail pressure sensor and relief valve.

This system controlled the fuel injection pressure by moderating signals to and from the common rail pressure relief valve (PRV) and common rail pressure transducer (CPT). The system provided power to both the CRV and CPT and moderated the output signals which provided feedback on the current pressure. The two main sub-units of the control system were the control box in the control room and the signal box in the test cell.

The control box read the pressure sensor output and displayed a voltage value which is converted to pressure manually. The control box also had a frequency and duty cycle input which were used to generate an appropriate PWM signal to control the pressure relief valve (PRV). The common rail (injection) pressure was set by manual adjustment of the frequency or duty cycle inputs during tests.

The signal box modulated two power sources; a 12 V supply from the battery box and a 5 V supply from a power supply unit. The 12 V was conditioned appropriately by the control box to supply the PWM signal for the PRV and the 5 V supply provided power for the common rail pressure sensor.

4.6. Starting switch

The final equipment addition for engine operation was a pair of 12 V, 135 A batteries, connected in series for a 24 V supply to the starter motor. The batteries were connected directly to the engine starter motor and grounded on the engine chassis. The engine starter relay received a 12 V signal from a separate power supply and was controlled by an ignition switch inside the control room for the test cell.

4.7. Power and speed control

Operating the D8k engine generated an excess of power which must be dissipated. A Schenk W 130 eddy current dynamometer was therefore connected to the D8k with a shaft coupling. However, the maximum power which can be absorbed by the dyno is far lower than the maximum power output of the D8k. The Schenk dyno has a maximum capacity of 130 kW and nominal torque of 400 Nm at a minimum speed of 1250 rev/min as can be seen in Figure 4.8, which is far lower than the 156.6 kW power output and 1,300 Nm torque of the D8k operating under normal conditions at this speed. To ensure safe testing conditions with the equipment available, the D8k operated a lower load than typical by modifying the injector opening durations, ensuring the W 130 could safely dissipate the power generated from the tests.

During tests, the number one injector was opened for 6.5 CAD and with an injection pressure of 700 bar, the IMEP was measured at 7.2 bar, which was a suitable baseline for the tests. The injector opening time for remaining back five injectors was set at 2.5 CAD to ensure smooth engine operation. The dynamometer was set to control this load at a speed of 800 +/- 20 RPM.
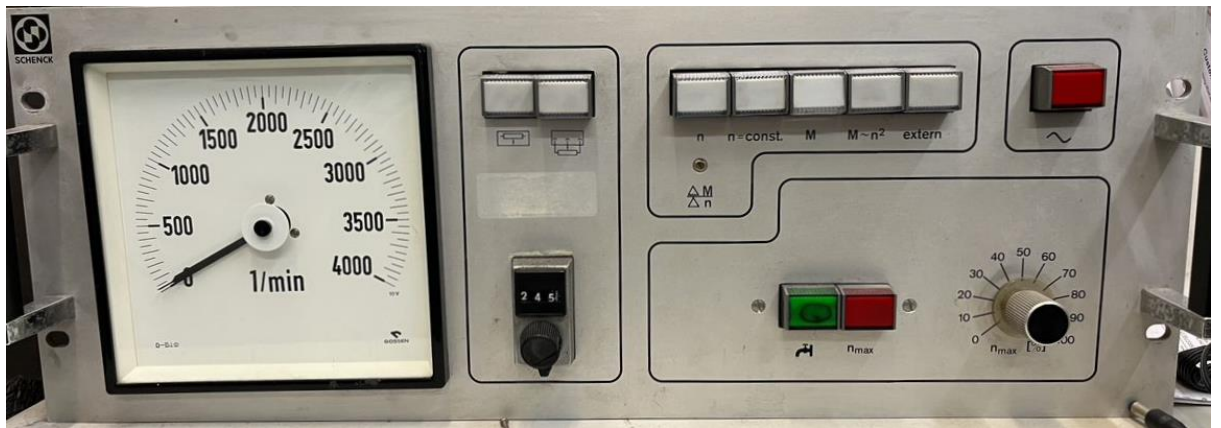
Figure 4.7: Schenk W 130 dynamometer control panel
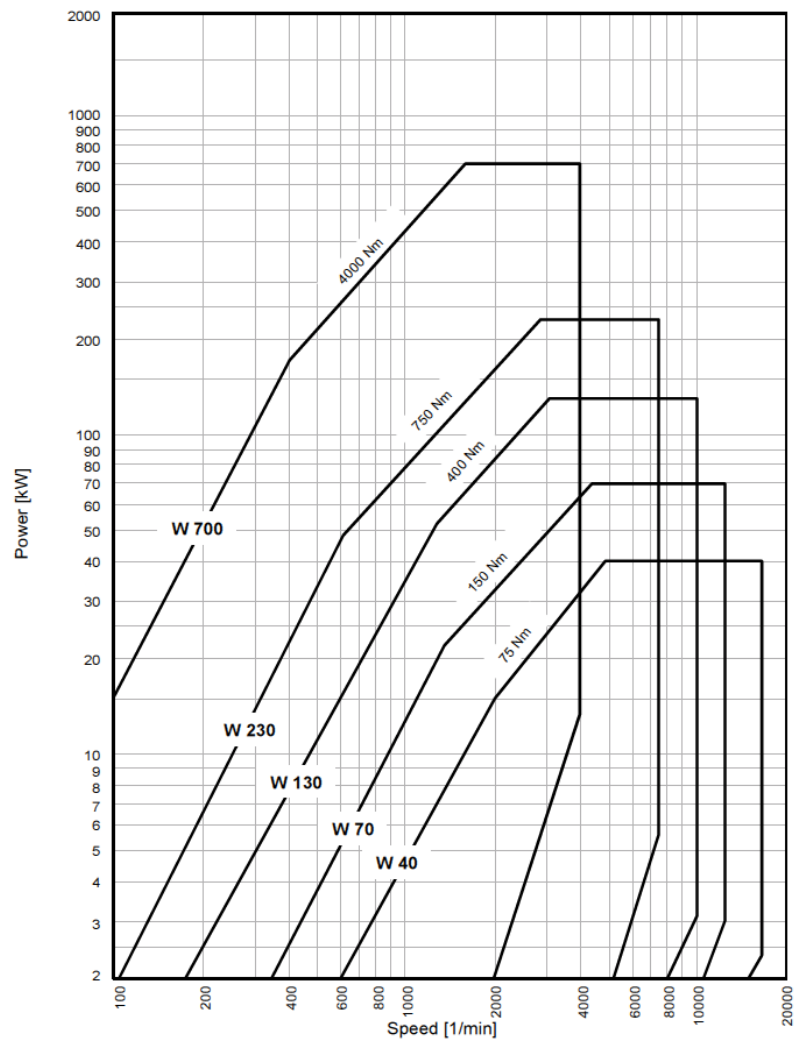
Figure 4.8 Schenck Eddy-current dynamometer capacity range.[136]

4.8. Data acquisition and engine control

This section will outline the equipment installed on the D8k to replace the engine standard control unit (ECU) and some other equipment required for in-cylinder pressure measurements. Access to the software for the ECU was not available and there was no access to a manual for the engine sensors and other electronic control systems. It was therefore necessary to install devices which could provide similar functions.

4.8.1. Shaft encoder

An incremental encoder was installed on the engine crankshaft with a resolution of 3,600 pulses per revolution. This provided 7,200 pulses per combustion cycle for measurement of in-cylinder pressure relative to crank angle degree. The encoder was powered with 5 V from a mains power supply and the output signals were read by LabVIEW DAQ (described in Section 4.8.3) in the test cell control room. The encoder sat on a rod which spun true with the crankshaft, protruding from a plate secured onto the engine crankshaft at the location where the engine fan was previously attached. Figure 4.9 shows the design of the incremental encoder mounting and shows the installation on the engine. As the crankshaft rotates, so does the plate, rod and the internal rotor of the encoder. The external case of the encoder was held stationary by a plate with a perpendicular rod fixed between a stationary fork.
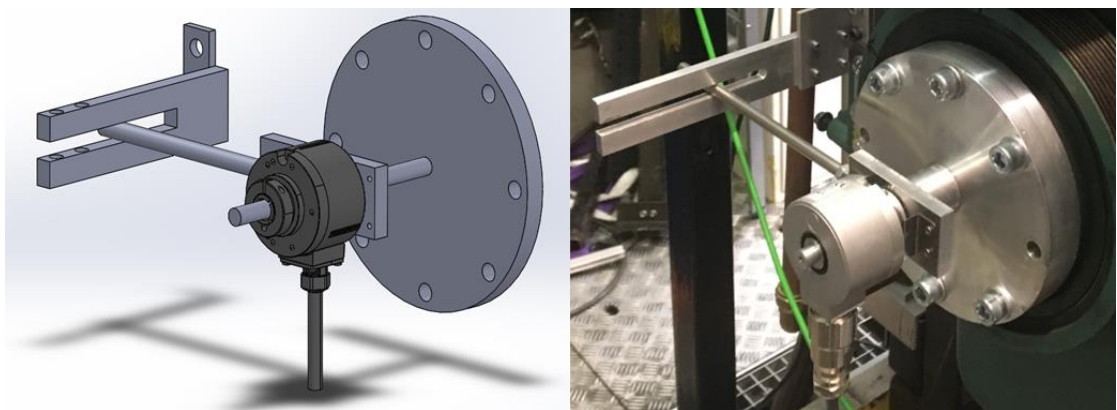
Figure 4.9: Baumer EIL580T Incremental encoder design image (left) and set up on D8k (right).

4.8.2. Engine timing unit

Without access to the D8k engine ECU, control of the injector opening time and duration was achieved with an AVL Engine Timing Unit (AVL), which could operate up to 8 independent injectors. With this level of control, a sperate injection timing and duration could be used for all 6 injectors on the D8k. This was important as the test fuel used in cylinder one would have potentially different properties relative to the fossil diesel and therefore require a different injection volume, injection duration or injection time relevant to TDC. Figure 4.10 shows a schematic of the AVL inputs and outputs.
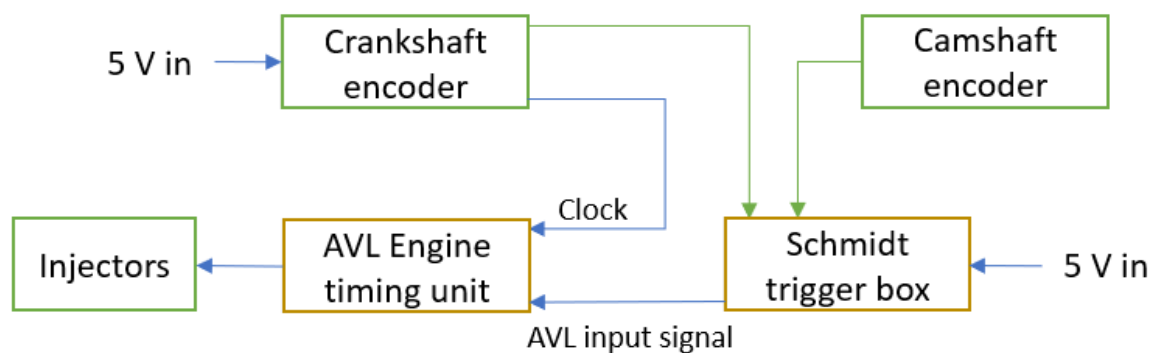
Figure 4.10 AVL ETU control system.

For operation the AVL ETU required synchronisation with the engine cycle which was achieved with the aid of an optical crankshaft encoder (Section 3.7) and a variable reluctance camshaft sensor. The camshaft sensor was secured in the camshaft cover directed at the cam which acts on the intake valve for cylinder one. The sensor was a normally open, NPN sensor which sends a 15 V signal when open and switches to 1 V when closed. The proximity sensor produced a wide signal covering a high number of CAD. The signal produced was analogue and was first converted into a digital signal by a Schmidt trigger before further conditioning.

The crankshaft encoder produces two TDC signals per combustion cycle, so the encoder was aligned such that only one of the TDC signals per combustion cycle aligned with the wider camshaft signal, which occurs only once per combustion cycle. The two signals were finally combined in an AND gate, the output of which is taken as the AVL input signal.

4.8.3. LabView

For logging of experimental data three independent non-networked PCs were utilised: one for logging in-cylinder pressure data, a second for logging exhaust gas composition data and temperature data, and a third for logging measurements of particulate size and number. The PC for in-cylinder pressure data was equipped with an internally mounted National Instruments PCI-6251 multifunction I/O device, PCI 16 channel input data acquisition card. The PCI-6251 card, referred to as 'high-speed', was capable of sampling at 1.25 MS/s with a single analogue to digital converter in conjunction with a multiplexer.

The PC logging temperatures and gaseous emissions was equipped with a similar an internally mounted National Instruments PCI-6224 data acquisition card, referred to as 'low-speed'. The NI 6224 card and had a peak sampling rate of 250 KS/s also with a single analogue to digital converter. This PC was also equipped with an NI USB-6001 multifunction I/O device, with a sampling speed of 20 kS/s, referred to as 'USB-card'.

The high-speed card was utilised for sampling the analogue outputs of the in-cylinder pressure transducer, air intake pressure, engine speed from the crankshaft encoder clock and the timing control signal from the AVL unit. The low-speed card was used to read temperatures at several points in the facility (engine coolant circuit, engine oil, air intake and fuel temperature) and the USB-card was used to send a PID signal to the Burkert valve.

The data acquisition software utilised to process and log the incoming signals was a graphical programming environment, National Instruments Labview 19.1. The DAQ software was first developed for the testing facility by Schönborn (2009) and further adaptations by Hellier (2013).[135,137] The major update to the code for this work was changing the card locations and splitting the written software between the two PCs, further details are available in Section 3.11.
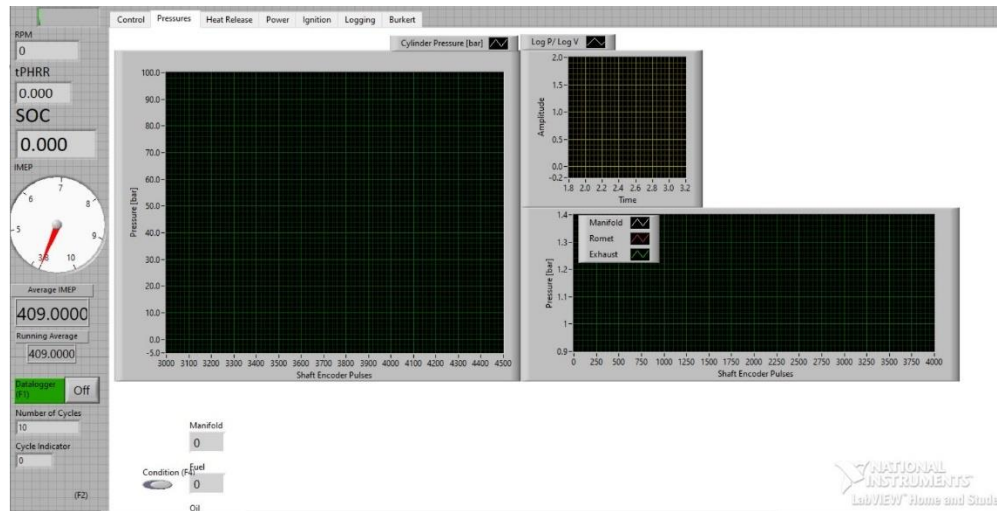
Figure 4.11: In-cylinder pressure DAQ screenshot

Figure 4.11 shows a screenshot of the DAQ program interface. Data was acquired at a resolution of 0.1 CAD and recorded, stored and processed as one complete engine cycle. An optical shaft encoder coupled to the crankshaft gave 3600 square-form signals per crankshaft revolution, thus defining the resolution of pressure measurements as 0.1 CAD. The clock signal was used in conjecture with a timing signal generated by the AVL ETU. This allowed for all high-speed measurements to be synchronised according to engine cycle, rather than crankshaft rotation, and thus instantaneous display of the acquired data and real-time processing. Using the engine geometry parameters stored in the DAQ software, the position of TDC (determined according to the method of entropy developed by Tazerout et al. (1999)[132]) and the timing signals, several combustion variables were calculated and displayed in real time. These included: indicated mean effective pressure (IMEP), heat release rate, cumulative heat release rate, mass fraction burnt, global in-cylinder temperature, entropy, time of start of combustion and time of peak heat release rate. The data acquisition software displayed and logged (in tabular format in an ASCII format file) the original measurements and the calculated parameters.

The low-speed card at a rate of 10 S/s sampled signals from seven thermocouples, the test fuel pressure transmitter, and the gaseous emission readings through a GBIP to USB module (National Instruments GPIB-USB-HS) from a Horiba MEXA 9100 HEGR. The temperature and gaseous emissions data acquired from the low-speed card was also shown in real time for better experimental control and logged in an ASCII format file.

The USB-card sent a variable 0-10 V PWM control signal to the Burkert control valve in the coolant circuit, generated as a proportional response to thermocouple readings from the coolant circuit. To have better control over the experimental conditions and to avoid temperature fluctuations, the DAQ software included a limiting control which kept the maximum control signal voltage at 7.5 V, with a manual override available if the real-time temperature was too high to cool effectively.
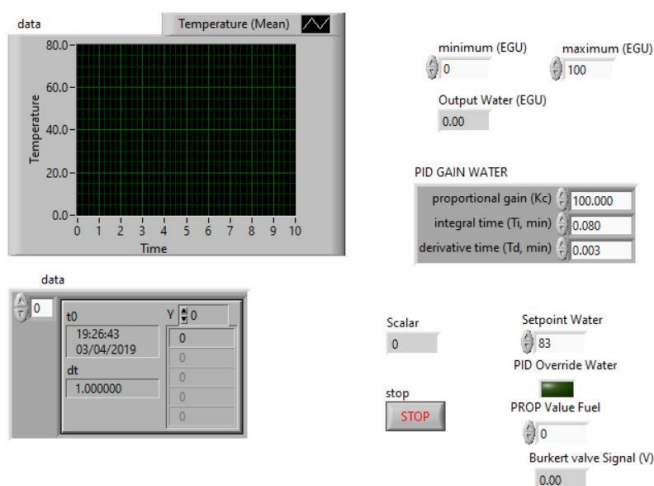
Figure 4.12: Burkert control valve live temperature display and manual override screenshot

The third PC was reserved exclusively for control of and data logging from the fast particulate spectrometer. Both were performed with the PC user interface supplied by the instrument manufacturer (Cambustion DMS User Interface V2.13, 4.05 and 4.07); Figure 4.12 shows a screenshot of the spectrometer interface.
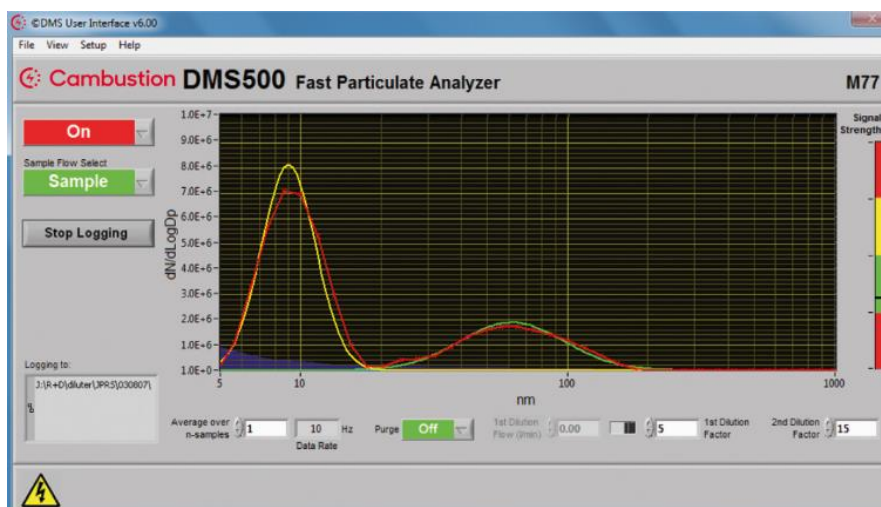
Figure 4.13: DMS500 Fast particulate analyser data acquisition software (DMS500 Brochure).[138]

4.9. Kistler pressure transducer

When characterising the performance of a fuel several properties must be determined, such as the burning rate, IMEP and duration of combustion, which are derived from heat release rate analysis of the in-cylinder pressure and cylinder volume. The cylinder volume is calculated from cylinder geometry and engine speed. In-cylinder pressure can be measured directly and for this purpose a Kistler 6052 C pressure transducer was acquired. The specifications are shown in Table 12.2 in the Appendix.

An appropriate location was found and a hole drilled according to the transducer installation specifications, 18 mm in length at a 20° elevation angle. Further discussion on how this position was found is available in Section 3.2.

The signal output from the transducer was connected to a charge amplifier and then to the LabVIEW DAQ in the test cell control room.

4.10. Heat release rate analysis

A custom Matlab code was used to plot the raw in-cylinder data against CAD, which was able to provide insight on the duration of both ignition delay and combustion. This code was used by Hellier (2013) and adapted match the D8k geometries and increased file size resulting from a new shaft encoder with twice the resolution from the previous test facility. To discuss how differences in chemical structure may lead to differences in fuel performance, the apparent heat release rate over a number of CAD must be determined.

In order to calculate heat release rate from in-cylinder pressure data, the cylinder geometry (combustion chamber) at each interval of CAD must be known. The total cylinder volume (V) at any given CAD is calculated using the geometrical values provided in Table 4.2 and the following calculation:

$$V = V_{\text{clear}} + [A_{\text{bore}} (l_{\text{con}} + r_{\text{crank}} - \sigma)]$$

where A_{bore} is the cylinder bore area, r_{crank} is the crank radius, V_{clear} is the clearance volume and σ the instantaneous stroke. A_{bore} can be found from

$$A_{bore} = \frac{D^2{}_{bore}}{4} \pi$$

where D_{bore} is the cylinder bore diameter.

The instantaneous stroke position can be found by

$$\sigma = \text{acos}(\theta) + \sqrt{l^2{}_{con} - a^2 \sin^2(\theta)}$$

where θ is the crank angle from the TDC position

To calculate the heat release of combustion occurring within the combustion chamber, a number of assumptions are made for properties which cannot be accurately determined within the scope of this project. These assumptions designate all heat-release rate analysis in this work as 'apparent net heat release of combustion' (Heywood, 2018).[139] These are: the cylinder contents are assumed to be at a uniform instantaneous temperature (T), no mass flow occurs across the system boundaries for the duration of heat release, the calculation of net heat release the system is adiabatic and the cylinder contents can be modelled as an ideal gas. The net heat release is therefore the difference between the gross heat release of the fuel during combustion and the heat transfer from the system to the cylinder walls in accordance with the first law of thermodynamics. Therefore, the net heat release rate at any given position in the combustion cycle can be expressed as

$$\frac{dQ_n}{d\theta} = \frac{\gamma}{\gamma - 1} p \frac{dV}{d\theta} + \frac{1}{\gamma - 1} V \frac{dp}{d\theta}$$

For all combustion experiments presented in this work, this expression (Equation 4-4) was used to calculate the apparent net heat release rate at increments of CAD equivalent to the resolution of the shaft encoder (0.1 CAD)

utilised in recording in-cylinder pressure data. The values of dp dθ and dV dθ used were the difference between the values of P and V at the CAD for which Qn was calculated (as measured and calculated according to Equation 4-1 respectively).

The values of the ratio of specific heats used in Equation 4.12, were those suggested by Heywood (2018), namely γ = 1.35 during the compression stroke prior to TDC and γ = 1.28 subsequent to TDC during the expansion stroke.

4-5

$$\gamma = \frac{C_p}{C_v}$$

Where C_p is the specific heat capacity of a gas at constant pressure and C_v is the specific heat capacity at constant volume.

The ideal gas constant, R, can be found by

4-6

$$R = C_p - C_v$$

Hence the ratio of specific heats can be found by knowing the molar ratios of each chemical in the system and their specific heat capacities at constant volume. The conditions employed in this study result in a lean air/fuel mixture, so prior to autoignition the mixture inside the combustion chamber can be assumed to be equivalent to low density air. Reynolds et al. (1979) states the γ for low density air between 800 to 1200 K falls from 1.350 to 1.324. The specific heat capacities of CO_2 and water for constant pressure and volume are closer in value than air, hence the γ of the burned mixture is lower than unburnt.[140]

The assumed values of γ could be considered restrictive, as specific heats will change with temperature and the exact chemical composition of air fuel mixture in the combustion chamber prior to and after TDC is not precisely known.

Changing the value of γ at TDC also assumes every fuel will ignite at TDC, which is unlikely. Furthermore, it assumes the transition between unburnt and burnt gases is instantaneous. Changing the value of γ at TDC results in very different heat release calculations, as a 0.1 CAD change results in very little change in in-cylinder pressure or volume, but the γ value change from 1.35 to 1.28 will drastically change the heat release calculation. Whilst this is not

representable of real engine conditions, assessing the chemical composition of the exhaust gases at every increment of the shaft encoder would require far more time than is acceptable for the minor improvement in the accuracy of results.

4.10.1. In-cylinder global temperature

Using the previously stated assumptions for calculation of apparent net heat release rate, the global temperature of the cylinder contents may be calculated with the ideal gas law (Equation 4-7).

4-7

$$pV = nRT$$

Temperature (T) is calculated from the measured pressure (p), known volume at each CAD (V), molar gas constant (R) and the number of mols of air present (n). The mols of air present were calculated from the temperature measured at the inlet valve, the known density of air and the total in-cylinder volume. Considering compression ignition engines operate with lean combustion, the contents of the cylinder were assumed to have a fixed composition of air.

4.11. Exhaust analysers

Exhaust gas composition was determined by individually measuring the concentrations present in the exhaust gas of the following chemical species: CO, CO2, O2, THC, NO and NOx. These measurements were performed by a Horiba MEXA 9100 HEGR, incorporating individual instruments to analyse concentrations of each of the species above except THC, which was measured in a Horiba FIA Ov-04 flame ionisation detector.

Two heated lines (held at a constant temperature of 190 ºC) conveyed exhaust gases from the exhaust sampling points to the analysers, with the gas sample taken by the main analyser subject to filtering and condensation of water vapour and gaseous hydrocarbons before entering the individual analysers. Measurements of exhaust gas composition by the analyser rack were recorded on PC via a GPIB output from the rack control unit.

4.11.1. CO and CO2

CO and CO2 both absorb light in the infrared spectrum, so the concentration of each species in a gas sample will change the amount of light absorbed by the gas molecules. Accurate determination of gas concentration relies on optimising light intensity, if the intensity is low, it will be completely absorbed by a high concentration of gas and vice versa, a high light intensity with low concentration of gas will be difficult to accurately determine (Horiba Instruments 1984).[141]
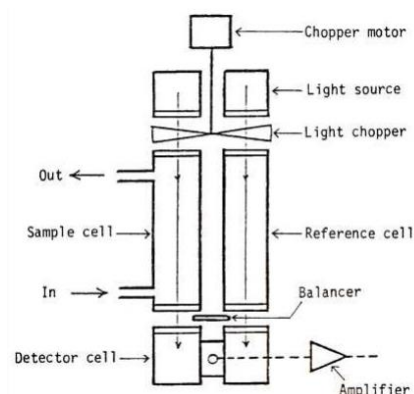
Figure 4.14 CO and CO2 analyser schematic (Horiba Instruments 1984)[141]

Figure 4.14 shows a basic single detector system, with two cells placed in parallel. The gas sample being analysed flows through one cell and the second cell contains an IR inert reference gas such as N2. An infrared light beam passes through both cells at the same time and then impacts on a detector cell. CO and CO2 present in the sample cell will absorb the light at particular frequencies, leading to a difference in light intensity on the two detector cells. The light beam interacts with a metallic membrane and capacitive sensor to produce an electrical output.

Two separate infrared absorption detector systems were employed within the analyser used (Horiba AIA-120) for measurement of CO and CO2. One system was specially configured to accurately measure low concentrations of CO (< 3000 ppm) and achieved this high sensitivity through the addition of a second detector cell in series with the first. In this dual detector system, the first detector features infrared transparent windows allowing the beam to exit and enter the adjacent second detector cell.[103] This arrangement is beneficial as it allows the first detector to respond primarily to the sample, with only a small portion of the output signal produced by an interferent species (such as CO2 in the case of CO detection) and the second detector behaves in the inverse

manner. A compensated composite signal can then be produced that effectively removes the influence of the interferent.

The second unit within the analyser was a stacked detector system that simultaneously measured CO_2 levels and higher concentrations of CO (< 3000 ppm). As the absorption wavelengths of CO_2 and CO do not overlap, utilising two separate detector cells allows for concentrations of both to be determined from the same sample when both species are present at similar ranges of concentration. As in the case of a dual detector system, the detector cells are arranged in series, with the detector signals processed by separate amplifier networks for independent output (Horiba Instruments 1984).

4.11.2. Oxygen detection
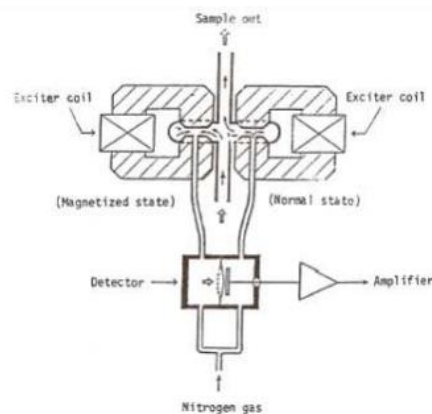
Figure 4.15 O_2 Analyser schematic (Horiba Instruments 1984)

Figure 4.15 shows in schematic form the magneto-pneumatic analyser (Horiba FMA-125) utilised to determine levels of O_2 present in the sample gas. Oxygen possesses a much higher paramagnetic susceptibility than the other gases present in the exhaust stream and this property is exploited in determining the O_2 concentration present. The sample gas flowed past two pairs of poles which are alternately magnetised by excited coils. Oxygen is drawn to whichever of the poles is currently magnetised and this disrupts the flow of nitrogen from an orifice located within the poles. Thus, at any time the flow of N_2 from one orifice will be restricted while the other is not. This pressure differential of the N_2 is converted by the detector (a condenser microphone) to an electrical output equivalent to the concentration of O_2 present (Horiba Instruments, 1984).[141]

4.11.3. Unburnt hydrocarbons

Quantification of hydrocarbons present in the exhaust gases was conducted by a hydrogen flame ionisation detector which consisted of a rack controller (Horiba FMA-125) and an external heated oven cabinet (Horiba FIA OV-04) held at a constant temperature of 190 °C. Located within the oven unit, a constant hydrogen flame was maintained and through which the sample gas flowed. Any hydrocarbons present in the sample gas would pass through the high temperature flame and undergo breakdown of the carbon-carbon bonds and produce ionised current. Two electrodes with a steady direct current voltage applied across them were positioned either side of the flame, and thus the ionisation of hydrocarbons within the sample gas would result in production of a current proportional to the number of carbon atoms ionised (Horiba Instruments, 1984).

4.11.4. NO$_x$

The NO and NOx analyser (Horiba CLA-150) utilised the chemiluminescent method of detection for both species. The reaction of NO with ozone outlined below is well studied, the relevant extinction coefficients of species and rate constants of the reactions allow for accurate determination of species concentration. Photons emitted from NO2 relaxation are detected and the intensity of emission is correlated directly to initial NO.[142]

$$NO + O_3 \rightarrow NO_2{}^* + O_2$$

$$NO_2{}^* \rightarrow NO_2 + h\nu$$
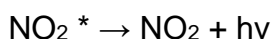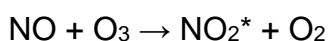
(hν = emitted photon & * denotes an excited energy state)

The sample gas was mixed with O3 and then fed to an evacuated reaction chamber where the NO + O3 reaction took place. A photo multiplier measured the resulting luminescence which was proportional to the amount of NO present. To measure any NO2 present in the sample concurrently by the same method, prior to entering the reaction chamber, the whole exhaust sample flowed through a NO2 converter. Any NO2 present in the heated converter in the presence of a catalyst, will then dissociate to form NO, i.e.

$$NO2 + C \rightarrow NO + CO$$
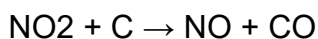
The analyser unit (Horiba CLA-150) included a vacuum pump so that the above reactions could take place in the reaction chamber under reduced pressure conditions. This reduced the possibility of collision between excited NO2* and other molecules prior to their relaxation and thus any interference due to other species present in the sample (Horiba Instruments, 1984).

4.11.5. Particulates

Figure 4.16 shows the fast particulate spectrometer (Cambustion DMS500) utilised to determine the size distribution of particulates (5 to 1000 nm) in the exhaust gas. Figure 4.17 shows the flow of sample gases through the spectrometer. From the exhaust sampling point, the sample gas was conveyed through stainless steel pipe (of length 320 mm) to a heated cyclone which was kept at constant temperature (80 $^{\circ}$C). This cyclone was required to dilute the sample gas with dry compressed air prior to entering the instrument for two reasons: dilute the exhaust gas sample so that the water dew point of the sample gas would be below the ambient operating temperature of the instrument and also reduce the concentration of particulates, thus reducing accumulation of particulates in the instrument and extending cleaning intervals.

Figure 4.16: DMS500 Fast Particulate Spectrometer.

The dilution ratio (air: sample) at the cyclone was maintained at four to five throughout the running of experiments. The cyclone also served to remove any particles present in the exhaust stream greater than 1 µm. To further prevent condensation of water vapour, the sample gas flowed from the cyclone to the main instrument via a heated line maintained at constant temperature (5 m length at 80 °C). The compressed air supply to the remote cyclone was also conveyed through the same heated line, albeit along a different path.
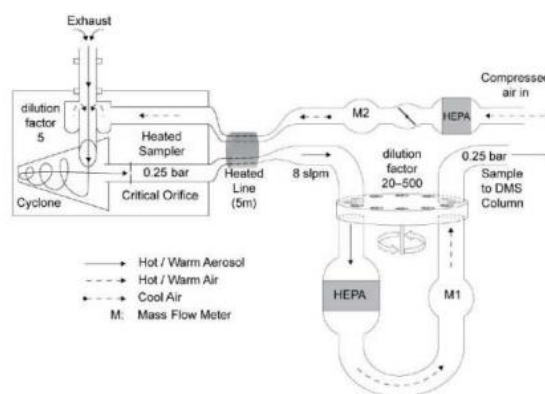
Figure 4.17 Sample flow of DMS500 (Cambustion, 2010)

On entering the instrument, the sample flow was subject to secondary dilution (ratio of 100) through a second heated cyclone (80 °C) positioned in series and downstream of the first cyclone described above. From the second cyclone the sample flowed through a corona discharge charger and into the classifier column (particle sizer), which was maintained constantly at an absolute pressure of 0.25 bar by an external vacuum pump (Figure 4.17). Figure 4.19 shows the classifier column which consisted of a uniform, cylindrical column of air flowing around a central high voltage electrode and surrounded by a sheath of particle free air (Cambustion, 2010). Twenty-two grounded rings surrounded the sheath flow and repulsion from the central high voltage electrode caused particulates within the sample flow to deflect on to the grounded rings. Charge from the particulates was then transferred to the grounded electrode ring; the magnitude of the charge and the ring position were determined by the electrical mobility of the particles, a function of a particle's charge and size. The aerodynamic drag of a particle can be related to the particle diameter (assuming a spherical form), which will thus will affect particle velocity on entering the classifier. Therefore, it can be seen that the angle of deflection towards the grounded electrode rings will be determined by particle velocity and the

magnitude of the particle charge creating attraction between the particle and grounded electrode rings. The PC instrument interface would then translate the charge and ring data into particle number and size data which was displayed graphically in real time and also logged.
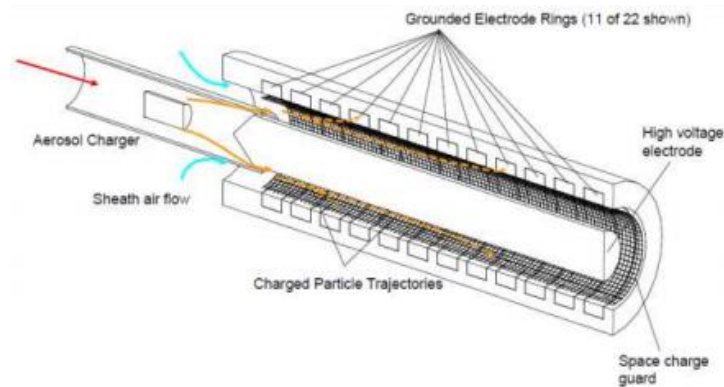
Figure 4.18 DMS500 classifier column, Cambustion (2010)

4.12. Laboratory layout

An overhead view of the laboratory is shown in Figure 4.19, which provides an overview of the approximate distances between analysers, testing equipment and the data acquisition equipment. The previously mentioned gas analysers were situated in the service corridor and the DMS500 was located in the engine test cell.
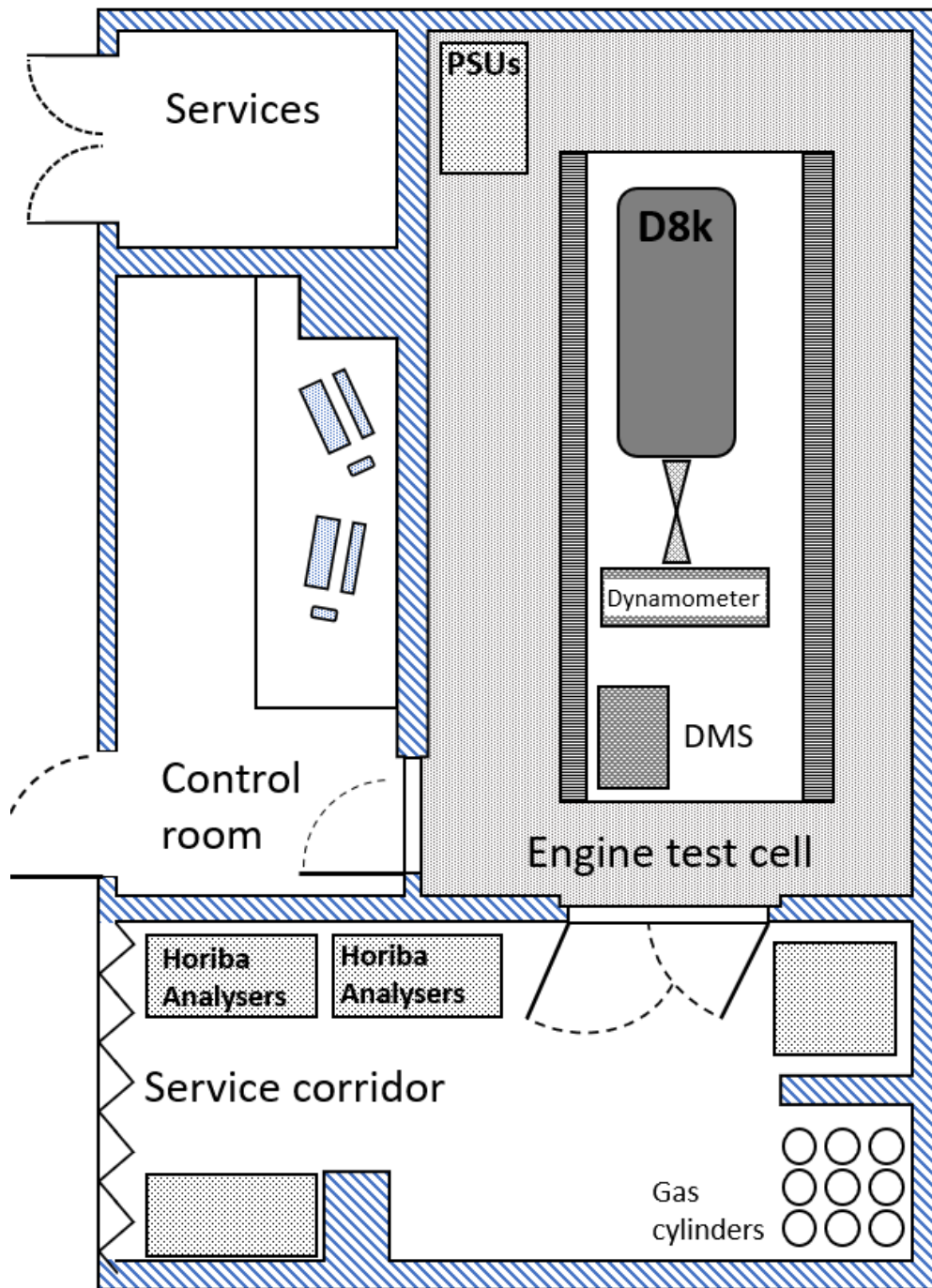
Figure 4.19 Overhead view of laboratory, office/ control room and service corridor

4.13. Experimental operation

This section gives a brief description of how a set of experiments was performed on any given day. Greater detail for any system described is given in the subsequent sections of this chapter.

The D8k coolant circuit was set to preheat for approximately two hours until the engine coolant reached a temperature of $72^{O}C$ and the coolant valve control signal was being received.

Whilst the engine was warming, the Horiba Mexa 9100 analyser and DMS particulate spectrometers were both turned on, warmed up and calibrated. The low volume fuel system was cleaned from any previous tests and o-rings were replaced. When the D8k had reached satisfactory temperatures, the facility control systems were turned on and the engine was run for 5-10 minutes off the common rail diesel supply to warm up the engine lubricating oil. Once satisfactory temperature readings were observed from the engine testing facility and coolant circuit, the tests commenced.

The low volume fuel system was filled with the reference fossil diesel to provide a control reference for the fuel tests. The D8k was run for 10-12 minutes on the fossil diesel whilst data from the; in-cylinder pressure transducer, facility thermocouples, DMS spectrometer and Horiba emissions analysers were logged using a custom LabView data acquisition (DAQ) environment.

At the end of the test, the fuel system was cleaned out and the process outlined in the previous paragraph was repeated for several test fuels. At the end of the day, the engine was operated a second time on the reference fossil diesel, such that any changes in engine performance during the day could be quantified.

For all the results shown in this work, the test fuel was only injected into cylinder one, defined as the cylinder opposite the flywheel and contains the in-cylinder pressure transducer. The injector in cylinder one was opened for a duration of 6.5 CAD and cylinders two to six were opened for a duration of 2.5 CAD to maintain smooth engine turnover. The injector in cylinder one was opened 5.3 CAD BTDC – chosen as this is the ignition delay of the reference fossil diesel.

The brake was kept in speed control mode and held the D8k at 800 ± 20 RPM during the tests. The brake and AVL did not have capability to cooperate for a 'constant load' condition, whereby the injection duration would vary each combustion cycle and keep the IMEP consistent across test fuels. This operating condition would remove some of the variability in IMEP caused by lower calorific values or higher viscosities which would lead to lower injection volumes of the test fuels relative to the reference fossil diesel. Therefore, given this constraint, all the tests were run with a constant injection duration and injection timing unless otherwise noted.

Considering the physical properties of the fuels tested within this work span a wide range of viscosity and density, it should be noted that the conditions employed limit the comparisons which can be made between test fuels. Where the viscosity is higher, it can be assumed that a lower volume of test fuel enters the chamber each injection relative to the reference diesel. Similarly, for fuels with a higher density but comparable density to the reference diesel it can be assumed that more fuel will enter the chamber during injection. Differences in the mass of fuel delivered will result in different amounts of chemical energy being available during combustion, which will directly result in different IMEPs and in-cylinder temperatures.

The custom LabVIEW control code compiled the combustion cycle readings every 100 cycles and from the testing conditions employed, between 10 to 14 of these compiled files were generated for each test fuel. Typically, the first, second and final two files were not representable of stable engine conditions as the ignition duration for the 100 results in these files had a high coefficient of variance. From the remaining seven or eight result files, a representable '100 cycles' selected to represent the test fuel according to consistent temperature readings in the test facility and low coefficients of variance, showing the 100 combustion cycles resulted in reproducible readings. For a single test run with any fuel, one such file is chosen and every measured property is taken as the average of these 100 combustion cycles. These averages are used to represent the test fuel in all further data analysis, unless a repeat run of the test fuel was performed, in which case an average of the single averages taken from both test runs is used, with data bars included. As the reference diesel was tested at the start and end of each day, the error bars on the 'Ref. Diesel' data points are generated from the average of a single file from every diesel experimental run performed on the same days as the chapter focus. For example, the lactone tests discussed in Chapter 6 were performed over three days, so the 'Ref. Diesel' IMEP data point presented on Figure 6.7 is the average IMEP of six sets of 100 combustion cycles, taken from the start and end diesel over three days.

5. The impact of ester chain length and alcohol moiety in Michael Acceptor fatty acid esters on ignition delay, pressure, heat release and emissions.

The development of renewable future fuels presents an opportunity to incorporate molecular structural functionality to improve ignition quality and the efficiency of energy release during combustion. One such functional group is the Michael Acceptor which has not yet been widely discussed or investigated as a means of improving fuel performance.

The leading idea for how a typical hydrocarbon undergoes 'combustion' is via the reactions outlined in Equation 2-1 Equation 2-7 (Section 2.1.5). The first of these reactions is hydrogen abstraction from the fuel molecule by either OH or HO_2 radicals or by O_2 molecules. The Michael Acceptor as a functional group has not yet been considered in the process of combustion, but the functional group may have significance to the process as an addition reaction with OH radicals may outpace the traditional hydrogen abstraction, offering an alternative pathway for low temperature reaction kinetics to proceed.

The Michael addition reaction is the nucleophilic addition of a carbanion (or other nucleophile) to an α,β-unsaturated carbonyl compound which was first classed by Arthur Michael in 1897.[143] These two different regents are commonly referred to as a Michael donor (nucleophile) and Michael acceptor (unsaturated carbonyl). Figure 5.1 shows a textbook example of the reaction. The Michael Acceptor is a specific functional structure, but the Michael donor can be any negatively charged species and does not require a specific structural motif.[144]
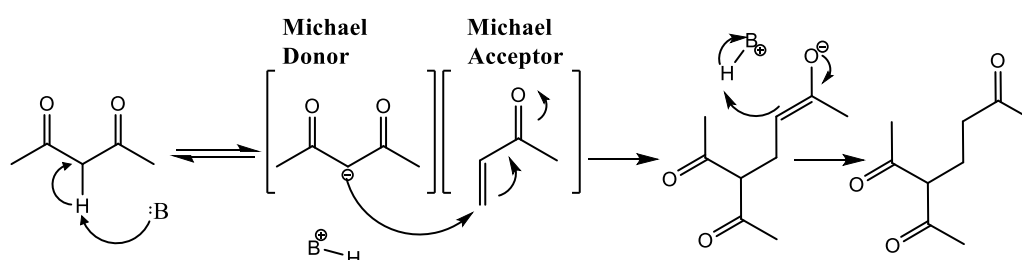
Figure 5.1: The Michael Addition reaction, a conjugated addition onto an α, β-unsaturated ketone[145]

Atkinson et al. (1983) investigated the reaction rates of hydroxyl radicals with 1,4 α β-unsaturated carbonyl compounds (which can all act as Michael acceptors) and cyclohexane as a comparative molecule.[146] When these compounds react with OH radicals, they can either undergo hydrogen abstraction of any hydrogen present in the molecule forming water and a carbon centred radical or it can undergo 1,4 addition to the molecule, similar, to a Michael donor as shown in Figure 5.2.[147]
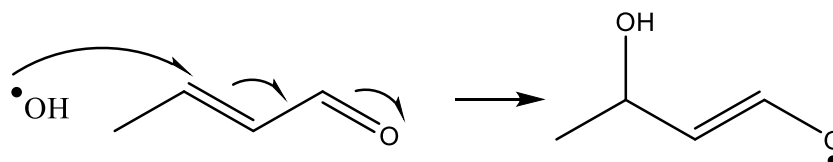
Figure 5.2: 1,4 addition of a hydroxyl radical to crotonaldehyde.

Hydrogen abstraction forming water and a carbon centred radical is the only reaction available when a hydroxyl radical encounters cyclohexane, as this is a fully saturated cyclo-alkane. Atkinson et al.'s investigation showed that the addition reaction to the alkene portion at the 4' position as is typical of a Michael addition reaction had ~ 2 to 10 times higher reaction rate constant than hydrogen abstraction of cyclohexane. In the cases of reaction with the 1,4 α β-unsaturated ketones it is stated with certainty that the reaction proceeds with the addition reaction, but in the case of aldehydes hydrogen abstraction from the aldehyde carbon can also proceed, with the ratio of these two reactions competing not quantified.[147]

The 1, 4 α β-unsaturated carbonyl could be produced by engineering the fatty acid biosynthesis pathway in microbes.[148,149] This pathway is controlled enzymatically and can potentially be modified such that triglycerides or fatty acids containing contain the Michael acceptor functional group can be isolated and then converted into suitable biofuels.[150]

Kinetic model and shock tube experiments have often focused on esters to as these are the most common biofuel sold. Early studies often included as methyl crotonate as a simple surrogate for the unsaturated esters found in biodiesel. By coincidence of choosing methyl crotonate (methyl but-2-enoate), these studies compared saturated esters to α-β unsaturated esters, but without recognition of the unique reactivity available to the latter as Michael Acceptors.[151] These models improved upon previous schemes with the

underlying assumptions extrapolated from simple ideal hydrocarbon models, and as further experimental data became available these models were updated to reflect new results. Recognising the rising importance of biofuels in research and the lack of oxygenated fuel combustion models, Fisher et al. (2000) presented an early model of methyl butanoate and methyl formate combustion, based on existing hydrocarbon models. They compared their model against available experimental data, which set the groundwork for further computational kinetic studies, supported by gas phase kinetic studies in jet stirred reactors and ignition studies in shock tubes.[151–156]

Sarathy et al. (2007) studied methyl butanoate (MB) and methyl but-2-enoate (M2B, is a Michael Acceptor) in flame burners and jet stirred reactors, and developed a model without consideration of radical addition to the Michael Acceptor.[151] Gail et al. (2008) updated the models for MB and M2B to include several additional reaction pathways. Commenting on several potential addition reactions between the M2B and H, OH and HO_2 radicals, the authors noted that these were not dominant pathways for fuel consumption, but, were amongst the most significant pathways to be considered.[153]

Kinetic models continued to be updated frequently and depending on the conditions employed by the authors, the radical addition to α β-unsaturated carbonyls would either be considered a dominant pathway or alternatively unimportant in ester decomposition. This changed when Johnson et al. (2021) and Chong et al (2022) reviewed these models and focused on including several potential reaction routes which were previously not considered, specifically updating the models to better reflect the radical additions which are available to alkenes.[157,158] Johnson et al.'s main finding was that their new methyl but-2-enoate model came significantly closer to matching experimental observations than the earlier work of Sarathy and Gail, which was attributable to the new reactions included. Johnson et al.'s updated model found H or O addition products to M2B to account for 31% of initial fuel consumption during combustion. Chong et al. comparing two structural isomers methyl acrylate (Michael Acceptor) and vinyl acetate (not a Michael Acceptor) in a shock tube found that methyl acrylate exhibited a shorter duration of ignition delay than vinyl acetate and was significantly more active at lower temperatures prior to autoignition. The authors attributed this higher reactivity to hydrogen addition

reactions on the double bond (as a Michael Acceptor addition reaction) being the major consumer of fuel.[157,158]

The literature discussed so far on Michael Acceptor combustion has focused on experiments in shock tubes, jet stirred reactors and burners which were used to validate kinetic data. These cannot fully replicate the real environment of a combustion chamber in an engine, and to date only one previous work could be found where a Michael Acceptor was tested in an actual engine. Zhang et al. (2009) investigated how premixed ignition reactivity changes with double bond position in C9 unsaturated esters, which did include a Michael Acceptor ester structure but this unique structure was not noted by authors.[159] Their work included a comparative set of a saturated ester, an alpha-beta unsaturated ester, (Michael acceptor), and a beta-gamma unsaturated ester which was unable to undergo the Michael reaction. Their experiments were performed in a cooperative fuel research engine using a gasoline direct injector in the air intake manifold to provide a homogeneous mixture to the combustion cylinder. The fuels were tested at variable compression ratios, starting at CR 4.43 and increasing until significant high temperature heat release was observed. The main finding from this study was that methyl nonanoate exhibited significantly higher reactivity in the low temperature region than both methyl nonenoate isomers and that the C2 unsaturated isomer was more reactive than the C3 isomer. Methyl nonanoate exceeded a threshold of 80% of the maximum possible fuel carbon conversion to CO_2 at a compression ratio of 7:1, whilst methyl non-2-enoate (Michael Acceptor) reached this CO_2 value at a CR of 8.5:1 and finally methyl non-3-enoate reached this CO_2 value at CR 9.5:1.[159] The authors concluded that regardless of any additional reaction pathways available, the addition of a C to C double bond in methyl nonanoate reduced its reactivity. However, it is clear that methyl non-2-enoate exhibited appreciably improved combustion relative to methyl non-3-enoate, which the authors attributed to the double bond at the C3 position reducing the number of 5 and 6 membered rings which can be formed in the low-temperature branching reactions.

The current chapter presents the results of engine experiments in which three series of fatty acid ester molecules were tested. The series were chosen to each include a molecule which contained a Michael Acceptor functional group

and could be compared to similar molecules which did not contain this group. Relative to previous studies of Michael Acceptors, this is the first to utilise a modern direct injection heavy-duty compression ignition engine with significantly higher compression ratios than previous tests. The hypothesis proposed here is that the inclusion of a double bond on the alpha and beta carbons adjacent to the carbonyl in an ester group, thereby forming a Michael Acceptor, may reduce the duration of ignition delay in a slow-speed compression ignition engine.

5.1. Experimental outline
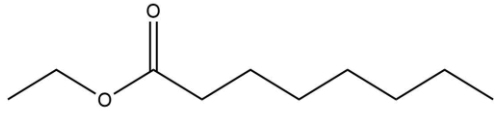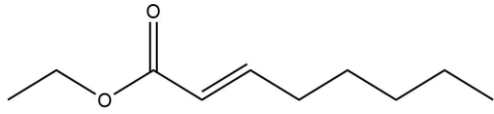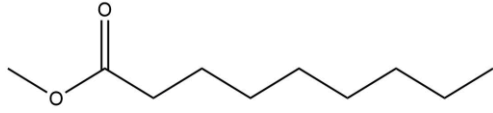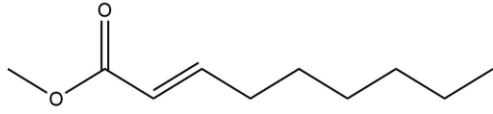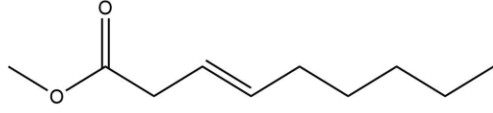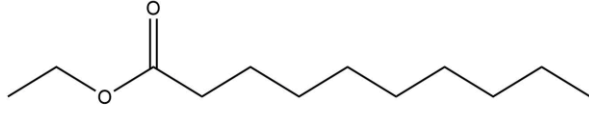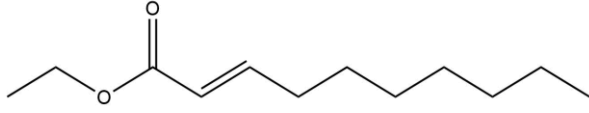
Seven fatty acid esters were tested as pure components to investigate the effect of including the Michael Acceptor structure on compression ignition combustion and emissions. Table 5.1 provides an overview of these single component fuels with a clear indication of their chemical structure and which ones can undergo the Michael reaction. Table 5.2 further shows some chemical and physical properties which can influence air/fuel spray mixing, compression ignition, and combustion. Finally, Table 5.3 introduces the experimental conditions and shows some key values from combustion tests with the test fuels.

5.1.1. Single component test fuels

Three sets of similar molecules were used, two ethyl C8 esters, three methyl C9 esters and two ethyl C10 esters. As shown in Table 5.1, each of these sets contains the Michael Acceptor equivalent molecule of the fatty acid ester (FAE) single component fuel. The methyl C9 set further contains methyl non-3-enoate, which is a structural isomer of the Michael Acceptor fuel, but the change in double bond position prevents it from undergoing the Michael reaction.

These molecules were selected so as to allow observation of the resulting effects from inclusion of the Michael acceptor within FAEs. Differences between the ethyl C8 and C10 fuel sets allowed determination of the effects of fatty acid chain length on Michael Acceptor combustion behaviour. The methyl C9 fuels provided insight on the significance of Michael Acceptor structure compared to similar unsaturated esters. From this set of test fuels, combustion behaviour arising from the alcohol moiety of Michael Acceptors could be observed.

Table 5.1:Overview of the single component ester fuels tested alongside an abbreviation for each fuel, a clear indication of whether or not they are Michael Acceptors and a skeletal depiction of their molecular structure.

Fuel (Nomenclature)	Michael Acceptor?	Chemical structure
Ethyl Octanoate (EtO)	X	
Ethyl Oct-2-enoate (EtO2)	✓	
Methyl Nonanoate (MN)	X	
Methyl Non-2-enoate (MN2)	✓	
Methyl Non-3-enoate (MN3)	X	
Ethyl Decanoate (EtD)	X	
Ethyl Dec-2-enoate (EtD2)	✓	

5.1.2. Apparatus

All of the combustion experiments described in the current chapter were performed using the heavy-duty compression ignition engine and ultra-low volume fuel system research facility described in Chapter 4)

5.1.3. Experimental procedure

Each of the single component FAE fuels and reference diesel were tested under identical conditions discussed in Chapter 4. A summary of these conditions is shown in Table 5.3 alongside some key combustion parameters evaluated from the experimental results. The viscosities and lower heating values for the test fuels outlined and are shown in Table 5.2. The viscosities were measured in a Brookfield III-Ultra Rheometer, set to a revolution speed of 200 and 250 RPM to produce an average viscosity. Each test fuel was measured at temperatures of 25 $^{\circ}$C and 50 $^{\circ}$C. The calorimetry values were taken as the average of three 1 g samples tested in an IKA C1 Calorimeter. This was the same procedure performed for the remaining results chapters.

Table 5.2: Overview of physical and chemical properties which should be considered during fuel tests of the fatty acid esters and the reference diesel. Purity, boiling point and density data provided by the supplier, Merck. *a measured using a Brookfield III-Ultra rheometer. *b measured using an IKA C1 bomb calorimeter. *c technical data for the reference diesel provided by Haltermann Carless.

Fuel (Nomenclature)	Michael Acceptor?	Chemical Formula	Purity (%)	Boiling point (°C)	Density (g/cm³)	Viscosity [a] at 50 °C (Cp)	Gross calorific value [b] (J/g)
Ethyl Octanoate (EtO)	X	$C_{10}H_{20}O_2$	≥98	206-208	0.867	1.225 ± 0.015	35,539.3 ± 136.9
Ethyl Oct-2-enoate (EtO2)	✓	$C_{10}H_{18}O_2$	≥98	222	0.883	1.540 ± 0.030	34,975.3 ± 16.2
Methyl Nonanoate (MN)	X	$C_{10}H_{20}O_2$	≥96	213	0.875	-	
Methyl Non-2-enoate (MN2)	✓	$C_{10}H_{18}O_2$	≥97	215	0.895	1.580 ± 0.020	34,568.7 ± 108.9
Methyl Non-3-enoate (MN3)	X	$C_{10}H_{18}O_2$	≥96	213	0.885	1.425 ± 0.025	34,370.7 ± 169.0
Ethyl Decanoate (ED)	X	$C_{12}H_{24}O_2$	≥98	245	0.865	1.555 ± 0.035	37,230.7 ± 46.0
Ethyl Dec-2-enoate (ED2)	✓	$C_{12}H_{22}O_2$	≥95	251	0.880	1.890 ± 0.030	36,732.0 ± 30.8
Reference Diesel (Ref. D)	X	$C_{12}H_{23}$	-	189.9 – 355.5 [c]	0.832 [c]	2.245 ± 0.035	45,800 [c]

Table 5.3: Experimental test conditions and key experimental results for the single component fuel tests in the D8k engine.

Fuel	Michael Acceptor?	Engine speed (RPM)	Fuel injection pressure (bar)	Injection timing (CAD BTDC)	Injection duration (CAD)	IMEP (Bar)	Ignition delay (CAD)	PHRR (j/deg)	Max average in-cylinder temperature (K)
Ethyl Octanoate (EtO)	X	820 ± 20	695 ± 10	5.3	6.5	5.05	6.4	541.7	1749.7
Ethyl Oct-2-enoate (EtO2)	✓	820 ± 20	695 ± 10	5.3	6.5	5.10	8.8	727.3	1805.3
Methyl Nonanoate (MN)	X	820 ± 20	695 ± 10	5.3	6.5	5.06	6	417.7	1706.4
Methyl Non-2-enoate (MN2)	✓	820 ± 20	695 ± 10	5.3	6.5	5.31	5.9	450.0	1776.8
Methyl Non-3-enoate (MN3)	X	820 ± 20	695 ± 10	5.3	6.5	5.14	8.4	800.6	1826.9
Ethyl Decanoate (EtD)	X	820 ± 20	695 ± 10	5.3	6.5	5.59	5.5	348.2	1774.5
Ethyl Dec-2-enoate (EtD2)	✓	820 ± 20	695 ± 10	5.3	6.5	5.39	7.1	687.9	1790.9
Reference Diesel	X	820 ± 20	695 ± 10	5.3	6.5	7.12 ±0.09	5.2 ±0.09	312.2	1896.5

5.2. Results

5.2.1. Methyl nonanoate esters
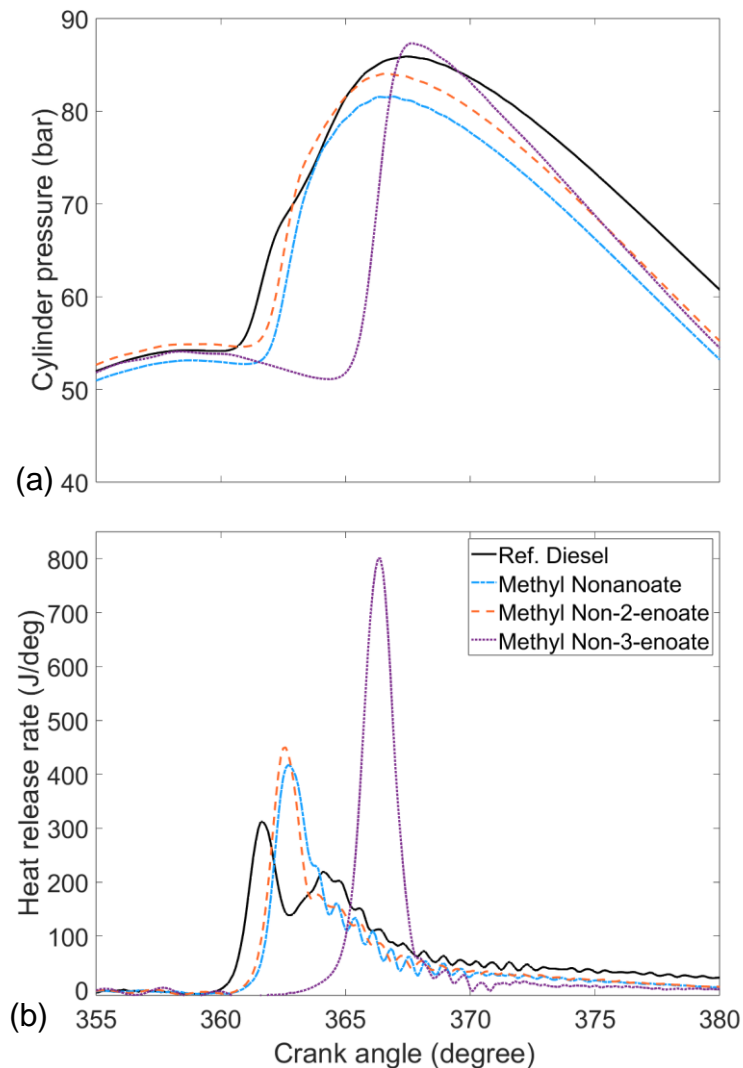
Figure 5.3: (a) In-cylinder pressures and (b) apparent net heat release rates of methyl nonanoate, methyl nonenoate isomers and reference fossil diesel.

Figure 5.3 shows the in-cylinder pressures and apparent net heat release rates of methyl nonanoate (MN), methyl nonenoate isomers (MN2 & MN3) and reference fossil diesel. Immediately apparent is the significantly longer duration of ignition delay and, as a consequence, the fastest rate of pre-mixed combustion exhibited by MN3 relative to the other isomer fuels tested. It can also be seen that all three ester fuels had a larger premixed combustion fraction and smaller diffusion-controlled combustion period compared to the reference diesel.

Also visible from the heat release rates (Figure 5.3) is that MN exhibits a higher amount of diffusion-controlled combustion relative to the unsaturated esters.

Finally, from Figure 5.3 we can observe that moving the double bond from the second to third carbon of the alkyl moiety, from MN2 to MN3, further reduces the extent of diffusion-controlled combustion observed.

5.2.2. Ethyl octanoate esters
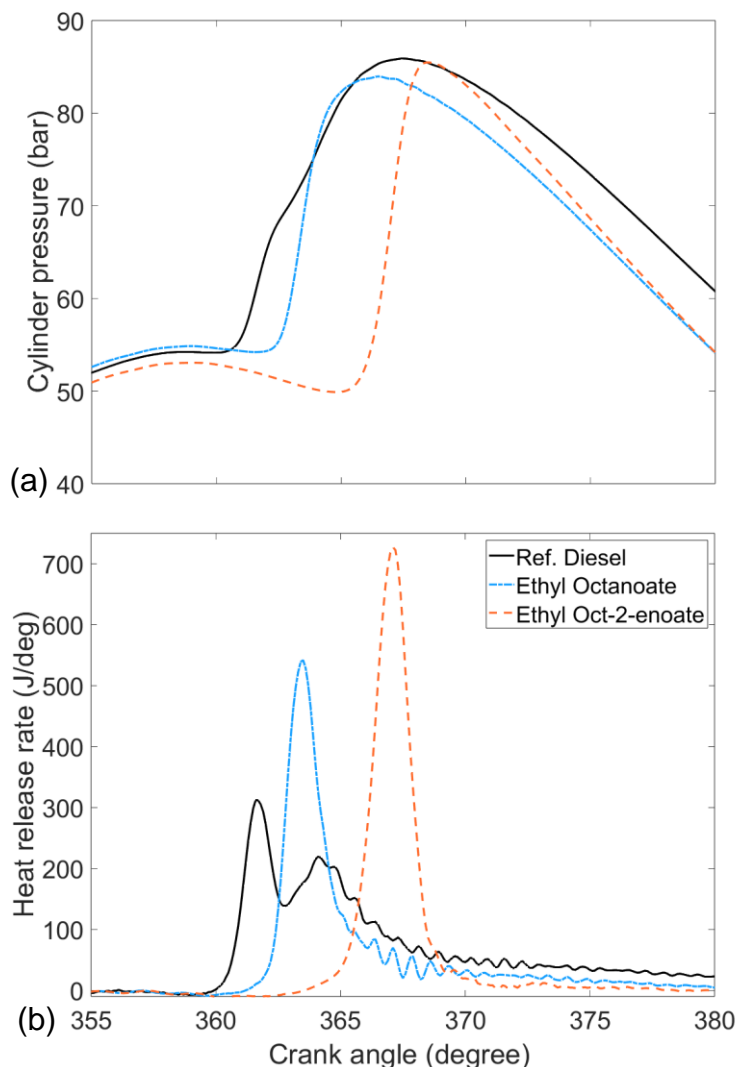
Figure 5.4: (a) In-cylinder pressures and (b) apparent net heat release rates of ethyl octanoate, ethyl octenoate and reference fossil diesel.

Figure 2.2 shows the in-cylinder pressures and apparent net heat release rates of ethyl octanoate (EtO), ethyl oct-2-enoate (EtO2) and reference fossil diesel. Apparent is the larger period of premixed combustion and lower levels of diffusion-controlled combustion exhibited by both esters compared to reference diesel. It can also be seen that in EtO2 inclusion of a double bond at the 2-position led to a longer ignition delay and higher peak heat release rate relative to the fully saturated EtO.

5.2.3. Ethyl decanoate esters
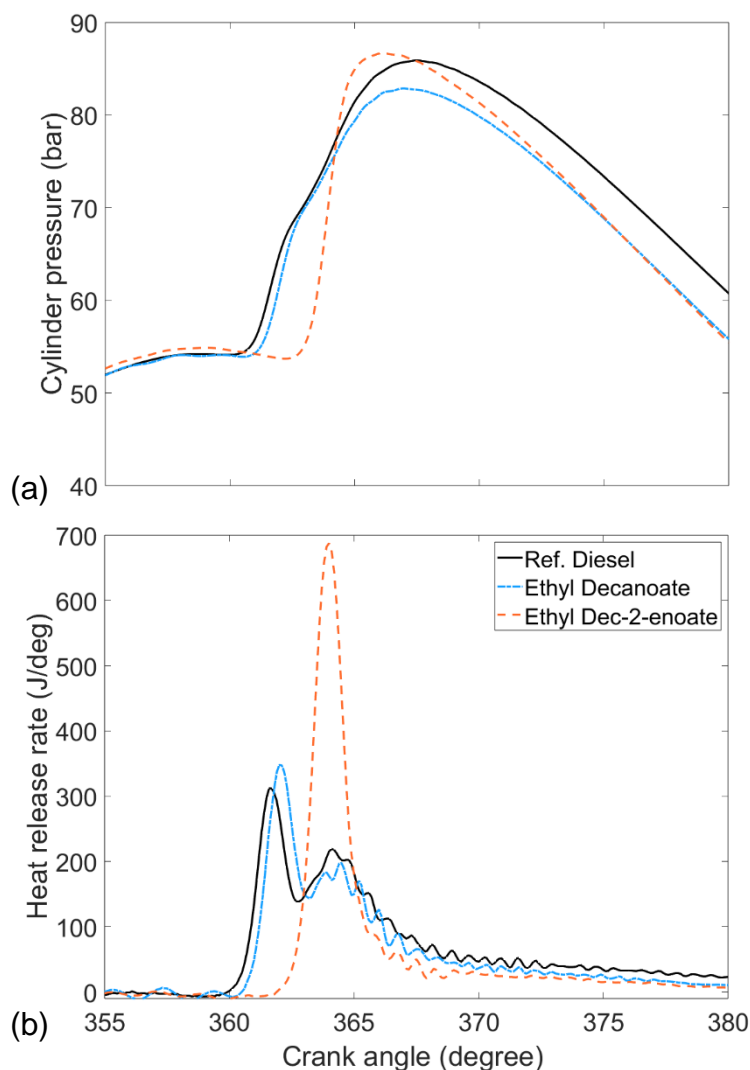
Figure 5.5: (a) In-cylinder pressures and (b) apparent net heat release rates of ethyl decanoate, ethyl decenoate and reference fossil diesel.

Figure 5.5 shows the in-cylinder pressures and apparent net heat release rates of ethyl decanoate (EtD), ethyl dec-2-enoate (EtD2) and reference fossil diesel. Apparent is the majority of heat release occurred during the premixed burn fraction in the case of EtD2. Inclusion of a double bond at the 2-position lead to a longer ignition delay and higher peak heat release rate relative to EtD. However, unlike the shorter saturated esters MN and EtO, EtD exhibits a similar pattern of heat release as exhibited by the reference diesel with a larger diffusion-controlled phase than Figure 5.3 and Figure 5.4. This is attributed to EtD's longer alkyl chain length than MN and EtO, which would lead the shorter ignition delay exhibited by EtD. A shorter ignition delay allows less time for the fuel and air to mix before the start of combustion, further leading to a lower premixed burn faction.

5.2.4. Ignition delay and IMEP
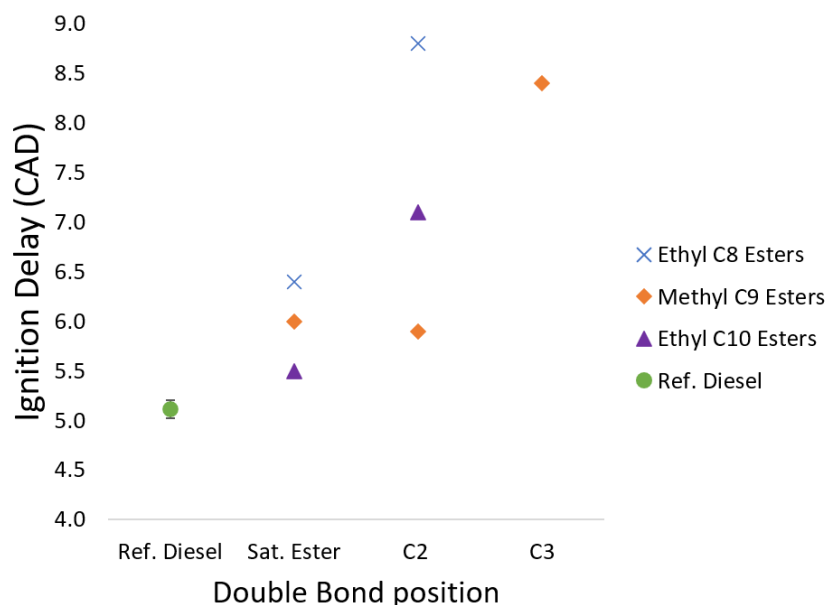
Figure 5.6: Influence of unsaturation and double bond position in the fatty acid esters on ignition delay.

Figure 5.6 shows the impact of the Michael Acceptor chemical structure on the duration of ignition delay in ethyl C8, methyl C9 and ethyl C10 saturated and unsaturated esters. In this figure and all subsequent references, ignition delay is defined as the interval between start of fuel injection signal supplied to the injector control system and the start of combustion as determined from the apparent net heat release rate. Additionally, in this figure and all subsequent figures the error bars are generated from the standard variation of the reference diesel tests at the start and end of each day the fuels described were tested on.

The reference diesel ignited at 360 CAD. Constant injection timing for all fuels was selected, so apparent from Figure 5.6 is that all of the fatty acid ester tested exhibited an ignition delay longer than that of the reference diesel.

Figure 5.6 also shows a general trend of increasing ignition delay where a carbon-to-carbon double bond is included in the ester alkyl moiety. However, while inclusion of the double bond at the 2-position, creating the Michael Acceptor chemical structure, increases ignition delay in both EtO2 and EtD2, MN2 displays a reduction in ignition delay relative to the saturated ester of equivalent chain length. Moving the double bond to the 3-position in MN3 also leads to an increased ignition delay.

The reduced ignition delay trend displayed by the saturated esters as the alkyl moiety chain length increases is expected and in agreement with the literature.[160,161] With inclusion of the double bond at the 2-position, this trend is still observed for the ethyl C8 and C10 ester, but not the methyl C9 ester which unexpectedly exhibits a shorter ignition delay than the C10 ester.

Finally, from Figure 5.6 it is clear the boiling points and viscosities shown in Table 5.2 had little effect on the wide range of ignition delays observed. MN2 and MN3 present with similar values for both physical properties, but the two fuels exhibited ignition delays 2.5 CAD apart. This was larger than the difference in ignition delay of 0.7CAD exhibited between EtO, which has the lowest boiling point and viscosity, and EtD2, which has the highest boiling point and viscosity. It is therefore reasonable to assume that the 40°C difference in boiling point between the two was an insignificant driver in the trends discussed.

Figure 5.7 shows the IMEP of the saturated, unsaturated esters and reference diesel. It can be seen in Figure 5.7 that all of the ester fuels exhibited an IMEP lower than that of the reference diesel, which is to be expected given the constant injection duration and lower calorific value of the oxygenated fuels (Table 5.3).

MN and EtO are structural isomers of each other, both having the chemical formula of $C_{10}H_{20}O_2$. These esters both produced around 5.1 bar IMEP, whilst the larger EtD produced a 10% increase in IMEP, attributed to its higher calorific value (Table 5.3).
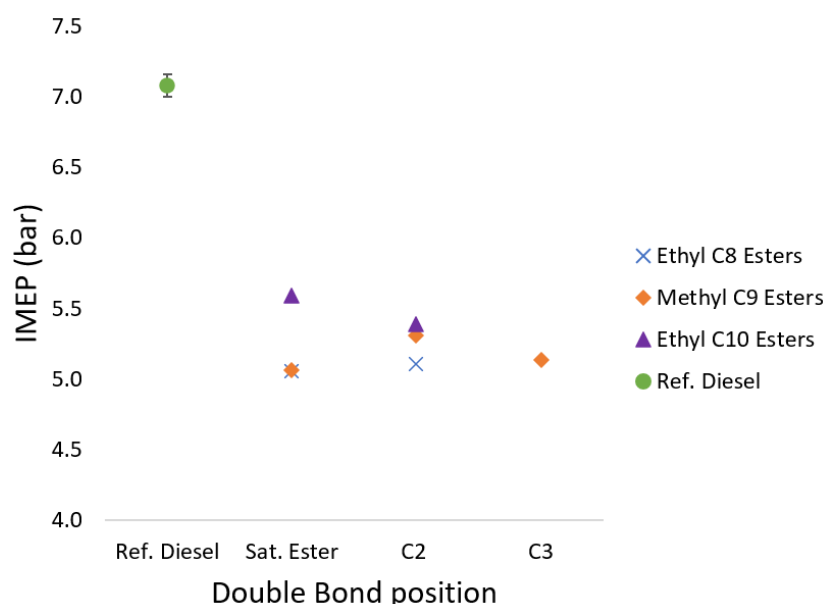
Figure 5.7: Indicated mean effective pressure (IMEP) of esters and reference diesel at constant injection timing and duration.

Figure 5.7 also shows the impact on IMEP of introducing a double to the ester alkyl moiety. Apparent is the slight reduction in IMEP exhibited by EtD2 relative to EtD, likely due to the lower calorific value of the unsaturated ester (Table 5.3). Also apparent is the increase in IMEP displayed by MN2 than MN contrary to the lower calorific value of MN2. Of further note to that, the IMEP produced by MN2 is that it is appreciably higher than that of other esters with the same carbon count; MN, EtO, MN3 and EtO2 all exhibit an IMEP value of 5.10 ±0.05 bar, while an IMEP of 5.31 bar was recorded in the case of MN2.
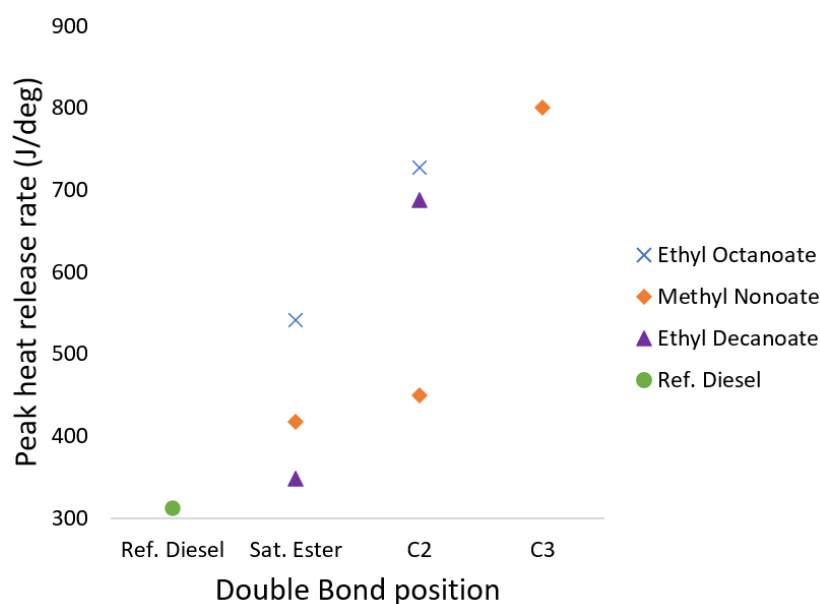
Figure 5.8: Peak apparent heat release rate of ethyl C8 & C10 esters, methyl C9 esters and reference diesel. Error bars are plotted, but are visually insignificant owing to the low variation in reference diesel tests.

133

Figure 5.8 shows the peak apparent heat release rate of the saturated and unsaturated esters tested. The trend also shown by the two ethyl esters remains the same. It would be expected that the ignition delay of the fuels tested would be the dominating feature of their combustion given the similarity of physical properties between the fuels tested (Table 5.3). Ignition delay directly controls the extent of the premixed combustion zone, which we can see with the heat release plots in Figure 5.3 to Figure 5.5, a longer ignition delay led to a larger premixed combustion fraction. The premixed burn phase is defined as the combustion of fuel which has mixed to within the flammability limits during the ignition period.[20] The longer ignition delay observed allows for greater air fuel mixing, increasing the amount of fuel burnt and energy released during this time period.

The direct influence ignition delay has on the energy release during the premixed combustion phase causes the trends observed in PHRR seen to closely align with the trends seen in ignition delay, previously shown in Figure 5.6. The relative trends between the saturated esters and the unsaturated esters remain the same, except for MN2, which compared to MN exhibited a higher peak heat release rate despite a shorter ignition delay.

Finally, as this is the first discussion of PHRR results, the following should be noted for this chapter and further chapters in this work; the significantly higher PHRRs observed from some test fuels relative to the reference diesel represents very high instantaneous pressure release. Combined with their long duration of ignition delay, it is apparent the cetane number of such fuels are low and with such explosive combustion these fuels would not be utilised in practise. Hot spots would form from instantaneous combustion in the cylinder, exacerbating NOx formation which would be difficult to control.[162]
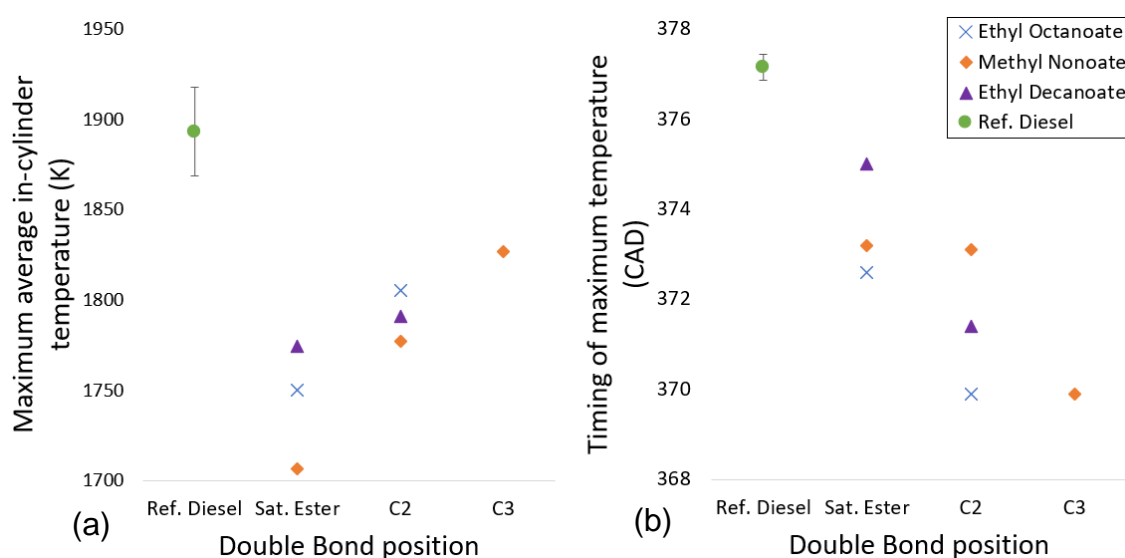
Figure 5.9: Maximum average cylinder temperature (a) and timing of maximum temperature (b) vs fatty acid ester double bond position.

Figure 5.9a and 2.7b show the calculated maximum in-cylinder global temperature and time at which it occurs respectively for the fatty acid esters tested and reference diesel. The trend apparent in Figure 5.9a and 5.9b is that the reference diesel reaches a significantly higher average temperature, and it reaches this temperature at a later stage in combustion than the fatty acid esters. This can be attributed to the small premixed burn fraction of combustion and larger mixing-controlled phase than the ester test fuels (Figure 5.3 to Figure 5.5). Additionally, the maximum average cylinder temperature increases for the fatty acid esters with the inclusion of the double bond and increases further as this double bond is moved from the 2-position to 3-position in methyl C9 esters. Finally, the timing of the maximum in-cylinder temperature occurs earlier in the fatty acid esters with the inclusion of the double bond and earlier still as the double bond moves from the 2-position to the 3-position in the methyl C9 esters.

These trends observed in the maximum average in-cylinder temperature, as with the heat release rate, are influenced by the ignition delay of the test fuels. Figure 5.9b shows a reverse trend to the ignition delay shown in Figure 5.6 and to the PHRR show in Figure 5.8. A longer ignition delay leads to a higher PHRR, which in turn would be expected to lead to an earlier timing of the maximum average in-cylinder temperature.[32,163]

Two exceptions to trends within the fatty acid esters should be noted; the first is that the inclusion of the double bond at the 2-position reverses the relative order

135

of the esters. Whilst saturated, EtD exhibits the highest maximum average in-cylinder temperature and unsaturated at the 2-position EtO2 now exhibits a higher temperature than EtD2. The second notable exception is that the methyl esters do not follow the trend of an earlier maximum average in-cylinder temperature with the unsaturated ester at the 2-position, instead MN and MN2 reach their maximum average in-cylinder temperature at almost the same time (± 0.1 CAD). Further details on these observations will be discussed in Section 5.3.
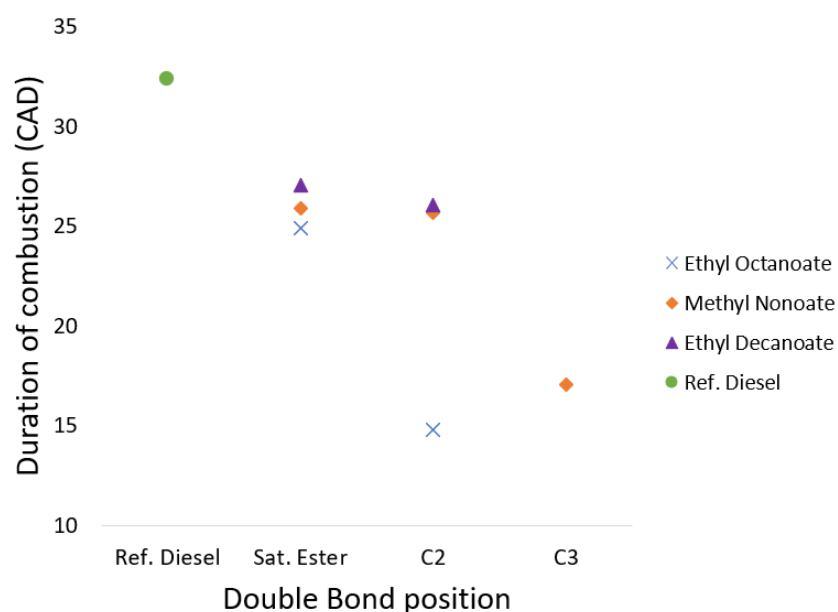
Figure 5.10: Calculated duration of combustion of the saturated esters, unsaturated esters and the reference diesel. Error bars are plotted, but are visually insignificant owing to the low variation in reference diesel tests.

Figure 5.10 shows the duration of combustion exhibited by the ethyl C8, ethyl C10, methyl C9 esters and the reference diesel. The initial trend to note is that inclusion of a double bond at the 2-position shortened the duration of combustion in all the esters. This reduction is largest in EtO2, whilst MN2 and EtD2 remain close to their saturated counterparts. Moving the double bond to the 3-position further leads to a significantly reduced duration of combustion in MN3. It can further be seen that the three saturated esters exhibit a similar duration of combustion and finally it can be seen that all the ester test fuels exhibit a shorter duration of combustion than the reference diesel.

Previously shown in Figure 5.6 was MN3 and EtO2s' long ignition delay, both autoigniting 2.4 CAD after their respective saturated esters. A long duration of ignition delay allows for more of the air and fuel to be well mixed prior to

autoignition. Premixed combustion has a short duration and, therefore, the overall combustion period reduces as the amount of premixed combustion increases.[24,163]

5.2.5. Exhaust emissions
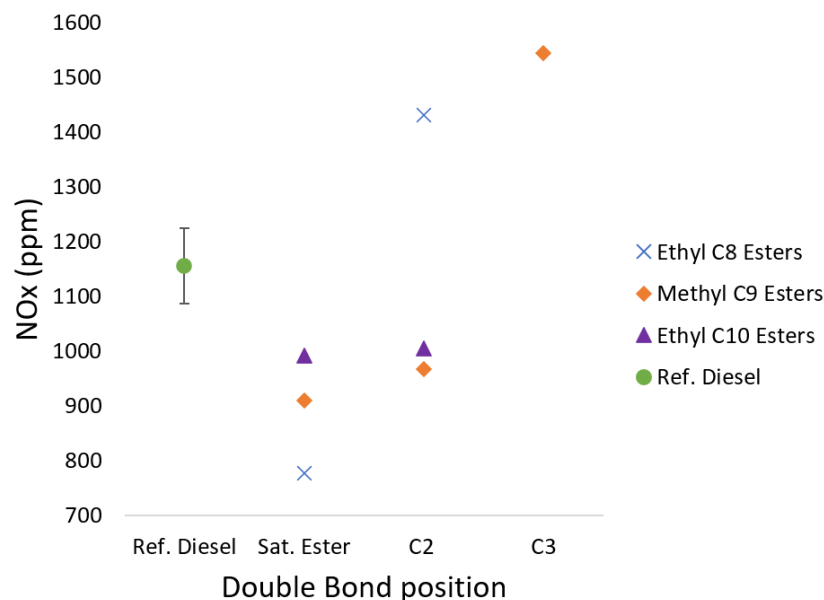
Figure 5.11: Exhaust gas NO$_x$ emissions of ethyl octanoate, ethyl decanoate, methyl nonanoate esters and reference diesel vs double bond position.

Figure 5.11 shows the measured NO$_x$ emissions during combustion of the three groups of fatty acid esters and reference diesel. An apparent observation is that the NO$_x$ emissions of EtO2 and MN3 are far higher than those of the other esters and of the reference diesel. This is an unexpected result, as NO$_x$ emissions would typically correlate with IMEP, however as shown previously by Table 5.3 and Figure 5.7 MN, MN3, EtO and EtO2 all exhibited roughly similar IMEPs, approximately 5.1 ± 0.1. Figure 5.12 shows the calculated in-cylinder temperature curves for the investigated fuels, in which EtO2 and MN3 exhibit the sharpest gradient relative to the remaining test fuels. NOx production requires temperatures higher than 1600 K, and as shown in Figure 5.12 all the fuels investigated surpass this threshold.[89]
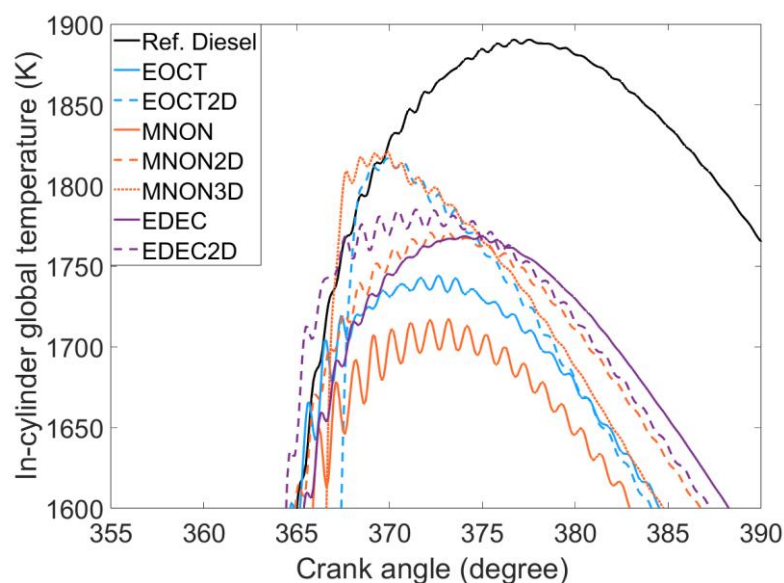
Figure 5.12: Calculated in-cylinder global temperature for the fatty acid esters and reference diesel.

NOx production relies on the residence time and stoichiometry of the hot gaseous products of combustion. As discussed in Section 2.3.1, NOx production is highly time dependent and the thermochemical kinetics will 'freeze' during the expansion stroke when the in-cylinder temperature and pressure decrease.

The reference diesel's longer duration of combustion (Figure 5.10), large mixing-controlled burn phase (Figure 5.3 to Figure 5.5) and higher in-cylinder temperatures (Figure 5.12) relative to remaining test fuels account for the higher measured NOx value of the reference diesel over all the ester fuels except EtO2 and MN3.[14,89]

EtO2 and MN3's significantly higher NO_x emissions from combustion can instead be attributed to these two esters exhibiting the longest durations of ignition delay (Figure 5.6) which allowed for greater air fuel mixing prior to autoignition. With most of the fuel well-mixed prior to autoignition, the premixed burn phase dominated the combustion process and led to a shorter duration of combustion relative to the other test fuels (Figure 5.10). Reaching a higher maximum in-cylinder temperature and completing combustion faster than the ester fuels allows more time for the hot gaseous combustion products to remain at high pressure prior to freezing of NOx kinetics.[164]
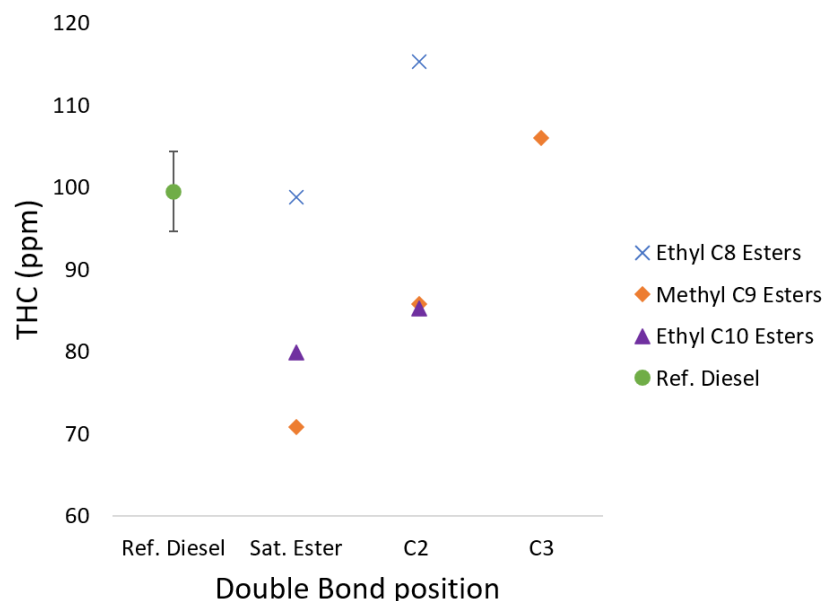
Figure 5.13: Exhaust gas unburnt hydrocarbon emissions of ethyl octanoate, ethyl decanoate, methyl nonanoate esters and reference diesel vs double bond position.

Figure 5.13 shows the unburnt hydrocarbon emissions of the fatty acid esters and reference diesel. The apparent observation is the high THC value of EtO2 and MN3, which is attributable to their long ignition delay and large premixed burn phase. A long ignition delay allows for greater air fuel mixing, over-diluting the fuel spray fringe, and creating areas in the chamber which are too lean to auto-ignite or support a self-propagating flame, increasing the amount of unreacted and partially-reacted fuel.[93]

Also apparent is the effect of including a double bond in the alkyl chain. In the ethyl C8, ethyl C10 and methyl C9 esters the inclusion of a double bond led to an increase in THC. This is to be expected, as fuels with increased olefinic content increase the duration of ignition delay which increases the amount of unreacted fuel.[32,165]
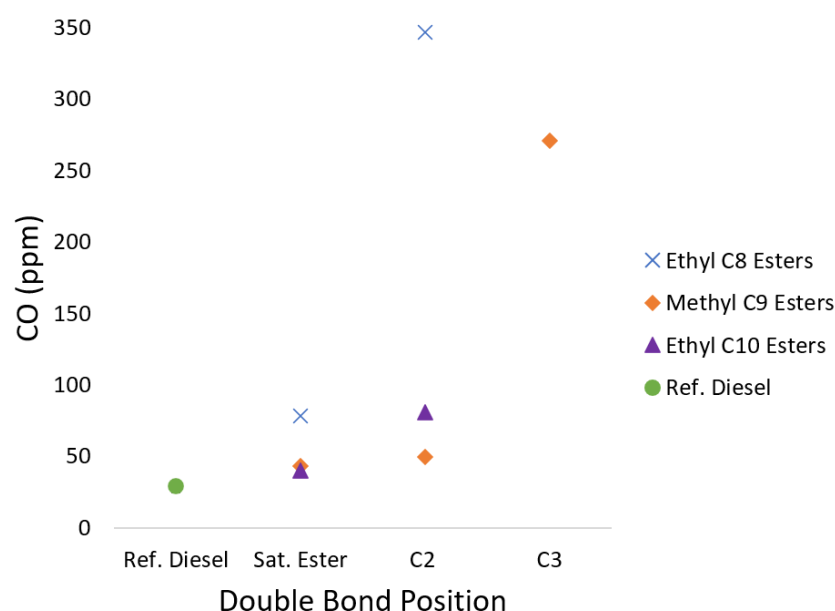
Figure 5.14: Exhaust gas CO emissions of ethyl octanoate, ethyl decanoate, methyl nonanoate esters and reference diesel vs double bond position. Error bars are plotted, but are visually insignificant owing to the low variation in reference diesel tests.

Figure 5.14 shows the CO emissions of the fatty acid esters and reference diesel. Apparent is the detected CO from the reference diesel are lower than the test fuels. High CO in diesel engines if often an indication of either rich pockets of fuel air mixture which only partially burned, or lean (overdiluted) pockets which have combusted at lower temperatures and only partially oxidised to CO.[92] The engine has been designed and optimised to run on fossil diesel, so the oxygen-bearing molecules, with their physical properties being quite different to those of fossil diesel fuel are expected to have suboptimal air fuel mixing characteristics. The calorific value of diesel is substantially greater (~28% greater) than any of the single component esters, so more energy was released per cycle and the combustion chamber run considerably hotter, aiding rapid fuel evaporation and mixing in comparison to the oxygen-bearing molecules.

Also apparent is the significantly higher emissions of EtO2 and MN3, both of which also exhibited increased unburnt hydrocarbon emissions. As discussed previously, the long ignition delay leading to areas of air fuel mixture which are too lean to support a self-propagating flame. CO is a product of incomplete combustion, so it would be expected that fuels with a high THC would likewise exhibit high CO emissions. As with THC emissions, the inclusion of a double bond in the ethyl C8, ethyl C10 and methyl C9 esters led to increased CO emissions.

140
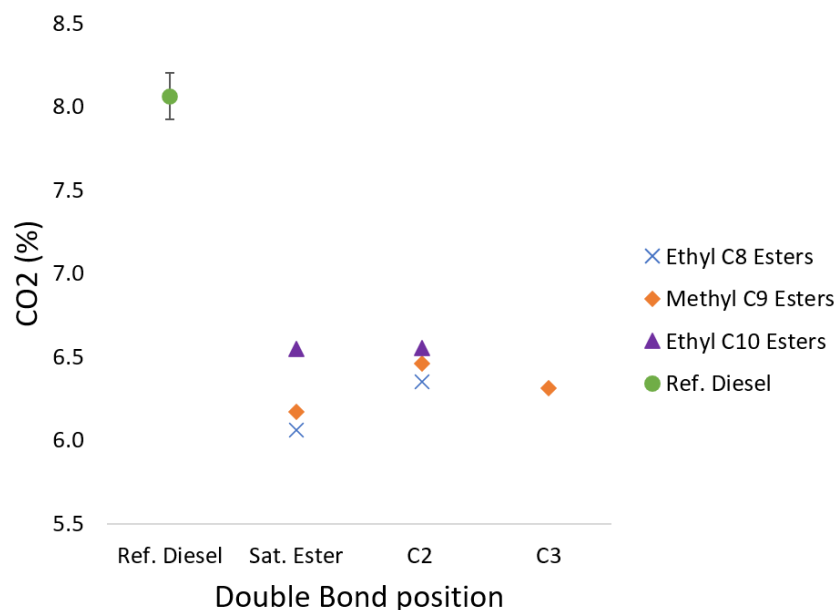
Figure 5.15: Exhaust gas CO_2 emissions of ethyl octanoate, ethyl decanoate, methyl nonanoate esters and reference diesel vs double bond position.

Figure 5.15 shows the CO_2 emissions of the ethyl octanoate, ethyl decanoate, methyl nonanoate esters and reference diesel. Apparent is the lower CO_2 produced from the esters investigated than the reference diesel. All of the test fuels were injected for the same duration (Table 5.3), so the lower CO_2 detected from the test fuels can be attributed to the lower carbon content by mass resulting from the esters' oxygen content. By molecular weight, the reference fossil diesel has a carbon content of 86.7%, whilst the esters are close to 70%, with EtO and MN being 69.7% and EtD2 being 72.7%. The esters therefore contain 16-20% less carbon by mass, which closely aligns with the observation of the esters emitting 18-24% less CO_2. This effect of decreased carbon content is likely to be the most significant driver of the difference in CO_2 content. It is therefore correct to assume that the observed difference in CO_2 emissions between the test fuels and reference diesel would be far less pronounced if the experimental conditions were adapted for a constant IMEP, as this would increase the total mass of fuel injected for lower calorific fuels such as the esters.

5.3. Impact of the Michael Acceptor group on combustion

It is clear from the results discussed in sections 2.1 to 2.3 that MN2, a Michael Acceptor molecule, exhibits similar combustion phasing (Figure 5.3) and levels of exhaust emissions profiles (Figure 5.11 to Figure 5.15) as its saturated analogue, MN. It has a slightly reduced ignition delay (Figure 5.6), which correlates with the expectation of radical addition to the double bond outpacing H-abstraction. To further investigate the unique potential of the Michael Acceptor functional group within target fuel molecules, a structural isomer of MN2 was also investigated, MN3, which is unable to undergo Michael addition. As a single component fuel MN3 exhibits a significantly longer ignition delay than MN2, a lower IMEP, higher NO_x and CO emissions, which are all indicators of poorer performance as a fuel.

Previous work by Zhang et al.[159] investigated the ratio between the low temperature and high temperature heat release for the same methyl C9 esters investigated within this work. The test fuels were tested in a CFR engine, at increasing compression ratios until significant high temperature heat release was observed, starting at a CR of 4.43 up to a CR of 9.5. They found that MN was far more reactive than MN2 in the low temperature region. In the work presented here, MN and MN2 are observed to exhibit similar heat release rates (Figure 5.3) and MN2 exhibits a shorter ignition delay than MN (Figure 5.6) indicating higher reactivity. These results observed in the D8k can be attributed to the significantly different experimental set up and higher compression ratio of 17.5, which is more applicable to current engine designs.

Also clear from the engine tests is that the ethyl C8 and C10 ester test fuels do not follow the same trend with structure as seen in the methyl C9 esters. In both cases the Michael Acceptor molecules, EtO2 and EtD2 do not exhibit the clear similarities relative to the equivalent structural esters as shown between MN and MN2. Of particular note is that EtO and MN are structural isomers, as are EtO2 and MN2, therefore differences observed in combustion characteristics must result from the structural isomerism. This difference in reactivity can be attributed to a unimolecular decomposition reaction unique to fatty acid esters with alcohol moieties longer than one carbon. Shown in Figure 5.16, this

reaction has a low activation energy. Studies by Li et al.[166] and Bennadji et al.[154] have shown that during the combustion of fatty acid ethyl esters, 98 % of fuel molecule decomposition is initiated by this initial reaction.
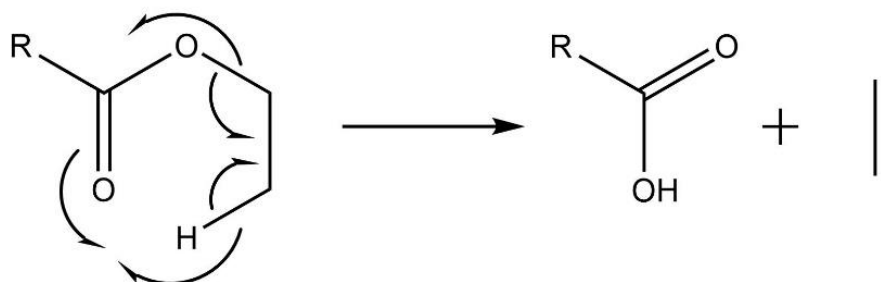
Figure 5.16: Ethyl ester undergoing unimolecular decomposition forming a free fatty acid and ethylene

In the case of the unsaturated ethyl esters, it can still be expected that they will undergo unimolecular decomposition before any potential Michael addition can occur, as intramolecular reactions generally occurs faster intermolecular reactions. Following unimolecular decomposition, the remaining molecule is an unsaturated carboxylic acid. The carboxylic acid group is significantly less electron withdrawing than an ester group and reduces the reactivity of the unsaturated carbonyl, making the Michael reaction unlikely to occur.[167]

Further to the lower Michael Acceptor reactivity, Namysl et al.[168] have shown that H-abstraction in carboxylic acids preferably proceeds at the C2 position, which in an alpha beta unsaturated carboxylic acid are the unsaturated hydrogens which have a higher bond dissociation enthalpy than saturated positions. As an unsaturated carboxylic acid, oct-2-enoic acid would now be expected to exhibit poor combustion. A final point of note, Yanowitz et al.'s[124] compendium of experimental cetane numbers demonstrates that moving from a fatty acid ester to either the fatty acid or unsaturated fatty acid ester both lead to a reduction in cetane number.

As with EtO2, the breakdown of EtD2 will initiate via the unimolecular decomposition reaction. In the observed rates of heat release and exhaust emissions EtD2 compared to EtD exhibits poorer performance, with a longer ignition delay, higher PHRR, higher CO and exhibits a lower IMEP than its saturated counterpart. However, the differences observed between EtD and EtD2 are not as significant as with EtO and EtO2, which can be attributed to the longer carbon chain in the fatty acid moiety of the fatty acid ester. Following

unimolecular decomposition EtD2 produces dec-2-enoic acid which allows an increased number of six- or seven- member transition state rings to form relative to oct-2-enoic acid. As discussed in Chapter 2, these transition state rings are a key feature of the low temperature reactions leading to autoignition and their ability to form directly correlates with fuel performance. Increasing alkyl chain length is known to reduce ignition delay and improve a molecules cetane number, so it is expected that the unsaturated carboxylic acid with a longer alkyl chain would ignite better despite the poor reactivity of carboxylic acids.[124,169]

5.4. Conclusions

This chapter has discussed engine tests designed to investigate the potential differences in combustion caused by α-β unsaturated carbonyls (Michael Acceptors) as their chemical structure provides a unique reaction pathway with radicals, which could shorten the ignition delay of the ester.

- In methyl nonanoate inclusion of an alpha beta unsaturated carbon bond, described as a Michael Acceptor in synthetic chemistry research, to form methyl non-2-enoate leads to a reduced ignition delay and higher IMEP relative to methyl nonanoate. This agrees with the proposed hypothesis that structures which facilitate radical addition to fuel molecules could reduce ignition delay.

- The observed impact of Michael Acceptors in a practical engine is contradictory to a previous study on unsaturated methyl nonoate esters which found methyl non-2-enoate in shock tube and cooperative fuel research (CFR) engine studies. The study found methyl non-2-enoate to exhibit lower reactivity and a longer ignition time than methyl nonanoate. This contradiction is believed to be due to differences in the experimental facilities of this study and those for the previous study, the most impactful being the use of a heavy-duty diesel engine direct injection with a high compression ratio in this work vs a premixed injection and low compression ratio engine in the previous study.

- Movement of the double bond to form methyl non-3-enote from methyl non-2-enoate leads to a longer ignition delay, lower IMEP and an increase in undesirable NO_x and CO emissions. This is in agreement with previous studies in which methyl non-3-enoate to exhibit poorer reactivity than methyl nonanoate and methyl non-2-enoate.

- In ethyl octanoate inclusion of an alpha beta unsaturated carbon bond to form ethyl oct-2-enoate leads to a significant increase in ignition delay and emissions of NO_x and CO. Likewise, the inclusion of the alpha beta unsaturated carbon bond in ethyl decanoate to form ethyl dec-2-enoate led to a longer ignition delay and increased pollutant emissions, but to a lesser extent than observed for ethyl octanoate esters.

- The increased ignition delay and poorer performance as a single component fuel of the ethyl ester Michael Acceptors can be attributed to the rapid decomposition of the fuel from an unsaturated ester to a less reactive unsaturated carboxylic acid.

6. The influence of alkyl straight chain length in gamma and delta lactones on combustion and emissions.

Lactones are any class of cyclic organic compound which contain an ester group, found widely from natural sources such as fruit, wood and foodstuffs as key building blocks for hormones, neurotransmitters and enzymes.[170] Gamma-valerolactone has remained a popular subject of research in spark ignition engines as a blended fuel, for its anti-knock properties and the ease from which it can be produced from biomass.[171] As mentioned previously in Chapter 2, larger lactones can be isolated from biomass sources and there is continual research into one-pot synthetic routes, yet these have not yet received attention as single component biofuels. Research into the fuel performance of lactones with long alkyl chains and high molecular weight has been discussed in concept, but publications focused on biofuel production from these lactones has instead focused on catalytic conversion to saturated alkanes prior to testing.[172,173,174]

The current chapter presents the results of engine experiments in which two series of lactone molecules were tested. The gamma and delta lactone rings are significantly more stable than lactones with other ring sizes and both can be isolated or produced from biomass sources.[175] Both lactone series contain an alkyl chain substituent adjacent to the ring bound oxygen in the lactone ester group, which increases in length through the series.
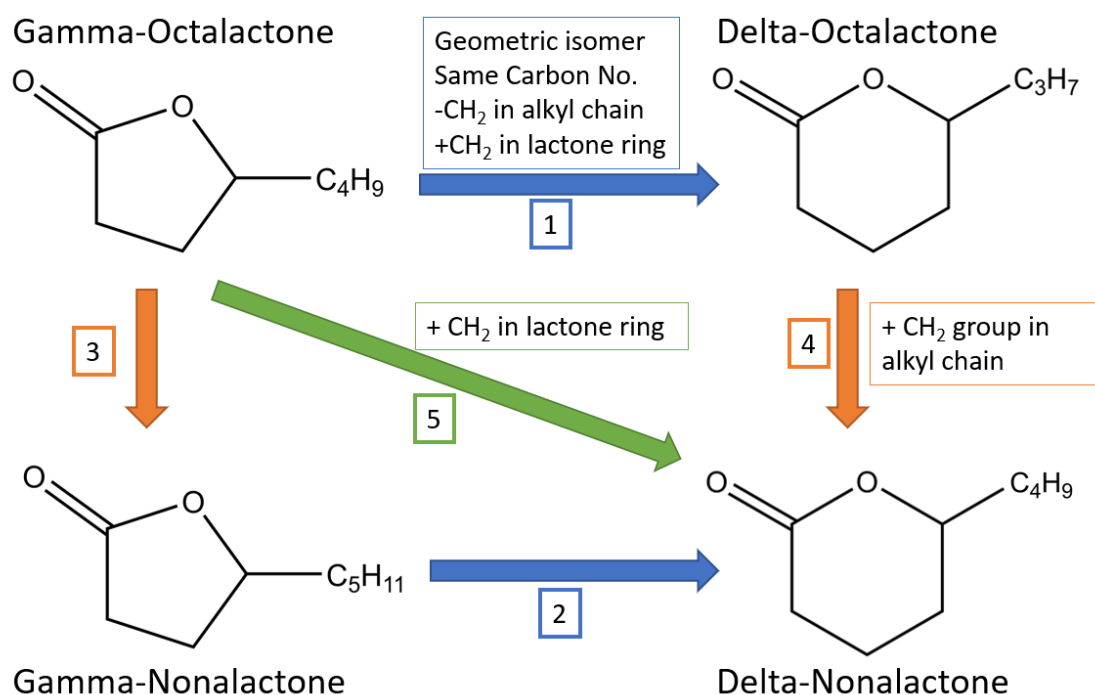
Figure 6.1: The interconnected relationships between gamma and delta lactones with equivalent carbon counts or substituent alkyl chain lengths.

Figure 6.1 shows an example of four lactones which provide a useful introduction to some of the structural differences which will be referenced frequently in this chapter. The two important metrics of comparison between the lactone single component fuels presented here are the lactone ring isomer and the substituent alkyl chain length.

Arrows 1 & 2 represent the structural isomerism between gamma and delta lactones with the same chemical formula and carbon count. It is important to note that by definition, the delta lactone alkyl chain will always be one -CH_2 group shorter than the gamma lactone. Arrows 3 & 4 represent the addition of a -CH_2 group in the substituent alkyl chain, increasing the total carbon count and alkyl chain length. Arrow 5 represents a gamma and delta lactone which both have the same alkyl chain length. These two are not isomers, by definition delta lactone will always have a higher carbon count.

6.1. Experimental outline

Twelve lactones (CAS identifiers in Appendix 12.4) were tested as pure components to investigate the effect of increasing the substituent alkyl chain length for two different ring sizes on compression ignition combustion and emissions. Table 6.1 provides an overview of these single component fuels and

their chemical structure. Table 6.2 further shows some chemical and physical properties of the 12 lactones. Finally, Table 6.3 introduces the experimental conditions and shows some key values from combustion tests with the test fuels.
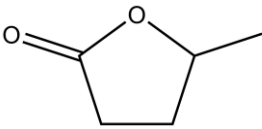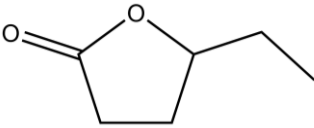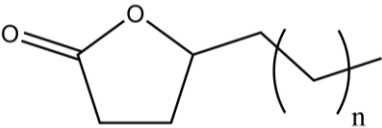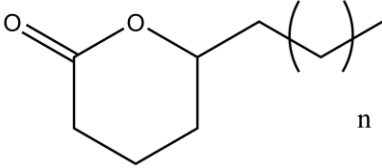
6.1.1. Single component test fuels

Two sets of similar molecules were used, eight gamma lactones with an alkyl chain length increasing from one to eight carbons, and four delta lactones with a chain length increasing from four to seven carbons.

These single component fuel tests allow observation of the resulting effects from increasing the alkyl chain length on these lactones. The different ring size and overlap in alkyl chain length between the two different lactone series allows comparison between the gamma and delta lactones with the same chemical formula or equivalent chain length. Gamma and delta nonalactone are both chemical formula of $C_9H_{16}O_2$, but different alkyl chain lengths so differences in fuel performance arising from chain length and ring size may be inferred. Likewise, gamma nonalactone and delta decalactone have a substituent alkyl chain containing five carbons so differences in fuel performance from the lactone ring size may be observed. Three comparisons are available between any two lactones:

1. Constant ring size with a varying chain length
2. Constant alkyl chain length with a varying ring size
3. Constant carbon count, with a varying chain length and ring size.

Table 6.1: Overview of the single component lactone test fuels alongside an abbreviation for each fuel and a skeletal depiction of their molecular structure.

Fuel (Nomenclature)	n =	Chemical structure
Gamma-Valerolactone (GVl)	N/A	
Gamma-Hexalactone (GHxl)	N/A	
Gamma-Heptalactone (GHpl)	1	
Gamma-Octalactone (GOl)	2	
Gamma-Nonalactone (GNl)	3	
Gamma-Decalactone (GDl)	4	
Gamma-Undecalactone (GUl)	5	
Gamma-Dodecalactone (GDdl)	6	
Delta-Nonalactone (DNl)	2	
Delta-Decalactone (DDl)	3	
Delta-Undecalactone (DUl)	4	
Delta-Dodecalactone (DDdl)	5	

6.1.2. Apparatus

All of the combustion experiments described in the current chapter were performed using the heavy-duty compression ignition engine and ultra-low volume fuel system research facility described in Chapter 4.

6.1.3. Experimental procedure

Each of the single component lactone fuels, and reference fossil diesel, were tested in the Volvo D8k engine under identical conditions, those of, constant injection timing condition outlined in Section 4.13. Of the lactones shown in Table 6.1, an attempt was made to combust Gamma valerolactone, hexalactone and heptalactone as single component fuels at the same experimental conditions, but they either did not ignite od exhibited highly unstable combustion late into the expansion stroke. Three further lactones, not shown in Table 6.1, Delta octalactone and either gamma or delta tridecalactone, were considered for the experiments but were not commercially available at reasonable cost.

A subset of the lactone fuels, the lowest and highest carbon count from both series were additionally tested at variable injection timings, which was varied according to the ignition delay of each fuel so that start of combustion was constant at TDC.

A summary of these conditions is shown in Table 6.3 and Table 6.4 alongside some key results from the experiments. The viscosities and lower heating values of the test fuels are shown in Table 6.2.

*Table 6.2: Physical and chemical properties of the lactones and the reference diesel. Purity, boiling point and density data provided by the supplier, Merck. Viscosity measured using a Brookfield III-Ultra rheometer. Gross calorific value measured using an IKA C1 bomb calorimeter. *c technical data for the reference diesel provided by Haltermann Carless.*

Fuel (Nomenclature)	Chemical Formula	Purity (%)	Boiling point (°C)	Density at 25 °C (g/cm^3)	Viscosity at 50 °C (Cp)	Gross calorific value (J/g)
γ-Valerolactone (GVl)	$C_5H_8O_2$	≥99	207[176]	1.05	1.48	26,257.00 ± 91.84
γ-Hexalactone (GHxl)	$C_6H_{10}O_2$	≥98	215[177]-219[178]	1.023	1.77	28,332.97 ± 203.26
γ-Heptalactone (GHpl)	$C_7H_{12}O_2$	≥98	230.2[179]	0.999	1.86	30,769.00 ± 45.59
γ-Octalactone (GOl)	$C_8H_{14}O_2$	≥97	248.4[179]	0.981	2.34	31,970.33 ± 207.27
γ-Nonalactone (GNl)	$C_9H_{16}O_2$	≥98	265.5[179]	0.976	2.77	33,234.00 ± 111.15
γ-Decalactone (GDl)	$C_{10}H_{18}O_2$	≥98	281.7[179]	0.952	3.18	34,430.00 ± 112.54
γ-Undecalactone (GUl)	$C_{11}H_{20}O_2$	≥98	290.0[180]	0.949	3.85	35,657.88 ± 140.55
γ-Dodecalactone (GDdl)	$C_{12}H_{22}O_2$	≥97	311.5[181]	0.936	4.48	35,963.52 ± 40.21
δ-Nonalactone (DNl)	$C_9H_{16}O_2$	≥98	267.0[179]	0.994	3.39	33,496.59 ± 60.64
δ-Decalactone (DDl)	$C_{10}H_{18}O_2$	≥98	283.2[179]	0.954	3.54	34,756.67 ± 29.53
δ-Undecalactone (DUl)	$C_{11}H_{20}O_2$	≥97	297.0[180]	0.969	4.29	35,610 ± 117.36
δ-Dodecalactone (DDdl)	$C_{12}H_{22}O_2$	≥97	312.7[182]	0.942	5.01	36,404.00 ± 84.76
Reference Diesel (Ref. D)	$C_{12}H_{23}$	-	189.9 – 355.5 [c]	0.832 [c]	2.245	45,800 [c]

Table 6.3: Experimental test conditions and key experimental results for the single component fuel tests in the D8k engine at constant injection timing.

Fuel (Acronym)	Engine speed (RPM)	Fuel injection pressure (bar)	Injection timing (CAD BTDC)	Injection duration (CAD)	IMEP (Bar)	Ignition delay (CAD)	PHRR (j/deg)	Max average in-cylinder temperature (K)
γ-Valerolactone (GVl)	820 ± 20	695 ± 10	5.3	6.5	N/A	N/A	N/A	N/A
γ-Hexalactone (GHxl)	820 ± 20	695 ± 10	5.3	6.5	N/A	N/A	N/A	N/A
γ-Heptalactone (GHpl)	820 ± 20	695 ± 10	5.3	6.5	N/A	N/A	N/A	N/A
γ-Octalactone (GOl)	820 ± 20	695 ± 10	5.3	6.5	4.93	9.2	543.50	1760.8
γ-Nonalactone (GNl)	820 ± 20	695 ± 10	5.3	6.5	5.16	6.7	624.27	1728.6
γ-Decalactone (GDl)	820 ± 20	695 ± 10	5.3	6.5	5.34	6.2	501.30	1736.6
γ-Undecalactone (GUl)	820 ± 20	695 ± 10	5.3	6.5	5.64	5.4	310.58	1763.1
γ-Dodecalactone (GDdl)	820 ± 20	695 ± 10	5.3	6.5	5.71	5	259.89	1768.5
δ-Nonalactone (DNl)	820 ± 20	695 ± 10	5.3	6.5	5.34	7.7	750.16	1786.0
δ-Decalactone (DDl)	820 ± 20	695 ± 10	5.3	6.5	5.51	6.5	539.38	1744.6
δ-Undecalactone (DUl)	820 ± 20	695 ± 10	5.3	6.5	5.60	6	397.01	1742.3
δ-Dodecalactone (DDdl)	820 ± 20	695 ± 10	5.3	6.5	5.63	5.5	314.56	1741.9
Reference Diesel (Ref. D)	820 ± 20	695 ± 10	5.3	6.5	7.18 ±0.09	5.2 ±0.09	328.42	1902.1

Table 6.4: Experimental test conditions and key experimental results for the single component fuel tests in the D8k engine with modified injection times for constant start of combustion at TDC.

Fuel (Acronym)	Engine speed (RPM)	Fuel injection pressure (bar)	Injection timing (CAD BTDC)	Injection duration (CAD)	IMEP (Bar)	Ignition delay (CAD)	PHRR (j/deg)	Max average in-cylinder temperature (K)
δ-Nonalactone (DNl)	820 ± 20	695 ± 10	7.8	6.5	5.06	7.5	739.54	1782.5
δ-Dodecalactone (DDdl)	820 ± 20	695 ± 10	5.5	6.5	5.60	5.5	308.03	1748.6
γ-Octalactone (GOl)	820 ± 20	695 ± 10	9.1	6.5	5.04	9.1	760.56	1849.5
	820 ± 20	695 ± 10	11.7	6.5	4.78	9.1	752.49	1871.0
γ-Dodecalactone (GDdl)	820 ± 20	695 ± 10	5.2	6.5	5.50	5.2	262.57	1738.2
Reference Diesel (Ref. D)	820 ± 20	695 ± 10	5.3	6.5	7.18 ±0.09	5.2 ±0.09	328.42	1902.1

6.2. Results

6.2.1. In-cylinder pressure and heat release rate
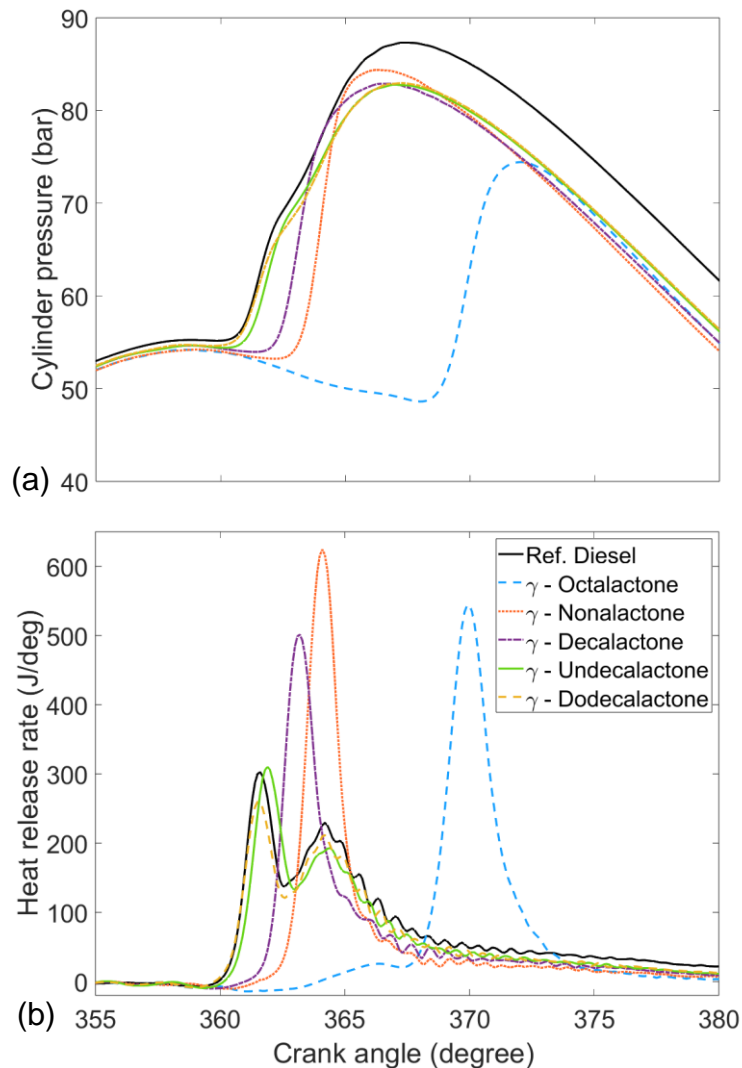
Figure 6.2: (a) In-cylinder pressures and (b) apparent net heat release rates of the single component gamma lactone test fuels and reference fossil diesel.

Figure 6.2 shows the in-cylinder pressures and apparent net heat release rates of gamma octalactone (GOl), nonalactone (GNl), decalactone (GDl), undecalactone (GUl), dodecalactone (GDdl) and reference fossil diesel. Immediately apparent is the significantly longer duration of ignition delay exhibited by GOl relative to the remaining lactone fuels and the two-stage ignition undergone, where HRR sees a positive increase at 363 CAD followed by a distinct positive increase in HRR at 367 CAD. As with GOl but not as obvious, GNl also exhibits two-stage ignition (Figure 6.2.b). For the GDdl, GUl, GDl and the reference diesel is can be seen that once the gradient for the heat release turns positive, it continues to increase until the PHRR is reached, but for

154

GOl and GNl the initial positive heat release is followed by a plateau or decrease in HRR before a second positive change in HRR occurs. Two-stage ignition is commonly observed in tests with two separate fuels blended, such as n-heptane and toluene, and is assumed to be resultant from the low temperature reactions prior to autoignition not generating significant heat to sustain the combustion process until a higher pressure is also reached.[183,184]

It is also apparent from Figure 6.2.a that GDdl and GUl exhibit very similar in-cylinder pressures during combustion. Additionally, the premixed burn and diffusion-controlled combustion periods exhibited by GDdl and GUl closely resemble that of the reference fossil diesel, whilst GDl, GNl and GOl each display a significantly larger premixed burn fraction than the fossil reference diesel (Figure 6.2.b).

Considering the molecular structures of the gamma lactones, it is visible from Figure 6.2 that each addition of a -CH_2 group to the substituent alkyl chain from GOl to GUl shortens the duration of ignition delay, leading to a smaller premixed burn fraction combustion period.
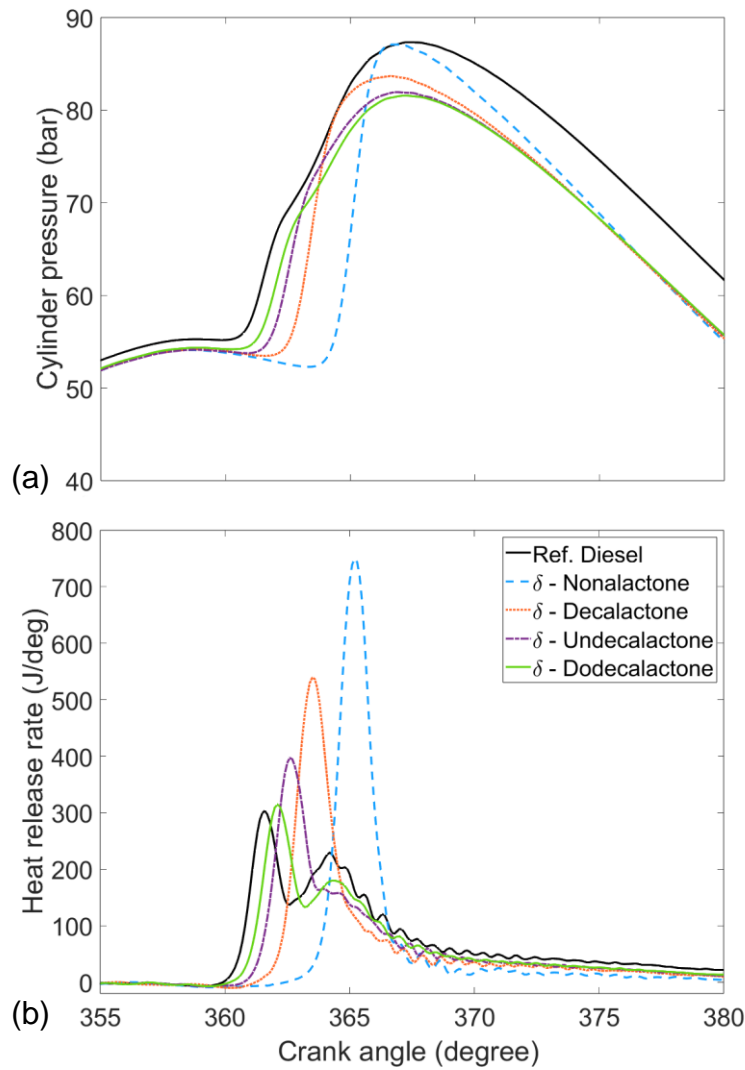
Figure 6.3: (a) In-cylinder pressures and (b) apparent net heat release rates of the single component delta lactone test fuels and reference fossil diesel.

Figure 6.3 shows the in-cylinder pressures and apparent net heat release rates of delta nonalactone (DNl), decalactone (DDl), undecalactone (DUl), dodecalactone (DDdl) and reference fossil diesel. Apparent is the increase in duration of ignition delay and size of the premixed fraction of combustion as the substituent alkyl chain length decreases from DDdl to DNl, similar to the previously shown gamma lactones (Figure 6.2).

However, unlike the gamma lactones, no two-stage ignition is visible amongst any of the delta lactone test fuels. Furthermore, the premixed burn and diffusion-controlled periods of combustion exhibited by DDdl and DUl show a more distinct difference relative to the fossil diesel than the gamma lactones of equivalent carbon number (GUl and GDl respectively).
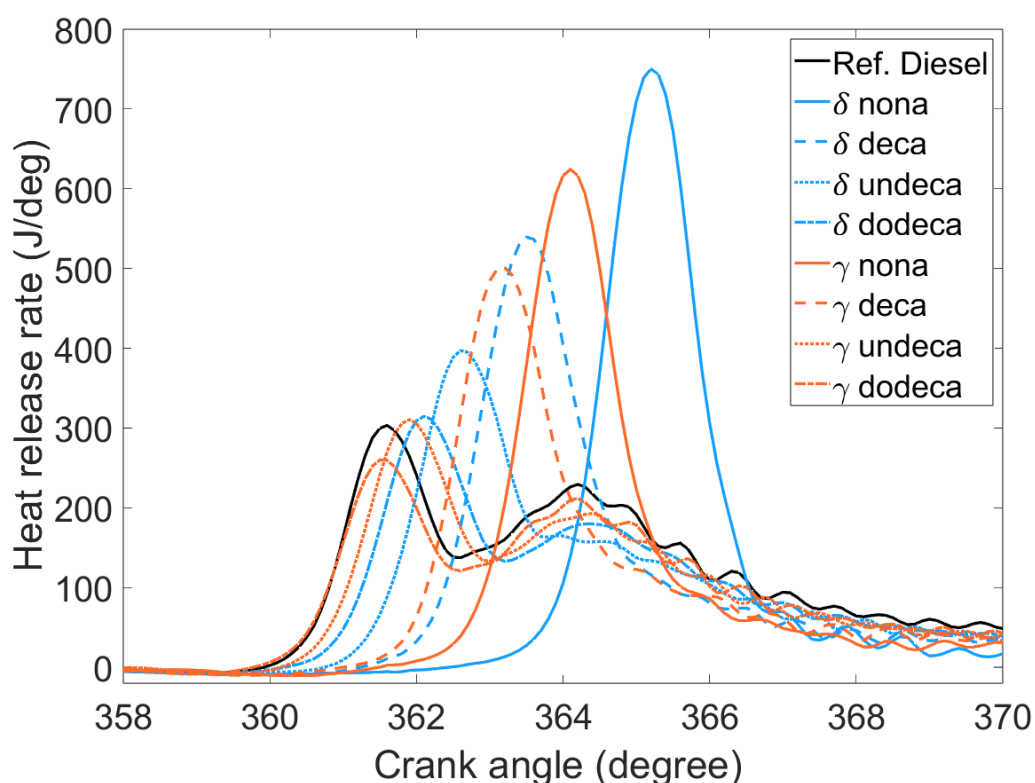
Figure 6.4: The apparent net heat release rate of the delta and gamma lactone single component test fuels with a total carbon count of C9 to C12 and the reference fossil diesel.

Figure 6.4 Shows the net apparent heat release rate of both the gamma and delta nonalactones, decalactones, undecalatones, dodecalactones and the reference fossil diesel tested at a constant injection timing. The trend apparent is that for each pair of lactones with an equivalent carbon number (e.g., gamma and delta dodecalactone), the gamma lactone exhibits a shorter period of ignition delay and the delta lactone exhibits a larger premixed burn period of combustion. As shown in Table 6.2, GNI and DNI have the same C:H:O ratio, as does GDI and DDL and so on, therefore differences in fuel behaviour must arise from differences in chemical structure.

The difference in lactone ring size between the equivalent carbon number gamma and delta lactone causes a difference in the length of the alkyl chain substituent. An in-depth discussion of these observations in Section 6.3. As shown in Table 6.1, the alkyl chain in GNI contains 3 -CH_2 groups, whilst DNI contains 2 of these groups. It has previously been shown that increasing the available number of alkyl chain -CH_2 groups leads to a reduction in duration of ignition delay as there are more sites in each single fuel molecule for combustion to initiate.[185] Alkyl free chains have higher mobility than organic

157

rings such as lactones, so it can be assumed that the intermediate cyclic species formed during the low temperature kinetic reactions can more readily propagate combustion on the alkyl chain than the saturated ring.[186] It is therefore to be expected that the gamma lactones will experience easier autoignition than the delta lactones of the same carbon count, where carbon atoms are effectively move from the ring to the alkyl chain.

However, of note in Figure 6.4 is the heat release exhibited by GUl, which as expected exhibits a shorter duration of ignition delay than DUl, but unexpectantly also a shorter duration than DDdl. DDdl and GUl both have an alkyl chain containing 7 carbons, but as shown in Table 6.2 DDdl has a higher total carbon count and higher calorific value.
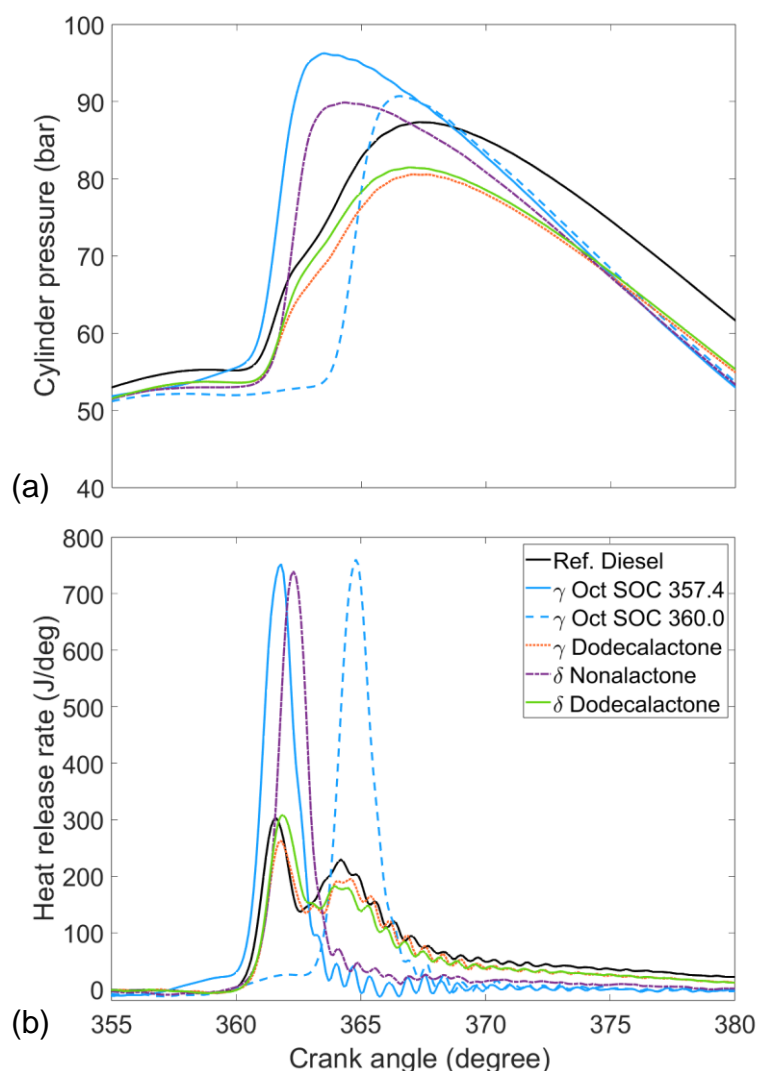
Figure 6.5: (a) In-cylinder pressure and (b) apparent net heat release rate of gamma octalactone, gamma dodecalactone, delta nonalactone, delta dodecalactone single component test fuels and reference fossil diesel variable injection timing for constant start of combustion at TDC, or for the second stage of GOI to occur at TDC.

Figure 6.5 shows the in-cylinder pressure and apparent net heat release rates of delta nonalactone (DNI), delta decalactone (DDI), gamma octalactone (GOI), gamma dodecalactone (GDdl) and reference fossil diesel at a constant start of combustion (SOC) timing. For each fuel the injection timing was varied so that the start of combustion always occurred at TDC. As GOI has been found to exhibit two-stage ignition and so was tested twice; once so that the 1st ignition event occurred at TDC, and secondly such that the 2nd ignition and main heat release event occurred at TDC. All the test fuels ignite within 0.3 CAD of TDC, besides GOI SOC 357.4. Predicting the change in two-stage ignition exhibited by GOI at constant injection timings led to this disparity in SOC timing.

The most apparent feature of Figure 6.5 is the significantly larger premixed burn fraction of combustion exhibited by GOI and DNI compared to the reference diesel, GDdl and DDdl. Adjustment of injection timing does not appear to affect the two-stage ignition exhibited by GOI, however bringing forward the injection timing does increase the observed PHRR compared to the constant injection timing condition (Figure 6.2).

At constant SOC, the observed heat release rates exhibited by GDdl and DDdl appear very similar to that of the reference diesel (Figure 6.5).

6.2.2. Combustion characteristics
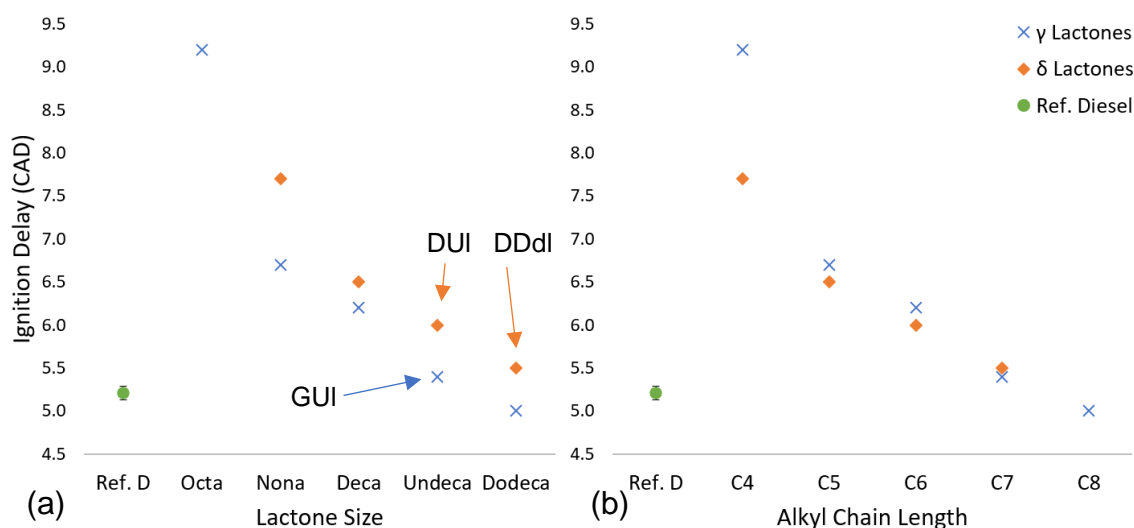
Figure 6.6: Variation of ignition delay with (a) lactone carbon number and (b) lactone alkyl chain length at constant injection timing.

Figure 6.6 shows the impact of carbon number and alkyl chain length on ignition delay in substituted gamma and delta lactones at constant ignition timing.

Apparent in Figure 6.6a is a general trend of decreasing ignition delay with increasing lactone size and a consistent offset where the gamma lactones exhibit a shorter ignition delay than the delta lactones. As shown in Table 6.1, the difference in ring size between the equivalent gamma and delta lactones means the gamma isomer will have a longer substituted alkyl chain length than the delta isomer at equivalent carbon counts. The shorter ignition delay exhibited by the gamma lactones is therefore expected.[187] As mentioned in Chapter 2, the rate of the low temperature reactions which propagate radical formation increase with alkyl chain length, as a higher number of six or seven membered transition states can form.[159] Apparent also in Figure 6.6b is that increasing the alkyl chain length in both the gamma and delta lactones shortens the duration of ignition delay. This is an expected result as increasing alkyl chain length has previously been shown to shorten the duration of ignition delay in straight chain alkane single component fuels.[185]

Plotting according to substituent alkyl chain length (Figure 6.6b) further shows that at lengths of 4 to 6 carbons, the delta lactones exhibit a shorter ignition delay. This is also expected, as the delta lactone ring contains one additional -CH_2 group and for equivalent lactones with the same chain lengths the delta lactones constitute a higher calorific value. At a chain length of 4 carbons this difference is most pronounced and this is not surprising given the lactones which contained fewer carbons than gamma octalactone did not combust. GOl is the first lactone to exhibit stable combustion and the delta lactone with an equivalent alkyl chain length would have a lower carbon to oxygen ratio, increasing the likelihood of stable combustion occurring.

However, a surprising result shown in Figure 6.6 is that GUl exhibits a shorter ignition delay than both DUl and DDdl. As shown in Table 6.2, DDdl has a higher carbon count and calorific value, so it would be expected that DDdl would have a shorter ignition delay than GUl.

The shorter ignition delay of GUl than DDdl may imply that gamma ring structure does uniquely influence the duration of ignition delay in addition to the inherent longer carbon chain length for equivalent carbon numbers.
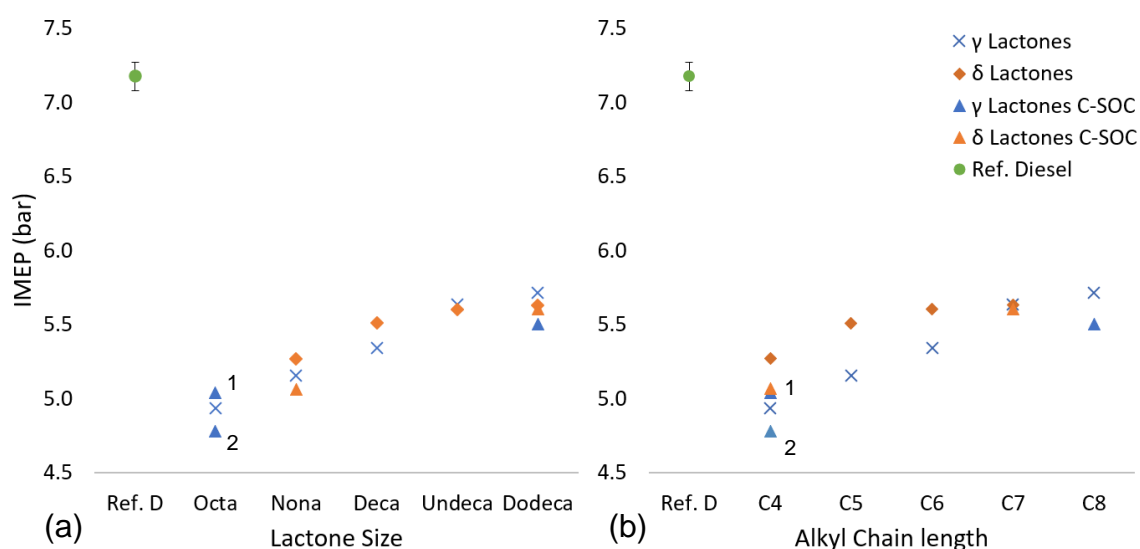
Figure 6.7: Indicated mean effective pressure (IMEP) of the lactone single component fuels and reference diesel, tested at constant injection timing and duration. Constant injection conditions and variable timings for constant start of combustion at TDC (C-SOC) shown. 1* GOI 1st ignition at TDC, 2* GOI 2nd ignition at TDC.

Figure 6.7 shows the IMEP of the gamma lactones, delta lactones and the reference diesel, shown both against the lactone size and substituent alkyl chain length at constant injection duration. GOI, GDdl, DNI and DDdl were tested at both the constant injection and constant SOC test conditions. GOI experiences two-stage ignition and a second test was performed with the 2nd stage of ignition occurring at TDC with an injection timing of 11.7 CAD BTDC.

For both the gamma and delta lactones the IMEP increases with lactone size, with the trend becoming less apparent as the lactone size increases and the IMEP converges. The error for the reference diesel is 0.09 bar and as shown in Table 6.3 this value is larger than the difference in IMEP exhibited between the undeca and dodeca lactones. Additionally, DNI and DDI both exhibit a higher IMEP than GNI and GDI respectively, whilst at the larger lactones DUI and DDdl exhibit a lower IMEP than GUI and GDdl respectively. Prior to the convergence in IMEP exhibited by the lactones at carbon numbers greater than C10, it is clear that the delta isomer exhibits a higher IMEP than the gamma isomer.

The convergence in IMEP exhibited by the lactones at first seems unintuitive, as increasing the carbon size, calorific value and length of straight alkyl chains in the single component fuels all increase the amount of available energy in the chamber during combustion. However, when moving to the larger lactones and the carbon numbers increase, the proportional decrease in lactone oxygen becomes less pronounced. Moving from an octa to nona lactone changes the

161

carbon to oxygen ratio more significantly than going from an undeca to dodeca lactone. Additionally, as shown in Table 6.2, as the lactone size increases in both the delta and gamma lactones, the density decreases and viscosity increases. The combustion tests were undertaken at a constant injection duration with no correction for fuel volume or mass. Under these conditions, a lower fuel density and a higher fuel viscosity would both reduce the mass of fuel entering the chamber each combustion cycle. Kim et al. (2019) investigated how fuel viscosity impacts fuel spray behaviour and found that increasing viscosity will reduce the injected mass of fuel.[188] In the case of the lactone single component fuels, it is feasible that the higher calorific value of the dodecalactones than the undecalactones is offset by lower mass of fuel and therefore energy available during combustion.

Finally, a trend observed at the constant SOC test conditions is the slight reduction in IMEP when GOI's second-stage ignition occurred at TDC relative to the first stage occurring at TDC. Despite the same amount of energy available, if the first stage of ignition occurs prior to TDC then chemical energy is resisting the compression stroke instead of providing useful work in the expansion stroke. GDdl and DDdl ignited close to TDC under the constant injection timing condition, and the small change in injection timing necessary to ensure ignition at TDC was not sufficient to change the measured IMEP significantly (Figure 6.7).
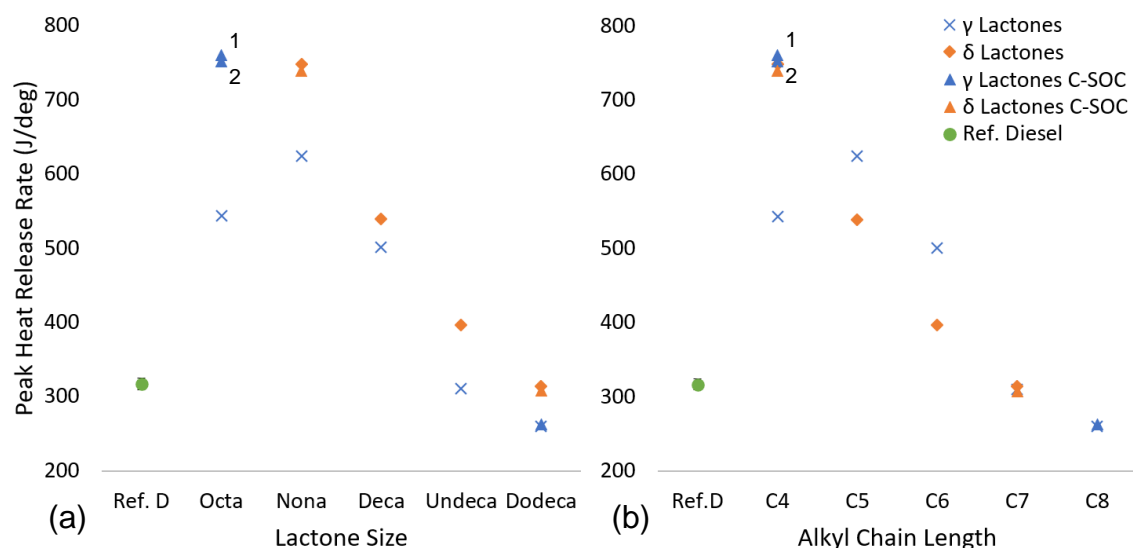
Figure 6.8: Peak apparent heat release rate of single component gamma and delta lactone test fuels and reference diesel. Constant injection conditions and variable timings for constant start of combustion at TDC (C-SOC) shown. 1* GOI 1st ignition at TDC, 2* GOI 2nd ignition at TDC.

Figure 6.8 shows the peak apparent heat release rate of the gamma lactones, delta lactones and the reference diesel. The trend apparent from both subfigures is that with the exception of GOI tested at the constant injection timing condition, increasing lactone size in both the gamma and delta lactones decreases the magnitude of PHRR observed. The sensitivity to the injection

timing for GOI implies that bringing forward the injection timing and bringing ignition closer to TDC is necessary for clarifying how GOI should behave in trend with larger lactones. It is shown in Figure 6.8a that for each lactone size the gamma lactone exhibits a lower PHRR than the delta lactone, in agreement with the observed longer ignition delay of the equivalent carbon number delta lactones (Figure 6.6a). As discussed in Chapter 2, the duration of ignition delay directly impacts the PHRR, as longer durations allow for greater air-fuel mixing to occur prior to combustion, thus increasing the extent of the premixed burn fraction.[120,189]

It is interesting to note however that the PHRR exhibited by GOI at constant injection timing does not correlate with the observed relationship between PHRR and the duration of ignition delay. As shown in Figure 6.2, GOI exhibited two-stage ignition, with two distinct periods of change in the rate of heat release. It has previously been suggested that single component fuels exhibiting two-stage ignition strongly facilitate chain propagation over chain branching reactions during the low temperature regions.[190] As discussed in Chapter 2,

163

chain propagation reactions maintain a constant number of radicals within the system, whereas chain branching increase the number of radicals within the system. The cool combustion time period between the first and second ignition delay will partially oxidise the fuel.[191] Partial fuel oxidation would reduce the potential for energy release during the second ignition stage, a possible cause for the observed peak heat release rate of GOI being lower than GNI despite a longer ignition delay.

Bringing forward the injection timing of GOI so that either the 1st or 2nd stage of ignition occurs at TDC significantly increases the apparent PHRR, at constant SOC timing GOI displays the longest duration of ignition delay and highest peak heat release rate. The 1st or 2nd stage of ignition occurring at TDC does not significantly change the PHRR any further, additionally changing the injection timing of DNI also does not significantly impact the PHRR. This implies that the low PHRR observed during combustion of GOI at constant injection timing could instead be caused by the physical properties of the combustion chamber during this time and not the chemical properties of the fuel. At the time of autoignition, the piston will have moved away from TDC, exposing more of the cylinder walls providing more surface area for the transfer of heat away from the air fuel mixture. GOI auto-ignites 3.9 CAD ATDC during which the in-cylinder pressure and temperature have both decreased, leading to less efficient combustion.
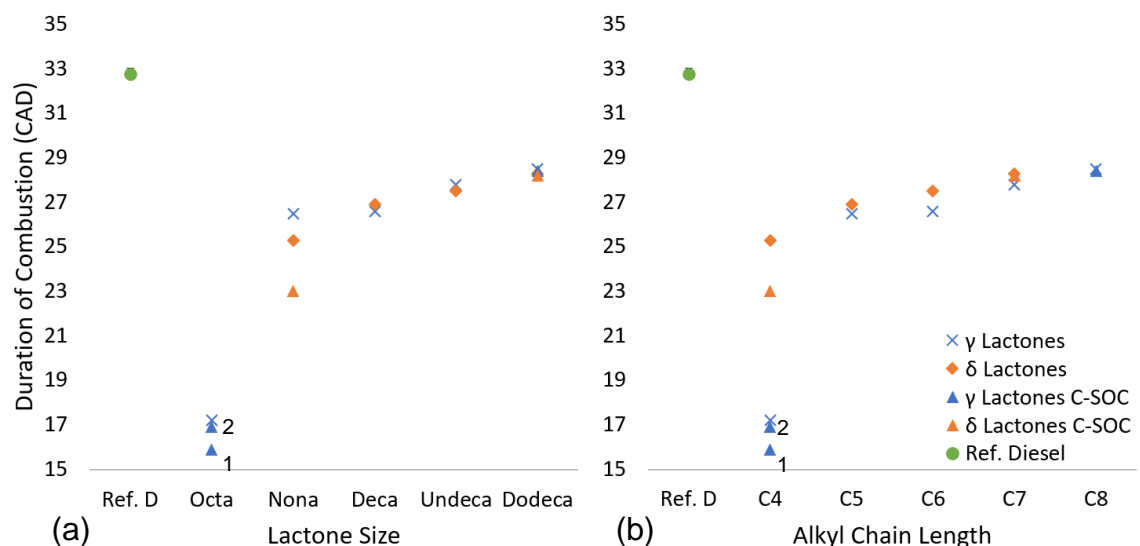
Figure 6.9: Calculated duration of combustion of single component gamma and delta lactone test fuels and reference diesel. Constant injection conditions and variable timings for constant start of combustion at TDC (C-SOC) shown. 1* GOI 1st ignition at TDC, 2* GOI 2nd ignition at TDC.

Figure 6.9 shows the calculated duration of combustion of the gamma lactones, delta lactones and the reference diesel. The trend apparent is that increasing lactone size increases the duration of combustion. Previously shown in Figure 6.2 and Figure 6.3 were the heat release plots during combustion of the lactone single component fuels. As previously mentioned, increasing lactone size reduced the duration of ignition delay, so less time was available for air fuel mixing prior to autoignition. Increasing lactone size therefore leads to a smaller premixed burn phase and larger mixing-controlled phase of combustion. Further apparent is lack of difference in duration between the delta and gamma deca, undeca and dodecalactones, indicating that gamma / delta ring size isomerism does not impact duration of combustion once a total carbon number has been surpassed. For lactones with the same alkyl chain length, the delta lactones have a slightly longer duration, clearly indicating that the total carbon to oxygen ratio has a bigger impact on duration of combustion than gamma / delta lactone isomerism as for equivalent chain lengths the delta lactones larger ring size will always result in a higher carbon to oxygen ration.

A further observation is that bringing forward the injection timing reduces the duration of combustion of DNI and GOI with both injection timings.

6.2.3. Exhaust emissions
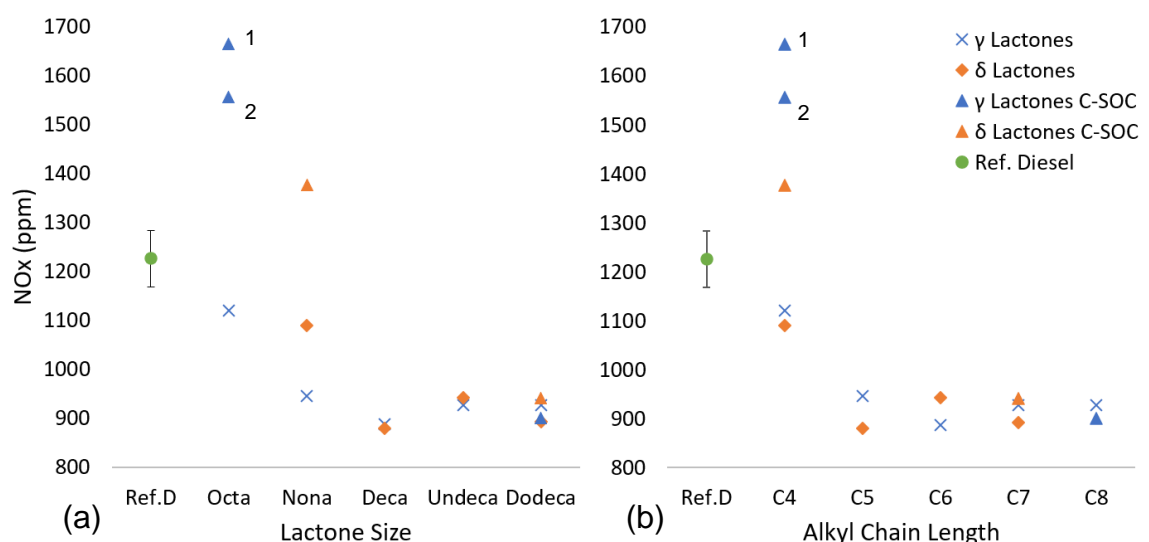
Figure 6.10: Exhaust gas NO$_x$ emissions of the delta lactone and gamma lactone single component fuels and reference diesel vs lactone structure. Constant injection conditions and variable timings for constant start of combustion at TDC (C-SOC) shown. 1* GOI 1st ignition at TDC, 2* GOI 2nd ignition at TDC.

Figure 6.10 shows the measured NO_x emissions during combustion of the delta lactones, gamma lactones and the reference diesel at constant injection conditions and subset of the fuels were further tested at variable ignition timings.

Immediately apparent is the significant increase in NO_x emissions resultant from GOI and DNI relative to both diesel and the other lactones tested. This observed increase in emissions can be attributed to their long ignition delay allowing for greater air fuel mixing prior to autoignition, leading to combustion dominated by the premixed burn fraction and a short duration of combustion.

As mentioned in Chapter (Michael acceptors results) NOx production relies on the residence time of hot gases at high pressure, close to stoichiometric ratios with higher production occurring during the mixing-controlled combustion phase than the premixed phase. NOx production is highly time dependent, as the thermochemistry kinetics will 'freeze' during the expansion stroke as the in-cylinder temperature and pressure both decrease during gas expansion.

Changing the injection timing to facilitate combustion of GOI at TDC causes an intense, short premixed flame to dominate the combustion process which quickly consumes all the fuel as shown by the short duration of combustion (Figure 6.9). Reaching a higher temperature and completing combustion 6 – 7 CAD faster than GDdl and GNI allows more time for the hot gaseous combustion products to remain at high pressure prior to freezing of NOx kinetics.[164]

Apparent is the lower NO_x emissions detected during combustion of the single component test fuels compared to the reference diesel at the constant injection timing test condition. Previously shown in Table 6.3 are the IMEP and maximum in-cylinder average temperatures. Thermal production of NO_x requires temperatures above 1600 K and while each of the lactone test fuels displayed average temperatures of 1700-1800 K, the reference diesel exhibits a significantly higher temperature of 1900 K so therefore the lower NOx emissions of the lactones are to be expected.[42]
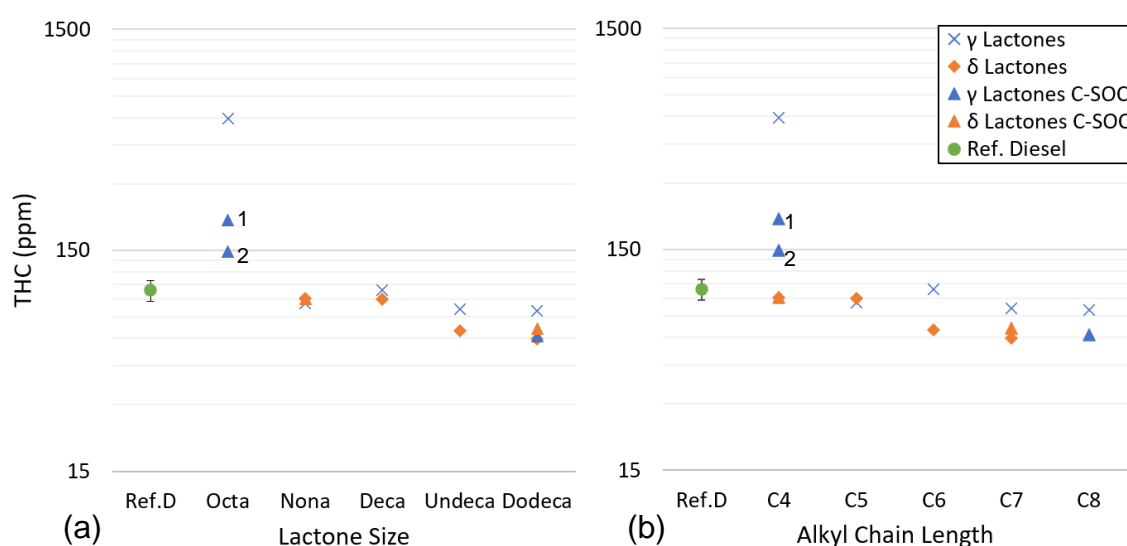
Figure 6.11: Exhaust gas unburnt hydrocarbon emissions of the gamma lactones, delta lactones and reference diesel, vs lactone size & substituent alkyl chain length. Constant injection conditions and variable timings for constant start of combustion at TDC (C-SOC) shown. 1* GOI 1st ignition at TDC, 2* GOI 2nd ignition at TDC.

Figure 6.11 shows the unburnt hydrocarbon emissions of the two groups of lactone single component fuels and the reference diesel at constant injection conditions and subset of the fuels tested at variable ignition timings.

Immediately apparent is the significantly high THC value of GOI which can be attributed to the observed long ignition delay and resultant premixed burn faction dominating combustion. A long duration of ignition delay allows for greater air fuel mixing, creating areas of fuel spray within the chamber which are too lean to auto-ignite or support a self-propagating flame, increasing the amount of un-reacted fuel. Bringing forward the injection timing such that the 1st or 2nd stage of ignition occurs at TDC significantly reduces the THC measured during combustion. As previously mentioned, the significantly delayed SOC of GOI under the constant injection testing condition resulted in combustion occurring at a lower pressure and temperature, lowering the overall efficiency in the process of combustion.

Further apparent is the lower levels of THC emissions resultant from the delta deca, undeca and dodeca lactones than the gamma lactones. This is unexpected as THC arising from over lean mixtures resultant from long durations of ignition delay are assumed to be the most important contributor to THC formation, but for each equivalent lactone the delta isomer exhibits a longer ignition delay (Figure 6.6).[192] The delta lactones all exhibit a higher viscosity than the equivalent gamma isomers and unburnt hydrocarbons

167

typically result from air fuel mixture too lean or too rich to sustain combustion. The slightly lower viscosity of the gamma lactones versus their equivalent delta isomer may cause some fuel droplets to spread further into the chamber prior to autoignition and become too lean to ignite.[193]
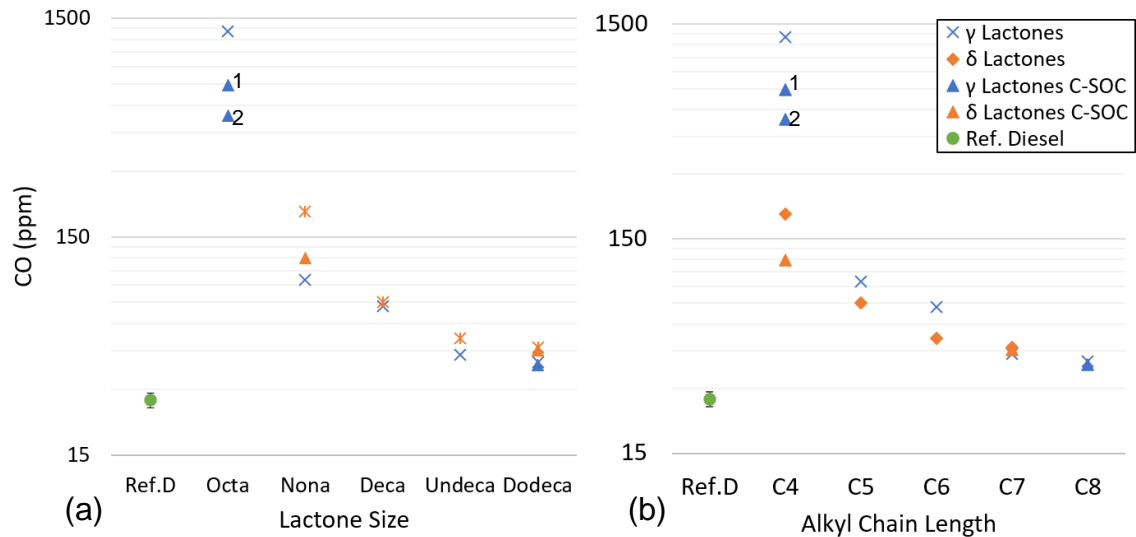
Figure 6.12: Exhaust gas CO emissions of the delta lactones, gamma lactones and reference diesel vs lactone size. Constant injection conditions and variable timings for constant start of combustion at TDC (C-SOC) shown. 1* GOI 1st ignition at TDC, 2* GOI 2nd ignition at TDC.

Figure 6.12 shows the CO emissions during combustion of the delta lactones, gamma lactones and reference diesel at constant injection conditions and subset of the fuels tested at variable ignition timings.

Strikingly apparent is the significantly higher emissions resulting from combustion of GOI at each injection timing and DNI. The measured CO from both GOI and DNI significantly reduces as the injection timing is brought forwards. CO is a product from incomplete combustion and the significant duration of ignition delay exhibited by GOI and DNI leads to autoignition occurring further into the expansion stroke than the remaining lactones. Bringing forward the time of injection timing ensures that autoignition occurs closer to TDC, which is the point of highest pressure and heat in the combustion chamber during the four-stroke cycle.

Further apparent is the reduction in CO emissions as lactone size increases and the higher CO emissions detected during combustion of the delta lactones over their equivalent gamma isomer. This trend matches the trend observed in ignition delay and the premixed burn fraction of combustion. A longer duration of ignition delay allows for greater air fuel mixing and the formation of over-lean

mixture in the chamber which may not auto ignite or fail to sustain a self-propagating flame, resulting in incomplete combustion.[92] The previous observed trend in ignition delay (Figure 6.6) was that of the alkyl chain length having greatest influence on the duration of delay, whilst the total lactone size had greater influence on the CO results which also reflect the differences in boiling point between the lactones (Table 6.2).
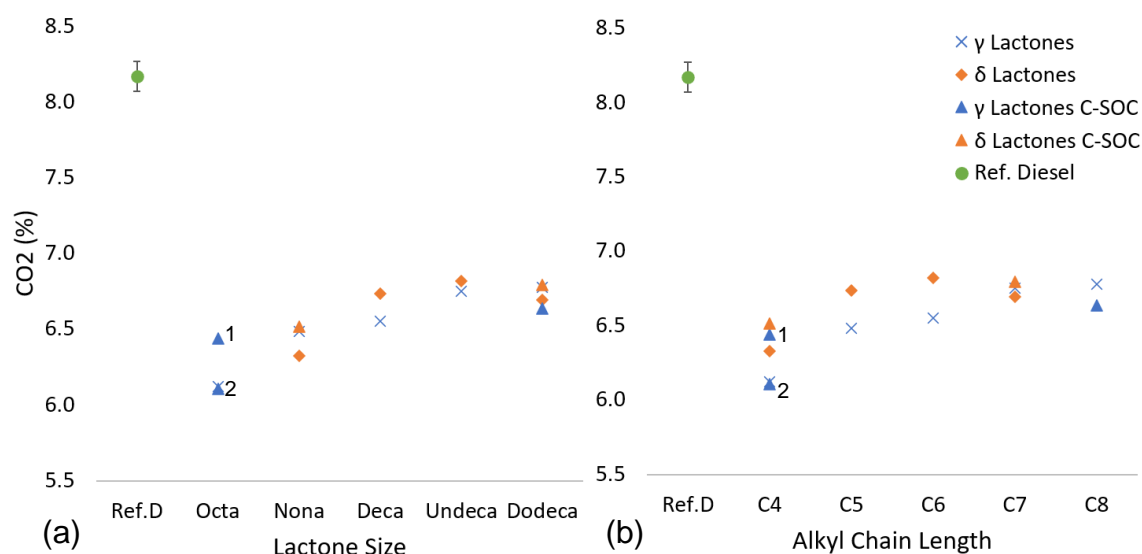
Figure 6.13: Exhaust gas CO_2 emissions of the delta lactones, gamma lactones and reference diesel vs lactone size. Constant injection conditions and variable timings for constant start of combustion at TDC (C-SOC) shown. 1* GOI 1st ignition at TDC, 2* GOI 2nd ignition at TDC.

Figure 6.13 shows the CO_2 emissions during combustion of the delta lactones, gamma lactones and the reference diesel at constant injection conditions and subset of the fuels tested at variable ignition timings.

Apparent is the trend of increasing CO_2 emissions with lactone size. This trend is stronger with the gamma lactones than the delta lactones, as DDdl exhibits slightly lower CO_2 emissions than DUl. Increasing CO_2 emissions with lactone size is expected as with increasing size the carbon ratio by weight % increases with lactone size. Further apparent is a slight increase in CO_2 % detected from GOI and DNI at the constant SOC timing. The trends in CO_2 emissions match closely with that of IMEP (Figure 6.7), which is expected as oxidation of carbon contributes significantly to the energy generated during combustion.
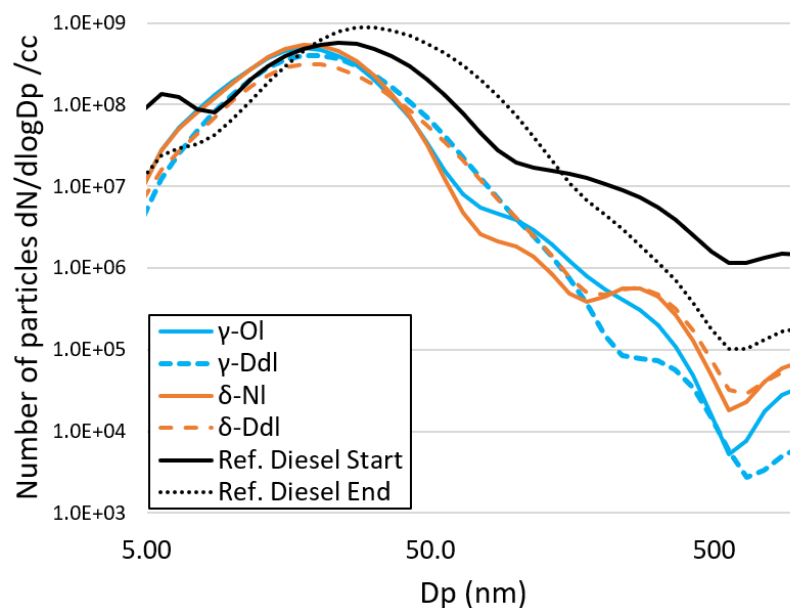
Figure 6.14: Particle emissions of GOl, GDdl, DNl, DDdl and reference diesel at constant start of combustion at TDC. Ref. Diesel is the end of day diesel

Figure 6.14 shows the particle number size distribution of GOl, GDdl, DNl, DDdl and the reference diesel tested at the start of combustion at TDC test condition.

Apparent is the similarity in nucleation mode particulate count (Dp ≤ 50 nm) exhibited by all the lactones. The gamma lactones then emit very similar or a lower number of accumulation mode particles (Dp 50 ≤ 500 nm) than the delta lactones. Compared to the reference fossil diesel all the lactones emit fewer particles at particle sizes larger than 15 nm.
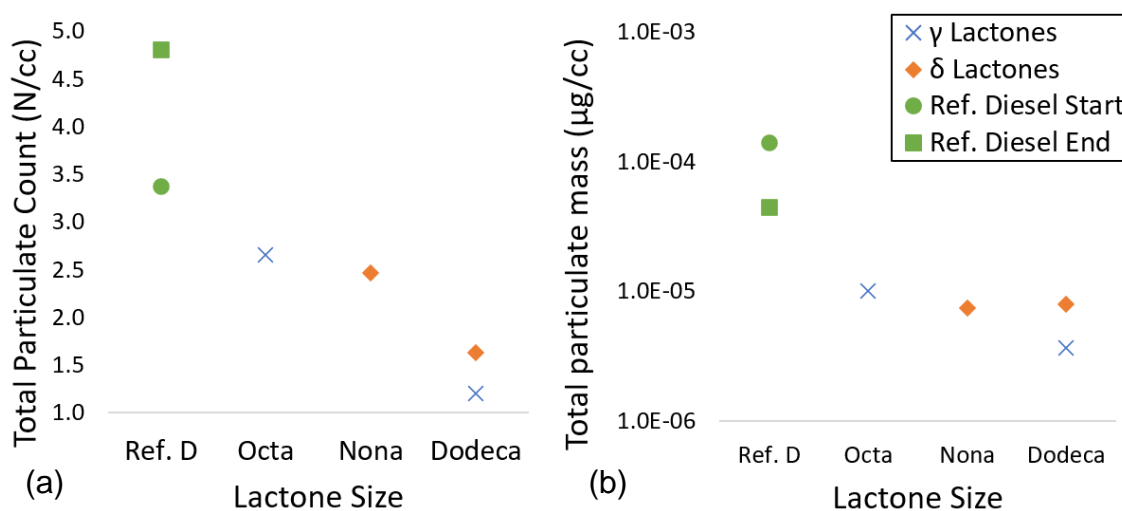
Figure 6.15: Total particulate count (a) and total particulate mass (b) emitted from GOl, GDdl, DNl, DDdl and reference fossil diesel at constant SOC at TDC.

170

Figure 6.15a shows the total particulate count and Figure 6.15b shows the total particulate mass measured during combustion of GOl, GDdl, DNl, DDdl and reference fossil diesel, at constant start of combustion.

Apparent is the reduction in total particulate count as lactone size increases. GDdl exhibits a lower total count than DDdl, implying the gamma lactones typically emit fewer particles than their delta lactone counterparts, but particulate measurements from further lactone pairs would be required to confirm this. From the data available, it appears ignition delay is the determinant factor on total particulate count, as the dodecalactones which exhibited short durations of ignition delay emitted a lower particulate count. Despite being an oxygenated species, GOl emits a relatively higher total particular mass than the other lactones, attributable to its longer duration of ignition delay and short duration of combustion, leaving little time for continued oxidation of any particulate species formed prior to opening of the exhaust valves.

Of final note, there is a slight increase in total mass emitted by the delta lactones as size increases, implying that despite the reduction in particulate count, DDdl does not see a reduction in particulate precursors during combustion.

6.3. Impact of lactone isomerism and alkyl chain lengths on combustion

Apparent from the results discussed in sections 2.1 to 2.3 that increasing the length of the alkyl substituent chain adjacent to the ring bound oxygen within lactones improves their combustion performance as single component fuels. Increasing alkyl chain length reduces ignition delay (Figure 6.6), the premixed burn fraction during combustion (Figure 6.2 Figure 6.4) and reduces the emissions of NO_x (Figure 6.10), THC (Figure 6.11) and CO (Figure 6.12).

To investigate potential differences arising from lactone isomerism, two sets of lactones were tested, the gamma and the delta lactone single component fuels. As previously stated, by definition of their isomerism equivalent gamma lactones will always have a longer substituent alkyl chain. A longer alkyl chain increases the number of free -CH_2 groups which are crucial to low temperature chain branching kinetics in hydrocarbon oxidation. For this reason, for each

lactone size the gamma lactone exhibited a shorter duration of ignition delay than the delta counterpart (Figure 6.6). Additionally, it is possible the gamma lactone is able to further improve upon ignition delay. The trend observed for both gamma and delta lactones were a shorter duration of ignition delay with increasing alkyl chain length. As in trend with the remaining lactones, gamma undecalactone exhibited a shorter ignition delay than delta undecalactone and unexpectedly a shorter delay than delta dodecalactone despite its higher carbon count and lower heating value. This shorter ignition time exhibited by the gamma lactones can be attributed to higher reactivity caused by their configuration. In cyclic organic molecules, the 6 membered ring configuration experiences less ring strain than all other potential organic rings. Ring strain is a property which emerges from repulsive forces of electrons held in atomic bonds. In the simplest organic molecule, methane (CH_4) the angles between C-H bonds are 109.5° and this is the lowest energetic arrangement. If the bonds were forced to have a smaller internal angle, a repulsive force arises between electrons held in the bonds. In a 6 membered ring the bonds forming the structure can arrange such that the internal angles are closest to that of methane compared to all other ring sizes. The increased ring strain experienced by 5-membered rings is attributed to a higher reactivity and heat of combustion.[194,195] The ring strain in lactones however present counter-intuitively to this as the ester functional group has different bonding angles to hydrocarbons. Instead, gamma lactones hold a slightly lower ring strain energy than delta lactones, but how this changes with an alkyl substituent has not been investigated.[196]

A further observation resulting from isomerism is the lower THC, higher CO and higher CO_2 value exhibited by the delta lactones over their gamma lactone counterparts. Resulting again from the observed differences in ignition delay, the shorter delay exhibited by the gamma lactones allows less time for air fuel mixing to occur prior to autoignition. With less air fuel mixing than their delta lactone counterpart, the combustion is more dictated by a mixing-controlled flame, potentially leading to areas within the spray that are too rich to oxidise. Shown in Figure 6.9, the duration of combustion for the larger lactones saw little change between the two isomers. It can be therefore assumed that the delta lactones slightly longer ignition delay than the gamma lactones facilitate just

enough air fuel fixing prior to autoignition for a more complete oxidation of the fuel, reducing the THC levels. If more fuel is partially oxidised and propagating the flame, it would lead to higher CO and CO_2 by definition of less fuel contributing to THC.

Finally, the difference between the gamma and delta lactones appears to have no impact of measured NOx apart from what would be attributable to differences in IMEP for lactones with an alkyl chain length above 5 carbons. This indicates that the higher NO_x exhibited by GOI and DNI is attributable to their long duration of ignition delay resulting from a limited number of accessible -CH_2 groups in their substituent alkyl chain.

6.4. Conclusions

This chapter has discussed engine tests designed to investigate the potential differences in combustion caused by delta / gamma lactone isomerism and effects caused by increasing the length of a substituent alkyl chain.

- A series of gamma and delta lactones with an alkyl chain substituent were tested as single component test fuels and were found to perform well as fuels.

- Increasing the length of the alkyl substituent chain on both lactone isomers (increasing their total carbon count) was found to reduce the duration of ignition delay, increase the duration of combustion, and decrease the measured emissions of nitrogen oxides, unburnt hydrocarbons, CO and particulates.

- Gamma Undecalactone exhibits a shorter ignition delay than all the gamma lactones with a smaller carbon count, as would be expected, but it further exhibits a shorter ignition delay than delta lactones with a higher carbon count indicating that gamma lactones may directly shorten the duration of ignition delay.

- Gamma lactones with an increasing substituent alkyl chain with a total carbon count of $8 \leq 12$ exhibit shorter ignition delays than their delta isomers, likely resulting from a higher reactivity derived from their ring strain.

- The slight reduction in THC and increase in CO / CO_2 in delta lactones could be attributed to their slightly longer duration of ignition delay compared to the gamma lactones.
- Further studies could be performed to investigate the particulate emissions from the full set of lactones as time constraints prevented a full investigation.

7. Investigations on date pit derived biodiesel

The work presented in this chapter focuses on the fuel performance of a biodiesel derived from date pits as compared with rapeseed methyl ester and reference fossil diesels. This study was undertaken in collaboration with researchers optimising the production of date pit methyl esters (DPME) for the biodiesel market in Oman.

Introduced in Chapter 2, biodiesels are mono-alkyl esters produced through the transesterification of vegetable oils or animal fats. Biodiesels contain fewer chemical components than fossil diesel typically, and regardless of the biodiesel source the fuel is 90 % comprised of the same six common fatty acid esters, shown in Figure 7.1. An example of similarity between widely varying natural sources is apparent when comparing the compositions of beef tallow and soybean oils. Beef tallow is made up of 24 % palmitic acid and 44 % oleic acid whilst for soybeans this is 13 % and 23 % respectively.[197–199] As previously discussed in Chapter 1, increased use of biofuels is vital for progress towards climate goals and reducing anthropologic CO_2 emissions. The greater homogeneity offered by biodiesels regardless of their origin allows the opportunity to study their unique combustion characteristics so that engine design modifications facilitate more favourable performance and emissions.
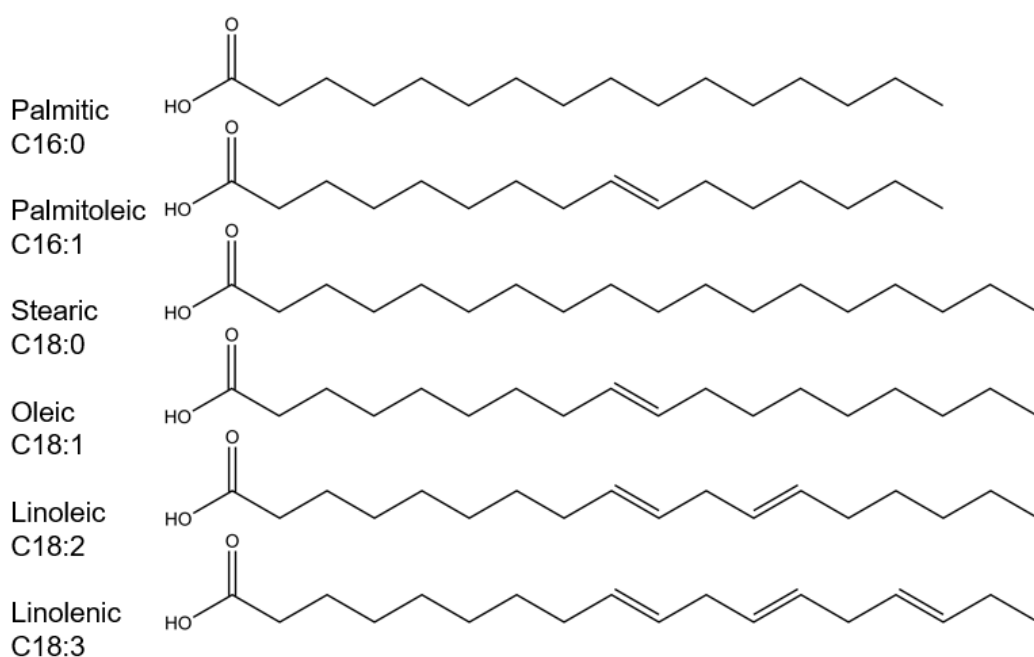
Figure 7.1: Chemical structures of the most common fatty acids identified in animal fat and vegetable oils which are converted to alkyl esters.

Fatty acid methyl acids are the predominant renewable diesel fuel used and a 7 % blend with fossil diesel (B7) has been widely available in the UK since 2019, and the Volvo D8k engine used as the testing facility for this work was advertised as being 'biofuel' ready.[133,200] The main components of diesel are typically long saturated alkyl chains from 8 to 24 carbons in size. Bioderived fatty acid esters (Figure 7.1) are therefore considered ideal biofuels for use in compression ignition engines due to their similar structure to diesel, high boiling points, high calorific values and exhibits higher combustibility than fossil diesel.[201] Furthermore, the base chemistry governing the synthesis of biodiesel is well studied[202] and biodiesel research has now moved onto the sourcing, conversion and testing of 3rd generation biomass feedstocks.[38,197]

The influence of FAMEs on compression ignition engine emissions is highly sensitive to changes in the fatty acid profile. The ratio of the common fatty acid molecules changes the fuel performance of the biodiesel used by influencing the fuel viscosity, boiling point, carbon to oxygen ratio and levels of unsaturation. Reviews from Hasan et al. (2015), Patel et al. (2016) and Datta et al. (2016) highlight that when looking at multiple unique sources of biodiesel, key emissions such as NO_x, CO, unburnt hydrocarbons and particulates (or smoke) can all either increase or decrease depending on the unique fatty acid profile of the biodiesel source.[203–205] Some studies indicate that the lower flame temperatures from oxygenated fuels may lead to areas of air/fuel mixture becoming too lean or too rich, leading to higher CO and THC emissions. Other studies suggest the higher cetane numbers of FAMEs lead to lower THC emissions.[14, 41, 165,201] Finally, NO_x is known to be highly sensitive to in-cylinder temperatures and the residence time of the gaseous combustion products at high pressure.[89] The duration of ignition delay also has significant influence on NOx as a long duration allows for greater air/fuel mixing prior to autoignition, longer delays therefore lead to higher peak heat release rates which result in high in-cylinder temperatures.[164,206] As fatty acids derived from plant mass are likely to contain unsaturated acids, such as linolenic, linoleic and oleic acid, the carbon double bonds present will lead to higher adiabatic flame temperatures irrespective of ignition delay, which in turn leads to higher PHRRs and therefore higher NOx emissions exhibited by FAME relative to diesel.[207,208] The degree of fatty acid unsaturation is unique to the biological source from which the FAME is

produced which leads to each source having a unique influence on NOx emissions.[169] Testing a heavy-duty engine in real world conditions, Mizushima et al. (2014) drove a vehicle around Tokyo with an built in emissions sampler. The vehicle was operated with FAME, ultra-low sulfur diesel, hydrogenated vegetable oil and a biomass to liquid fuel. Whilst accounting for different days of the year and different driving conditions, they found that FAME in particular led to increased NOx emissions compared to the other test fuels.[209]

Jamil et al. (2016) investigating waste biomass feedstocks focused on the potential of inedible date pits as these are a widely available waste stream in Oman. Following dehydration and mechanical grinding triglycerides were extracted from the date pits which were converted to fatty acid methyl esters via a base catalysed transesterification reaction. The extraction method yielded similar mass yields to soybean biodiesel production and the fatty acid profile analysis showed similarity to palm oil. The resultant date pit biodiesel properties, such as viscosity, density, flash point, cetane number etc were all found to be within the ASTM 6751 limits, concluding that date pits were a viable biodiesel source for Oman.[210]

Hellier et al. (2019) built upon the work of Famil et al. by testing the produced date pit methyl esters in a direct injection single cylinder compression ignition engine, comparing the fuel to soybean (SME) and rapeseed (RME) methyl esters which are commonly available in European biodiesel markets. Hellier et al. found that the DPME exhibited a similar duration of ignition delay as SME and RME at B20 and B100 blends. However, DPME exhibited a faster increase in peak heat release rates (PHRR), attributed to have a higher cetane number relative to SME and RME. DPME further exhibited lower NO_x than expected relative to SME and RME, suggested to arise from the higher degree of saturation of the former. Finally, there was little difference observed in the measured CO, THC and exhaust particulates between the DPME and RME B100 blends.[210,211]

Zhu et al (2016)[112] investigated the impact of FAME chemical structure on compression ignition engines, similar to the work of Schönborn et al (2009)[208]. The work performed by Zhu used a larger compression ignition engine, with a cylinder volume of 980cc and compression ratio of 17.5 which represents a significant increase in engine size from that used by Schönborn which had a

cylinder volume of 499.56cc and compression ratio of 15:1. The size difference between the two engines is significant enough to represent the change in operation from light to medium or heavy-duty CI engines and the engine used in Zhu's work is close in size to the D8k used in the work presented in this thesis. Both engines were operated at 1,200 RPM and controlled for constant IMEP (Schönborn) or constant BMEP (Zhu), which is different to this work which controlled engine speed at 820 RPM and without control for constant power. The tests were performed with single component FAMEs which are common in biodiesel, C12:0, C16:0, C18:0 and C:18:1. Schönborn et al. and Zhu et al. found the FAMEs exhibited shorter durations of ignition delay as the carbon number increased from C12 to C18 and both groups found the addition of a double bond to the fatty acid chain increased the duration of ignition delay. In both studies the single component esters produced higher nucleation mode particulates than the reference diesel. Schönborn et al. observed a clear difference with ester alkyl chain length and the number of nucleation mode particulates, C12 and C14 esters produced significantly fewer particulates than C16 and C18 esters with the number increasing from C12 to C18 whilst Zhu et al. observed no effect of chain length in their study indicating the physical environment of the larger engine's combustion chamber has less influence on particulate formation than the smaller engine.

Discussed in Chapter 1, given the continued electrification of light duty vehicles and the difficulty to bring fully electric heavy goods vehicles to market, it is likely that engines similar in size, or larger, than the Volvo D8k engine will remain reliant on liquid fuels for the foreseeable future. Engine speed and combustion chamber size have significant impact on air/fuel mixing and these physical parameters of engine design see the greatest change between light duty and medium duty engines.[28] As progress continues in removing the reliance of small vehicles on combustion engines with a concurrent need to increase utilisation of biofuels in large vehicles it is important to investigate how future fuels, such as DPME, perform in research facilities more representative of the engines which remain using these fuels.

7.1. Experimental outline

Three fatty acid methyl esters, RME and two DMPE samples from different production methods were tested at three blend ratios of B7, B30 and B100 to determine the fuel performance of a novel biodiesel derived from easily accessible waste streams in a heavy-duty compression ignition engine. Table 7.1 provides an overview of the fatty acid profile of the FAMEs tested. Table 7.2 further shows some chemical and physical properties of the FAMEs which can influence combustion. Finally, Table 7.3 provides an overview of the experimental conditions and shows some key values from combustion tests.

Table 7.1: Overview of the methyl ester test fuels and the mass ratios of the fatty acid esters in the fuel. 1. DPME GC-MS data assumed to be near identical to Jamil et al.[210] RME GC-Ms data assumed to be near identical to Hellier et al.[211]

FAME	Percentage FAME composition (% m/m)							
	C12:0	C14:0	C16:0	C16:1	C18:0	C18:1	C18:2	C18:3
DPME[1]	16.44	9.96	9.54	-	2.38	55.36	6.52	-
RME[2]	-	-	7.6	0.6	2.3	51.7	19.7	9.1

7.1.1. Apparatus

All of the combustion experiments described in the current chapter were performed using the heavy-duty compression ignition engine and ultra-low volume fuel system research facility described in Chapter 4. Unlike the experiments discussed in Chapters 5 and 6, the work presented here utilised an Omani fossil diesel as the reference diesel, provided by the researchers alongside the two DPME samples.

7.1.2. Experimental procedure

Each of the fatty acid ester fuels and Omani reference diesel were tested under identical conditions, the constant injection timing condition outlined in Chapter 4, where injection duration is held constant and IMEP varied according to fuel properties. Two samples of DPME provided were from different production methods to determine any change in fuel performance resulting from these two methods. The first sample was produced using date seed oils purchased in a local market and the second sample was produced using date seed oils extracted by the research team at Sultan Qaboos University (SQU). Due to a

limited volume available, the second sample, referred to as 'DPME-alt', was tested as a B100 blend only. The DPME produced from the primary production method and RME were tested at blend ratios of B7, B30 and B100 % (v/v) with the Omani reference diesel. Throughout this chapter, every reference to any fuel blend was mixed volumetrically unless otherwise stated.

A summary of these conditions is shown in Table 7.3 alongside some key results from the experiments. The viscosities and lower heating values for the test fuels are shown in Table 7.2. The quantity provided of the second DMPE sample was insufficient to derive any further experimental data apart from its engine test and is assume to be similar in property to the first production method, for which calorific values, density and viscosity is available.

*Table 7.2: Overview of physical and chemical properties which should be considered during fuel tests of the lactones and the reference diesel. Viscosity measured using a Brookfield III-Ultra rheometer. Gross calorific value measured using an IKA C1 bomb calorimeter. *c technical data for the reference diesel provided by Haltermann Carless.*

Fuel (Nomenclature)	Boiling point (^{o}C)	Density at 25 ^{o}C (g/cm^3)	Viscosity at 50 ^{o}C (Cp)	Gross calorific value (J/g)
Oman Reference Diesel (ORef. D)		-	2.260	46074 ± 166.03
Oman Date Pit Methyl ester (DPME)		0.870	3.315	39777 ± 61.00
Rapeseed methyl ester (RME)	-	-	3.310	39940 ± 73.1
Reference Diesel Ref. D	189.9 – 355.5 [c]	0.832 [c]	2.245	45,800 [c]

Table 7.3: Experimental test conditions and key experimental results for the fuel blend tests in the D8k engine at constant injection timing and injection times for constant start of combustion.

Fuel and blending ratio (v/v %)	Engine speed (RPM)	Fuel injection pressure (bar)	Injection timing (CAD BTDC)	Injection duration (CAD)	IMEP (Bar)	Ignition delay (CAD)	PHRR (j/deg)	Max average in-cylinder temperature (K)
Oman Reference Diesel	820 ± 20	695 ± 10	5.3	6.5	7.22 ± 0.05	5.1	297.50	1882.42
DPME B7	820 ± 20	695 ± 10	5.3	6.5	7.06	5	272.27	1867.81
RME B7	820 ± 20	695 ± 10	5.3	6.5	7.07	5.1	284.24	1897.53
DPME B30	820 ± 20	695 ± 10	5.3	6.5	6.67	5	256.57	1827.22
RME B30	820 ± 20	695 ± 10	5.3	6.5	6.99	4.9	268.55	1885.61
DPME B100	820 ± 20	695 ± 10	5.3	6.5	6.16	4.8	234.11	1786.65
DPME-alt B100	820 ± 20	695 ± 10	5.3	6.5	6.02	5	249.05	1775.57
RME B100	820 ± 20	695 ± 10	5.3	6.5	6.08	5	257.03	1800.10

7.2. Results

7.2.1. In-cylinder pressure and heat release rate
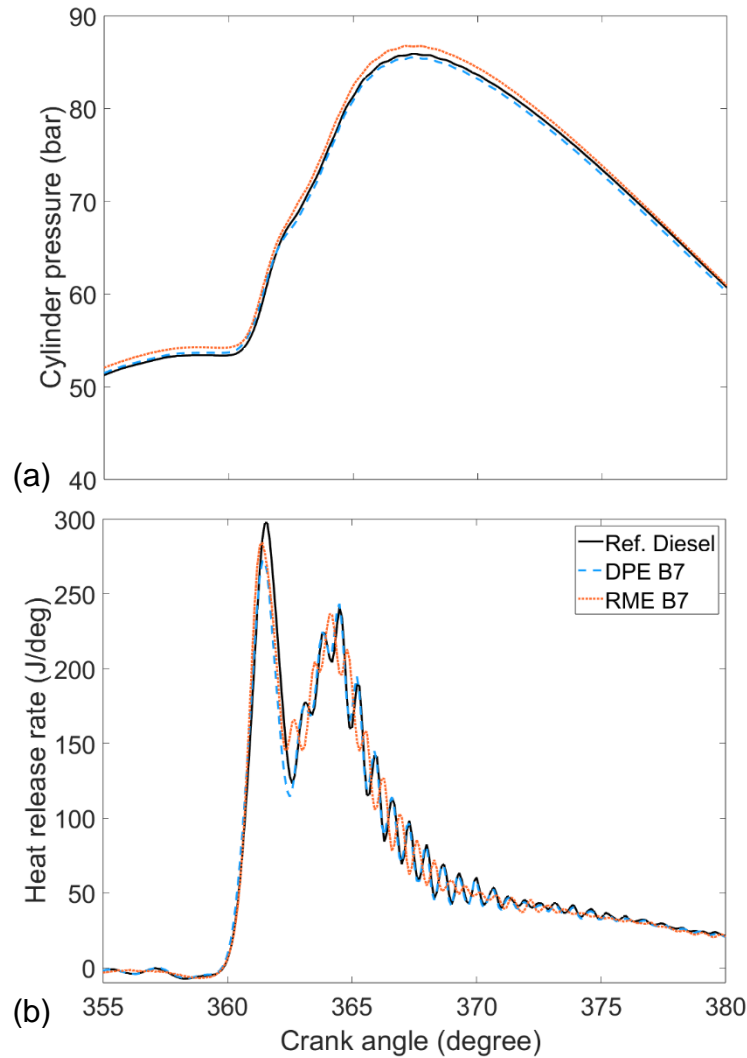
Figure 7.2: (a) In-cylinder pressures and (b) apparent net heat release rates of DPME and RME B7 blends and Omani reference fossil diesel.

Figure 7.2 shows the in-cylinder pressures and apparent net heat release rates of DPME and RME blended at a 7 % (v/v) blend ratio with Omani reference diesel, alongside undiluted Omani reference diesel. Apparent is the similarity between the three fuels tested, with the fuels exhibiting the same duration of ignition delay, similar peak heat release rates (PHRR) and level of premixed burn to diffusion-controlled combustion. This similarity is expected as the FAME content by % is very low; the US Department of Energy considers existing compression ignition engines as able to operate on biodiesel

blends up to 20 % (v/v) without any modification, therefore it would be expected that significant changes in fuel behaviour would be observed at blending ratios higher than 20 %.[212]
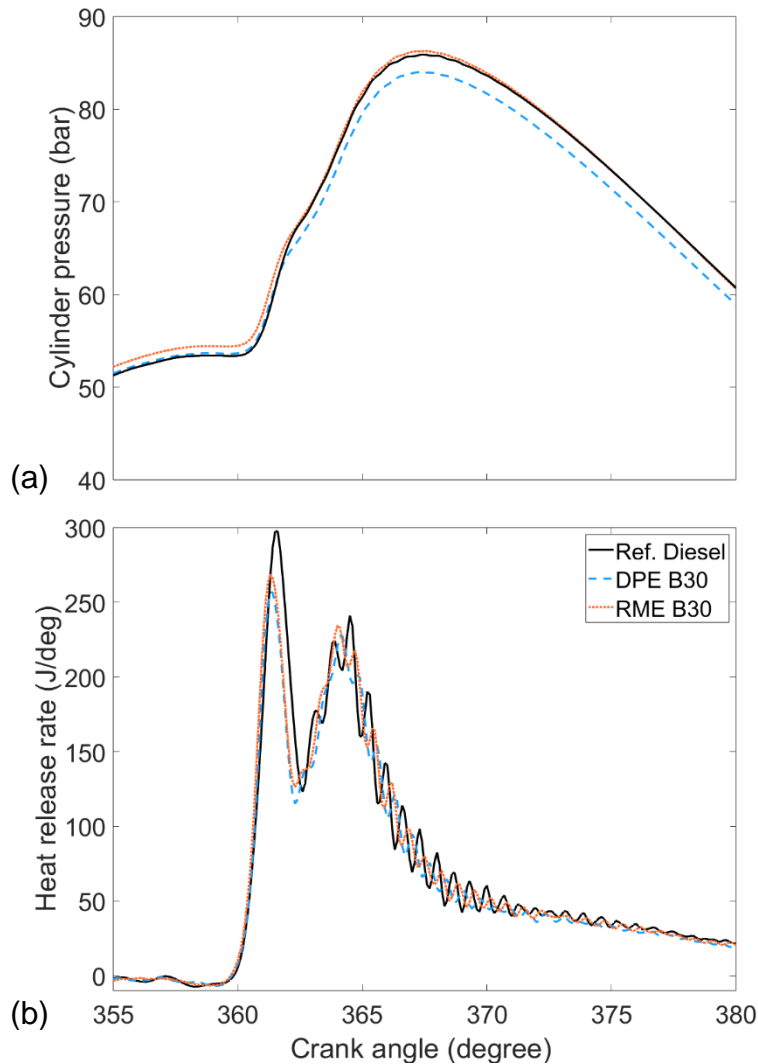
Figure 7.3: (a) In-cylinder pressures and (b) apparent net heat release rates of DPME and RME B30 blends and Omani reference fossil diesel.

Figure 7.2 shows the in-cylinder pressures and apparent net heat release rates of DPME and RME blended at 30 % with Omani reference diesel, alongside undiluted Omani reference diesel. Apparent is the continued similarity in the ratio of premixed burn to diffusion-controlled phases of combustion between the three fuels. The B30 blends are diffusion control dominated, following a short duration of ignition delay the premixed burn phase does not reach significantly higher peak heat release rates than observed in the diffusion control period, an observation in agreement with recent

works investigating B30 blend ratios of biodiesels in light and medium-duty engines.[189,213]

The DPME and RME B30 blends exhibit noticeably lower PHRRs than the reference diesel, but do not exhibit a significant difference to each other. Previously shown in Table 7.2, DPME and RME have very close lower heating values which are ~14 % lower than the Omani reference diesel. It is therefore expected that as the FAME content increases in the fuels blends that less energy is available per mL of the biodiesel blends. Table 7.2 also shows that the biodiesels have a higher viscosity than the reference fossil diesels and previously shown in Figure 7.6 the B30 blends have a shorter duration of ignition delay, by 0.1 CAD compared to the reference diesels. The lower PHRRs could also be attributed to a more viscous fuel blend and shorter ignition delay leading to less air-fuel mixing prior to ignition, and therefore lower peak heat release occurring.[169]
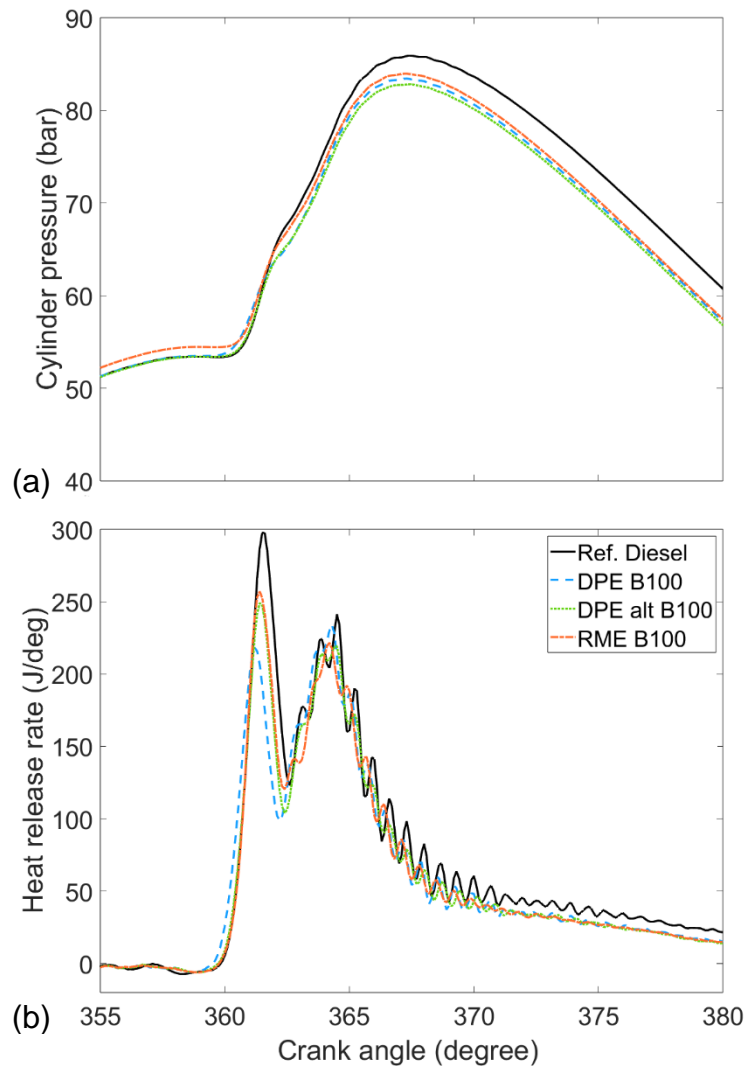
Figure 7.4: (a) In-cylinder pressures and (b) apparent net heat release rates of DPME and RME B100 blends and Omani reference fossil diesel.

Figure 7.2 shows the in-cylinder pressures and apparent net heat release rates of DPME and RME undiluted as B100 and alongside undiluted Omani reference diesel. Apparent is significantly lower PHRR exhibited by DPME-alt than the reference diesel. Shown in Figure 7.6, DPME-alt exhibited the lowest duration of ignition delay. A longer ignition delay allows for greater air / fuel mixing prior to autoignition so a larger portion of the mixture is close to stoichiometric prior to autoignition. Therefore a longer ignition prior to autoignition allows a greater portion of the fuel's chemical energy to be released during the premixed burn combustion phase.[214] Also apparent is the similar heat release rates in the diffusion-controlled

burn period, suggesting that the FAME test fuels each burn similarly to fossil diesel during this period.

It should also be highlighted that a more rapid decline in the HRR than fossil diesel is observed after 371 CAD, indicating a shorter duration of combustion. Finally, it is further apparent at this blending ratio that close similarity in ignition delay and PHRR is exhibited by the DPME and RME B100 blends, both of which is lower than the reference fossil diesel.
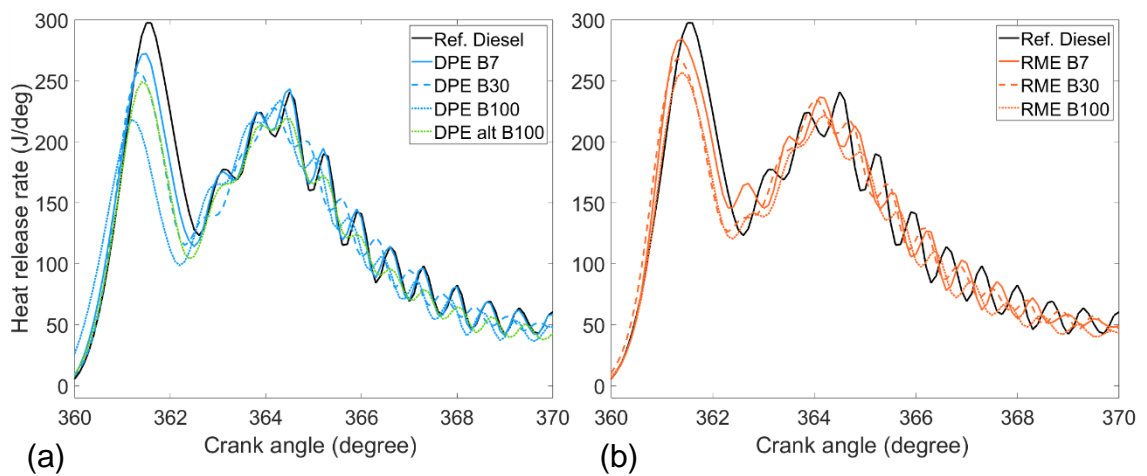
Figure 7.5: Apparent net heat release rates of DPME (a) and RME (b) fuel blends with Omani reference diesel (B0 test fuel blend).

Figure 7.5 shows the apparent net heat release rates of the DPME and RME test fuel blends. The trend apparent in both Figure 2.5a and 2.5b is that increasing the blend ratio in both DPME and RME leads to lower PHRRs. It can be further seen that the decreasing size of the premixed burn fraction is more pronounced in DPME than RME as the blend ratio increases. The observed fall in PHRR and the relative size of the premixed burn phase is in agreement with Sathyamurthy et al.'s (2021) recent work on distiller's corn oil methyl ester fuel blends tested in a light duty engine, observing that increased blend ratios from B0 to B30 lead to lower PHRRs and smaller premixed burn factions relative to the reference diesel.[213]

Increasing the blend ratio had an effect on lowering the HRRs observed during the premixed burn period but did not significantly

187

lower the rates observed during the diffusion-controlled burn phase, which will affect the NOx and particulate emissions which are sensitive to the duration of each combustion phase. Similar behaviour during the diffusion-controlled burn phase suggests that the premixed burn phase is influenced by more by the flow of fuel into the combustion chamber and the shorter ignition delays exhibited by increasing the blend ratio.

7.2.2. Ignition delay
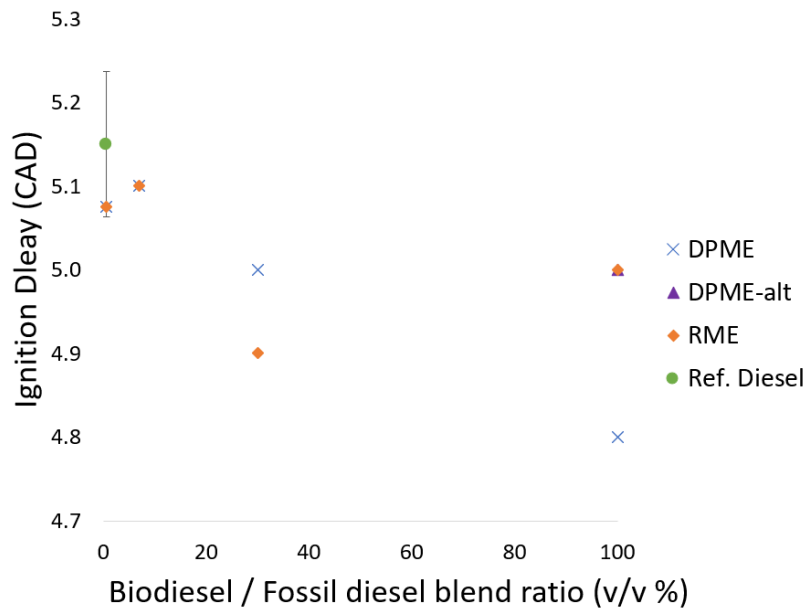
Figure 7.6: Ignition delay of DPME and RME fossil diesel blends and DPME alt B100. Reference diesel shown is the standard diesel throughout all tests, B0 is the Omani reference diesel with which the esters are blended.

Figure 7.6 shows the impact on the duration of ignition delay resultant from varying the level of either DPME or RME in blends with diesel. As previously stated in Chapter 2, ignition delay is defined as the interval between fuel injection and the start of combustion. The general trend apparent for both RME and DPME blends is a reduction in the duration of ignition delay as the biodiesel fraction in the fuel blends increases (Figure 7.6). It should be noted that the resolution of the shaft encoder in the testing facility is 0.1 CAD, so it is not possible to state with certainty that this is a significant trend. As discussed in Chapter 4, each data point is the average over 100 combustion cycles, so it can be concluded that as an undiluted fuel,

DPME exhibits a shorter duration of ignition delay than RME. Of further note is that the secondary production process of the date pit ester (DPME-alt) results in a duration of ignition delay closer to RME than that of the biodiesel produced by the primary production method (DPME B100).

Perhaps of greater importance however, than any overall impact of FAME blend level on ignition delay, is the observation that at all blending ratios, with the exception of the undiluted biodiesels, there is little difference between DPME and RME (Figure 7.6).

7.2.3. IMEP
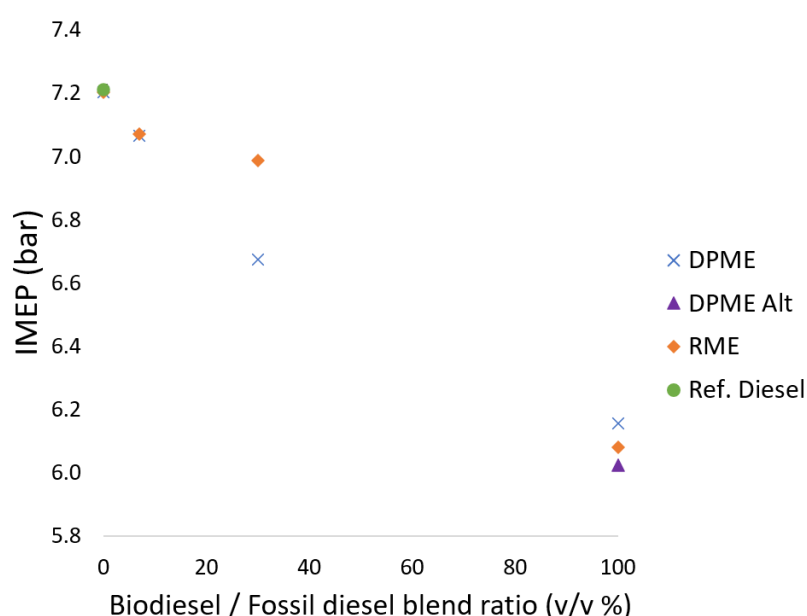
Figure 7.7: Indicated mean effective pressure (IMEP) of fatty acid methyl ester blends and reference diesel at constant injection timing and duration. Error bars are plotted, but are visually insignificant owing to the low variation in reference diesel tests.

Figure 7.7 shows the IMEP of the DPME and RME B0, B7, B30 and B100 blends. Readily apparent is a reduction in IMEP exhibited by the fuels as the biodiesel portion in the blend increases. This is expected as the experiments were performed with a constant injection duration and the FAMEs have a lower calorific value (Table 7.2), therefore as the volumetric % of the FAME increases, a lower amount of chemical energy is available each combustion cycle. The reduction in IMEP observed is proportional to the calorific content,

with the B100 blends exhibiting IMEP's approximately 14% lower than the B0, matching the difference in calorific values.

At the B7 and B100 blend ratios, DPME and RME exhibit similar IMEPs, indicating little difference in combustion performance between the biological oil sources.
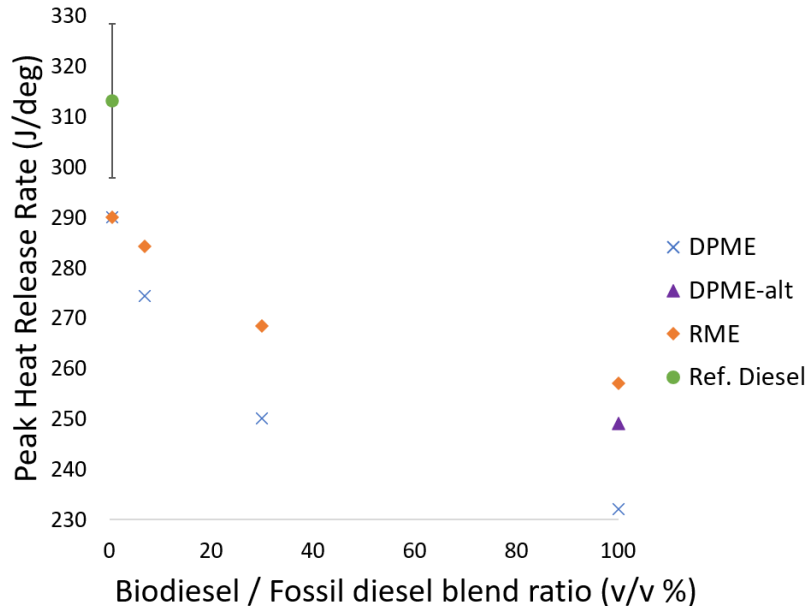
Figure 7.8: Peak apparent heat release rate of DPME and RME B0, B7, B30 and B100 % (v/v) blends with Omani reference fossil diesel. All the observed PHRRs observed occur during the premixed burn phase of combustion, except for DPME B100 which occurs during the diffusion-controlled phase.

Figure 7.8 shows the apparent PHRRs of the DPME and RME blends. The trend apparent is a reduction in the PHRR as the blending ratio increases for both the DPME and RME blends. Previously shown in Figure 7.6 there is a slight trend in reduced ignition delay with increased blending ratio. Duration of ignition delay is associated with a higher PHRR as it allows time for greater air / fuel mixing prior to autoignition and a greater portion of the fuel is mixed to within the flammability limits. Thus, less fuel is consumed in the premixed burn faction of combustion and is instead consumed over a longer period of time during diffusion combustion.[20] The injection duration used in the tests is longer than the duration of ignition delay exhibited by the FAMEs, so the duration of the diffusion flame depended on the rate fuel enters the chamber. The DPME

190

B100 blend exhibited the lowest PHRR of all the fuel blends tested and was also the only fuel test for which the PHRR was observed during the diffusion-controlled combustion phase. DPME also exhibited the shortest duration of ignition delay, indicating that compared to the remaining fuel blends, a significantly smaller amount of the fuel had sufficiently mixed with air prior to combustion.

Also apparent is the lower PHRR exhibited by DPME relative to RME at each blending ratio. DPME has a higher cetane number than RME (58 vs 52), so increased reactivity during the low temperature region prior to autoignition would be expected, even though this does not reflect in significantly different durations of ignition delay at the B7 and B30 blend ratios (Figure 7.6) as higher reactivity will shorten the time available for air fuel mixing prior to autoignition.[124,210,211]

Of interest is how this result compares to the previous work from Hellier et al. (2019), where in a light duty high speed diesel engine DPME was found to have higher PHRR's than RME and SME, attributed to its higher reactivity.[211] The ignition delay of DPME B100 was reported as 4.0 CAD, shorter than the finding presented in this work. Additionally, the engine testing facility was operated at 1200 RPM, significantly faster than the Volvo D8k testing speed of 820 RPM. The slower speed of the D8k and longer durations of ignition delay than previously reported have led to a significant change in the fuel's behaviour relative to the reference RME. Hellier et al reported that DPME exhibited a similar ignition delay and higher PHRR relative to RME, but in the work presented here a shorter ignition delay and lower PHRR relative to RME was observed. The timing of PHRR has also changed from the premixed burn phase in the high speed to engine to later in mixing-controlled diffusion phase in the slow speed engine, whilst the behaviour of RME has remained similar. In the smaller engine, the PHRRs and ignition delays observed were insensitive to the differences in fuel chemistry and reactivity, in contrast the higher reactivity of DPME relative to RME results in a shorter ignition delay and lower PHRR which result in

DPME exhibiting a longer duration of combustion. This highlights the importance that future fuels be tested within the context of the internal combustion engines which will remain reliant on these fuels.
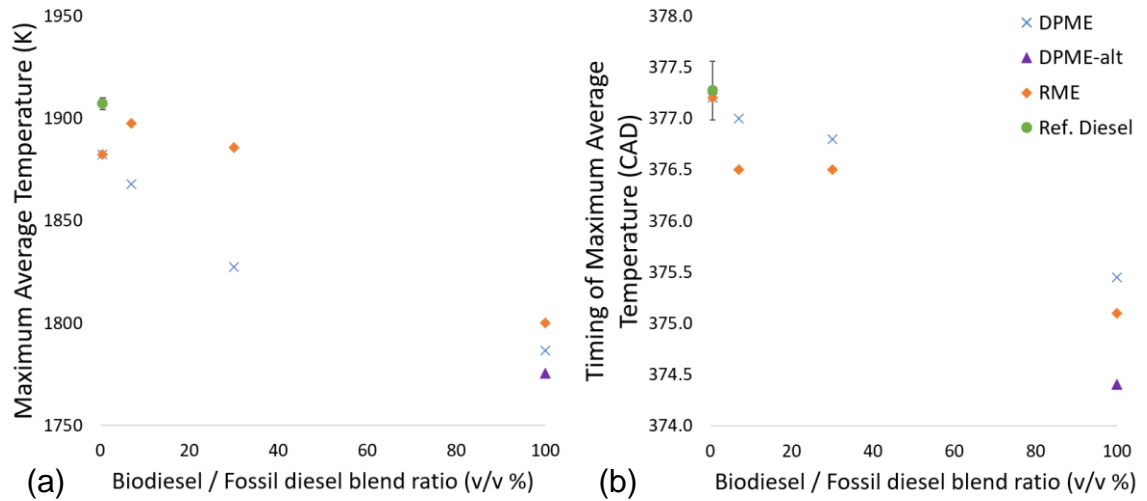
Figure 7.9: Maximum average cylinder temperature (a) and timing of maximum temperature (b) vs DPME and RME blend ratio.

Figure 7.9a and Figure 7.9b show the calculated maximum in-cylinder global temperature and time at which it occurs respectively for the DPME and RME blends with Omani reference diesel. A trend observed in Figure 7.9a is that increasing the blend ratio of DPME to diesel content lowers the maximum calculated average temperature. The RME B100 blend also exhibits a significantly lower maximum temperature then the reference diesel (B0), so similar to DPME B100, but the B7 and B30 RME blends exhibit a higher temperature than B0.

Apparent from Figure 7.9b is that for both DPME and RME, increasing the blend ratio leads to an earlier onset of the maximum average temperature. The duration of ignition delay exhibited by the blends differs only by a maximum of 0.3 CAD (Figure 7.6) and the maximum temperature is reached almost 2 CAD earlier. Discussed previously, increasing the blend ratio reduces the amount of energy available from each fuel injection and a higher blend ratio is also associated with a lower PHRR (Figure 7.5). The maximum in-cylinder

average temperature occurring earlier as blend ratio increases correlates with lower maximum in-cylinder temperature. It is suggested therefore that the earlier in-cylinder maximum temperature is entirely attributable to less energy being available each cycle. This can be seen in Figure 7.10, where increasing the blending ratio of DPME in the test fuel leads to a consistent reduction in temperature throughout combustion.
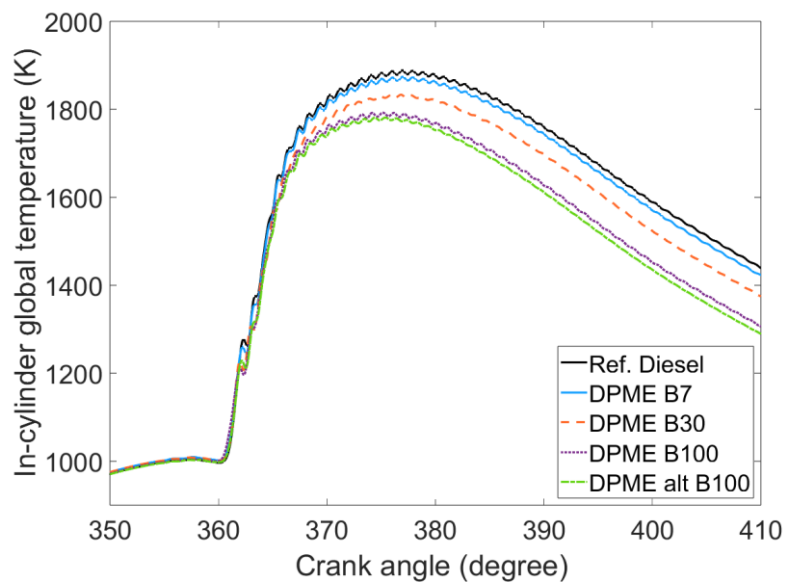
Figure 7.10: In-cylinder global temperature of the DPME fuel blends and Omani reference Omani diesel.

Figure 7.10 shows the calculated in-cylinder global temperatures during combustion of the DPME test fuel blends. Apparent is the lower temperatures achieved throughout combustion as the blending ratio increases. In-cylinder temperatures are cumulative and dependent on the amount of energy available to burn. As previously discussed, the lower calorific value of DPME than the reference diesel, and the constant injection duration employed leads to a lower amount of total energy being available from each fuel injection as the FAME blending ratio increases. As the durations of ignition delay are similar between the blends (Figure 7.6), the lower amount of energy available from the higher blend ratios results in a lower maximum temperature will be achieved sooner.

193
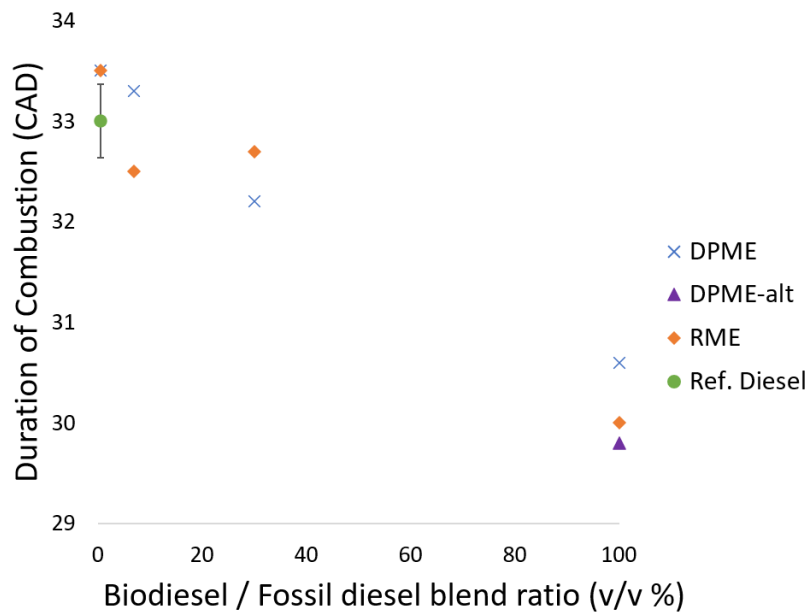
Figure 7.11: Calculated duration of combustion for the DPME and RME test fuel blends with Omani reference diesel.

Figure 7.11 shows the duration of combustion for the DPME and RME test fuel blends. Clearly apparent is the shorter durations of combustion exhibited by the B100 test fuel blends. This is to be expected given the reduced level of fuel energy supplied each combustion cycle owing to the lower calorific values of the FAMEs tested relative to the reference diesel.

An important result observed here is the longer duration of combustion exhibited by DPME than RME or DPME-alt at the B100 blend ratio. This related to the previously discussed shorter duration of ignition delay and the PHRR occurring in the diffusion-controlled combustion phase, indicating the combustion of DPME is dominated by the slower diffuse flame.

7.2.4. Exhaust emissions
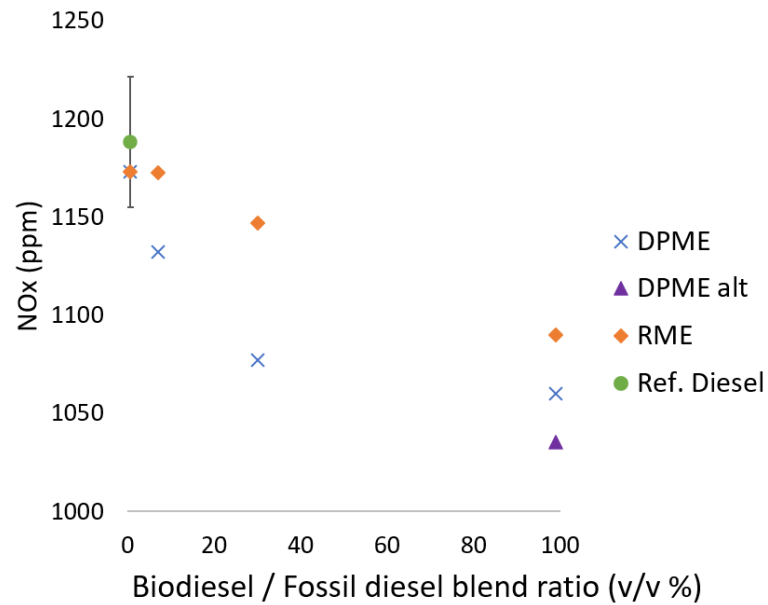
Figure 7.12: Exhaust gas NO$_x$ emissions of DPME and RME fuel blends with Omani reference diesel. DPME results taken as an average of two runs on separate days.

Figure 7.12 shows the measured NO$_x$ emissions during combustion of the DPME and RME test fuel blends and Omani reference diesel (B0). An additional fossil reference diesel is shown with error bars which are generated from multiple runs at the beginning and end of each day of experiments to show the variability of the set-up. Apparent is a linear decrease in NO$_x$ emissions as the blending ratio of both FAMEs increases. The observed trend aligns closely with that of IMEP (Figure 7.7), which is expected as thermal NO$_x$ production is highly dependent on elevated in-cylinder temperatures (>1600 K) and the residence time of the gaseous combustion products in the cylinder.[207,208]
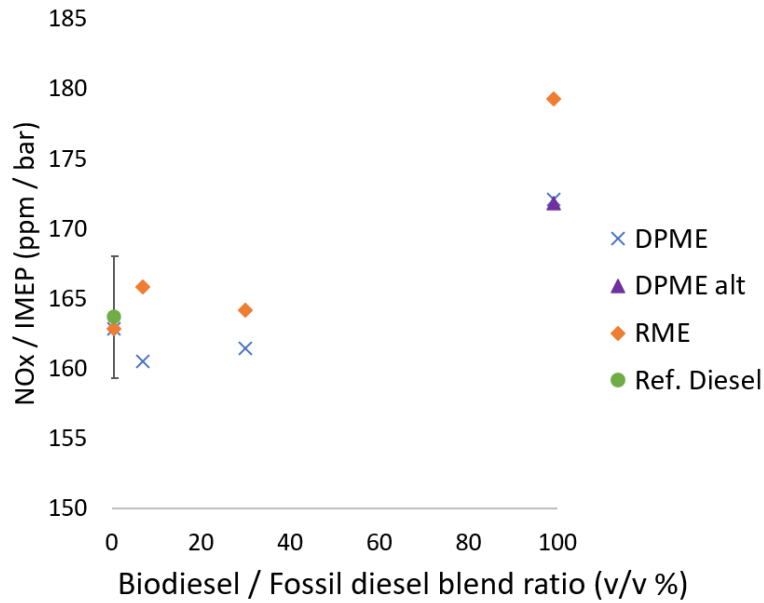
Figure 7.13: Exhaust gas NOx emissions of DPME and RME fuel blends with Omani reference diesel, normalised with respect to IMEP.

Normalising the NO_x values with respect to IMEP yields Figure 7.13. While the B0 to B30 fuel blends no longer show a clear trend in NOx, clearly apparent is that the B100 fuel blends exhibit higher than expected NO_x emissions for the in-cylinder pressures measured during combustion. This can be attributed to the shorter duration of ignition delay (Figure 7.6) and durations of combustion (Figure 7.11) exhibited by the DPME and RME B100 blend ratios. Earlier autoignition than the reference diesel and shorter duration of combustion allows a longer time for the gaseous products of combustion to mix in the cylinder at high temperatures and pressures prior to the freezing of NO_x kinetics.[164,215] The lower NOx emitted by both DPME B100 test fuels could also be attributed to a theoretically lower adiabatic flame temperature. DPME has a higher degree of saturation and exhibits a shorter ignition delay than RME, both of these observations have been previously linked to a lower adiabatic flame temperature and lower resultant NOx emissions.[185, 208, 210,216]
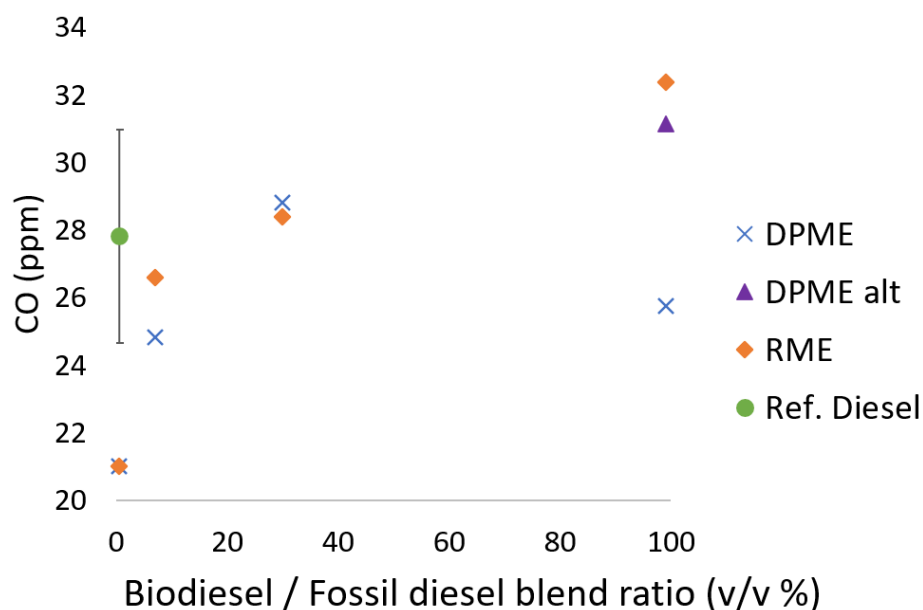
Figure 7.14: Exhaust gas CO emissions of DPME and RME test fuel blends with reference Omani fossil diesel. Ref. Diesel and error bars included to show experimental variability.

Figure 7.14 shows the measured gaseous CO emissions from the DPME and RME test fuel blends. It is difficult to attach much weight to results shown as the magnitude of the observed emissions is remarkably small, likely due to the relatively slow speed of the D8k and lean combustion conditions facilitating complete combustion. An observation which can be made when considering the B100 tests, is the lower emissions of DPME relative to DPME-alt and RME. A lower CO value exhibited by DPME than RME is possibly due to the shorter fatty acids found in date pits than rapeseed (Table 7.2), so DPME contains a higher ratio of molecular bound oxygen to carbon than RME, which may facilitate more complete combustion and thus less CO. The lower CO may also be attributable to the shorter ignition delay exhibited by DPME over the remaining two B100 FAMEs. A longer duration of ignition delay allows for more fuel to enter the combustion chamber and move away from the jet prior to autoignition, so over dilution of some parts of the air fuel mixture can occur, where the fuel does not sufficiently ignite, generating products of incomplete combustion such as CO.
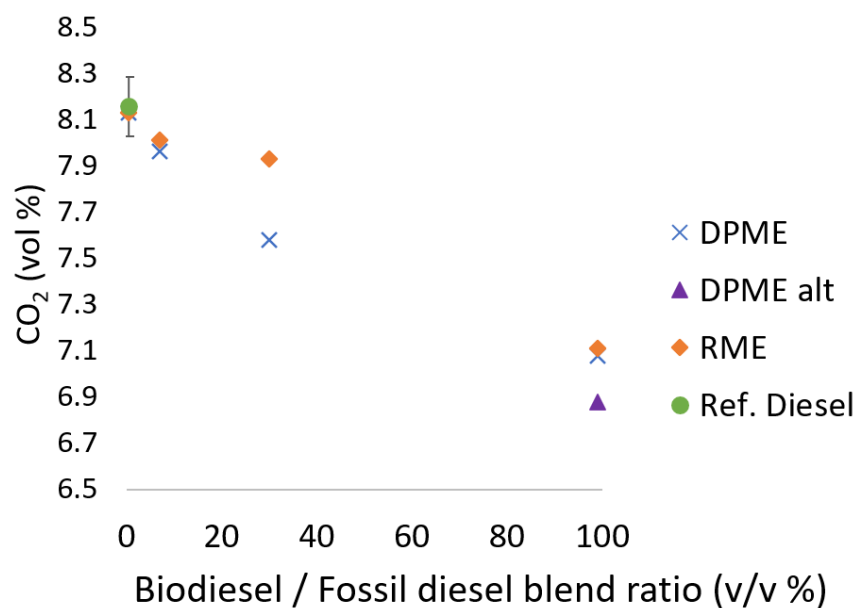
Figure 7.15: Exhaust gas CO2 emissions of DPME and RME test fuel blends with reference Omani fossil diesel. Ref. Diesel and error bars included to show experimental variability.

Figure 7.15 shows the measured gaseous CO_2 emissions from the DPME and RME test fuel blends. The trend apparent is a reduction in the volume of CO_2 measured as the test fuel blending ratio increases. This trend aligns closely with the IMEP values shown previously in Figure 7.7. CO_2 results from the complete oxidation of the available fuel carbon and so the level detected is reliant on the amount of fuel carbon provided. As discussed previously, the constant injection duration testing conditions and oxygen content of DPME and RME means that less carbon is available during combustion as the FAME blend ratio increases.
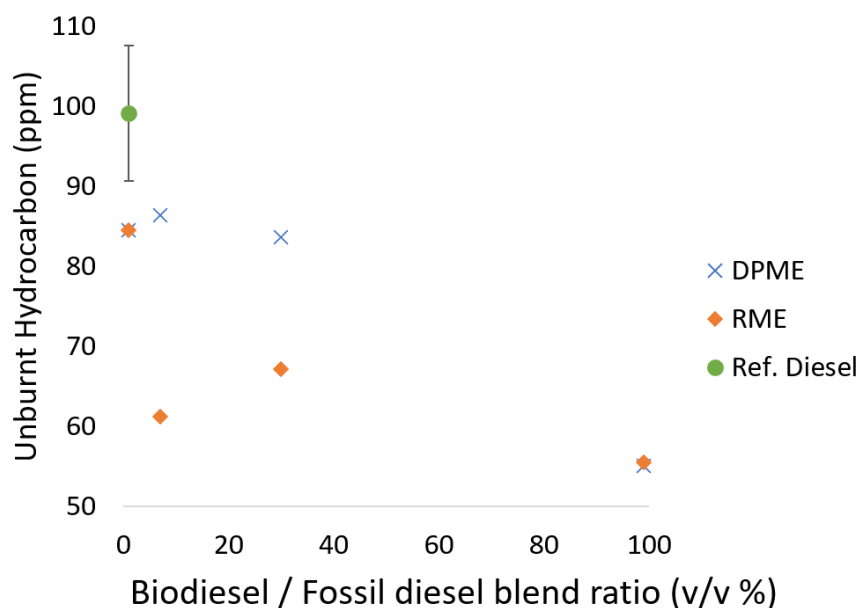
Figure 7.16: Exhaust gas unburnt hydrocarbon emissions of DPME and RME test fuel blends with reference Omani fossil diesel. Ref. Diesel and error bars included to show experimental variability. Results shown are from different tests than previous results due to equipment error. DPME-alt was not available for this test batch.

Figure 7.16 shows the unburnt hydrocarbon (THC) emissions of the DPME and RME test fuel blends with Omani reference diesel. The trend apparent is a reduction in THC as the blending ratio increases. Unburnt hydrocarbons form when either very lean or very rich areas of air / fuel mixture fail to sustain a self-propagating flame, which will leave areas of air fuel mixture unconsumed.[93]

DPME and RME exhibit similar levels of THC emissions as unblended test fuels, whilst at the B7 and B30 blending ratios DPME exhibits higher THC emissions than RME. DPME has a higher cetane number than RME, so it might be expected that DPME undergoes a more efficient combustion process. However, previously shown in Figure 7.9a, the DPME B7 and B30 blends reach lower calculated maximum average in-cylinder temperatures than the RME blends, whilst the B100 blends are quite similar. The higher THC emissions from the DPME B7 and B30 blends therefore may be attributable to lower in-cylinder temperatures relative to the RME blends, leading to comparatively less efficient combustion.
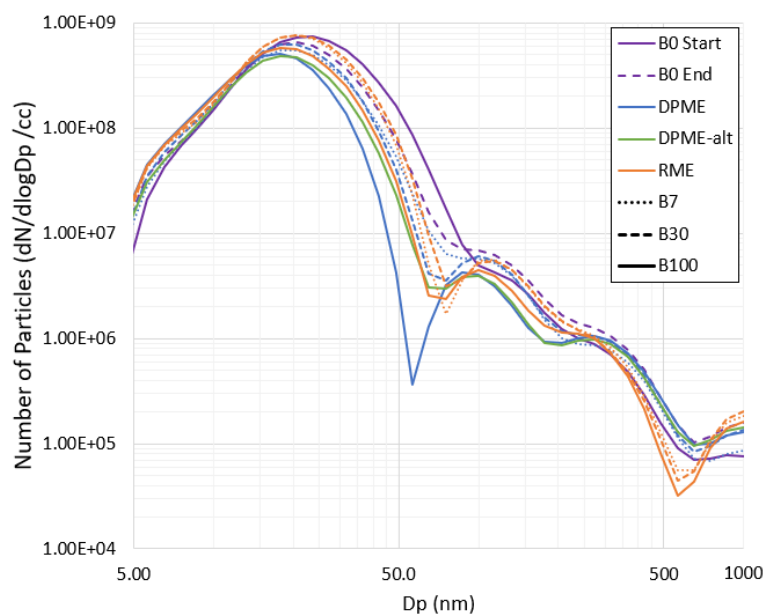
Figure 7.17: Particulate emissions of the DPME and RME test fuel blends.

Figure 7.17 shows the particulate emissions of the DPME and RME test fuel blends and also two measurements of the B0 measurements of B0 reference fuel so as to provide an indication of variability. Immediately apparent is the significantly lower number of nucleation mode particulates (>50 nm) detected from the DPME B100 blend than the remaining FAME blends and the reference diesel. This is likely due to the higher degree of saturation of DPME relative to RME (Table 7.1). Higher levels of unsaturation in the alkyl chain facilitates PAH formation as fewer H-abstractions are required to form unsaturated C2 and C3 species which act as precursors to benzene.[165] DPME also has a relatively higher oxygen content than RME which may also lead to reduced soot formation, which occurs in fuel-rich areas of the air/fuel mixture and insufficient oxygen availability allows pyrolysis reactions to occur. The higher oxygen content available will facilitate the oxidation of newly formed soot particles.[169, 208,217]

Each of the DPME and RME test fuel blends emit a higher level of ultrafine particles (<10 nm) than the reference Omani diesel. However, a cross-over occurs at ~20 nm where the reference diesel begins to emit a much larger number of particles and continues to do

200

so up to sizes of ~ 100 nm. The end of day diesel run continues to emit a higher number of particulates up to 400 nm.

Each of the RME fuel blends emit a lower number of particulates than the DPME blends and the reference diesel between 400 to 750 nm. This may be attributable to the higher in-cylinder temperatures achieved by the RME blends than DPME blends, allowing for more soot present in the later stages of combustion to be burnt off in the diffusion flame.

The final point observable from the particulate size distribution is the higher levels of accumulation particulates above 750 nm detected from all the DPME and RME blends relative to the reference diesel. This can be attributed to the shorter durations of combustion as the blending ratio of FAME increases (Figure 7.11), which would prevent the production of further soot precursors but also stop oxidation of soot particles, allowing a longer time at high pressure for soot agglomeration to occur.

Comparing the observed particulate distribution to the previous work by Hellier et al. DPME tested in the D8k forms soot more readily relative to fossil diesel, as there is little difference in the number of nucleation mode particulates observed but the D8k's slower engine speed possibly allowed more time for agglomeration to occur, forming larger soot species.[211]
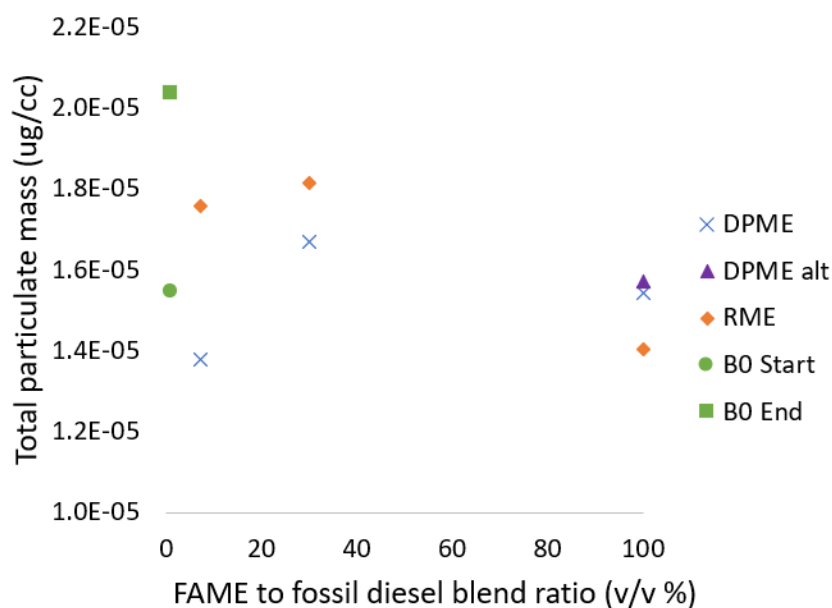
Figure 7.18: Total particulate mass emitted by the DPME and RME test fuel blends.

Figure 7.18 shows the total particulate mass emitted by the DPME and RME test fuel blends. Apparent is the similarity in total mass of the detected particulates, highlighting that the previously mentioned shorter duration of combustion could lead to a reduction in nucleation mode particles but significant increase in accumulation mode particles emitted from the DPME and RME test blends.

The B100 blends emitted fewer particulates than the B7 and B30 blends, which is to be expected as increasing the blend ratio reduces the fossil diesel content. Fossil diesel contains a high number of aromatic species which act as soot percussors, so as the blending ratio increases, the amount of these soot percussors decreases. FAMEs typically produce lower total particulates than reference fossil diesel, owing to more efficient combustion and the oxygen content available to oxidise soot.[121,205]

However, the results imply the testing conditions employed were not optimised in consideration of the physical differences between FAME and fossil diesel, as the RME B7, B30 and DPME B30 blends produced a higher number of particulates relative to the fossil diesel. This result is unique to the D8k, as Hellier et al. found that the

202

particulate mass decreases as the blend ratio of DPME and RME increases.[211]

7.3. Viability of date pit fatty acid methyl esters

It is clear from the results discussed in Sections 2.1 to 2.4 that date pit methyl ester, which is the focus of this study, exhibits similar combustion phasing (Figure 7.2 to Figure 7.4), gaseous emissions (Figure 7.12 to Figure 7.16) and particulates (Figure 7.17 to Figure 7.18) to rapeseed methyl ester, a commonly used biodiesel blend component in Europe.

DPME contains less unsaturated esters than RME and this change in molecular structure has observable impacts on the combustion profiles. As a B100 test fuel DPME has a shorter duration of ignition delay (Figure 7.6) than RME, resulting from its higher level of saturation and which leads to lower peak heat release rates (Figure 7.5).[169] This further impacts the observed emissions from DPME by leading to lower in-cylinder temperatures (Figure 7.9), therefore causing a slight decrease in measure NO_x emissions (Figure 7.12) and slightly higher unburnt hydrocarbon emissions (Figure 7.16) relative to the RME blends.

From the results it is also clear that the B30 blend ratios of DPME and RME exhibited a significant difference in IMEP (Figure 7.7), maximum in-cylinder temperature (Figure 7.9a) and CO_2 % (Figure 7.15) which is more pronounced than any difference between the B7 and B100 blends. Further work would be needed to determine if this resulted from experimental error, or, if at other blending ratios DPME changes the test fuel blend properties at lower blend ratios than RME.

7.4. Conclusions

This chapter presented an investigation of date pit methyl esters relative to rapeseed methyl esters in a heavy-duty compression engine, building upon previous research to source new viable waste streams for biofuel feedstocks.

- Date pit methyl esters exhibit a shorter duration of ignition delay and lower peak heat release rate than rapeseed methyl esters, attributable to the higher degree of saturation in the date pit fatty acid profile.

- At the B7 and B100 blending ratio, the observed differences in IMEP, duration of combustion, maximum in-cylinder temperature, gaseous emissions and particulates were small but significant enough to observe less NO_x and more THC from the DPME blends than the RME blends.

- At the B30 blending ratio significant difference in IMEP and maximum in-cylinder temperature was observed between the DPME and RME test fuels, leading to a more pronounced reduction in gaseous NO_x emissions and increase in THC emissions.

- The observed lower NO_x emissions and higher THC emissions from the DPME blends is in agreement with previous work investigating date pit esters in a light-duty high speed compression ignition engine, so it can be concluded that the chemical differences between DPME and RME which control the formation of these two pollutants, are persistent regardless of engine size.

- In their work, Hellier et al. found DPME to exhibit higher peak heat release rates than RME and commented that the lower observed NO_x is counterintuitive to this result. In the heavy-duty D8k, DPME was observed to have lower peak heat release rates than RME which better aligns with the observed lower gaseous NO_x values of DPME than RME. DPME's should exhibit higher reactivity in the period of low temperature reactions prior to autoignition, as it has a higher cetane number than RME. The medium-duty D8k engine's slower speed relative to the previous work presents more time for differences in chemical reactivity between fuels to present more clearly as unique combustion properties.

- DPME B100 exhibited a shorter duration of ignition delay than the RME B100, attributed to DPME's higher relativity, which was significant enough to limit fuel consumption in the premixed-burn phase relative to RME. DPME instead favoured higher rates of heat release in the diffusion-controlled burn phase and a longer duration of combustion than RME.

- From this work it is clear that date pit waste streams should receive further attention as a source of biofuels. At the B7 and B30 test fuel blend ratios, despite clear trends presenting between DPME and RME, the absolute difference in combustion behaviour presented is not significant enough to disregard the potential of a date pits as a biofuel feedstock. At the B100 test fuel blend a significant difference in combustion phasing was observed, but, B100 is not a commercially available fuel in major road fuel markets.

8. Upgrading readily available simple molecules to compression ignition viable future fuels

This chapter differs from those presented thus far in this work. The previous chapters have focused on engine testing of test fuels which were readily available from chemical suppliers. This chapter differs from the previous as we include a chemical synthesis to produce a specific molecule and then optimise an alternative route to produce a novel fuel blend. The synthesis of the novel mixture will be discussed in full followed by testing of the product in engine experiments, in a similar format to the previous chapters.

The starting component for the synthesis undertaken and for these blends is tetrahydrofurfuryl alcohol (THFA), the molecular structure of which is shown in Figure 8.1. THFA is a poor candidate for use as a single component fuel or major blend component for compression ignition engines highlighted by its low cetane number of 17.9.[124]
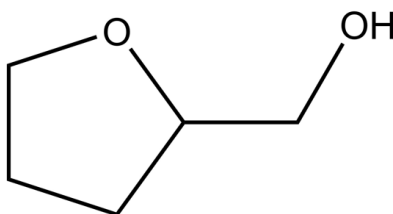
Figure 8.1: Molecular structure tetrahydrofurfuryl alcohol.

As previously discussed in Section 2.2.7, THFA can be easily produced from processing hemicellulosic sugars found in biomass making it an ideal molecule to consider as a biofuel.[176] THFA has been a research focus for decades finding many uses in the chemical, agricultural and construction industries. In 1939, the Quaker Oats company published an outlook on their furan productions claiming that THFA has found uses as a motorcycle fuel and diesel fuel ignition improver.[218,219]

Xing et al. (2011) published an extensive study of both the technical and economical optimization of furfural production and were able to produce furfural at \$366 per tonne, as of 2011, (with crude oil costing \$412 per tonne at this time).[76,77] The natural abundance of hemicellulose and ease with which furfural can be produced makes it an ideal starting point for future fuels. Furfural can be readily converted into many different alcohols, all of which can be converted to ethers, however THFA is unique amongst these alcohols as there is a functional limitation to its reactivity. Under catalytic acidic conditions, furfuryl alcohol's aromaticity would lead to branching macrocyclic products and pentanediol would polymerise into a plastic.[78,220]

To convert THFA into a fuel which is more suitable for a compression ignition engine, the cetane number must be improved by chemical conversion into a more suitable form. Previous work into producing large molecules which resemble those found in diesel often focuses on catalytically breaking the furan ring to form a straight chain or by chemically combining furan monomers into large oligomers and then hydrodeoxygenating with heavy metal catalysts.[221] This final hydrodeoxygenation requires higher pressures and further heavy metal catalysis than the hydrogenation of furan alone[78]

An alternative possible route to upgrade THFA to a molecule with preferable performance in compression ignition engines would be to convert it to an ether, which are known ignition improvers.[222] Shown below in Figure 8.2 and Figure 8.3 is a brief outline of how changing the number of carbons, presence of oxygenates and bonding structure of oxygenates leads to improved ignition quality. By looking at the changes in cetane number resultant from simple chemical changes predictions can be made about molecules which have not yet been investigated for ignition quality.
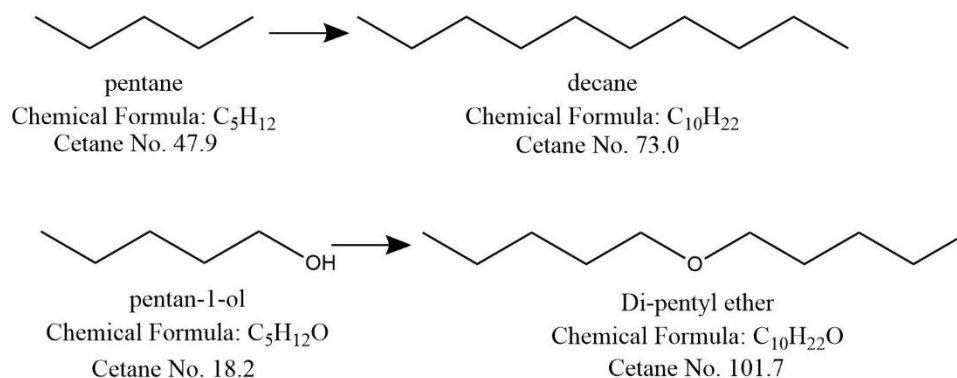
Figure 8.2: Overview of cetane numbers of n-alkanes, alcohols and ethers built from the C5 pentane unit. Cetane numbers taken from the Compendium of Experimental Cetane Numbers, Ratcliffe et al. 2017.[124]

Figure 8.2 shows four different molecules derived from n-pentane and their cetane numbers. Firstly, it can be seen that doubling the size of n-pentane to n-decane increases the cetane number from 47.9 to 73.0. Secondly, the inclusion of an alcohol group to pentane decreases the cetane number from 47.9 to 18.2. Thirdly, converting pentanol to a bis-ether increases the cetane number significantly from 18.2 to 101.7. Finally, it can be seen that the inclusion of an ether oxygen group in n-decane increases the cetane number from 73.0 to 101.7. This is important to note as it shows that the position and bonding environment of an oxygen molecule in alkanes is critical to predicting changes in cetane number. Alcoholic oxygens decrease the cetane number (pentan-1-ol vs pentane), whilst etheric oxygens increase the cetane number (di-pentyl ether vs pentan-1-ol).
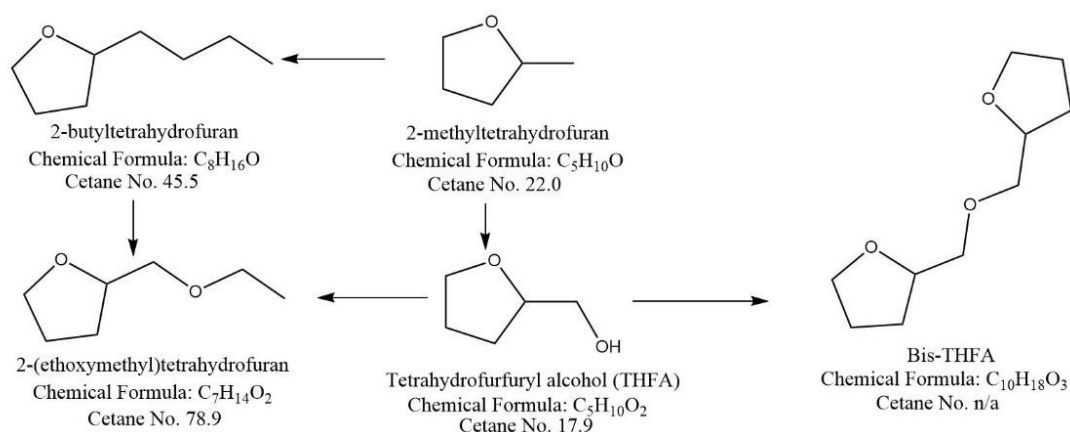
Figure 8.3: Overview of cetane numbers of alcohols and ethers containing 2-methyl THF. Cetane numbers taken from the Compendium of Experimental Cetane Numbers, Ratcliffe et al. 2017.[124]

Figure 8.3 shows four important changes in the chemical structures of saturated furans, starting from 2-methyl THF and the resultant changes in cetane number. Firstly, the effect of increasing the length of an alkyl chain is again observed, as increasing the side chain on 2-methyl THF by 3 -CH_2 groups to 2-butyl THF more than doubles the cetane number. The second change shown is the changing of a -CH_2 group in 2-butyl THF to an etheric oxygen which increases the cetane number from 45.5 to 78.9. Thirdly, as seen before in Figure 8.2, the inclusion of an alcohol group to form THFA from 2-methyl THF reduces the cetane number. The final conversion shown of THFA to 2-ethoxylmethyl THFA is that of the alcohol group to an ether and emulates that of pentanol to di-pentyl ether, shown in Figure 8.2, which resulted in a significant increase in cetane number. Bis-THFA has not previously been investigated as a fuel, so the cetane number is not available, but based on the conversions discussed it is possible that bis-THFA has a significantly higher cetane number than THFA which would result in a lower duration of ignition delay.

Given the significant reduction in ignition delay associated with the ether functional group, it is possible that a cyclic alkane with ether bonds will have satisfactory performance in compression ignition engines without the need for further intense processing such as

hydrodeoxygenation. This work therefore focuses on investigating the viability of converting a poor performance molecule into a higher performance product by converting alcohols to ethers.

A typical occurrence in biofuel production and research is the continual conversion of bio-molecules into structures which become indistinguishable from fossil diesel, often necessitating the use of energy intensive processes and specialist catalysts containing rare earth metals.[223] Investigating the combustion characteristics of cyclic ethers relative to fossil diesel will provide insight into the practicality of using these easily producible fuels in compression ignition engines without further intensive conversions. Should these initial results provide a foundation for further research, optimising the fuel production on an industrial scale will lower the energy consumed in producing similar volumes of fuel.

8.1. Experimental methodology

This section presents the methodology employed for the etherification of THFA, details of the engine tests conducted on the resultant mixture are provided in Section 8.2

8.1.1. Bis-THFA synthesis

The following sections describe the specific experimental setup and reaction conditions for the synthesis undertaken.

The reaction between THFA and amberlyst-15 is non-selective, as there are two oxygen atoms in THFA which can be protonated by acid catalysts (such as amberlyst-15), which will result in the formation of side products. To confirm the presence of Bis-THFA in the product mixture, and the conversion ratio of THFA to bis-THFA, a fingerprint was required for GC analysis, to provide a calibration standard for the GC-MS library. This fingerprint is a pure form of the compound and the optimum way to produce this was with a Williamson ether synthesis.[224]

A modified Williamson ether synthesis of bis-THFA was adapted from Stenger-Smith et al, 2016.[225] The reactions shown in Sections 8.1.1.1 and 8.1.1.2 produced precursor reagents for the production of Bis-THFA shown in section 8.1.1.3. As a result of a water contamination in Reaction 8.1.1.2, the first attempt was unsuccessful. After correcting the source of water contamination, the second attempt was successful and using NMR, Bis-THFA was identified as the final product.

This sample of Bis-THFA was taken as a calibration standard and analysed with the GC-MS to develop a molecular fingerprint of bis-THFA. Comparison between this fingerprint and samples from reaction 4 allow the changes in selectivity to be quantified.

The general set up for these reactions is shown in Figure 8.4.
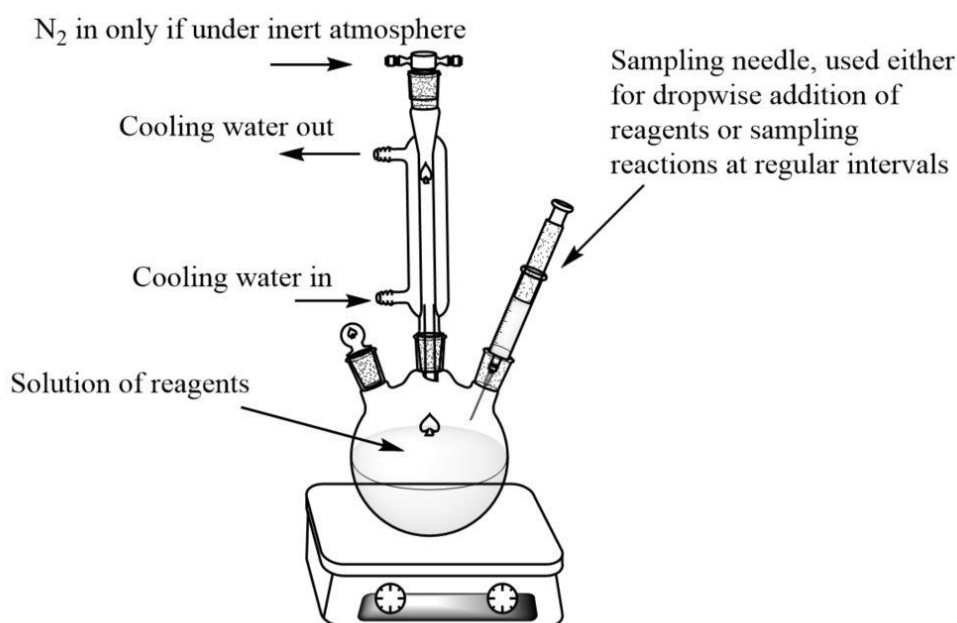
Figure 8.4: Set up of reactions which use a round bottom flask. Only reactions 1-3 used an N2 atmosphere. Variations of reaction 4 were not sealed.

8.1.1.1. Tetrahydrofurfuryl-mesylate
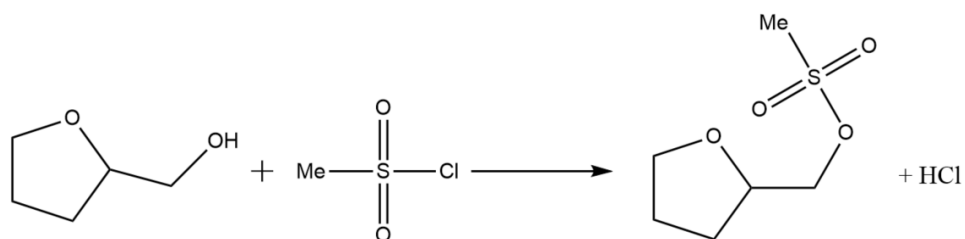
Figure 8.5: Reaction between tetrahydrofurfuryl alcohol and methanesulfonyl chloride

THFA (0.5 mL, 5 mmol, clear liquid) and pyridine (5 mL, 60 mmol, clear liquid) were added to a 25 mL round bottom flask (RBF). The solution was set to stir at 400 RPM and purged with N_2 for 30 minutes on ice. Methanesulfonyl chloride (0.5 mL, 4 mmol, clear liquid) was added dropwise over 1 hour. A white precipitate formed, and an additional 2 mL of pyridine was added. The solution was stirred for 48 hours at room temperature. After 48 hours 50 mL of 1.2 M HCl was added. The organic phase was extracted 3 times with 50 mL of DCM. The DCM was removed under vacuum and column chromatography was performed with a 1:1 ethyl acetate to hexane eluent. The reaction product was identified by thin layer chromatography (TLC) and   0.293 g of product was collected.

8.1.1.2. Sodium tetrahydrofurfuryl oxide
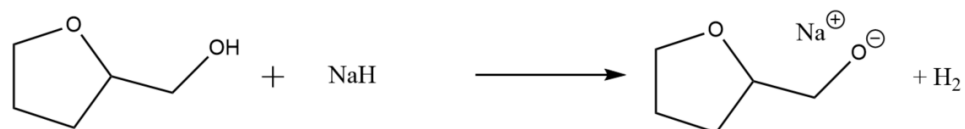
Figure 8.6: Reaction between tetrahydrofurfuryl alcohol and sodium hydride

Sodium hydride (60 % mineral dispersion, 0.0990 g, 2.48 mmol) and anhydrous THF (10 mL) were added to a 50 mL RBF. The solution was purged with N_2 and set to stir on ice. THFA (0.2 mL, 2.06 mmol) was added dropwise, with the resultant solution was left to stir for 1 hour under N_2.

8.1.1.3. Bis-THFA
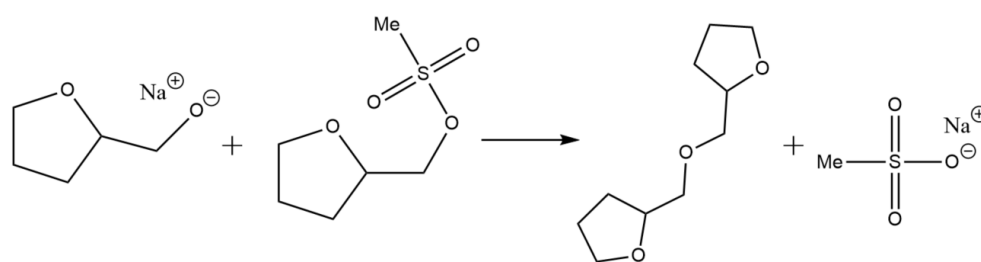
Figure 8.7: Reaction between sodium tetrahydrofurfurylate and tetrahydrofurfuryl mesylate

The THFA-mesylate from reaction 1 (0.293 g) was dissolved in 10 mL of anhydrous THF and added dropwise to the solution from reaction 2. The reaction was then heated to 80 °C and left for 48 hours. After 48 hours the reaction was heated to 170 °C for 10 minutes. TLC comparison showed reaction completion. Column chromatography was performed with a 1:1 ethyl acetate to hexane eluent followed by combination of product factions and solvent removed under vacuum.

Bis-THFA ether was produced, 0.0565 g (0.3 mmol) and identified via NMR, shown in Figure 8.8. The spectrum was identified as follows:

^{1}H NMR (CDCl$_3$, 400 MHz) δ = 4.09-4.01 (broad, m, 2H), 3.88-3.81 (broad, m, 2H), 3.78-3.70 (broad, m, 2H), 3.54-3.43 (broad, m, 4H), 1.99-1.79 (very broad, m, 6H) 1.67-1.56 (broad, m, 2H). This matches the NMR produced from literature.[225]
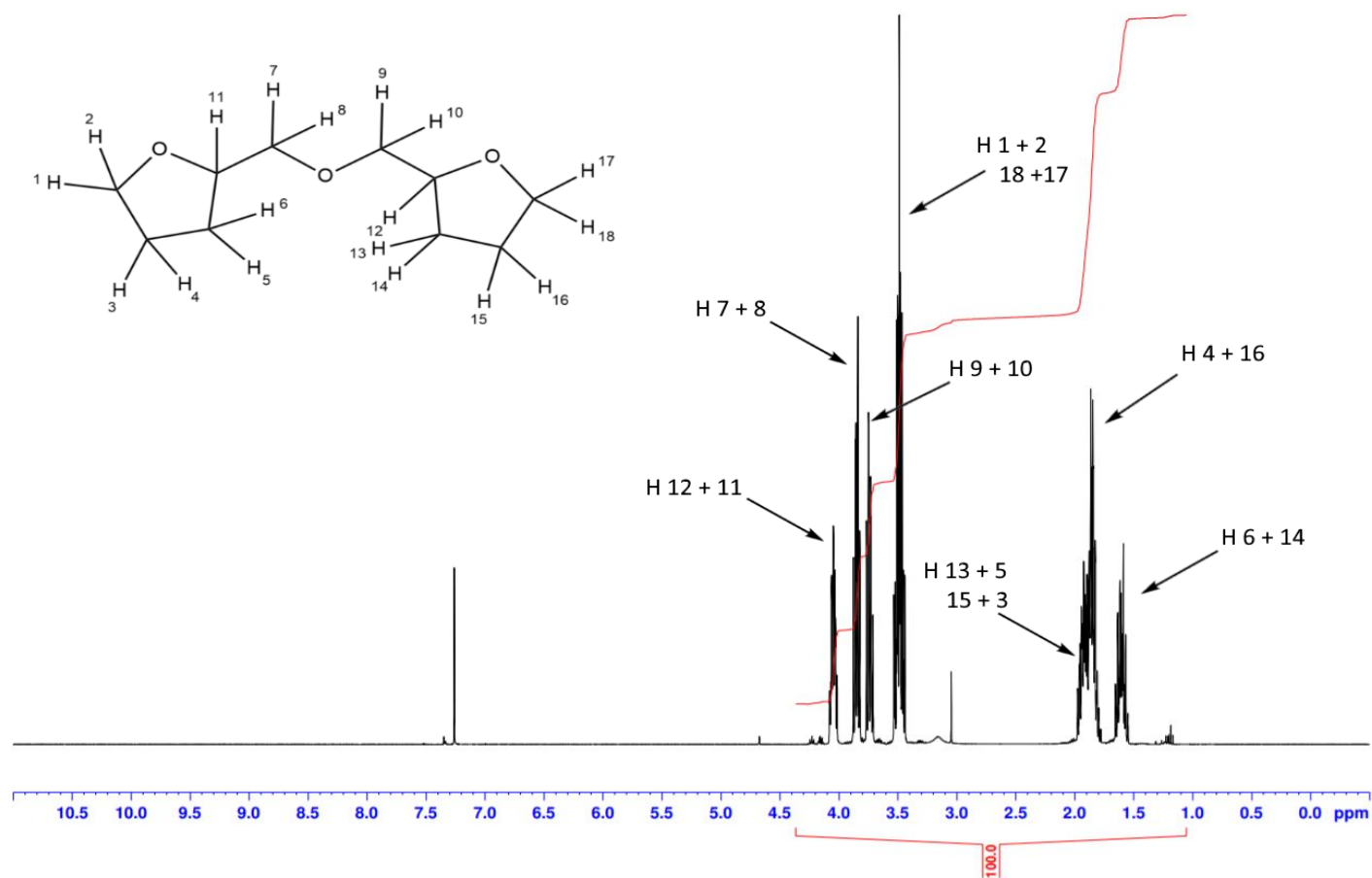
Figure 8.8: NMR Proton assignment of bis-tetrahydrofurfuryl alcohol. Spectrum shown is in agreement with supporting literature (Stenger-Smith et al 2018).[226]

8.1.2. Initial optimisation reactions

THFA (clear liquid) and Amberlyst-15 (grey solid) were added to a 100 mL RBF. The solution was set to stir at 400 RPM, for 24 hours and at the temperatures outlined in Table 8.1. Following this duration, the reaction was cooled to room temperature and filtered through sodium bicarbonate to remove moisture. GC-MS analysis was performed on the resultant filtered solution, diluted with DCM as a solvent. The GC oven temperature setpoint was 300 ^{o}C, gas carrier pressure was set to 21.2 psi and RXi-17SIL non-polar column.

Table 8.1: Initial optimisation experiments performed as non-selective synthesis of Bis-THFA using Amberlyst-15.

Experiment number:	THFA / mL	Amberlyst-15 / g	Temp / ^{o}C
TD-23	20	0.1	60
TD-25	20	0.1	80
TD-27	20	0.1	100

A GC-MS spectrum of a sample taken from TD-27 following a reaction duration of 24 hours is shown in Figure 8.9, highlights Bis-THFA as the major product present. The spectrum further highlights two additional peaks with a high intensity and same molecular weight as the target Bis-THFA. These peaks suggest the presence of structural isomers of Bis-THFA and indicate the lack of reaction selectivity.

Figure 8.9 also shows the GC-MS trace for samples taken at 1 hour, 4 hours and 24 hours during reaction TD-27. Apparent is that the peak intensity for all three molecules increases as the duration of reaction TD-27 increases. In the sample taken after 4 hours, the peak intensities of the three major products remain relatively similar, however, after 24 hours the peak indicating Bis-THFA is now significantly larger compared to all others, showing a longer time duration may increase product selectivity for Bis-THFA.
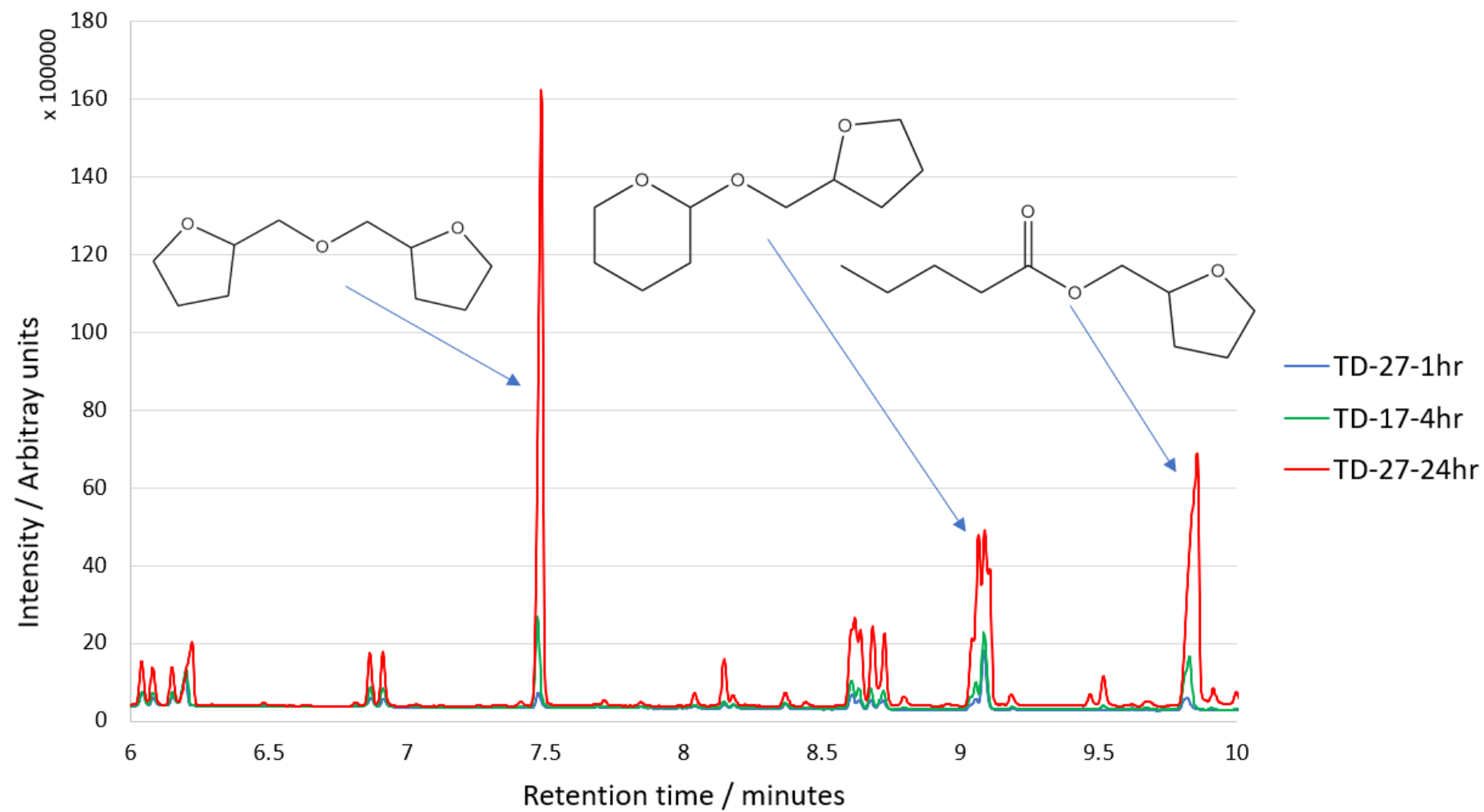
Figure 8.9: GC-MS spectrum of optimisation reaction TD-27, sampled at 1, 4 and 24 hours.

216

8.1.3. Further optimisation reactions

Optimisation of the reaction between THFA and Amberlyst-15 was further improved upon by Xueqing (2022).[227] Following the procedure outlined in Section 8.1.2, but omitting the addition of sodium hydroxide in place of 4 Å molecular sieves to remove any water side product, a series of optimisation reactions were performed to further isolate the effects of increasing the reaction temperature and duration. Shown in Table 8.2 are the reaction conditions considered and resultant reactant conversion levels.

Table 8.2: Experimental conditions and results of scaling up the conversion of THFA to Bis-THFA reaction, adapted from Xueping (2022).

Experiment number:	THFA / mL	Time / hr	Amberlyst-15 / g	Temperature / ^{o}C	Bis-THFA conversion / %	Total THFA conversion / %
XL-7.5	60	30	0.3	110	2.324	5.902
XL-9	600	30	3	120	1.524	3.622

Reaction XL-9 from this work was used as the Bis-THFA blend test fuel for the D8k engine tests discussed later within this chapter.
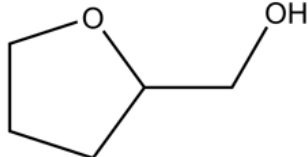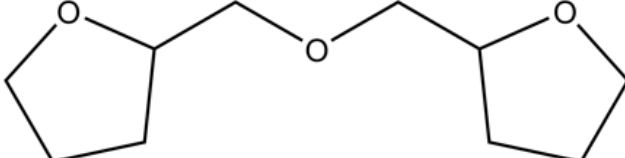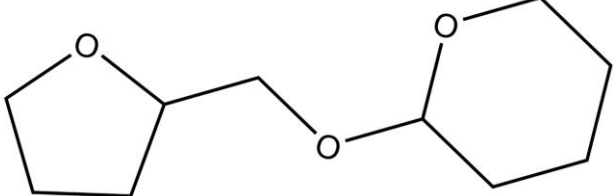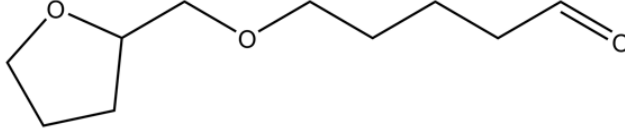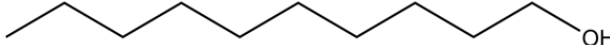
8.1.4. Synthesis conclusion

THFA was heated in the presence of a solid acid catalyst to facilitate a self-etherification reaction, forming a catalysed mixture with a conversion rate of 3.6 %, of which the target product, bis-THFA, constitutes 1.5 % (GC-FID results are in arbitrary units). In this catalysed mixture, the remaining 96.4 % of mixture remains unreacted THFA. At this point and in all further references, Bis-THFA solution refers to this resultant product mixture.

8.2. Engine test methodology

Bis-THFA solution and unreacted pure THFA were both blended volumetrically with 1-decanol in a 70:30 blend ratio to ensure ignition and enable observation of the effects of THFA conversion to Bis-THFA on combustion and emissions characteristics. An attempt was made to test both THFA and Bis-THFA unblended with decanol, however, both fuels failed to ignite. This was expected given the low cetane number of THFA and the low conversion yield in the Bis-THFA solution. The structures of THFA, Bis-THFA and decan-1-ol are shown in Table 8.2.

Table 8.3: Overview the molecules where were found in the Bis-THFA fuel blend alongside an abbreviation for each molecule and a skeletal depiction of the molecular structure.

Fuel (Nomenclature)	Chemical structure
Tetrahydrofurfuryl-alcohol (THFA)	
Bis-tetrahydrofurfuryl-alcohol (Bis-THFA)	
Tetrahydropyran 2-methoxy tetrahydrofuran (THP 2MTHF)	
Tetrahydropyran 2-methoxy pentanal (THP 2MP)	
Decanol (DecOH)	

218

8.2.1. Apparatus

All of the combustion experiments described in the current chapter were performed using the heavy-duty compression ignition engine and ultra-low volume fuel system research facility described in Chapter 4.

8.2.2. Experimental procedure

The blends of THFA and Bis-THFA with decanol were tested in the Volvo D8k facility at two injection timings of 5.3 CAD BTDC and 9.3 CAD BTDC, the latter was chosen as at this injection timing SOC for the blends was found to occur approximately at TDC. Table 8.4 highlights some of the key results from the combustion tests.

An initial test with fuel blends containing lower than 30% decanol showed that steady combustion of THFA and the Bis-THFA mixture was not possible without a minimum of 30% decanol.

Table 8.4: Experimental test conditions and key experimental results for the THFA and Bis-THFA decanol blends and reference diesel in the D8k engine at constant injection timing and injection times for constant start of combustion.

Fuel blend	Engine speed (RPM)	Fuel injection pressure (bar)	Injection timing (CAD BTDC)	Injection duration (CAD)	IMEP (Bar)	Ignition delay (CAD)	PHRR (j/deg)	Max average in-cylinder temperature (K)
THFA	820 ± 20	695 ± 10	5.3	6.5	4.86	9.6	666.2	1811.4
Bis-THFA	820 ± 20	695 ± 10	5.3	6.5	4.78	9.3	737.4	1818.6
THFA	820 ± 20	695 ± 10	9.3	6.5	4.67	9.2	847.7	1861.4
Bis-THFA	820 ± 20	695 ± 10	9.3	6.5	4.89	9	840.0	1885.5
Ref Diesel	820 ± 20	695 ± 10	5.3	6.5	7.04 ±0.09	5.2	321.9	1905.8

8.3. Results

8.3.1. Ignition delay
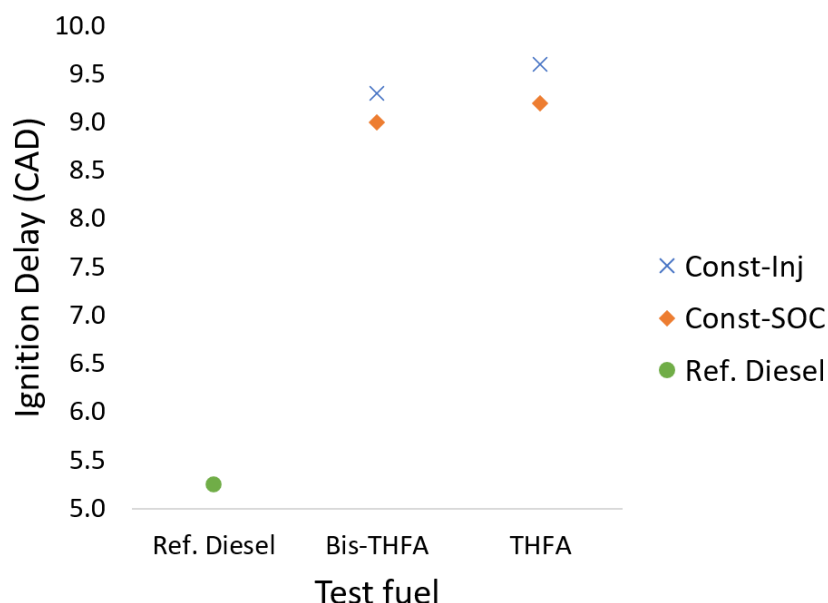
Figure 8.10: Duration of ignition delay of THFA and Bis-THFA decanol blends and reference diesel. Error bars are plotted on the reference diesel, but are visually insignificant owing to low testing variation.

Figure 8.10 shows the impact on duration of ignition delay of THFA, Bis-THFA and reference diesel at injection timings of 5.3 and 9.3 CAD BTDC. Immediately apparent is the significantly longer duration of delay exhibited by the THFA and Bis-THFA blends relative to the reference diesel.

An important trend observed is the shorter duration of ignition delay exhibited by the Bis-THFA fuel blend as compared to the unreacted THFA decanol blend, by 0.3 and 0.2 CAD at the constant injection and constant SOC testing conditions respectively. This observation is significant as the total converted products identified by mass spectrometry was only 3.6 % of the Bis-THFA prior to blending with decanol. The mixture was further diluted with 30 % 1-decanol volumetrically, therefore the composition difference between the Bis-THFA and THFA blends is only 2.52 % by volume, yet this difference is significant enough to cause at least a 0.2 CAD shorter duration of ignition delay.

Further apparent is the shorter duration of ignition delay exhibited by the test fuel blends at the earlier injection timing during the constant SOC tests. The earlier injection timing allows greater air fuel mixing to occur prior to top dead centre in the combustion chamber, where the greatest temperatures and

pressures are reached prior to autoignition, facilitating easier autoignition of the air fuel mixture.[20]

8.3.2. In-cylinder pressure and heat release rate
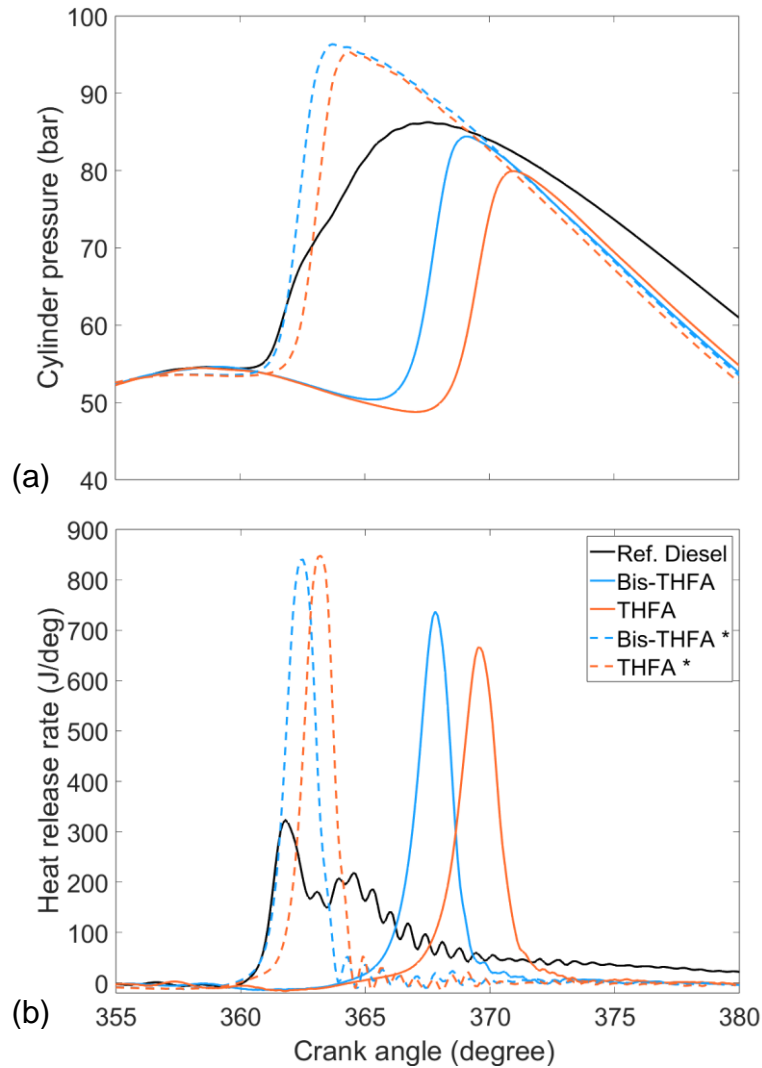
Figure 8.11: (a) In-cylinder pressure and (b) apparent net heat release rates of the THFA fuel blends and reference fossil diesel testing at constant injection timing and constant start of combustion (*).

Figure 8.11 shows the in-cylinder pressures and apparent net heat release rates of the THFA and Bis-THFA fuel blends at constant injection and constant SOC conditions.

The main observation of note is the steeper gradient of increasing heat release rates prior to the PHRR achieved by the Bis-THFA fuel blend relative to the THFA blend at the constant injection timing. As shown in Figure 8.10 the THFA blend auto ignites 0.3 CAD after the bis-THFA fuel blend and it can be seen in Figure 8.11 that the duration of combustion is slightly longer for the THFA fuel blend. Therefore, THFA exhibiting a lower PHRR relative to Bis-THFA is

expected as more of the cylinder wall is exposed during the combustion of the THFA blend, which allows for greater heat transfer to occur. Bringing the injection timing forward to the constant SOC test condition facilitates auto-ignition at a time with higher in-cylinder pressure, allowing for more efficient combustion and less difference in the PHRR's observed.

Another important observation is the relative change in PHRRs observed, at 5.3 CAD BTDC, THFA exhibits a lower PHRR than Bis-THFA but at 9.3 CAD BTDC THFA exhibits a higher PHRR. This could be attributed to either the longer duration of combustion exhibited by Bis-THFA, which by definition would require lower PHRRs, or to the fact that despite Bis-THFA exhibited a shorter than expected duration of ignition delay meaning autoignition did not occur at TDC.

Apparent is the higher peak heat release rate exhibited by both blends at the constant SOC test condition relative to the later injection timing. As previously shown in Figure 8.10, the duration of ignition delay does not significantly change as the injection timing is brought forward, so the higher peak heat release rates (PHRR) can be attributed to autoignition occurring close to TDC. At TDC the in-cylinder pressure and temperature is higher which would facilitate better combustion and levels of heat transfer can be expected to be lower than later in the expansion stroke given the smaller area of cylinder wall exposed.[20] A more efficient combustion process is further evident by the shorter durations of combustion observed of the constant SOC test condition for all fuels relative to the constant injection timing.

Also apparent is the effect of the long ignition delay on the combustion phasing as both test fuels exhibit combustion dominated by the premixed burn phase. A long ignition delay is expected to lead to a high pre-mixed burn as there is more time for greater air fuel mixing to occur prior to autoignition.[214]

8.3.3. IMEP and combustion characteristics
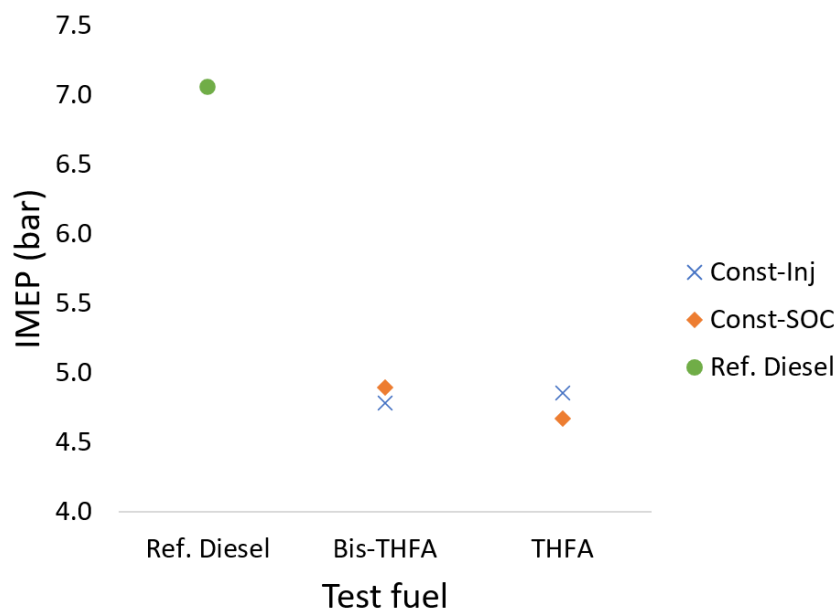
Figure 8.12: Indicated mean effective pressure (IMEP) of THFA and Bi-THFA fuel blends, and reference diesel at constant injection timing and constant SOC test conditions.

Figure 8.12 shows the IMEP of Bis-THFA relative to THFA, providing valuable information as to the usefulness of the etherification reaction. It also shows the change in IMEP caused by changing the injection timing of the THFA and Bis-THFA fuel blends.

The trend of note is the very similar values of IMEP exhibited by the THFA and Bis-THFA blends at both testing conditions. This is expected, as mentioned previously in Section 8.3.1, the conversion rate of THFA in the Bis-THFA mixture is minor and would result in a very small change in calorific value or physical properties which affect the mass of delivered fuel during injection.

Also apparent is the lower IMEP of the blends than the fossil reference diesel, which is expected as the fuels have a significantly higher oxygen to carbon ratio than diesel and therefore less energy available each combustion cycle as the duration of injection is kept constant across all tests.
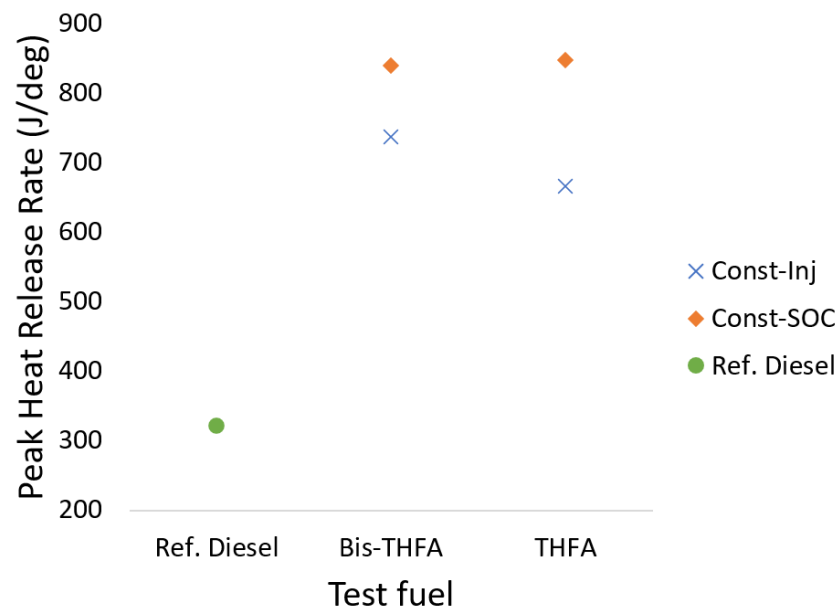
Figure 8.13: Peak apparent heat release rate of the THFA and Bis-THFA fuel blends and reference diesel at the constant injection and constant SOC test conditions.

Figure 8.13 shows the PHRR of the THFA fuel blends and reference fossil diesel. Also apparent is the significantly higher PHRR's exhibited by the blends than the fossil reference diesel. A long duration of ignition delay is associated with a high PHRR as there is a more time for air fuel mixing to occur and a higher volume of the air fuel mixture is well mixed prior to autoignition.[163]

No difference is observed between the two fuels at the constant SOC test condition, however the THFA fuel blend exhibits a lower PHRR than the bis-THFA blend at the constant injection condition. This is resultant from the longer duration of ignition delay exhibited by THFA relative to the Bis-THFA, as combustion is taking place later into the expansion stroke and thus at greater in-cylinder volume. With more of the cylinder walls exposed, a higher level of heat transfer from the combustion chamber gases to the walls can be expected.
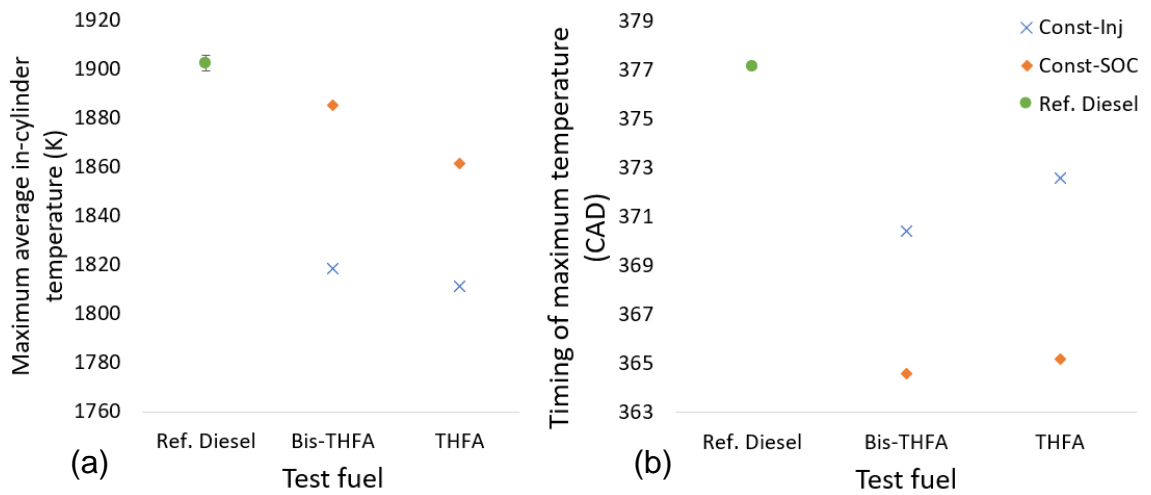
Figure 8.14: Maximum average in-cylinder temperature (a) and timing of maximum temperature (b) of the THFA and Bis-THFA fuel blends and the reference fossil diesel.

Figure 8.14a and 8.14b show the calculated maximum in-cylinder global temperature and time at which it occurs respectively for the THFA and Bis-THFA test fuel blends. The trend apparent is that of the Bis-THFA test fuel reaching a higher maximum average temperature than the THFA fuel blend and at an earlier CAD. This is expected given the shorter ignition delay of the Bis-THFA (Figure 8.10) and further highlights the slightly more favourable combustion exhibited by the bis-thfa fuel blend.

Of further note is the significantly earlier onset of the maximum average temperature exhibited by the test fuels at both test conditions compared to the reference diesel. While THFA and Bis-THFA reach the maximum temperature earliest at the constant SOC condition, the maximum temperature exhibited by the reference diesel is appreciably higher and is to be expected given the higher IMEP observed (Figure 8.12).
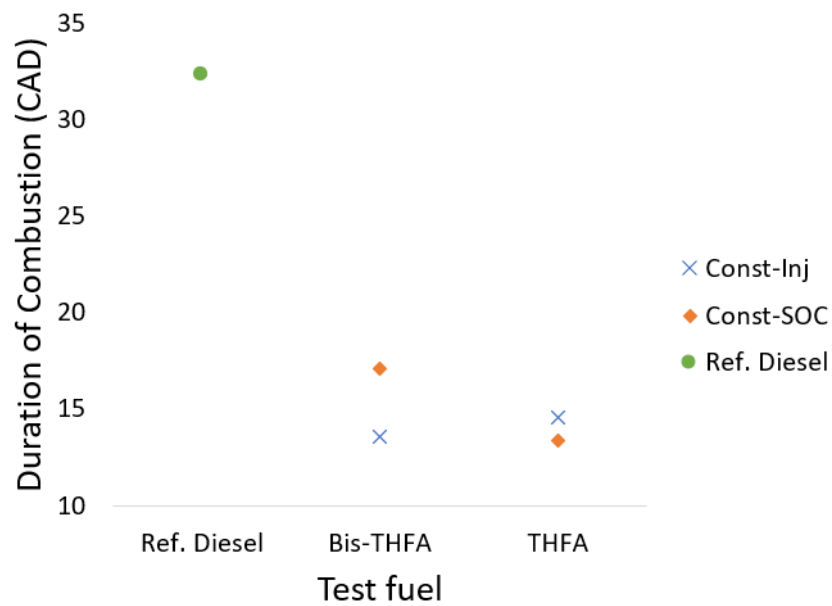
Figure 8.15: Calculated duration of combustion of the THFA, bis-thfa fuel blends and reference fossil diesel at the constant injection and constant SOC test condition.

Figure 8.15 shows the duration of combustion exhibited by the THFA and bis-thfa fuel blends. Apparent is the significantly shorter duration of combustion exhibited by the test fuels than the reference diesel. It can also be seen that at both testing conditions the fuel blends exhibit a similar duration of combustion, with the Bis-THFA exhibiting the longest duration at the constant SOC condition.

At the constant SOC timing condition, the duration of combustion of Bis-THFA is 3.5 CAD longer than that of the THFA fuel blends. The long ignition delay displayed by Bis-THFA and THFA ensures a well-mixed air fuel mixture and no diffusion-controlled combustion exhibited by either fuel blend (Figure 8.11). As the combustion is dominated by a premixed burn it is expected that several points within the air fuel mixture will ignite near simultaneously and the slightly longer duration of ignition delay exhibited by THFA relative to Bis-THFA ensured more of the fuel was well mixed prior to autoignition.

227

8.3.4. Exhaust emissions
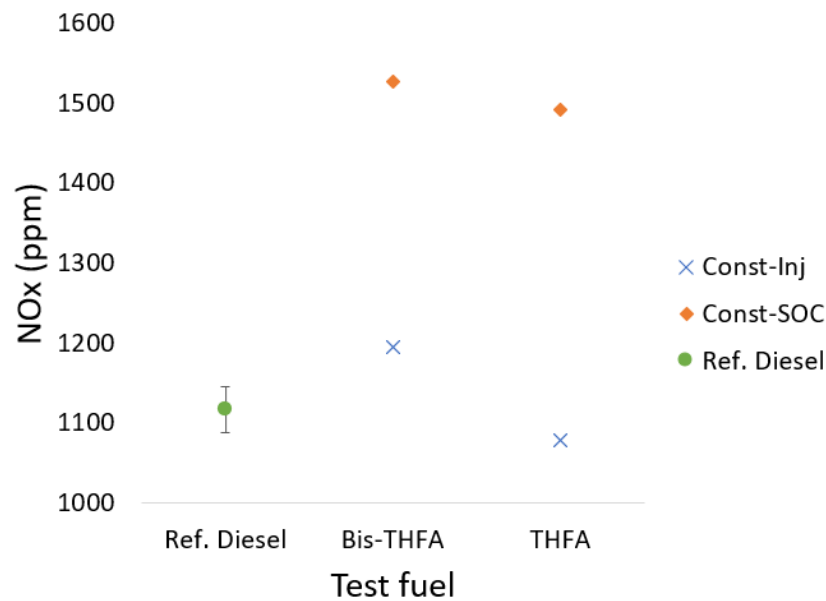
Figure 8.16: Exhaust gas NOx emissions of the THFA and Bis-THFA test fuel blends at constant injection and constant SOC timing.

Figure 8.16 shows the measured NO_x emissions during combustion of the THFA and Bis-THFA fuel blends. Apparent are the significantly higher NOx emissions measured during combustion of both THFA and Bis-THFA at the constant SOC condition. This is expected as a high NOx emission is correlated with high PHRRs (Figure 8.13), long ignition delays (Figure 8.10) and an earlier onset of the maximum in-cylinder average temperature (Figure 8.14).[42, 208,215]

An observation to note is that at both injection timings Bis-THFA exhibited higher NOx emissions than THFA. Thermal NOx production is highly sensitive to in-cylinder temperatures requiring temperatures higher than 1600 K.[162] A long ignition delay allows for greater air fuel mixing, in turn causing a high PHRR as a greater portion of the fuel is sufficiently mixed prior to autoignition. This leads to a large premixed burn fraction and sharp rise in temperature.[89] NOx production further relies on the residence time of the hot gases in the chamber at high pressure. The test fuels under the constant SOC condition reach their maximum temperature relatively early and have a short duration of combustion compared to the reference diesel, so the gaseous products produced from combustion have a long residence time at high pressure and temperatures during the early stage of the power stroke, facilitating thermal NOx production.[89] As Bis-THFA exhibits a shorter duration of ignition delay than THFA at both injection timings, the hot gaseous products resultant from combustion of Bis-

THFA have a slightly longer residence time at high temperature and pressure, facilitating higher NOx emissions relative to THFA.

At the constant injection timing condition, the long duration of ignition delay exhibited by the THFA and Bis-THFA results in the fuel blends auto-igniting at least 4 CAD after TDC which allows less time for the gaseous combustion products to mix and facilitate thermal NOx production prior to freezing of the production kinetics. This leads to the lower amount of NOx measured from the constant injection timing than constant SOC test condition.
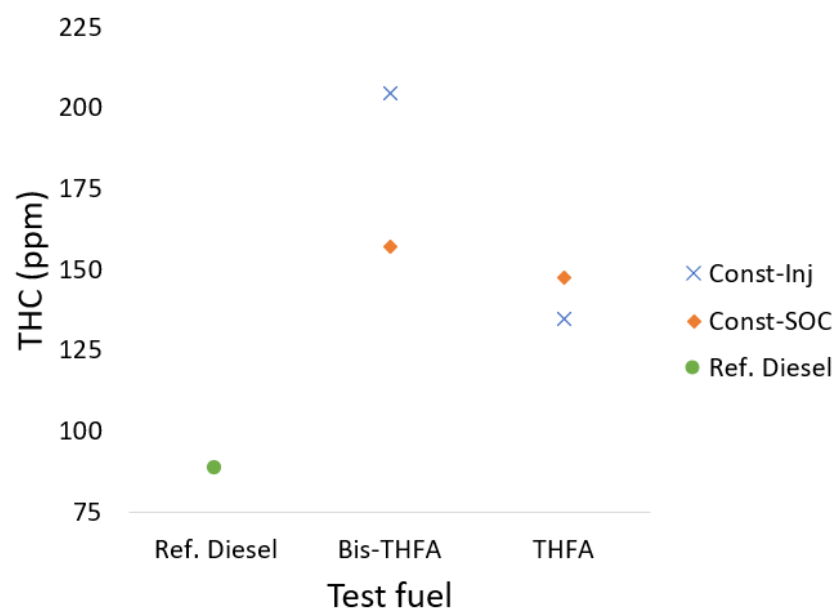
Figure 8.17: Exhaust gas unburnt hydrocarbon emissions of the THFA and Bis-THFA fuel blends at the constant injection and constant SOC test condition.

Figure 8.17 shows the unburnt hydrocarbon emissions of the THFA and Bis-THFA test fuel blends. One observation apparent is the higher THC measured during combustion from all the test fuels than the reference diesel, which is attributable to their long ignition delay and large premixed burn phase. A long ignition delay allows for greater air fuel mixing which can lead to areas of mixture within the chamber which are too lean to auto-ignite or support a self-propagating flame, increasing the amount of unreacted fuel.[228]

Under the constant SOC test condition there is little difference between the THFA and Bis-THFA fuel blends, whilst at the constant injection timing condition, a significantly higher number of unburnt hydrocarbons was measured from the Bis-THFA blend than the THFA blend. However, during the test of Bis-

THFA at constant injection, a higher than usual level of background hydrocarbons was noted, but not for the remaining tests.
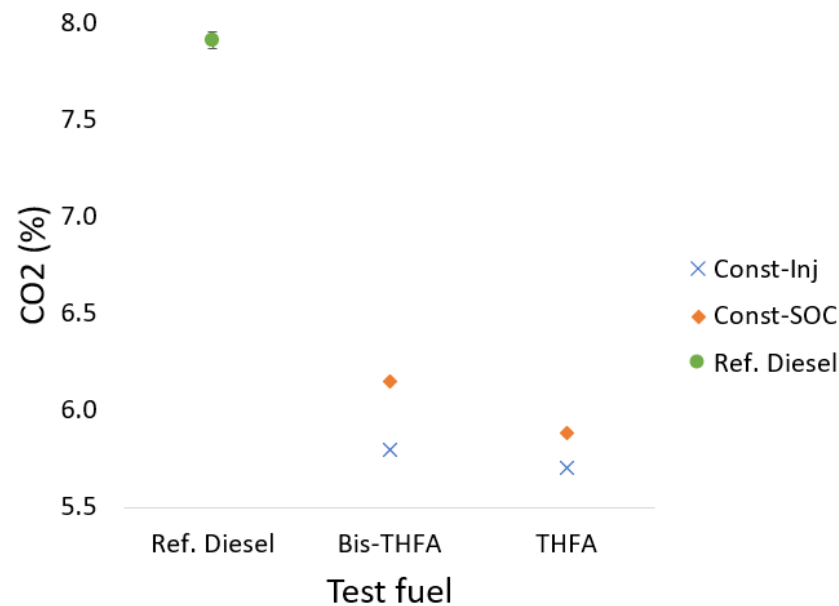
Figure 8.18: Exhaust gas CO2 emissions of the THFA and Bis-THFA fuel blends at the constant injection and constant SOC test condition.

Figure 8.18 shows the CO2 emissions of the THFA and Bis-THFA test fuel blends. Apparent is the lower CO2 produced from these blends than the reference diesel, attributable to the lower carbon content by mass in the THFA fuel blends and is in agreement with the lower IMEP (Figure 8.12).

The THFA fuel blends at both conditions, and the Bis-THFA fuel blend at the constant injection duration condition, all exhibit similar levels of CO_2 emissions whilst the Bis-THFA fuel under the constant SOC condition exhibits a slightly higher CO_2. This observation would be expected as Bis-THFA under the constant SOC condition also exhibited the longest duration of combustion amongst the test fuels (Figure 8.15). The majority of the energy released during combustion comes from the oxidation of carbon and the tests are performed with constant injection duration for all the fuels, so a longer duration of combustion implies a more complete combustion of the available fuel, thus a higher CO_2 emitted. Alternatively, there is possibly a loss in thermal efficiency caused by the Bis-THFA at the constant SOC timing igniting before TDC, as earlier injection timings can affect thermal efficiency.[229] Despite a higher CO_2 emission at constant SOC, the IMEP exhibited by Bis-THFA (Figure 8.12) does not change significantly between the two injection timings, implying a decrease in thermal efficiency.

8.4. Viability of low-yield etherification reactions as combustion improvers

The upgrading process of heating THFA with a solid acid catalyst currently lacks a thorough isolation of the dimer molecules produced from the starting material and the overall yield remained low. The Bis-THFA solution used for these tests was still mostly THFA, with only 4 % of the starting THFA undergoing conversion. The reaction was non-selective and whilst the Bis-THFA molecule has been fingerprinted through selective synthesis, the remaining products identified in the GC trace (Figure 8.9) are predictions according to molecular weight, splitting patterns and retention time. However, it is clear from the results discussed in Sections 8.3.1 to 8.3.3 that the low conversion yield has still led to an observed improvement in fuel performance.

The Bis-THFA solution exhibited a shorter duration of ignition delay relative to THFA (Figure 8.11) at both injection timings in agreement with the hypothesis. Bis-THFA also exhibited higher average in-cylinder temperatures (Figure 8.14a) than the THFA solution at both the constant injection and constant start of combustion testing conditions. Additionally, during the constant start of combustion tests the Bis-THFA solution exhibited a longer duration of combustion and a higher volume of measured CO_2 exhaust gases than the THFA solution. These findings are significant when the minor chemical conversion ratio is considered, and it is likely that further tests with higher concentration of purity Bis-THFA blends would result in further reductions in ignition delay.

From the IMEP (Figure 8.12), PHRR (Figure 8.13), and gaseous NOx emissions (Figure 8.16) it is clear that there is no significant difference between the THFA and Bis-THFA blends when these metrics are considered. The similarity in these results is expected as there is only a 4 % difference in the products between the THFA and Bis-THFA solutions.

8.5. Conclusions

This chapter has discussed a synthetic process to convert a platform chemical (THFA) which is readily available from processing of a majority of common biomass sources into a compression ignition engine suitable biofuel. The following conclusions highlight the main findings:

- Despite only a 1.52 % Bis-THFA conversion yield and 3.6 % total product conversion yield, the Bis-THFA solution exhibited an appreciably shorter duration of ignition delay at two different injection timings. At the constant start of combustion test condition Bis-THFA, relative to THFA, exhibited a longer duration of combustion and higher gaseous CO_2 emissions, implying the fundamental combustion process was affected by the change in chemical composition. Bis-THFA also exhibited higher NOx emissions relative to THFA, resulting from a shorter duration of ignition delay leading to more thermal NOx forming in the gaseous products on combustion.

- Conversion of THFA to Bis-THFA was optimised to a 2.32 % yield from a small-scale reaction and 1.52 % yield in a large scale up. The conditions for the etherification reaction were optimised at small scale, with a reaction temperature of 120ºC and a reaction time of 30 hours found to give the highest Bis-THFA yield.[227]

- Targeted synthesis of Bis-THFA following a standard Williamson ether synthesis according to the literature procedure allowed for a fingerprint to be generated in the GC library. Subsequent optimisation reactions were possible using the Bis-THFA fingerprint to track reaction progress and observe how changes in reaction conditions affected product yield.

The observed reduction in ignition delay and improved combustion efficiency supports the hypothesis that readily available and easily producible molecules from biomass can be upgraded to improve their viability as target future fuels in heavy-duty compression ignition engines.

9. Conclusions and recommendations for future work

This chapter compiles the main conclusions from the work presented here and suggestions for further research based on the results obtained. Firstly, the major conclusions from the literature review and the four results chapters are reiterated individually. These are followed by overarching conclusions which are applicable to the experiments as a whole.

9.1. Literature review

From the literature reviewed in Chapter 2, the following conclusions can be drawn:

1. The scope of biofuels research for heavy-duty CI engines has been limited by the widespread use of fatty acid methyl esters as biodiesel. Systematic studies regarding engine performance, combustion characteristics and pollutant emissions are dominated by studies of fatty acid esters. Literature regarding the viability of biofuels derived from lignocellulosic biomass, or, regarding how changes in molecular structures not found in FAME impact the performance of heavy-duty engines is lacking.

2. Lignocellulosic biomass is assumed to be inherently limited as a feedstock for gasoline blending components, owing to the high oxygen content in biofuels produced from the feedstock. Biodiesel produced from oilseeds are by far the most prevalent biofuel, however, oilseeds are the feedstock most impacted by moves to reduce crop-based biofuels. Lignocellulosic biomass is not considered in this debate owing entirely to its significant natural abundance. Viable routes to produce suitable diesel blending components for compression ignition engines remains a knowledge gap with high importance to industry, not just academic research.

3. Undesirable emissions formed in CI engines during combustion are highly sensitive to the duration of ignition delay and the degree to which the air and fuel are mixed prior to autoignition. Products of incomplete combustion form in areas of the air fuel mixture which

are both overly lean or overly rich, and the formation of nitrogen oxides directly correlate with the timing of autoignition and residence time of the combustion products at high temperature.

4. The timing of autoignition can be advanced or delayed by certain molecular structures, and the inclusion of oxygen in a molecule has significant potential to lower carbon monoxide, unburnt hydrocarbon and soot emissions.

9.2. The impact of the Michael Acceptor functional group on ignition delay and emissions formation

From the discussion in Chapter 5 the following major conclusions may be drawn on how a molecular structure with unique radical reaction pathways influences the duration of ignition delay:

1. The inclusion of a double bond on the α carbon adjacent to an ester group, thereby forming a Michael Acceptor function group, reduces the duration of ignition delay in methyl nonanoate esters, in agreement with the hypothesis proposed. Relative to similarly unsaturated esters which lack the Michael Acceptor functional group, an appreciable improvement in combustion efficiency was observed.

2. The observed changes in ignition of the methyl nonanoate esters with the inclusion of the α, β unsaturated carbonyl were not replicated by two sets of ethyl esters, attributable to the unimolecular ethylene decomposition pathway available to the latter.

3. The result of methyl non-2-enote exhibiting a shorter duration of ignition delay than methyl nonanoate is in disagreement with previous literature which investigated both esters in a cooperative fuel research engine. This can be attributed to the significant difference in engine speed, geometry and compression ratio and the fuel injection strategy.

9.3. The influence of alkyl chain length and ring size in lactone single component fuels

From the discussion in Chapter 6 the following major conclusions may be drawn on how lactone ring size and substituent alkyl chain length influenced combustion and emissions:

1. A range of lactones were found to ignite and combust in a stable manner, despite their cyclic and highly oxygenated structure which are both assumed to inhibit stable performance. This highlighted the significant influence molecular structure has on the process of combustion, as gamma-octalactone has a carbon to oxygen ratio of 4:1, equivalent to fuels such as butanol, a poor fuel for compression ignition engines.
2. Increasing the length of the alkyl substituent chain on both lactone isomers (increasing the total carbon count) was found to reduce the duration of ignition delay, increase the duration of combustion, and decrease the measured emissions of nitrogen oxides, unburnt hydrocarbons, CO and particulates.
3. Gamma lactones consistently exhibited shorter durations of ignition delay than their delta lactone isomers, indicating that the length of the substituent alkyl chain was more significant than the ring size in lowering the duration of ignition delay.

9.4. On the viability of date pit methyl esters for heavy-duty compression ignition engines

The work presented in Chapter 7 was the first to test a biodiesel from waste date pits in a heavy-duty compression ignition engine. From the results presented, the following conclusions can be drawn:

1. Date pit methyl ester B7 and B100 blends exhibited a shorter or equal duration of ignition delay and lower peak net apparent heat release rates relative to the equivalent rapeseed methyl ester blends, resulting in longer durations of combustion and lower emissions of both nitrogen oxides and carbon monoxide.

2. The correlation between the net apparent peak heat release rates and nitrogen oxide emissions observed from the date pit and rapeseed methyl were in agreement with previous studies of biodiesels. The D8k engine's slower speed relative to previous tests of date pit methyl esters allowed greater time for differences in chemical reactivity between fuels to present more clearly as unique combustion properties.

3. Despite clear trends and differences between the date pit and rapeseed methyl esters, the absolute value of difference observed in the combustion analysis and measured emissions were minor enough that for all practical intents and purposes, date pit methyl esters are a viable biofuel for heavy-duty compression ignition engines.

9.5. On improving the combustive properties of lignocellulosic alcohols through chemical conversion

From Chapter 8, the following conclusions can be drawn on the synthesis of bis-tetrahydrofurfuryl alcohol and how fuel blends containing this ether influence combustion:

1. A significant reduction in the duration of ignition delay was observed from the Bis-tetrahydrofurfuryl ether fuel mixture, in agreement with previous observations of ether combustion, despite the chemical synthesis producing a mixture with a less than 2 % yield of the targeted ether.

2. The Williamson ether synthesis produced a high purity amount of the bis-tetrahydrofurfuryl ether, which was successfully used as a reference library fingerprint in a gas-phase mass spectrometer to quantify conversion yields of a non-specific reaction between tetrahydrofurfuryl alcohol and a solid acid catalyst.

3. The catalytic reaction employed to convert a large volume of tetrahydrofurfuryl alcohol into bis-tetrahydrofurfuryl ether was optimised for a 1.5 % conversion ratio. The conversion ratio improved with longer reaction durations, but the improvements

observed with a higher temperature were not found in a reaction scale-up.

9.6. General conclusions

In each study presented in this work, minor changes to molecular structures significantly altered the behaviour of single component future fuels and of future fuels blended with reference fossil diesel. Across Chapters 5 to 8 trends were observed irrespective of the fuels tested. These universal trends can be summarised as follows:

1. The heavy-duty engine tolerated a wide variety of biomass derived biofuels, differing in viscosity, boiling point and degree of oxygenation, without negative impacts on the combustion process or the engine hardware.

2. Gamma-dodecalactone and ethyl dec-2-enoate both have a molecular formula of $C_{12}H_{22}O_2$, yet gamma-dodecalactone exhibited a duration of ignition delay 2.1 CAD shorter than ethyl dec-2-enoate. Cyclic alkanes exhibit poorer combustion than n-alkanes and it would be assumed that lactones exhibit poorer ignitability than esters. However, the difference in ignition delay between these two molecules shows that fuel oxygen content alone cannot accurately predict fuel performance and that the overall fuel structure beyond a singular functional group plays a significant role in the combustion process.

3. In the lactone ring structure, the ring bound oxygen is bonded to two carbons, so can be considered etheric in nature. The shorter ignition delay exhibited by the bis-tetrahydrofurfuryl alcohol blends highlight the improved ignition properties of ethers. Therefore, the improved ignition quality of lactones compared to other cyclic structures can be attributed to the ether bound oxygen.

4. In all of the tests where the oxygenated fuels exhibited a duration of ignition delay less than 7.0 crank angle degree, the oxygenated fuels exhibited lower emissions of unburnt hydrocarbons and of nitrogen oxides.

5. The carbon monoxide emissions of the reference diesel in the D8k were notably low, especially when compared to the levels of carbon monoxide expected from high-speed compression ignition engines, highlighting the increased efficiency of the D8k. The carbon monoxide emissions observed from the oxygenated fuels were typically higher than the reference diesels, which is expected given the engine operating conditions were not changed to accommodate the different physical properties of the oxygenated fuels relative to the reference diesel.

6. The measured emissions of nitrogen oxides, unburnt hydrocarbons and carbon monoxide were highly sensitive to the combustion phasing of the fuels. Gaseous emission trends correlated most strongly with observed trends in the duration of ignition delay, size of the premixed burn phase and subsequent net apparent peak heat release rates.

9.7. Recommendations for further work

While this thesis has covered a significant amount of work in exploring the relationship between fuel molecular structure and combustion in a heavy-duty compression ignition engine, there are still several details which would benefit from further investigation to expand the knowledge of how these molecular structures influence combustion.

In the study of Michael Acceptor fuel reactivity, it was found that ethyl esters did not exhibit the expected reduction in ignition delay observed from the methyl esters. Acquiring further methyl esters to validate if the observed reduction was not unique to methyl nonanoate would provide further support to the hypothesis when incorporating Michael Acceptors in molecules which come more directly from biomass.

In the study of lactone isomerism, it was observed that gamma-undecalactone exhibited a lower duration of ignition delay than all of the tested delta lactones. The observed trend of shorter ignition delays with a longer alkyl chain in both lactone isomers was clearly becoming less pronounced as the lactones became

larger, and so it would be interesting to see if the ignition delay of gamma-undecalactone's ignition delay is shorter than delta-tridecalactone. It would also be of interest to test if after a certain carbon chain length, the ignition delay of both isomers no longer reduces and if the two isomers converge or the gamma lactones will always exhibit a shorter duration of ignition delay than the delta lactones. It should be noted that whilst the lactones tested in this work can be easily sourced from biomass, larger lactones become increasingly rare and unlikely to be sourced in any meaningful quantity, so the recommendations here are strictly academic.

Combining the studies of Michael Acceptors and lactones, both structures can be found in molecules isolated from lignocellulosic biomass. Of particular interest is beta-angelica lactone, which is a gamma lactone ring and also contains a carbon-carbon double bond on the α position to the ester carbonyl. By definition, beta-angelica lactone is both a lactone and a Michael Acceptor. Beta-angelica lactone can be easily produced from C5 sugars, making it more representable of molecules which can easily derived from lignocellulosic biomass and would highlight how different complex molecular structures in a single component biofuel interact with each other in the turbulent conditions of combustion.

The study of date pit methyl esters was limited to a single set of conditions. Changing the experimental conditions to better simulate on road conditions, such as increasing the engine speed to over 1,000 RPM or testing the fuels with a variable load would provide insights into DPME performance and emissions formation in real world conditions. Secondly, two batches of date pit methyl esters were delivered, from different production methods and were named DPME and DPME-alt. The second production method for DPME-alt was not sufficiently scaled up, so could only be tested as a B100 blend. Testing DPME-alt at the B7 and B30 blends would provide a better practical comparison as B7 and B30 are the most common biodiesel blend ratios used in real markets. Finally, the date pit esters could be compared to other biodiesels which can be produced in the Middle East, such as waste cooking oil methyl ester, to expand the knowledge on feedstock choice for the region.

The study on converting alcohols into ethers has merely progressed towards the full potential of this work. Alcohols are abundant in nature, but methods of

converting them into ethers are typically low yield or use expensive reagents. A full systematic study on optimising the reaction between tetrahydrofurfuryl alcohol and solid acid catalysts to synthesise a high yield product and testing higher v/v % fuel blends would not only be of great research interest but would also be of great practical use to furthering the goal of reducing fossil fuel consumption.

Finally, the physical properties of the future fuels tested in this work span a wide range of viscosities, between 1.23 Cp to 5.01 Cp, with the viscosity of the reference diesel being 2.25 Cp. For the practical implementation of very high fuel blends containing these future fuels, it would be necessary to characterise the full effect of viscosity changes in real engine conditions. In practicality, this could be done by increasing the injection pressure of these fuel blends whilst keeping all other parameters constant to observe any significant differences in the combustion phasing. It should be noted that modern engines should sufficiently handle fuels with higher viscosities as fuel injection pressure can be independently controlled with an electronic control unit, but older engines more reliant on mechanical control may not be able to handle significant differences in fuel viscosity relative to diesel. Additionally, the viscosity of fluids decrease with rising temperatures and in the work presented here each fuel was tested at 50°C. This temperature the fuel reached before injection is unknown and 50°C was chosen as an arbitrary compromise between the known oil temperature and the know fuel temperature at the engine's exterior. The laboratory set-up was designed to keep engine conditions as real as possibly, however, it is far more likely that in an on-road engine fuel delivery temperatures may differ. In Engines could also be retrofitted with heating elements to ensure the fuel is delivered at a specific temperature, thereby ensuring high blends with viscous fuels are heated sufficiently to reach a desirable viscosity. Expanding the range of workable viscosities would benefit industry by opening up more potential sources of biofuels. An example of this is gamma-dodecalactone, which showed exemplary combustive properties and observed emissions, despite having a significantly higher viscosity than the reference diesel.

10. Author contribution statement

In Chapter 3, I would like to acknowledge the work undertaken by Professor Paul Fromme. In the early stages of developing the D8k testing facility, Prof. Fromme dealt with the ultra-sonic signal tests necessary to identify a suitable location for the in-cylinder pressure transducer.

In Chapter 7 I would like to acknowledge the work of Dr. Lamya AL-Haj who provided the date pit ester test fuels, the motivation for the study discussed in that result chapter.

In Chapter 8 I would like to acknowledge the work of Xueping Lu, who continued the earlier work on optimising the reaction between THFA and Amberlyst-15, the result of which was used as the 'Bis-THFA' test fuel in the engine tests discussed.

Across all the chapters I shall acknowledge Professor Nicos Ladommatos, for designing the injector drivers without any information provided on the injector specifications from Volvo. These drivers are a crucial component of the testing facility, without which the D8k engine would not operate. Specifications on the design of these drivers are omitted from this work intentionally.

Across all the chapters I shall acknowledge Dr Paul Hellier, for the design and construction of the ultra-low volume fuel system used extensively in all the experiments discussed in this work. Dr Hellier also provided the author with revisions to the custom LabView and Matlab codes used to log and process the in-cylinder pressure and emissions data. Dr Alessandro Schönborn is acknowledged as the original author of these codes.

11. References

1.   Westerhold, T., Marwan, N., Drury, A. J., Liebrand, D., Agnini, C., Anagnostou, E., *et al.* An astronomically dated record of Earth's climate and its predictability over the last 66 million years. *Science (80-.).* **369**, 1383–1388 (2020).

2.   Moss, R. H., Edmonds, J. A., Hibbard, K. A., Manning, M. R., Rose, S. K., Van Vuuren, D. P., *et al.* The next generation of scenarios for climate change research and assessment. *Nature* **463**, 747–756 (2010).

3.   Shaftel, H., Callery, S., Jackson, R. & Biley, D. Evidence | Facts – Climate Change: Vital Signs of the Planet. *Earth Science Communications Team at NASA's Jet Propulsion Laboratory* https://climate.nasa.gov/evidence/ (2023).

4.   EEA. *Trends and projections in Europe 2022*. eea.europa.eu (2022) doi:10.2800/16646.

5.   A Study by Transport and Environment. *Electric Vehicles in Europe - 2016*. (2016). doi:10.2800/100230.

6.   Department for Business Energy & Industrial Strategy. 2021 UK greenhouse gas emissions, provisional figures. *Natl. Stat.* 1–19 (2022).

7.   Department for Business Energy & Industrial Strategy. Final UK greenhouse gas emissions national statistics. *National Statistics* https://www.gov.uk/government/collections/final-uk-greenhouse-gas-emissions-national-statistics (2018).

8.   Berjoza, D. & Jurgena, I. Influence of batteries weight on electric automobile performance. *Eng. Rural Dev.* **16**, 1388–1394 (2017).

9.   Chidambaram, K., Ashok, B., Vignesh, R., Deepak, C., Ramesh, R., Narendhra, T. M. V., *et al.* Critical analysis on the implementation barriers and consumer perception toward future electric mobility. *Proc. Inst. Mech. Eng. Part D J. Automob. Eng.* (2022) doi:10.1177/09544070221080349.

10.   Sato, S., Jiang, Y. J., Russell, R. L., Miller, J. W., Karavalakis, G., Durbin, T. D., *et al.* Experimental driving performance evaluation of battery-

powered medium and heavy duty all-electric vehicles. *Int. J. Electr. Power Energy Syst.* **141**, 108100 (2022).

11. Edwards, R., Padella, M., Giuntoli, J., Koeble, R., O'Connell, A., Bulgheroni, C., *et al. Definition of input data to assess GHG default emissions from biofuels in EU legislation, Version 1c.* (2017). doi:10.2790/658143.

12. Shamsul, N. S., Kamarudin, S. K., Rahman, N. A. & Kofli, N. T. An overview on the production of bio-methanol as potential renewable energy. *Renew. Sustain. Energy Rev.* **33**, 578–588 (2014).

13. Shameer, P. M. & Ramesh, K. Experimental evaluation on performance, combustion behavior and influence of in-cylinder temperature on NOx emission in a D.I diesel engine using thermal imager for various alternate fuel blends. *Energy* **118**, 1334–1344 (2017).

14. Hoekman, S. K. & Robbins, C. Review of the effects of biodiesel on NOx emissions. *Fuel Process. Technol.* **96**, 237–249 (2012).

15. Lapuerta, M., Armas, O. & Rodríguez-Fernández, J. Effect of biodiesel fuels on diesel engine emissions. *Prog. Energy Combust. Sci.* **34**, 198–223 (2008).

16. Koivisto, E., Ladommatos, N. & Gold, M. Systematic study of the effect of the hydroxyl functional group in alcohol molecules on compression ignition and exhaust gas emissions. *Fuel* **153**, 650–663 (2015).

17. Pacini, H. & Silveira, S. Consumer choice between ethanol and gasoline: Lessons from Brazil and Sweden. *Energy Policy* **39**, 6936–6942 (2011).

18. Majewski, W. A. & Jääskeläinen, H. What is Diesel Fuel. *DieselNet Technology guide* 1 https://www.dieselnet.com/tech/fuel_diesel.php (2916).

19. Stone, R. Introduction to Internal Combustion Engines. *MIT OpenCourseWare* 661 (1999) doi:10.1017/CBO9781107415324.004.

20. Heywood, J. B. Combustion in compression ignition engines. in *Internal combustion engine fundamentals* (eds. Duffy, A. & Morriss, J. M.) 491–497 (McGraw-Hill Inc, 1998).

21. Ganji, P. R., Singh, R. N., Raju, V. R. K. & Srinivasa Rao, S. Design of piston bowl geometry for better combustion in direct-injection compression ignition engine. *Sadhana - Acad. Proc. Eng. Sci.* **43**, 1–9 (2018).

22. Agnew, W. G. Room at the piston top contributions of combustion science to engine design. *Twent. Symp. Combust.* 1–17 (1984) doi:10.1016/S0082-0784(85)80482-3.

23. Dec, J. E. A Conceptual Model of DI Diesel Combustion Based on Laser-Sheet Imaging. *SAE Trans.* **106**, 1319–1348 (1997).

24. Heywood, J. B. Combustion in Compression-Ignition Engines. in *Internal Combustion Engine Fundamentals 2e* 836–839 (McGraw-Hill Education, 2018).

25. Dec, J. E. & Espey, C. Chemiluminescence imaging of autoignition in a di diesel engine. *SAE Tech. Pap.* **107**, 2230–2254 (1998).

26. Flynn, P. F., Durrett, R. P., Hunter, G. L., Zur Loye, A. O., Akinyemi, O. C., Dec, J. E., *et al.* Diesel combustion: An integrated view combining laser diagnostics, chemical kinetics, and empirical validation. *SAE Tech. Pap.* (1999) doi:10.4271/1999-01-0509.

27. Heywood, J. B. SWIRL, TUMBLE, SQUISH FLOW INTERACTIONS. in *Internal Combustion Engine Fundamentals 2e* 561–618 (McGraw-Hill Education, 2018).

28. Heywood, J. B. Charge Motion within the Cylinder. in *Internal Combustion Engine Fundamentals 2e* 561–611 (McGraw-Hill Education, 2018).

29. Westbrook, C.K. Chemical Kinetics of Hydrocarbon Ignition in Practical Combustion Systems. *Proc. Combust. Inst.* **28**, 1563–1577 (2000).

30. Westbrook, C. K., Curran, H. J., Pitz, W. J., Griffiths, J. F., Mohamed, C. & Wo, S. K. The effects of pressure, temperature, and concentration on the reactivity of alkanes: Experiments and modeling in a rapid compression machine. *Symp. Combust.* **27**, 371–378 (1998).

31. Tran, L., Herbinet, O., Li, Y., Wullenkord, J., Zeng, M., Bräuer, E., *et al.* Low-temperature gas-phase oxidation of diethyl ether : Fuel reactivity and

fuel-specific products. *Proc. Combust. Inst.* **37**, 511–519 (2019).

32. Koivisto, E., Ladommatos, N. & Gold, M. The influence of various oxygenated functional groups in carbonyl and ether compounds on compression ignition and exhaust gas emissions. *Fuel* **159**, 697–711 (2015).

33. Harford, T. How Rudolf Diesel's engine changed the world. *BBC world Service* (2016).

34. Kenar, J. A., Moser, B. R. & List, G. R. *Naturally Occurring Fatty Acids. Fatty Acids* vol. 2600 (2017).

35. Flagella, Z., Rotunno, T., Tarantino, E., Caterina, R. Di & Caro, A. De. Changes in seed yield and oil fatty acid composition of high oleic sunflower (Helianthus annuus L .) hybrids in relation to the sowing date and the water regime. **17**, 221–230 (2002).

36. Zhu, L., Cheung, C. S. & Huang, Z. Impact of chemical structure of individual fatty acid esters on combustion and emission characteristics of diesel engine. *Energy* **107**, 305–320 (2016).

37. Ertua. Transesterification FAME.svg - Wikimedia Commons. *Wikimedia Commons* https://commons.wikimedia.org/wiki/File:Transesterification_FAME.svg (2008).

38. Jain, S., Sharma, M. P. & Rajvanshi, S. Acid base catalyzed transesterification kinetics of waste cooking oil. *Fuel Process. Technol.* **92**, 32–38 (2011).

39. Anastopoulos, G., Zannikou, Y., Stournas, S. & Kalligeros, S. Transesterification of vegetable oils with ethanol and characterization of the key fuel properties of ethyl esters. *Energies* **2**, 362–376 (2009).

40. Marchetti, J. M. *Biodiesel Production Methods.* (Nova Science Publishers, Inc., 2010).

41. Dincer, K. Lower emissions from biodiesel combustion. *Energy Sources, Part A Recover. Util. Environ. Eff.* **30**, 963–968 (2008).

42. Mueller, C. J., Boehman, A. L. & Martin, G. C. An Experimental Investigation of the Origin of Increased NO $_x$ Emissions When Fueling a Heavy-Duty Compression-Ignition Engine with Soy Biodiesel. *SAE Int. J. Fuels Lubr.* **2**, 2009-01–1792 (2009).

43. Soam, S. & Hillman, K. Factors influencing the environmental sustainability and growth of hydrotreated vegetable oil (HVO) in Sweden. *Bioresour. Technol. Reports* **7**, 100244 (2019).

44. Handbook, N. Neste Renewable Diesel Handbook. *Neste* 1–33 (2015).

45. Yeoh, M. L. & Goh, C. S. Hydrotreated vegetable oil production from palm oil mill effluents: Status, opportunities and challenges. *Biofuels, Bioprod. Biorefining* **16**, 1153–1158 (2022).

46. No, S. Y. Application of hydrotreated vegetable oil from triglyceride based biomass to CI engines - A review. *Fuel* **115**, 88–96 (2014).

47. Chen, H. *Biotechnology of Lignocellulose.* (2014). doi:10.1007/978-94-007-6898-7.

48. Pelotas, U. F. De & Muniz, E. C. Hydrogels Nanocomposites Based on Crystals , Whiskers and Fibrils Derived from Biopolymers Hydrogels Nanocomposites Based on Crystals , Whiskers and Fibrils Derived from Biopolymers. (2015) doi:10.1007/978-81-322-2473-0.

49. Klemm, D., Heublein, B., Fink, H. & Bohn, A. Polymer Science Cellulose : Fascinating Biopolymer and Sustainable Raw Material Angewandte. 3358–3393 (2005) doi:10.1002/anie.200460587.

50. Lindstrom, T., Aulin, C. & Naderi, A. Microfibrillated cellulose. in *Encyclopedia of Polymer Science and Technology* 1–34 (John Wiley & Sons, Inc., 2013).

51. AMIS Secretariat. AMIS Market Monitor. *Market Monitor vol. 47* (2017).

52. Vieira da Rosa, A. *Fundamentals of Renewable Energy Processes*. (Elsevier Academic Press, 2005).

53. Karimi, K. & Taherzadeh, M. J. *Enzyme Based Hydrolysis Processes for Ethanol From Lignocellulosic Materials: a Review. BioResources* vol. 2

(2007).

54. Geddes, C. C., Nieves, I. U. & Ingram, L. O. Advances in ethanol production. *Curr. Opin. Biotechnol.* **22**, 312–319 (2011).

55. Zhang, Y. P., Berson, E., Sarkanen, S. & Dale, B. E. Sessions 3 and 8 : Pretreatment and Biomass Recalcitrance : Fundamentals and Progress. 80–83 (2009) doi:10.1007/s12010-009-8610-3.

56. Ingram, L. O. Deletion of methylglyoxal synthase gene (mgsA) increased sugar co-metabolism in ethanol-producing Escherichia coli. 1389–1398 (2009) doi:10.1007/s10529-009-0011-8.

57. Liu, Q., Luo, L. & Zheng, L. Lignins : Biosynthesis and Biological Functions in Plants. (2018) doi:10.3390/ijms19020335.

58. Ralph, J., Lundquist, K., Brunow, G., Lu, F., Kim, H., Paul, F., *et al.* Lignins : Natural polymers from oxidative coupling of 4-hydroxyphenyl-propanoids. 29–60 (2004).

59. Kleinert, M. & Barth, T. Phenols from lignin. *Chem. Eng. Technol.* **31**, 736–745 (2008).

60. Juliette Irmer. Lignin – a natural resource with huge potential - Bioeconomy. *Bioeconomy BW* 1 https://www.biooekonomie-bw.de/en/articles/dossiers/lignin-a-natural-resource-with-huge-potential/ (2017).

61. Gosselink, R. J. A., Jong, E. De, Guran, B. & Abächerli, A. Co-ordination network for lignin — standardisation , production and applications adapted to market requirements (EUROLIGNIN). **20**, 121–129 (2004).

62. Azadi, P., Inderwildi, O. R., Farnood, R. & King, D. A. Liquid fuels , hydrogen and chemicals from lignin : A critical review. *Renew. Sustain. Energy Rev.* **21**, 506–523 (2013).

63. Anna, E., Zdenka, H. & Heinze, T. Hemicellulose. in *Advanced Polymer Science* 4 (Springer Berlin, 2005).

64. Frei, E. & Preston, R. D. Cell wall organization and wall growth in the filamentous green algae Cladophora and Chaetomorpha II . Spiral

structure and spiral growth. (1961).

65. Gibson LJ. The heirarchial structure and mechanics of plant materials. *J. R. Soc. Interface* **9**, 2749–2766 (2012).

66. Shallom, D. & Shoham, Y. Microbial hemicellulases. *Curr. Opin. Microbiol.* **6**, 219–228 (2003).

67. Lynd, L. R., Weimer, P. J., van Zyl, W. H. & Pretorius, isak S. *Microbial Cellulose Utilization: Fundamentals and Biotechnology. MICROBIOLOGY AND MOLECULAR BIOLOGY REVIEWS* vol. 66 (American Society for Microbiology, 2002).

68. Hahn-Hägerdal, B., Jeppsson, H., Skoog, K. & Prior, B. A. Biochemistry and physiology of xylose fermentation by yeasts. *Enzyme Microb. Technol.* **16**, 933–943 (1994).

69. Moysés, D. N., Reis, V. C. B., de Almeida, J. R. M., de Moraes, L. M. P. & Torres, F. A. G. Xylose fermentation by saccharomyces cerevisiae: Challenges and prospects. *Int. J. Mol. Sci.* **17**, 1–18 (2016).

70. Fownes, G. An Account of the Artificial Formation of a vegeto-alkali. 253–262 (1845).

71. Brownlee, J. & Miner, S. INDUSTRIAL DEVELOPMENT OF FURFURAL. *Ind. Eng. Chem.* (1948) doi:10.1021/ie50458a005.

72. Chen, S., Wojcieszak, R., Dumeignil, F. & Marceau, E. How Catalysts and Experimental Conditions Determine the Selective Hydroconversion of Furfural and 5 - Hydroxymethylfurfural. (2018) doi:10.1021/acs.chemrev.8b00134.

73. Dalvand, K., Rubin, J., Gunukula, S., Wheeler, M. C. & Hunt, G. Biomass and Bioenergy Economics of biofuels : Market potential of furfural and its derivatives. *Biomass and Bioenergy* **115**, 56–63 (2018).

74. Win, D. T. Furfural – Gold from Garbage. **8**, 185–190 (2005).

75. Hong, E., Kim, J., Rhie, S., Ha, S., Kim, J. & Ryu, Y. Optimization of Dilute Sulfuric Acid Pretreatment of Corn Stover for Enhanced Xylose Recovery and Xylitol Production. **619**, 612–619 (2016).

76. Xing, R., Qi, W. & Huber, G. W. Production of furfural and carboxylic acids from waste aqueous hemicellulose solutions from the pulp and paper and cellulosic ethanol industries. *Energy Environ. Sci.* **4**, 2193–2205 (2011).

77. Market Insiders. Brent Oil price commodity. 1 https://markets.businessinsider.com/commodities/oil-price (2019).

78. Mariscal, R., Maireles-Torres, P., Ojeda, M., Sádaba, I. & López Granados, M. Furfural: a renewable and versatile platform molecule for the synthesis of chemicals and fuels. *Energy Environ. Sci.* **9**, 1144–1189 (2016).

79. Tarabanko, V. E., Chernyak, M. Y., Simakova, I. L. & Kaigorodov, K. L. Antiknock Properties of Furfural Derivatives. **88**, 1778–1782 (2015).

80. Application, F. & Data, P. (12) United States Patent MIXTURE OF FURFURAL AND 5-(ALKOXYMETHYL)FURFURAL DERVATIVES FROM SUGARS AND ALCOHOLS. **2**, (2012).

81. Dutta, S., De, S., Saha, B. & Alam, I. Catalysis Science & Technology MINIREVIEW Advances in conversion of hemicellulosic biomass to furfural and upgrading to biofuels. 2025–2036 (2012) doi:10.1039/c2cy20235b.

82. Corma, A., de la Torre, O., Renz, M. & Villandier, N. Production of High-Quality Diesel from Biomass Waste Products. *Angew. Chemie Int. Ed.* **50**, 2375–2378 (2011).

83. Environmental Protection Agency. Sources of Greenhouse Gas Emissions | US EPA. *Greenhouse Gas Emissions* https://www.epa.gov/ghgemissions/sources-greenhouse-gas-emissions (2022).

84. Kagawa, J. Health effects of diesel exhaust emissions - A mixture of air pollutants of worldwide concern. *Toxicology* **181**–**182**, 349–353 (2002).

85. Normann, F., Andersson, K., Leckner, B. & Johnsson, F. Emission control of nitrogen oxides in the oxy-fuel process. *Prog. Energy Combust. Sci.* **35**, 385–397 (2009).

86. B., Z. Y. The Oxidation of Nitrogen in Combustion and Explosions. *J. Acta Physicochim.* **21**, 577 (1946).

87. Masum, B. M., Masjuki, H. H., Kalam, M. A., Rizwanul Fattah, I. M., M Palash, S. & Abedin, M. J. Effect of ethanol-gasoline blend on NOx emission in SI engine. *Renew. Sustain. Energy Rev.* **24**, 209–222 (2013).

88. Fenimore, C. P. Formation of nitric oxide in premixed hydrocarbon flames. *Symp. Combust.* **13**, 373–380 (1971).

89. Heywood, J. B. NITROGEN OXIDES. in *Internal Combustion Engine Fundamentals 2e* 978–1005 (McGraw-Hill Education, 2018).

90. Merryman, E. L. & Levy, A. Nitrogen oxide formation in flames: The roles of NO2 and fuel nitrogen. *Symp. Combust.* **15**, 1073–1083 (1975).

91. Komiyama, K. & Heywood, J. B. Predicting NOx emissions and effects of exhaust gas recirculation in spark-ignition engines. *SAE Tech. Pap.* 1458–1476 (1973) doi:10.4271/730475.

92. Heywood, J. B. CARBON MONOXIDE. in *Internal Combustion Engine Fundamentals 2e* 1005–1010 (McGraw-Hill Education, 2018).

93. Heywood, J. B. HYDROCARBON EMISSIONS. in *Internal Combustion Engine Fundamentals 2e* 1010–1059 (McGraw-Hill Education, 2018).

94. Glassman, I. Soot formation in combustion processes. *Symp. Combust.* **22**, 295–311 (1989).

95. Bond, T. C., Doherty, S. J., Fahey, D. W., Forster, P. M., Berntsen, T., Deangelo, B. J., *et al.* Bounding the role of black carbon in the climate system: A scientific assessment. *J. Geophys. Res. Atmos.* **118**, 5380–5552 (2013).

96. Tree, D. R. & Svensson, K. I. Soot processes in compression ignition engines. *Prog. Energy Combust. Sci.* **33**, 272–309 (2007).

97. Michelsen, H. A. Probing soot formation, chemical and physical evolution, and oxidation: A review of in situ diagnostic techniques and needs. *Proc. Combust. Inst.* **36**, 717–735 (2017).

98. Bartok, W. & Sarofim, A. F. *Fossil fuel combustion : a source book*.

(Wiley, 1991).

99. Lee, K. O., Cole, R., Sekar, R., Choi, M. Y., Zhu, J., Kang, J., *et al.* Detailed characterization of morphology and dimensions of diesel particulates via thermophoretic sampling. *SAE Tech. Pap.* (2001) doi:10.4271/2001-01-3572.

100. Ladommatos, N. & Zhao, H. A guide to measurement of flame temperature and soot concentration in diesel engines using the two-colour method Part I: Principles. *SAE Tech. Pap.* (1994) doi:10.4271/941956.

101. Sato, H., Tree, D. R., Hodges, J. T. & Foster, A. D. E. A study on the effect of temperature on soot formation in a jet stirred combusto. (1990).

102. Hura, H. S. & Glassman, I. Soot formation in diffusion flames of fuel/oxygen mixtures. *Symp. Combust.* **22**, 371–378 (1989).

103. Xiao, Z., Ladommatos, N. & Zhao, H. The effect of aromatic hydrocarbons and oxygenates on diesel engine emissions. *Proc. Inst. Mech. Eng. Part D J. Automob. Eng.* **214**, 307–332 (2000).

104. Xiao, Z., Ladommatos, N. & Zhao, H. The effect of aromatic hydrocarbons and oxygenates on diesel engine emissions. *Proc. Inst. Mech. Eng. Part D J. Automob. Eng.* **214**, 307–332 (1999).

105. Ladommatos, N., Rubenstein, P., Harrison, K., Xiao, Z. & Zhao, H. The effect of aromatic hydrocarbons on soot formation in laminar diffusion flames and in a diesel engine. *Journal of the Institute of Energy* vol. 70 84–94 at https://doi.org/10.1016/s0140-6701(97)82206-0 (1997).

106. European Commission. Biofuels sustainability criteria. *Biofuels* https://energy.ec.europa.eu/topics/renewable-energy/bioenergy/biofuels_en (2018).

107. O'Malley, J., Pavlenko, N. & Searle, S. Estimating sustainable aviation fuel feedstock availability to meet growing European Union demand - International Council on Clean Transporation. *Int. Counc. Clean Transp.* (2021).

108. Dietsche, K.-H. History of the diesel engine. *Fundam. Automot. Engine Technol.* 8–17 (2014) doi:10.1007/978-3-658-03972-1_2.

109. Wang, W. G., Lyons, D. W., Clark, N. N., Gautam, M. & Norton, P. M. Emissions from nine heavy trucks fueled by diesel and biodiesel blend without engine modification. *Environ. Sci. Technol.* **34**, 933–939 (2000).

110. McCormick, R. L., Graboski, M. S., Alleman, T. L., Herring, A. M. & Tyson, K. S. Impact of biodiesel source material and chemical structure on emissions of criteria pollutants from a heavy-duty engine. *Environ. Sci. Technol.* **35**, 1742–1747 (2001).

111. Meteorological, F. Emissions Heavy-Duty Engine Aftertreatment Using Selected Biofuels With and.

112. Zhu, L., Cheung, C. S. & Huang, Z. Impact of chemical structure of individual fatty acid esters on combustion and emission characteristics of diesel engine. *Energy* **107**, 305–320 (2016).

113. Xue, J., Grift, T. E. & Hansen, A. C. Effect of biodiesel on engine performances and emissions. *Renew. Sustain. Energy Rev.* **15**, 1098–1116 (2011).

114. Altarazi, Y. S. M., Abu Talib, A. R., Yu, J., Gires, E., Abdul Ghafir, M. F., Lucas, J., *et al.* Effects of biofuel on engines performance and emission characteristics: A review. *Energy* **238**, (2022).

115. Mccormick, R. L., Ross, J. D. & Graboski, M. S. Effect of several oxygenates on regulated emissions from heavy-duty diesel engines. *Environ. Sci. Technol.* **31**, 1144–1150 (1997).

116. Shamun, S., Shen, M., Johansson, B., Tuner, M., Pagels, J., Gudmundsson, A., *et al.* Exhaust PM Emissions Analysis of Alcohol Fueled Heavy-Duty Engine Utilizing PPC. *SAE Int. J. Engines* **9**, 2142–2152 (2016).

117. Han, J., Wang, S., Maria Vittori, R. & Somers, L. M. T. Experimental study of the combustion and emission characteristics of oxygenated fuels on a heavy-duty diesel engine. *Fuel* **268**, 117219 (2020).

118. Han, J., Bao, H. & Somers, L. M. T. Experimental investigation of reactivity controlled compression ignition with n-butanol/n-heptane in a heavy-duty diesel engine. *Appl. Energy* **282**, 116164 (2021).

119. Büttgen, R. D., Maffei, L. P., Pelucchi, M., Faravelli, T., Frassoldati, A. & Heufer, K. A. Towards a better understanding of the combustion of oxygenated aromatic hydrocarbons . Comparing benzene , toluene , phenol and anisole with ignition delay times in a rapid compression machine. *Proc. Eur. Combust. Meet.* 1–7 (2019).

120. Talibi, M., Hellier, P. & Ladommatos, N. Impact of increasing methyl branches in aromatic hydrocarbons on diesel engine combustion and emissions. *Fuel* **216**, 579–588 (2018).

121. Xu, L., Wang, Y. & Liu, D. Effects of oxygenated biofuel additives on soot formation: A comprehensive review of laboratory-scale studies. *Fuel* **313**, 122635 (2022).

122. Han, J., Wang, S., Maria Vittori, R. & Somers, L. M. T. Experimental study of the combustion and emission characteristics of oxygenated fuels on a heavy-duty diesel engine. *Fuel* **268**, 117219 (2020).

123. Liu, H., Wang, Z., Li, Y., Zheng, Y., He, T. & Wang, J. Recent progress in the application in compression ignition engines and the synthesis technologies of polyoxymethylene dimethyl ethers. *Appl. Energy* **233**–**234**, 599–611 (2019).

124. Ratcliff, M. A., Mccormick, R. L. & Taylor, J. D. Compendium of Experimental Cetane Numbers Compendium of Experimental Cetane Numbers. (2017).

125. Tsuchiya, T. & Sato, Y. Development of DME engine for heavy-duty truck. *SAE Tech. Pap.* (2006) doi:10.4271/2006-01-0052.

126. Pélerin, D., Gaukel, K., Härtl, M., Jacob, E. & Wachtmeister, G. Potentials to simplify the engine system using the alternative diesel fuels oxymethylene ether OME1 and OME3−6 on a heavy-duty engine. *Fuel* **259**, 116231 (2020).

127. Alonso, D. M., Wettstein, S. G. & Dumesic, J. A. Bimetallic catalysts for upgrading of biomass to fuels and chemicals. *Chem. Soc. Rev.* **41**, 8075 (2012).

128. Volvo. Volvo Fe truck. *Volvo Trucks* https://www.volvotrucks.co.uk/en-

gb/trucks/volvo-fe.html (2019).

129. Volvo. Volvo FL truck. *Volvo Trucks* https://www.volvotrucks.com/en-en/trucks/volvo-fl.html (2019).

130. Volvo. Volvo B8R coach. *Volvo Trucks* https://www.volvobuses.co.uk/en-gb/our-offering/coaches/volvo-b8r.html (2019).

131. Volvo. Volvo FE - Powertrain specifications | Volvo TrucksPowertrain. https://www.volvotrucks.co.uk/en-gb/trucks/trucks/volvo-fe/specifications/powertrain.html (2022).

132. Tazerout, M., Corre, O. Le & Rousseau, S. SAE TECHNICAL TDC Determination in IC Engines Based on the Thermodynamic Analysis of the Temperature-Entropy Diagram. (1999).

133. Volvo. Volvo D8K engine. *Volvo D8K engine* https://www.volvotrucks.co.uk/en-gb/trucks/volvo-fe/features/d8k-engine.html (2019).

134. Volvo. *Taloring your Volvo FE.* https://www.volvotrucks.com/content/dam/volvo/volvo-trucks/masters/euro-6/pdf/trucks/volvo-fe/specifications/Volvo FE-Specifications-UK.pdf (2013).

135. Hellier, P. The molecular structure of future fuels. (University College London, 2013).

136. SCHENCK. Operating Instructions for Eddy Current Dynamometers. at (1977).

137. Schönborn, A. Influence of the molecular structure of biofuels on combustion in a compression ignition engine. 391 (2009).

138. Distributions, R. A. S. Real-time Aerosol Size Distributions Size , number and mass measurement.

139. Heywood, J. B. Heat-Release-Rate analysis. in *Internal Combustion Engine Fundamentals 2e* 858–860 (McGraw-Hill Education, 2018).

140. Gases - Specific Heats and Individual Gas Constants. https://www.engineeringtoolbox.com/specific-heat-capacity-gases-

d_159.html.

141. Horiba Instruments. *MEXA 9100HEGR instructions manual.* (1984).

142. Stedman, D. H., Daby, E. E., Stuhl, F. & Niki, H. Analysis of ozone and nitric oxide by a chemiluminescent method in laboratory and atmospheric studies of photochemical smog. *J. Air Pollut. Control Assoc.* **22**, 260–263 (1972).

143. Kohler, B. E. P. The Properties of Unsaturated Sulfur Compounds . **57**, (1930).

144. Mather, B. D., Viswanathan, K., Miller, K. M. & Long, T. E. Michael addition reactions in macromolecular design for emerging technologies. *Prog. Polym. Sci.* **31**, 487–531 (2006).

145. Wu, F., Li, H., Hong, R. & Deng, L. Construction of quaternary stereocenters by efficient and practical conjugate additions to α,β-unsaturated ketones with a chiral organic catalyst. *Angew. Chemie - Int. Ed.* **45**, 947–950 (2006).

146. Atkinson, R., Aschmann, S. M. & Pitts, J. N. Kinetics of the gas-phase reactions of OH radicals with a series of α,β-unsaturated carbonyls at 299 ± 2 K. *Int. J. Chem. Kinet.* **15**, 75–81 (1983).

147. Atkinson, R., Aschmann, S. M. & Pitts, J. N. Kinetics of the gas-phase reactions of OH radicals with a series of α,β-unsaturated carbonyls at 299 ± 2 K. *Int. J. Chem. Kinet.* **15**, 75–81 (1983).

148. Shang, Z., Khalil, Z., Li, L., Salim, A. A., Quezada, M., Kalansuriya, P., *et al.* Roseopurpurins: Chemical Diversity Enhanced by Convergent Biosynthesis and Forward and Reverse Michael Additions. *Org. Lett.* **18**, 4340–4343 (2016).

149. Miyanaga, A. Michael additions in polyketide biosynthesis. *Nat. Prod. Rep.* **36**, 531–547 (2019).

150. Vollenweider, S., Weber, H., Stolz, S., Chételat, A. & Farmer, E. E. Fatty acid ketodienes and fatty acid ketotrienes: Michael addition acceptors that accumulate in wounded and diseased Arabidopsis leaves. *Plant J.* **24**, 467–476 (2000).

151. Sarathy, S. M., Gaïl, S., Syed, S. A., Thomson, M. J. & Dagaut, P. A comparison of saturated and unsaturated C4 fatty acid methyl esters in an opposed flow diffusion flame and a jet stirred reactor. *Proc. Combust. Inst.* **31 I**, 1015–1022 (2007).

152. Sarathy, S. M., Vranckx, S., Yasunaga, K., Mehl, M., Oßwald, P., Metcalfe, W. K., *et al.* A comprehensive chemical kinetic combustion model for the four butanol isomers. *Combust. Flame* **159**, 2028–2055 (2012).

153. Gaïl, S., Sarathy, S. M., Thomson, M. J., Diévart, P. & Dagaut, P. Experimental and chemical kinetic modeling study of small methyl esters oxidation: Methyl (E)-2-butenoate and methyl butanoate. *Combust. Flame* **155**, 635–650 (2008).

154. Bennadji, H., Glaude, P. A., Coniglio, L. & Billaud, F. Experimental and kinetic modeling study of ethyl butanoate oxidation in a laminar tubular plug flow reactor. *Fuel* **90**, 3237–3253 (2011).

155. Coniglio, L., Bennadji, H., Glaude, P. A., Herbinet, O. & Billaud, F. Combustion chemical kinetics of biodiesel and related compounds (methyl and ethyl esters): Experiments and modeling-Advances and future refinements. *Prog. Energy Combust. Sci.* **39**, 340–382 (2013).

156. Fisher, E. M., Pitz, W. J., Curran, H. J. & Westbrook, C. K. DETAILED CHEMICAL KINETIC MECHANISMS FOR COMBUSTION OF OXYGENATED FUELS. **28**, 1579–1586 (2000).

157. Johnson, P. N., Lavadera, M. L., Konnov, A. A. & Narayanaswamy, K. Oxidation kinetics of methyl crotonate: A comprehensive modeling and experimental study. *Combust. Flame* **229**, 111409 (2021).

158. Li, C., Zhang, Z., He, L., Ye, M., Ning, H., Shang, Y., *et al.* Experimental and kinetic modeling study on the ignition characteristics of methyl acrylate and vinyl acetate: Effect of C[dbnd]C double bond. *Energy* **245**, (2022).

159. Zhang, Y., Yang, Y. & Boehman, A. L. Premixed ignition behavior of C9 fatty acid esters: A motored engine study. *Combust. Flame* **156**, 1202–1213 (2009).

160. Westbrook, C. K., Naik, C. V., Herbinet, O., Pitz, W., Mehl, M., Sarathy, S. M., *et al.* Detailed chemical kinetic reaction mechanisms for soy and rapeseed biodiesel fuels. *Combust. Flame* **158**, 742–755 (2011).

161. Yang, B., Westbrook, C. K., Cool, T. A., Hansen, N. & Kohse-Höinghaus, K. The effect of carbon-carbon double bonds on the combustion chemistry of small fatty acid esters. *Zeitschrift fur Phys. Chemie* **225**, 1293–1314 (2011).

162. Hebbar, G. S. NOx from diesel engine emission and control strategies - a review. *Int. J. Mech. Eng. Rob. Res* **3**, 471–482 (2014).

163. Heywood, J. B. IGNITION DELAY. in *Internal Combustion Engine Fundamentals 2e* 916–940 (McGraw-Hill Education, 2018).

164. Nada, Y., Komatsubara, Y., Pham, T., Yoshii, F. & Kidoguchi, Y. Evaluation of NOx Production Rate in Diesel Combustion Based on Measurement of Time Histories of NOx Concentrations and Flame Temperature. *SAE Int. J. Engines* **8**, 303–313 (2014).

165. Pinzi, S., Rounce, P., Herreros, J. M., Tsolakis, A. & Pilar Dorado, M. The effect of biodiesel fatty acid composition on combustion and diesel engine exhaust emissions. *Fuel* **104**, 170–182 (2013).

166. Li, W., Cao, C., Zhang, X., Li, Y., Yang, J., Zou, J., *et al.* Exploring combustion chemistry of ethyl valerate at various pressures: Pyrolysis, laminar burning velocity and kinetic modeling. *Combust. Flame* **227**, 27–38 (2021).

167. Critchfield, F. E. & Johnson, J. B. Determination of Alpha, Beta-Unsaturated Compounds by Reaction with Sodium Sulfite. *Anal. Chem.* **28**, 73–75 (1956).

168. Namysl, S., Pelucchi, M., Herbinet, O., Frassoldati, A., Faravelli, T. & Battin-Leclerc, F. A first evaluation of butanoic and pentanoic acid oxidation kinetics. *Chem. Eng. J.* **373**, 973–984 (2019).

169. Hellier, P. & Ladommatos, N. The influence of biodiesel composition on compression ignition combustion and emissions. *Proc. Inst. Mech. Eng. Part A J. Power Energy* **229**, 714–726 (2015).

170. Francis, A. C. & Robert, M. G. *Organic Chemistry*. (McGraw-Hill, 2011).

171. Liang, X., Duan, Y., Fan, Y., Huang, Z. & Han, D. Influences of C5 esters addition on anti-knock and auto-ignition tendency of a gasoline surrogate fuel. *Int. J. Engine Res.* (2021) doi:10.1177/14680874211030898.

172. Boot, M. D. Use of a perfume composition as a fuel for internal combustion engines. *World Intellectual Property Organization* (2013).

173. Ayodele, O. O., Dawodu, F. A., Yan, D., Lu, X., Xin, J. & Zhang, S. Hydrodeoxygenation of angelica lactone dimers and trimers over silica-alumina supported nickel catalyst. *Renew. Energy* **86**, 943–948 (2016).

174. Yan, K., Lafleur, T., Wu, X., Chai, J., Wu, G. & Xie, X. Cascade upgrading of γ-valerolactone to biofuels. *Chem. Commun.* **51**, 6984–6987 (2015).

175. Gil, S., Parra, M., Rodriguez, P. & Segura, J. Recent Developments in y-Lactone Synthesis. *Mini. Rev. Org. Chem.* **6**, 345–358 (2009).

176. Wang, S., Zhao, Y., Lin, H., Chen, J., Zhu, L. & Luo, Z. Conversion of C5 carbohydrates into furfural catalyzed by a Lewis acidic ionic liquid in renewable γ-valerolactone. *Green Chem.* **19**, 3869–3879 (2017).

177. gamma-hexalactone, 695-06-7. http://www.thegoodscentscompany.com/data/rw1006382.html.

178. Jensen, T., John, B. Y., Birkinshaw, H. & Raistrick, H. Cccvii . Studies in the Biochemistry of Micro-Organisms . of Terrestric Acid (Ethylcarolic Acid), a Metabolic Product of Penicillium. 2194–2200 (1936).

179. Kaori Nakano, A., Botelho Lourenco, C., Calvet, F. & Carrasco, C. A method for improving the performance of a fragrance or a fragrance mixture. 95–98 (2020).

180. UCHIYAMA, H. [US], WOO, R. A. [US], DUVAL, D. L. [US] & REECE, S. [US]. Compositions comprising cyclodextrin. 14 (2005).

181. Api, A. M., Belsito, D., Botelho, D., Bruze, M., Burton, G. A., Buschmann, J., *et al.* RIFM fragrance ingredient safety assessment, 4′-methylacetophenone, CAS Registry Number 122-00-9. *Food Chem. Toxicol.* **122**, S75–S83 (2018).

182. Api, A. M., Belsito, D., Botelho, D., Bruze, M., Burton, G. A., Buschmann, J., *et al.* RIFM fragrance ingredient safety assessment, δ-dodecalactone, CAS Registry Number 713-95-1. *Food Chem. Toxicol.* **153**, (2021).

183. Tanaka, S., Ayala, F. & Keck, J. C. A reduced chemical kinetic model for HCCI combustion of primary reference fuels in a rapid compression machine. *Combust. Flame* **133**, 467–481 (2003).

184. Hellier, P., Ladommatos, N., Allan, R. & Rogerson, J. Combustion and emissions characteristics of toluene/n-heptane and 1-octene/n-octane binary mixtures in a direct injection compression ignition engine. *Combust. Flame* **160**, 2141–2158 (2013).

185. Hellier, P., Ladommatos, N., Allan, R., Payne, M. & Rogerson, J. The impact of saturated and unsaturated fuel molecules on diesel combustion and exhaust emissions. *SAE Tech. Pap.* **5**, 106–122 (2011).

186. Perrin, C. L. Physical Organic Chemistry. in *Encyclopedia of Physical Science and Technology* 211–243 (Academic Press, 2003). doi:10.1016/B0-12-227410-5/00576-7.

187. Hellier, P., Talibi, M., Eveleigh, A. & Ladommatos, N. An overview of the effects of fuel molecular structure on the combustion and emissions characteristics of compression ignition engines. *Proc. Inst. Mech. Eng. Part D J. Automob. Eng.* 095440701668745 (2017) doi:10.1177/0954407016687453.

188. Kim, J., Lee, J. & Kim, K. Numerical study on the effects of fuel viscosity and density on the injection rate performance of a solenoid diesel injector based on AMESim. *Fuel* **256**, (2019).

189. Thakkar, K., Kachhwaha, S. S., Kodgire, P. & Srinivasan, S. Combustion investigation of ternary blend mixture of biodiesel/n-butanol/diesel: CI engine performance and emission control. *Renew. Sustain. Energy Rev.* **137**, 110468 (2021).

190. Kelly-Zion, P. L. & Dec, J. E. A computational study of the effect of fuel type on ignition time in homogeneous charge compression ignition engines. *Proc. Combust. Inst.* **28**, 1187–1194 (2000).

191. Yamada, H., Suzaki, K., Tezaki, A. & Goto, Y. Transition from cool flame to thermal flame in compression ignition process. **154**, 248–258 (2008).

192. Heywood, J. B. *Internal combustion engine fundamentals. Choice Reviews Online* vol. 1 (McGraw-Hill Education, 2018).

193. Chang, C. T. & Farrell, P. V. A study on the effects of fuel viscosity and nozzle geometry on high injection pressure diesel spray characteristics. *SAE Tech. Pap.* **106**, 558–567 (1997).

194. Wiberg, K. B. The Concept of Strain in Organic Chemistry. *Angew. Chemie Int. Ed. English* **25**, 312–322 (1986).

195. Wade, L. G. *Organic chemistry*. (Pearson Prentice Hall, 2006).

196. Brown, J. M., Conn, A. D., Pilcher, G., Leitão, M. L. P. & Meng-Yan, Y. On the strain energy of 5-ring and 6-ring lactones. *J. Chem. Soc. Chem. Commun.* 1817–1819 (1989) doi:10.1039/C39890001817.

197. Atabani, A. E., Silitonga, A. S., Ong, H. C., Mahlia, T. M. I., Masjuki, H. H., Badruddin, I. A., *et al.* Non-edible vegetable oils: A critical evaluation of oil extraction, fatty acid compositions, biodiesel production, characteristics, engine performance and emissions production. *Renew. Sustain. Energy Rev.* **18**, 211–245 (2013).

198. Atadashi, I. M., Aroua, M. K. & Aziz, A. A. High quality biodiesel and its diesel engine application: A review. *Renew. Sustain. Energy Rev.* **14**, 1999–2008 (2010).

199. Singh, S. P. & Singh, D. Biodiesel production through the use of different sources and characterization of oils and their esters as the substitute of diesel: A review. *Renew. Sustain. Energy Rev.* **14**, 200–216 (2010).

200. Griffiths, H. Official E5 petrol and B7 diesel fuel pump labels introduced on UK forecourts | Auto Express. *Autoexpress* 1 https://www.autoexpress.co.uk/car-news/106137/official-e5-petrol-and-b7-diesel-fuel-pump-labels-introduced-on-uk-forecourts (2019).

201. Wu, Y. G., Lin, Y. & Chang, C.-T. Combustion characteristics of fatty acid methyl esters derived from recycled cooking oil. *Fuel* **86**, 2810–2816 (2007).

202. Cheng, L. H., Cheng, Y. F., Yen, S. Y. & Chen, J. Ultrafiltration of triglyceride from biodiesel using the phase diagram of oil-FAME-MeOH. *J. Memb. Sci.* **330**, 156–165 (2009).

203. Hasan, M. M., Rahman, M. M. & Kadirgama, K. A review on homogeneous charge compression ignition engine performance using biodiesel-diesel blend as a fuel. *Int. J. Automot. Mech. Eng.* **11**, 2199–2211 (2015).

204. Patel, P. D., Lakdawala, A., Chourasia, S. & Patel, R. N. Bio fuels for compression ignition engine: A review on engine performance, emission and life cycle analysis. *Renew. Sustain. Energy Rev.* **65**, 24–43 (2016).

205. Datta, A. & Mandal, B. K. A comprehensive review of biodiesel as an alternative fuel for compression ignition engine. *Renew. Sustain. Energy Rev.* **57**, 799–821 (2016).

206. Musculus, M. P. B. On the correlation between NOx emissions and the diesel premixed burn. *SAE Tech. Pap.* (2004) doi:10.4271/2004-01-1401.

207. Ban-Weiss, G. A., Chen, J. Y., Buchholz, B. A. & Dibble, R. W. A numerical investigation into the anomalous slight NOx increase when burning biodiesel; A new (old) theory. *Fuel Process. Technol.* **88**, 659–667 (2007).

208. Schönborn, A., Ladommatos, N., Williams, J., Allan, R. & Rogerson, J. The influence of molecular structure of fatty acid monoalkyl esters on diesel combustion. *Combust. Flame* **156**, 1396–1412 (2009).

209. Mizushima, N., Kawano, D., Ishii, H., Takada, Y. & Sato, S. Evaluation of Real- World Emissions from Heavy-Duty Diesel Vehicle Fueled with FAME, HVO and BTL using PEMS. *SAE Tech. Pap.* **2014-Octob**, (2014).

210. Jamil, F., Al-Muhtaseb, A. H., Al-Haj, L., Al-Hinai, M. A., Hellier, P. & Rashid, U. Optimization of oil extraction from waste 'date pits' for biodiesel production. *Energy Convers. Manag.* **117**, 264–272 (2016).

211. Hellier, P., Jamil, F., Zaglis-Tyraskis, E., Al-Muhtaseb, A. H., Al Haj, L. & Ladommatos, N. Combustion and emissions characteristics of date pit methyl ester in a single cylinder direct injection diesel engine. *Fuel* **243**,

162–171 (2019).

212. Alleman, T. L. & McCormick, R. L. *Biodiesel Handling and Use Guide.* (US Department of Energy, 2016).

213. Sathyamurthy, R., Balaji, D., Gorjian, S., Muthiya, S. J., Bharathwaaj, R., Vasanthaseelan, S., *et al.* Performance, combustion and emission characteristics of a DI-CI diesel engine fueled with corn oil methyl ester biodiesel blends. *Sustain. Energy Technol. Assessments* **43**, 100981 (2021).

214. Lyn, W. T. Study of burning rate and nature of combustion in diesel engines. *Symp. Combust.* **9**, 1069–1082 (1963).

215. Garner, S. & Brezinsky, K. Biologically derived diesel fuel and NO formation: An experimental and chemical kinetic study, Part 1. *Combust. Flame* **158**, 2289–2301 (2011).

216. Cheng, A. S., Upatnieks, A. & Mueller, C. J. Investigation of the impact of biodiesel fuelling on NOx emissions using an optical direct injection diesel engine. *Int. J. Engine Res.* **7**, 297–318 (2006).

217. Song, J., Alam, M., Boehman, A. L. & Kim, U. Examination of the oxidation behavior of biodiesel soot. *Combust. Flame* **146**, 589–604 (2006).

218. Peters, F. N. Industrial uses of furans. *Ind. Eng. Chem.* **31**, 178–180 (1939).

219. Lifson, W. E. & Gordon, W. Motor Fuel - United States Patent Office. 3–5 (1952).

220. Zaccheria, F., Scotti, N. & Ravasio, N. Solid Acids for the Reaction of Bioderived Alcohols into Ethers for Fuel Applications. *Catalysts* **9**, 172 (2019).

221. Hronec, M., Fulajtárová, K., Horváth, B., Liptaj, T. & Dobročka, E. A facile conversion of furfural to novel tetrahydrofurfuryl hemiacetals. *Appl. Catal. A Gen.* **594**, 117471 (2020).

222. McCormick, R. L., Ratcliff, M. A., Christensen, E., Fouts, L., Luecke, J.,

Chupka, G. M., *et al.* Properties of oxygenates found in upgraded biomass pyrolysis oil as components of spark and compression ignition engine fuels. *Energy and Fuels* **29**, 2453–2461 (2015).

223. Wu, L., Moteki, T., Gokhale, A. A., Flaherty, D. W. & Toste, F. D. Production of Fuels and Chemicals from Biomass: Condensation Reactions and Beyond. *Chem* **1**, 32–58 (2016).

224. Williamson, A. XLV. Theory of ætherification. *London, Edinburgh, Dublin Philos. Mag. J. Sci.* **37**, 350–356 (1850).

225. Stenger-smith, J. D., Baldwin, L., Chafin, A. & Goodman, P. A. Synthesis and Characterization of bis (Tetrahydrofurfuryl) Ether. 297–300 (2016) doi:10.1002/open.201600013.

226. Stenger-smith, J. D. THFA ether production patent.pdf. (2018).

227. Lu, X. Influence of Reaction Parameters on Synthesis of An Improved Biofuel for Heavy Duty Diesel Engines. (UCL, 2022).

228. Tindal, M. J. & Uyehara, O. A. *Chapter Three Diesel Engines. Internal Combustion Engines* (Copyright © 1988 by ACADEMIC PRESS LIMITED, 1988). doi:10.1016/B978-0-12-059790-1.50009-2.

229. Schönborn, A., Ladommatos, N. & Bae, C. Diffusion- and homogeneous-charge combustion of volatile ethers in a compression ignition engine. *Energy and Fuels* **23**, 5865–5878 (2009).

230. Mandal, S., Mandal, S., Ghosh, S. K., Sar, P., Ghosh, A., Saha, R., *et al.* A review on the advancement of ether synthesis from organic solvent to water. *RSC Adv.* **6**, 69605–69614 (2016).

231. Patwardhan, S. A. & Dev, S. *Amberlyst-15, a superior catalyst for the preparation of Enol ethers and acetals.* (1973).

232. Pinto, B. P., De Lyra, J. T., Nascimento, J. A. C. & Mota, C. J. A. Ethers of glycerol and ethanol as bioadditives for biodiesel. *Fuel* **168**, 76–80 (2016).

233. Xu, S., Yin, C., Pan, D., Hu, F., Wu, Y., Miao, Y., *et al.* Efficient conversion of glucose into 5-hydroxymethylfurfural using a bifunctional Fe

3+ modified Amberlyst-15 catalyst. *Sustain. Energy Fuels* **3**, 390–395 (2019).

234. Rosatella, A. A., Simeonov, S. P., Frade, R. F. M. & Afonso, C. A. M. 5-Hydroxymethylfurfural (HMF) as a building block platform: Biological properties, synthesis and synthetic applications. *Green Chem.* **13**, 754–793 (2011).

235. Offnfopt. GC-MS diagram. *Wikimedia Commons* Gas Chromatograph.png (2015).

236. McMaster, M. C. *GC/MS A Practical users Guide*. (John Wiley & Sons, Inc., 2008).

237. S. Department of Commerce, U. NIST Standard Referance Data. *National Institute of Standards and Technology* https://www.nist.gov/srd/nist-standard-reference-database-1a-v17.

238. Bransden, B. H. *Physics of atoms and molecules /B. H. Bransden and C. J. Joachain.* (Harlow : Prentice Hall, 2003).

239. Roberts, J. *Nuclear Magnetic Resonance - Applications to organic chemistry.* (McGraw-Hill Inc, 1959).

240. Moseley, D. P., Houser, J. R., Mench, M. M., Aaron, D. S., Ertugrul, T. Y., Daugherty, M. C., *et al.* Critical Review—Experimental Diagnostics and Material Characterization Techniques Used on Redox Flow Batteries. *J. Electrochem. Soc.* **165**, A970–A1010 (2018).

241. Mlynarik, V. Introduction to muclear magnetic resonance. *Anal. Biochem.* **529**, 4–9 (2017).

12. Appendix

12.1. Additional discussion for Chapter 4

Williamson ether synthesis

The Williamson ether synthesis, as shown in Figure 12.1 is expensive as it requires multiple synthetic steps, has a low atom economy, uses expensive reagents and requires forcing conditions.
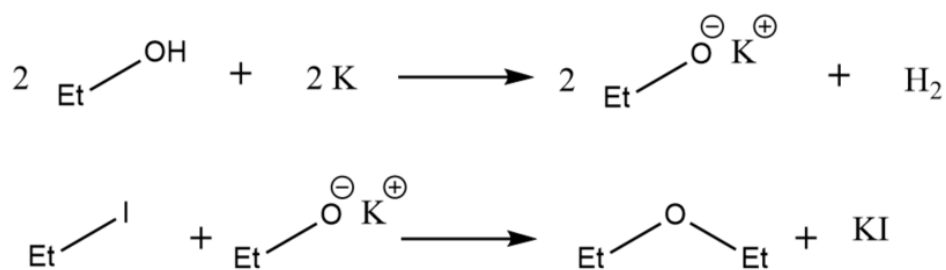
Figure 12.1: First reported Williamson Ether synthesis.

The Williamson ether synthesis was first reported in 1851 and it involved reacting iodoethane with potassium ethoxide to form an ether (Figure 12.1)This first reaction proceeds quickly, but when using larger alcohols, the haloalkane may not be available to purchase. This leads to extra synthetic steps and still necessitates the in-situ production of the alkoxide. The synthesis also produces side products which have low economic value and are potentially dangerous to the environment. There has been ongoing promising research to find alternative routes to a clean ether synthesis, such as utilising recyclable heavy metal catalysts.[230]

12.1.1. Amberlyst-15

Amberlyst-15 is a styrene supported sulfonic acid polymer, as shown in Figure 12.2, with diethenylbenzene cross linkers. This sulfonic group is strongly acidic, and the catalyst is insoluble, so it acts as an acidic heterogenous catalyst which can be filtered from the solution. The amberlyst-15 catalyst has been investigated extensively and has shown promise as a very safe alternative to traditional acid catalysed reactions.[231]

Figure 12.2: Ethenylbenzene sulfonic acid and diethenylbenzene.

Pinto et al. investigated amberlyst-15's ability for etherification between ethanol and glycerol. They demonstrated that amberlyst-15 has an excellent conversion factor and will proceed to etherify all three alcohol functional groups in glycerol at a higher rate than the other solid acid catalysts they studied.[232] Using amb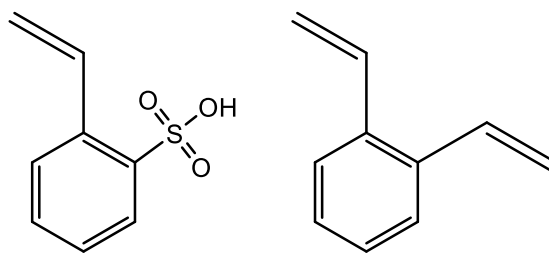erlyst-15 as an etherification catalyst removes the extensive steps needed for a Williamson ether synthesis and as a heterogenous catalyst can be easily recycled.

Xu et al. investigated the conversion of glucose to hydroxymethylfurfural (HMF) using Fe^{3+} supported on Amberlyst-15.[233] HMF, similar to furfural is a versatile platform chemical with many conversion routes to higher value chemicals or biofuels available.[234] Xu et al. showed that amberlyst-15 with supported Fe^{3+} can be recycled, with only a 12 % loss in iron sites after 4 reactions and a 3 % loss in sulfur sites.

Amberlyst-15's ability to etherify alcohols at relatively simple conditions compared to the traditional Williamson ether synthesis and its easy recyclability make it an ideal catalyst to produce potential future fuels which utilise the ether functional group.

12.2. Analytical chemistry techniques

12.2.1. GC-MS

Gas chromatography – mass spectrometry is an analytical chemistry tool used for identifying the individual compounds present in a mixture. A sample is vaporised and an inert carrier gas (usually nitrogen or helium), called the 'mobile phase' flows through a capillary column, the 'stationary phase', which can be made of a structural polymer, glass or metal. At the end of the column a detector is present which records time at which a compound completes travel

through the column. Figure 12.3 shows a schematic form of a typical GC-MS configuration.
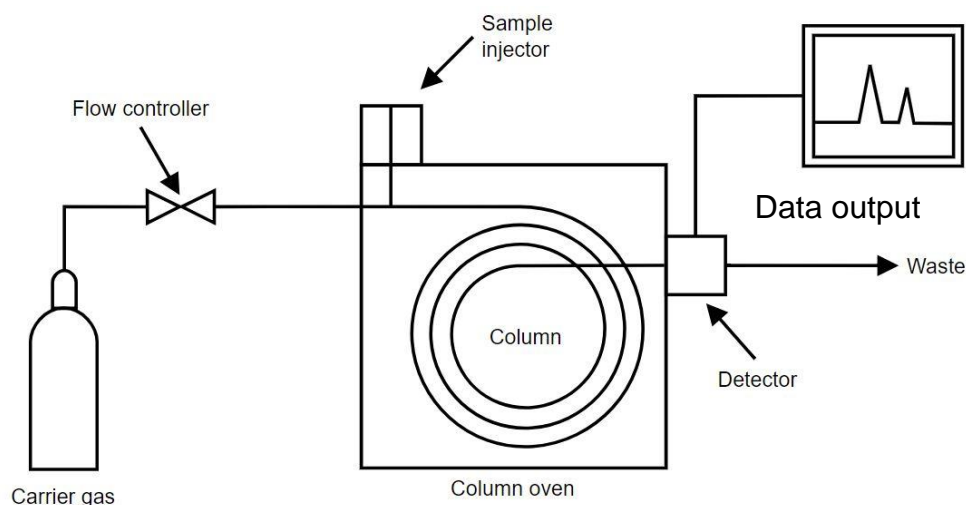
Figure 12.3: Basic diagram of a GC-MS set up[235]

The structure of a chemical compound will influence the difference in attraction between the mobile and stationary phase of the GC. Light, non-attractive molecules such as dichloromethane will pass through the column relatively quickly. Heavier, more attractive molecules will travel through the column more slowly. How fast a compound moves through the column is referred to as its 'retention time'.

When a mass spectrometer is used in conjunction with a GC, the compounds will exit the column after some time and enter the MS where the compound is bombarded with electrons produced from a filament. The electrons will fragment the compound and ionise the fragments which then enter a mass analyser. This measures the fragmentation pattern and the mass to charge ratio (m/z) of the fragment.[236]

The data collected by a GC-MS is the retention time, fragmentation pattern and molecular weight of a compound. The combination of these three pieces of information is unique and is often termed the compounds fingerprint. The GC-MS contains a library with thousands of compound's fingerprints contained and comparison of samples to this library yields the identification of unknowns.[237]

12.3. NMR

Nuclear magnetic resonance (NMR) spectroscopy is an analytical tool used to determine structural detail of molecules through the observation of resonant

absorption of radiofrequency (RF) radiation by nuclei in an applied magnetic field.

Protons and neutrons have an intrinsic quantum property called 'spin', both protons and neutrons have a spin of ½ which can be either up or down. Spin is an intrinsic angular momentum property of nuclei. Particles with a spin can process a magnetic dipole moment – analogous to a rotating electrical charged body in classical mechanics.[238]

When the total number of protons plus neutrons in a nucleus is odd, the nucleus of the atom has a spin moment and therefore a magnetic moment. These atomic nuclei are the focus of NMR spectroscopy. Many atoms are NMR active, with the two most useful ones for synthetic organic chemistry being ^{1}H (99.98 % abundance) and ^{13}C (1.1 % abundance).

An NMR spectrometer simply is a large magnet, RF emitter or oscillator and an RF detector. The sample to be tested is placed in a pole gap of the magnet and subjected to an RF field. Adsorption of the RF field occurs at particular combinations of the RF field and magnetic field strength. This generates a new RF signal, which is picked up at a detector. This provides information as to the chemical structure of a molecule as individual atoms will resonate at different values of the applied magnetic field.[239]
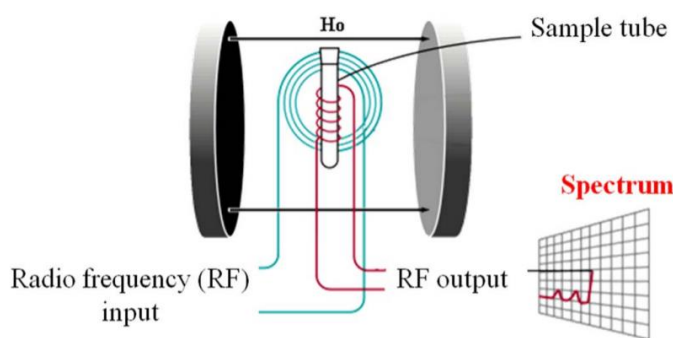
Figure 12.4: Simple diagram of an NMR experiment[240]

The electrons surrounding an atom carry an electric charge and as they orbit the atomic nucleus, generate a magnetic field which provides a level of shielding from the external magnetic field. This shielding effect will vary with the chemical environment as the presence of nearby atoms will affect the orbits of the electrons. This shielding from the magnetic field 'shifts' the atoms resonance frequency from the unshielded position.

The measured chemical shift (δ ppm) of the resonance is indicative of the chemical environment that an atom is in and so this shift is dependent on chemical structures present in a molecule.[241] This information on shielding effects surrounding atoms, and the change in the resonance allows, us to construct a prediction of the molecular structure.

12.4. Fuel specifications

Table 12.1: Test fuel specifications and CAS Numbers

Test fuel	CAS Number	Fuel supplier
γ-Valerolactone	108-29-2	Sigma Aldrich (Merck)
γ-Hexalactone	695-06-7	Sigma Aldrich (Merck)
γ-Heptalactone	105-21-5	Sigma Aldrich (Merck)
γ-Octalactone	104-50-7	Sigma Aldrich (Merck)
γ-Nonanoic lactone	104-61-0	Sigma Aldrich (Merck)
γ-Decalactone	706-14-9	Sigma Aldrich (Merck)
γ-Undecalactone	104-67-6	Sigma Aldrich (Merck)
γ-Dodecalactone	2305-05-7	Sigma Aldrich (Merck)
δ-Nonalactone	3301-94-8	Sigma Aldrich (Merck)
δ-Decalactone	705-86-2	Sigma Aldrich (Merck)
δ-Undecalactone	710-04-3	Sigma Aldrich (Merck)
δ-Dodecalactone	713-95-1	Sigma Aldrich (Merck)

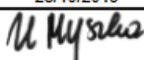| Ethyl octanoate	106-32-1	Sigma Aldrich (Merck)
Ethyl-trans-2-octenoate	7367-82-0	Sigma Aldrich (Merck)
Ethyl decanoate	110-38-3	Sigma Aldrich (Merck)
Ethyl trans-2-decenoate	7367-88-6	Sigma Aldrich (Merck)
Methyl nonanoate	1731-84-6	Sigma Aldrich (Merck)
Methyl trans-2-nonenoate	14952-06-8	Sigma Aldrich (Merck)
Methyl 3-nonenoate	13481-87-3	Sigma Aldrich (Merck)
Rapeseed methyl ester	n/a	Coryton Advanced Fuels
Date pit methyl ester	n/a	SQU University
Reference Omani fossil diesel	n/a	SQU University
Reference fossil diesel	n/a	Haltermann Carless

Certificate of Analysis

Fuel Blend No: CAF-G19/1431
Fuel Type: RME No Antioxidant
Customer: University College London

Contact: Daniel Southern
Order No: F45-2951996
Date: 28/10/2019

Test	Method	Unit	Limit Min	Limit Max	Result
Appearance	Visual		Report		C&B
Cetane Number	EN ISO 5165		51.0	-	52.0
Density @ 15°C	EN ISO 12185	kg/L	0.8600	0.9000	0.8827
Acid Value	EN 14104	mgKOH/g	-	0.50	0.40
Flash Point	EN ISO 2719	°C	101.0	-	151.0
Sulfur	EN ISO 20846	mg/kg	-	10.0	2.5
Viscosity at 40°C	EN ISO 3104	mm²/s	3.500	5.000	4.510
Water Content	EN ISO 12937	mg/kg	-	500	290
FAME Content	EN 14103	% m/m	96.5	-	99.9
Polyunsaturated Methyl Ester	EN 15779	% m/m	-	1.00	<1.00
Linolenic Acid Methyl Ester Content	EN 14103	% m/m	-	12.0	9.0
Monoglyceride Content	EN 14105	% m/m	-	0.70	0.32
Diglyceride Content	EN 14105	% m/m	-	0.20	0.09
Triglyceride Content	EN 14105	% m/m	-	0.20	0.11
Free Glycerol	EN 14105	% m/m	-	0.02	<0.01
Total Glycerol	EN 14105	% m/m	-	0.25	0.11
Iodine value	EN 14111	g I₂/100g	-	120	112
Methanol	EN 14110	% m/m	-	0.20	0.05
Oxidation Stability	EN 15751	h	8.0	-	8.8
Sulphated Ash Content	ISO 3987	% m/m	-	0.02	<0.01
Copper Corrosion (3h at 50°C)	EN ISO 2160	Rating	Class 1	-	Class 1
Total Contamination	EN 12662	mg/kg	-	24	15
Sodium + Potassium	EN 14538	mg/kg	-	5.0	1.8
Calcium + Magnesium	EN 14538	mg/kg	-	5.0	1.2
Phosphorus	EN 14107	mg/kg	-	4.0	0.3

Sample Received Condition: Good (No Seal)
Date Sample Received: 01/07/2019

Notes:

Date:	28/10/2019
Authorised by: **U Myszka** *Fuels Formulation Scientist*	*U Myszka*

Coryton Advanced Fuels Ltd
The Manorway
Stanford-le-Hope
Essex SS17 9LN, UK

Tel: +44 (0)1375 665707
Fax: + 44 (0)1375 678904
Email: admin@corytonfuels.co.uk
Website: www.corytonfuels.co.uk

Figure 12.5: CORYTON Advanced Fuels specification sheet for the rapeseed methyl ester.

271

Haltermann Carless

Department of Mechanical Engineerin
Roberts Building
London
WC1E 7JE

Certificate 100000184897

Date:	16/03/2020
Customer PO:	F45-3041017
Delivery Note:	80162210 000010
Order No.:	66154236 000010
Customer No.:	1764862

GMID:	2014685	Revision No.: 2
Material:	Carcal RF-06-03 K02N	
	54L KEG	
Cust. Mat.:		
Batch:	0000029075	
Dlvy. Qty:	216.0 L15	
Container ID:	COATES	
Ship from:	Harwich	Harwich, ES, United Kingdom Page: 1 / 2

Feature	Units	Results	Limits Minimum	Maximum	Method
Density 15° C	kg/m³	836.0	833.0	837.0	ASTM D4052
Density at 20° C	kg/m3	832.4			ASTM D4052
I.B.Pt.	° C	189.9			ASTM D86
10% v/v Recovered at	° C	216.4			ASTM D86
50% v/v Recovered at	° C	278.6	245.0	-	ASTM D86
90% v/v Recovered at	° C	332.0			ASTM D86
95% v/v Recovered at	° C	349.0	345.0	350.0	ASTM D86
F.B.Pt.	° C	355.5	-	370.0	ASTM D86
Cetane Number		52.2	52.0	54.0	ASTM D613
Aromatics by FIA	%(V/V)	22.5			ASTM D1319
Olefins by FIA	%(V/V)	5.6			ASTM D1319
Polycyclic Aromatic Hydrocarbons	%(m/m)	4.7	3.0	6.0	EN 12916
Water Content	mg/kg	110	-	200	IP 438
Strong Acid Number	mg	0.00 KOH/g	-	0.02	ASTM D974
Oxidation Stability	mg	< 0.1 /100ml	-	2.5	ASTM D2274
Copper Corrosion, 3hrs at 100° C	-	1B	-	-	ASTM D130
Viscosity at 40° C	mm2/s	2.941	2.300	3.300	ASTM D445
Sulphur content	mg/kg	1.0	-	10.0	ASTM D5453
Lubricity (WSD 1,4) at 60° C	µm	360	-	400	ISO 12156-1
Carbon Residue (on 10% Dist. Res)	%(m/m)	< 0.10	-	0.20	ASTM D4530
Ash	%(m/m)	< 0.001	-	0.010	ASTM D482
CFPP	° C	-18	-	-15	EN 116
Cloud Point	° C	-18			ASTM D2500
Gross Heat of Combustion	MJ/kg	45.80			IP 12
Net Heat of Combustion	MJ/kg	43.00			IP 12
Net Heat of Combustion	Btu/lb	18480			IP 12 / CALCULATION
Oxygen Content	%(m/m)	< 0.04			ELEMENTAL ANALYSIS

Haltermann Carless

Department of Mechanical Engineerin
Roberts Building
London WC1E 7JE

Delivery item/date
80162210 000010 / 17/03/2020

Page
2 / 2

Feature	Units	Results	Limits Minimum	Maximum	Method
Carbon Content	%(m/m)	86.78			ASTM D5291
Hydrogen Content	%(m/m)	13.22			ASTM D5291
Atomic H/C Ratio		1.8153			CALCULATION
Atomic O/C Ratio		< 0.0003			CALCULATION
C/H Mass Ratio		6.56			CALCULATION
Total Aromatic Hydrocarbons	%(m/m)	24.0			EN 12916
Water & Sediment	%(V/V)	< 0.010			ASTM D2709
Carbon Weight Fraction		0.8678			CALCULATION
Fatty Acid Methyl Ester (FAME) Content	-	None detected	-	-	EN 14078

COA Additional Information

The certificate is electronically generated and valid without signature.

Haltermann Carless UK Ltd.

For enquiries please contact Customer Service or local Sales

Figure 12.6: Haltermann Carless Certification of the reference fossil diesel.

12.5. Schematics & pictures of additional note

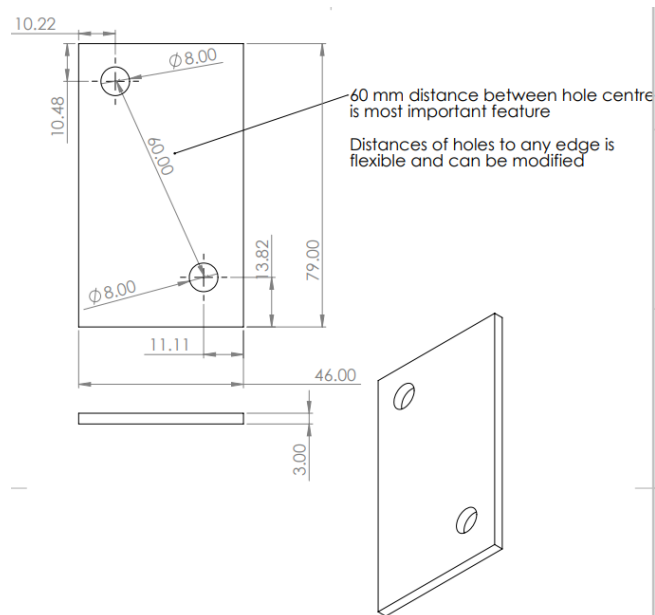*Figure 12.7: Piston head visible with engine head removed*

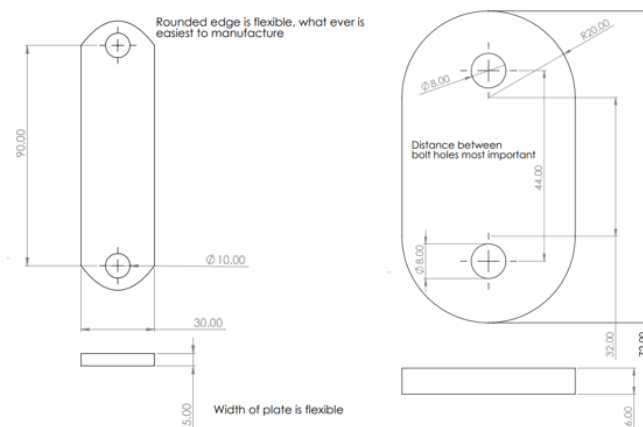*Figure 12.8: Blanking plate for coolant return from hydrocarbon after treatment.*

Figure 12.9: Air intake blanking plate (a) and oil breather tube blanking plate (b).

Figure 12.10: Steering manifold blanking plate with sealant to prevent oil leaks.

Kistler pressure transducer

Measuring range	bar	0…250
Calibrated partial ranges	bar	0…50, 0…100, 0…150, 0…250
Overload	bar	300
Sensitivity	pC/bar	≈-20
Natural frequency (measuring element)	kHz	≈160
Linearity, all ranges (at 23 ºC)	%/FSO	≤±0.3
Acceleration sensitivity axial radial	 mbar/g mbar/g	 <0.8 <0.5
Operating temperature range Temperature min./max.	ºC ºC	-20…350 -50…400
Sensitivity change 200 ºC±50 ºC 23…250 ºC	 % %	 ≤±0.5 ≤±2
Thermal shock error		

(At 1500 1/min, IMEP = 9	bar	≤±0.5
bar)	bar	≤±2
Δp (short-term drift)	bar	≤±1
Δp_{min}		
Δp_{max}		
Insulation resistance at 23 °C	Ω	$\geq 10^{13}$
Shock resistance	g	2000
Tightening torque	N m	1.5
Capacitance, without cable	pF	5
Weight with cable	grams	2
Connector, ceramic insulator	-	M4x0.35

Table 12.2: Design specifications for the Kistler type 6052C high temperature pressure sensor, taken from material provided with the sensor.
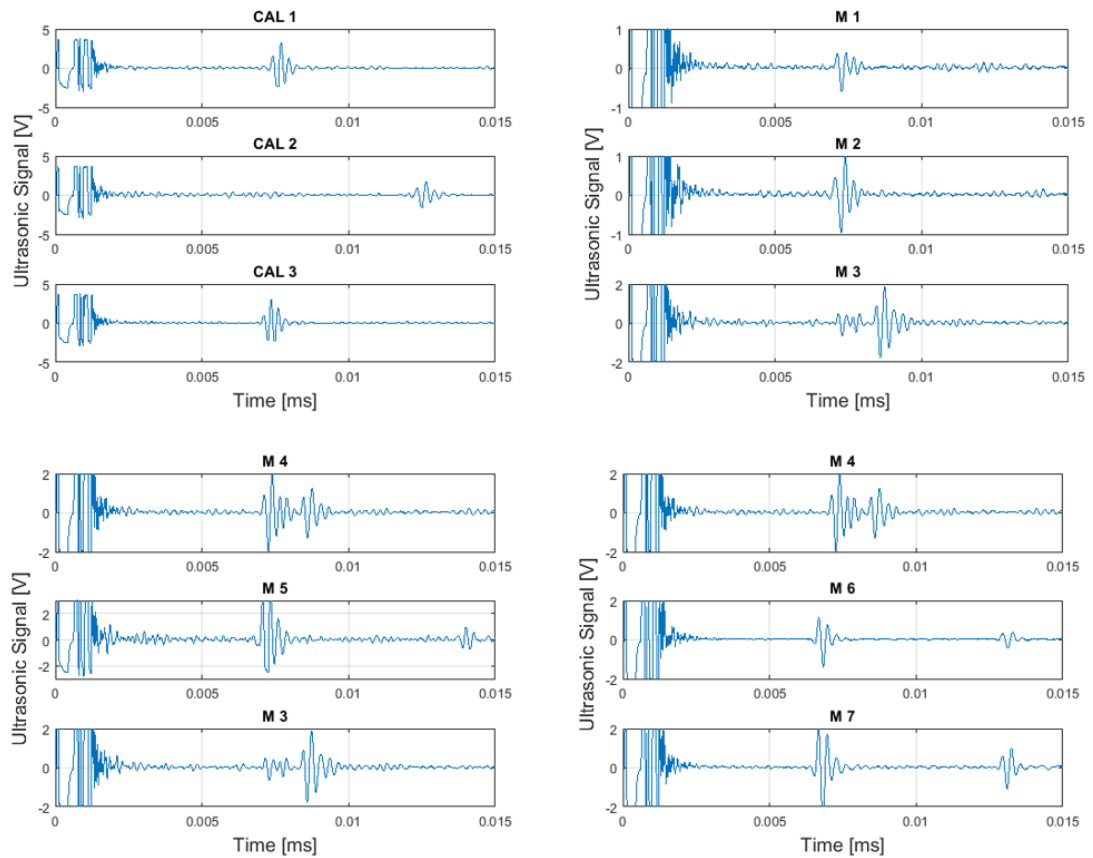

Figure 12.11: Ultrasonic signal tests to determine water / oil channel depth in D8k engine head.
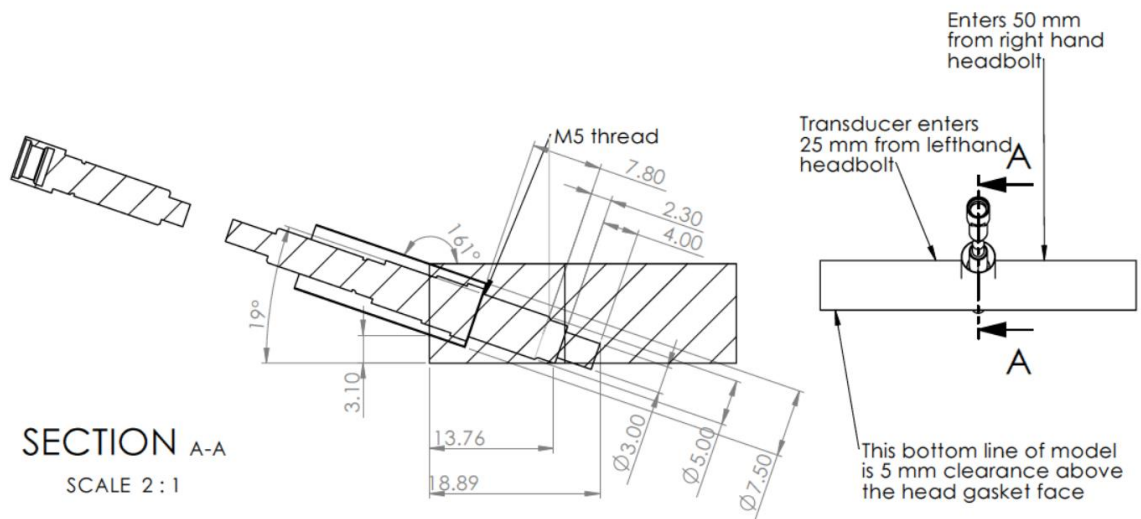
275

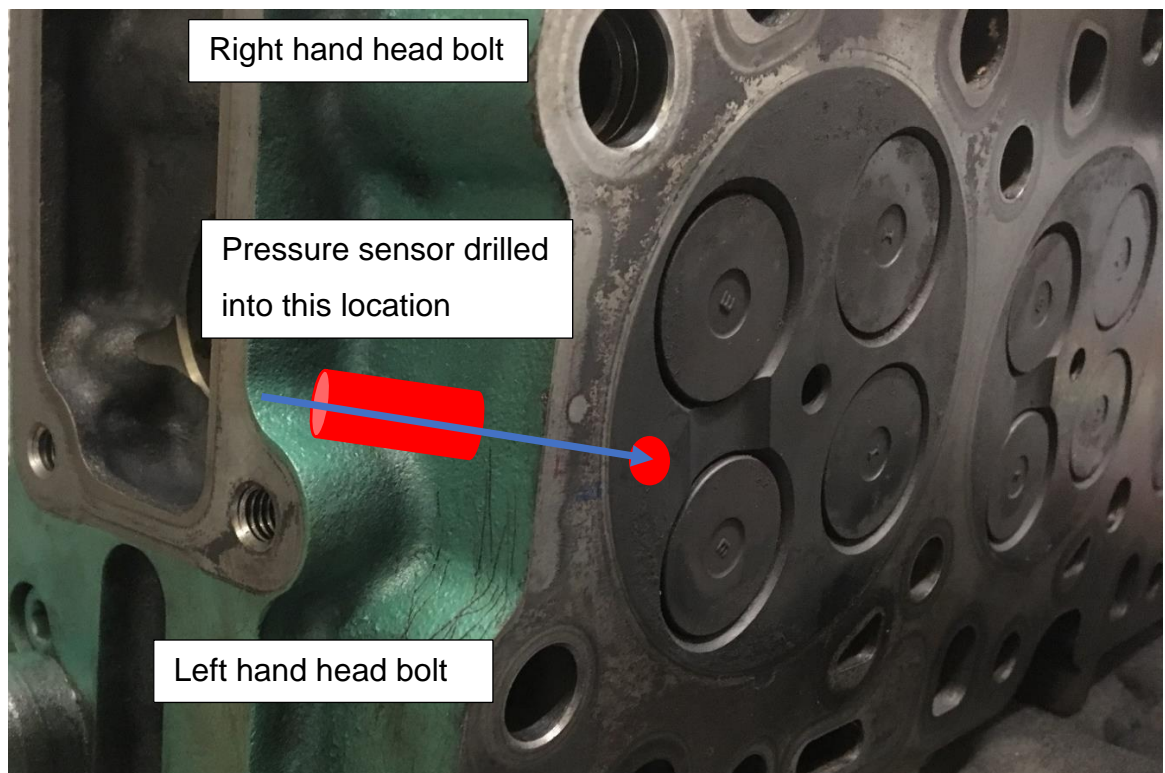*Figure 12.12: Simplified schematic view of the pressure transducer location*

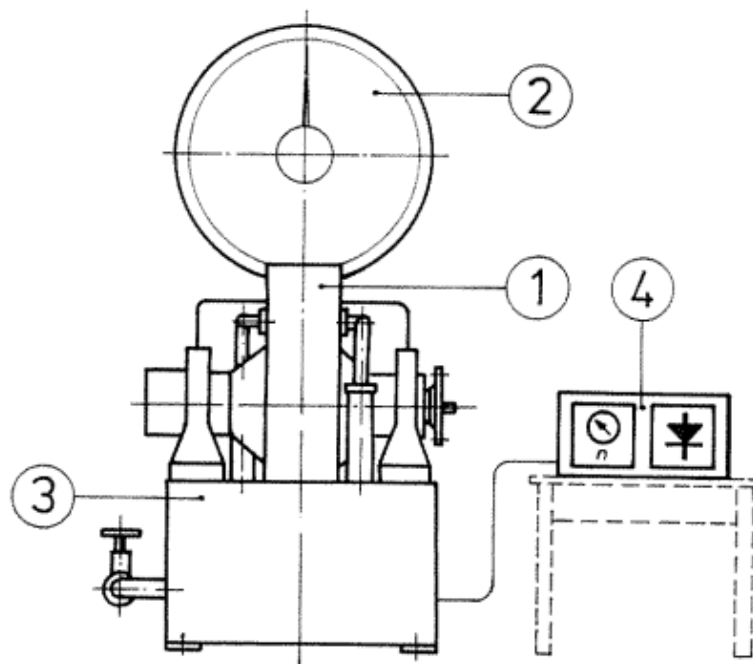*Figure 12.13: Simplified image of pressure transducer location*

276

Figure 12.14: Schematic view of the Schenk eddy-current dynamometer. 1, cradled dynamometer casing. 2, torque measuring equipment. 3, machine base. 4, control unit. Image taken from SCHENK Operating Instructions for Eddy Current Dynamometers, Size W130, Serial-No LW1037

Sketch 1: View of the Front Panel
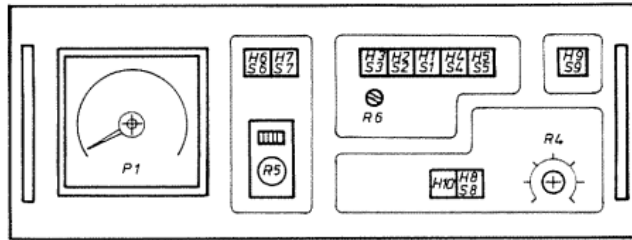
S9/H9 pushbutton with signal lamp (white): power on/off
H10   signal lamp (green): "ready for operation"
S1/H1 - S5/H5 pushbutton with signal lamp: characteristic
      curve
S6/H6 pushbutton with signal lamp: internal set point
      potentiometer (R5)

S7/H7 pushbutton with signal lamp: external setting of
      set point

S8/H8 pushbutton with signal lamp (red): "overspeed" with
      release pushbutton
P1   speed indicator
R4   potentiometer: max. speed
R5   potentiometer: internal set point
R6   potentiometer: steepness of the characteristic
      curve $\frac{\Delta M}{\Delta n}$

Sketch 2: View of the Multipoint Connector on the
          Rear Panel of the Control Unit
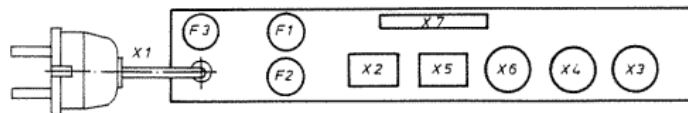
X1   mains connection
X2   connection for power supply to dynamometer
X3   connection for remote control
X4   connection for external setting of set point
X5   connection for safety equipment
X6   connection for measuring and monitoring units
X7   connection for data processing
F1/F2 mains fuses 16 Amp ultrarapid, F3 control fuse 0.5 Amp

Figure 12.15: Design of the Control Unit LSG 24/18. Image taken from SCHENK Operating Instructions for Eddy Current Dynamometers, Size W130, Serial-No LW1037.
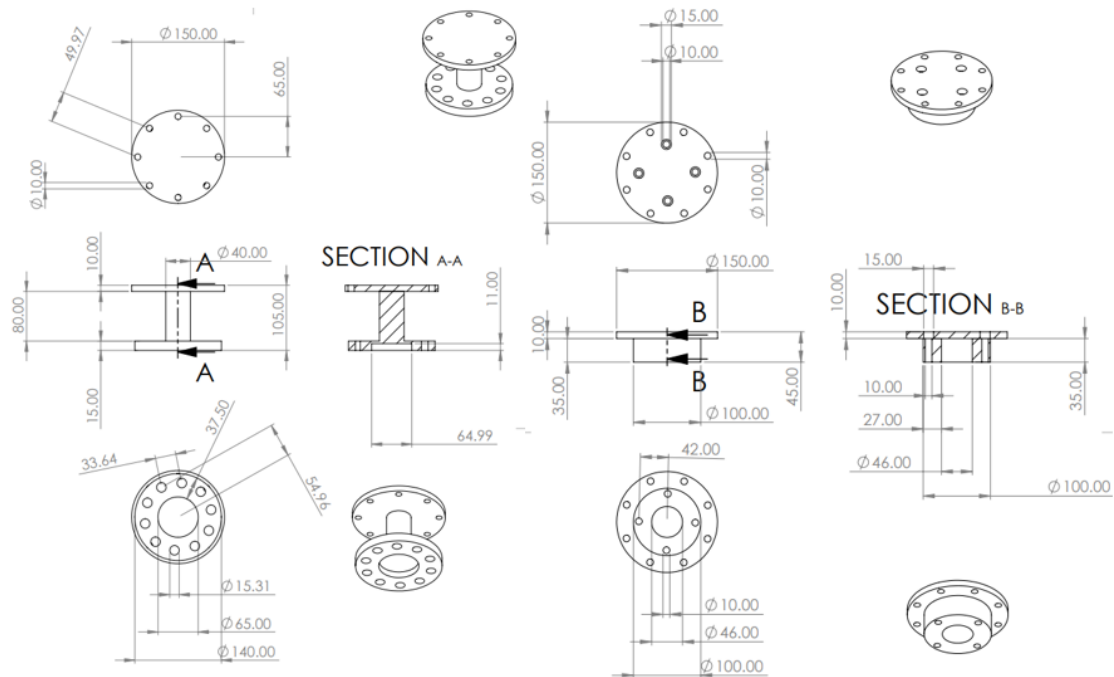
Figure 12.16: Design specifications of the flexible shaft coupling shaft. Diagram supplied by GKN powertrain

Figure 12.17: Flexible coupling unit adapter plate designs for connection to (a) the D8k flywheel and (b) the Eddy-current dyno.

EIL580-T - *OptoPulse®*

EIL580-T with through hollow shaft

Features

– **Size ø58 mm**
– **Precise optical sensing**
– **Output signal level TTL or HTL**
– **Through hollow shaft, ø8...15 mm**
– **Connection radial or tangential**
– **Pulses per revolution up to 5000**
– **High protection up to IP 67**
– **High resistance to shock and vibrations**

Technical data - electrical ratings	
Voltage supply	5 VDC ±5 % 8...30 VDC 4.75...30 VDC
Reverse polarity protection	Yes
Short-circuit proof	Yes (HTL) Yes (TTL, max. 1 s and 1 signal)
Consumption w/o load	≤70 mA
Pulses per revolution	100...5000
Phase shift	90° ±10°
Duty cycle	40...60 %
Reference signal	Zero pulse, width 90° ±10 %
Sensing method	Optical
Output frequency	≤300 kHz (TTL) ≤160 kHz (HTL)
Output signals	A+, B+, R+, A-, B-, R-
Output stages	TTL/RS422 HTL/push-pull
Interference immunity	DIN EN 61000-6-2
Emitted interference	DIN EN 61000-6-3
Approval	UL 508 / CSA 22.2

Technical data - mechanical design	
Size (flange)	ø58 mm
Shaft type	ø8...15 mm (through hollow shaft)
Protection DIN EN 60529	IP 65 (without shaft seal), IP 67 (with shaft seal)
Operating speed	≤3000 rpm (+20 °C, IP 67) ≤6000 rpm (+20 °C, IP 65)
Starting torque	≤0.025 Nm (+20 °C, IP 65) ≤0.03 Nm (+20 °C, IP 67)
Materials	Housing: aluminium die-cast Flange: aluminium
Operating temperature	-40...+85 °C
Relative humidity	90 % non-condensing
Resistance	DIN EN 60068-2-6 Vibration 30 g, 10-2000 Hz DIN EN 60068-2-27 Shock 250 g, 6 ms
Connection	Flange connector M12, 8-pin Flange connector M23, 12-pin Cable
Weight approx.	300 g

Figure 12.18: Baumer EIL580-T OptoPulse incremental shaft encoder design specifications
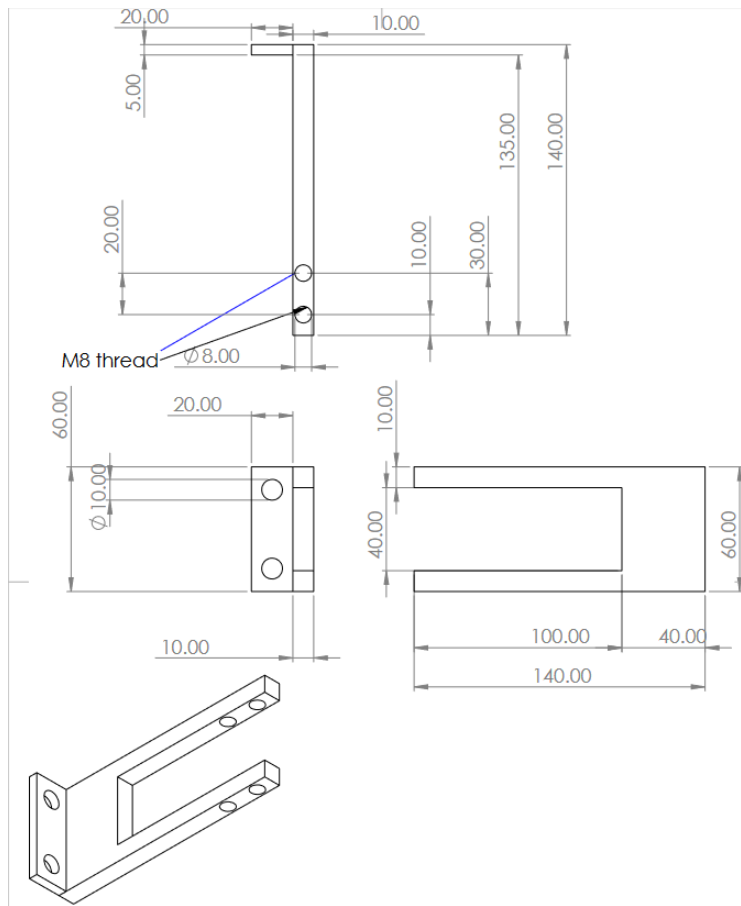
280

Figure 12.19: Metal prong design for fixing the crankshaft encoder in place.
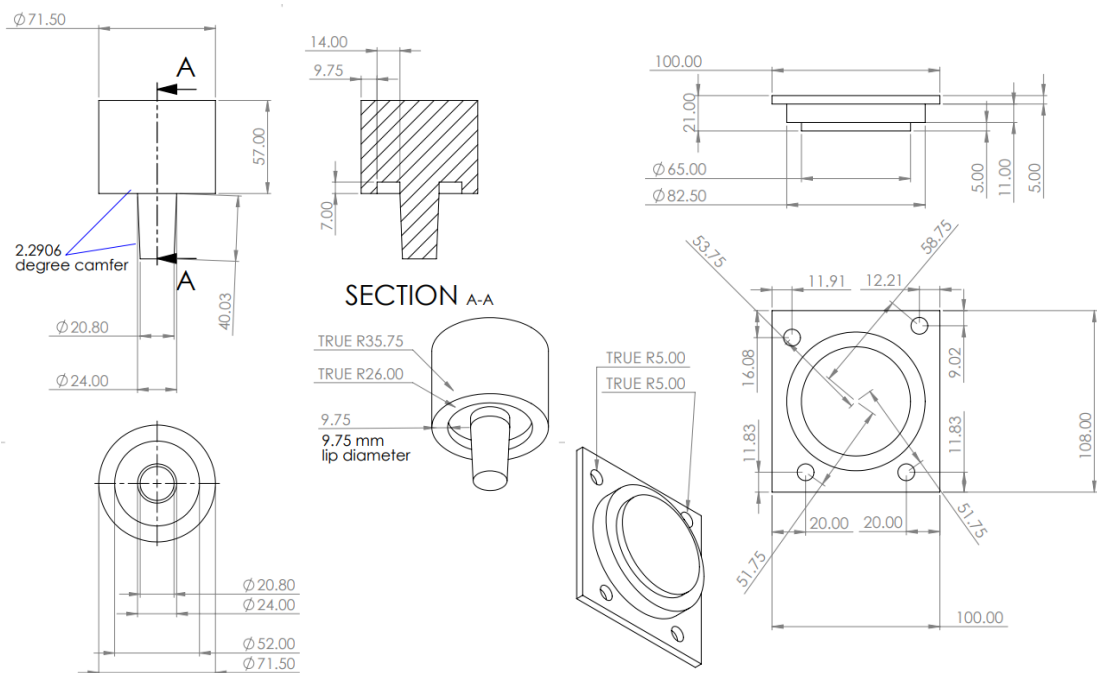

Figure 12.20: Acrylic plug for thermostat housing (a) and blanking plate for thermostat housing (b)

Figure 12.21: Oil spout for timing gears (a) and air compressor blanking plate (b).